Technische Universität München
Fakultät für Medizin

Immunoproteomic analysis of CNS lesions in a multiple sclerosis model

Dr. med. Daniel Engels

Vollständiger Abdruck der von der Fakultät für Medizin der Technischen Universität München zur Erlangung des akademischen Grades eines

Doctor of Philosophy (Ph.D.)

genehmigten Dissertation.

Vorsitzender: Prof. Dr. Thomas Korn

Betreuer: Prof. Dr. Martin Kerschensteiner

Prüfer der Dissertation:

1. Prof. Dr. Mikael Simons

2. Prof. Dr. Veit Rothhammer

Die Dissertation wurde am 21.01.2022 bei der Fakultät für Medizin der Technischen Universität München eingereicht und durch die Fakultät für Medizin am 31.03.2022 angenommen.

Table of contents

Abstract

Multiple sclerosis (MS) is an autoinflammatory disease of the central nervous system (CNS) and the most frequent cause of neurological disability in younger adults. Monocyte-derived mononuclear phagocytes are recruited from the peripheral blood, mature in the CNS parenchyma and contribute significantly to inflammatory lesions in the CNS, a hallmark of multiple sclerosis histopathology. Mononuclear phagocytes play crucial roles in tissue damage and repair. Previous studies on experimental autoimmune encephalomyelitis (EAE), an animal model of multiple sclerosis, have shown that macrophages acquire a pro-inflammatory phenotype (resembling M1 polarization) after migrating into the CNS and can switch to a putative reparative phenotype (resembling M2 polarization) during lesion recovery. Here, we aimed to further investigate the molecular phenotype and cell-cell communication pathways of these cells.

We used phenotype reporter mouse lines, cell sorting, quantitative mass spectrometry, next-generation sequencing and developed novel network-based computational algorithms (gene set enrichment analysis coupled to network analysis, *NezzworGS*, and functional protein-protein interaction coupled to network analysis, *FUPPINA*) to further analyze the molecular signatures of M1-like and M2-like macrophages in CNS lesions and decipher potential signaling pathways between macrophages and immune cells under neuroinflammatory conditions. We found gene sets related to immune cell signaling and proliferation enriched in M1 macrophage proteome and gene sets related to extracellular matrix organization, antigen presentation, G protein-coupled receptor signaling and the nervous system enriched in M2 macrophage proteome. Although the overall proteome-transcriptome correlation was low at single protein/transcript level, these gene sets were also enriched in M1 and M2 macrophage transcriptomes. Furthermore, we identified extracellular proteins, potentially secreted by M1 and M2 macrophages that could mediate the destructive and/or reparative effects of these polarization phenotypes. By measuring the proteomes of (infiltrating) immune cells in EAE (and healthy control) we unraveled possible ligand-receptor interactions between these cells and M1 and M2 macrophages, respectively.

In this study we identified molecular signatures of M1 and M2 macrophages as well as potential ligand-receptor interactions with other cell types that might serve as druggable targets in the context of neuroinflammation. These results further provide the basis for functional studies to comprehensively dissect the cellular interactions that drive formation and resolution of neuroinflammatory lesions.

Zusammenfassung

Die Multiple Sklerose (MS) ist eine chronisch-entzündliche Erkrankung des zentralen Nervensystems (ZNS) und die häufigste Ursache für neurologische Behinderungen bei jüngeren Erwachsenen. Aus dem Blut stammende mononukleäre Phagozyten werden rekrutiert, reifen im ZNS-Gewebe heran und tragen wesentlich zu den für die Multiple Sklerose typischen entzündlichen Läsionen im ZNS bei. Mononukleäre Phagozyten spielen eine entscheidende Rolle bei der Schädigung und Reparatur von Gewebe. Vorausgehende Beobachtungen bei der Experimentellen Autoimmun-Enzephalomyelitis (EAE), einem Tiermodell der Multiplen Sklerose, haben gezeigt, dass Makrophagen nach ihrer Einwanderung in das ZNS einen pro-inflammatorischen Phänotyp (M1-Polarisation) und im weiteren Krankheitsverlauf einen mit dem Gewebeaufbau assoziierten Phänotyp (M2-Polarisation) annehmen können. Ziel dieser Arbeit ist das bessere Verständnis des molekularen Phänotyps und der Zell-Zell-Kommunikationswege dieser Phänotypen.

Wir verwendeten Phänotyp-Reporter-Mauslinien, Durchflusszytometrie, quantitative Massenspektrometrie und *next-generation sequenzing* und entwickelten netzwerkbasierte bioinformatische Algorithmen (*gene set enrichment analysis coupled to network analysis, NezzworGS,* und *functional protein-protein interaction coupled to network analysis, FUPPINA*), um die molekularen Signaturen von M1- und M2-Makrophagen in ZNS-Läsionen weiter zu analysieren und mögliche Signalwege zwischen Makrophagen und Immunzellen unter neuroinflammatorischen Bedingungen zu entschlüsseln. Wir identifizierten molekulare Signaturen im Proteom der M1-Makrophagen, die mit der Signalübertragung und der Proliferation von Immunzellen zusammenhängen, sowie molekulare Signaturen im Proteom der M2-Makrophagen, die mit der Organisation der extrazellulären Matrix, der Antigenpräsentation, der Signalübertragung durch G-Protein-gekoppelte Rezeptoren und dem Nervensystem zusammenhängen. Obwohl die Korrelation zwischen Proteom und Transkriptom hinsichtlich der Protein- und RNA-Expression gering war, waren diese molekularen Signaturen auch in den Transkriptomen der M1- und M2-Makrophagen nachweisbar. Darüber hinaus identifizierten wir extrazelluläre Proteine, die möglicherweise von M1- und M2-Makrophagen sezerniert werden und die Effekte dieser Polarisierungsphänotypen vermitteln könnten. Durch die Messung der Proteome von (in das ZNS infiltrierenden) Immunzellen in der EAE (und in gesunden Kontrollen) konnten wir mögliche Liganden-Rezeptor-Interaktionen zwischen diesen Zellen und M1- bzw. M2-Makrophagen identifizieren.

In dieser Arbeit haben wir molekulare Signaturen von M1- und M2-Makrophagen sowie potenzielle Liganden-Rezeptor-Interaktionen mit anderen Zelltypen identifiziert, die möglicherweise als pharmakologische Zielstrukturen im Kontext neuroimmunologischer Erkrankungen dienen könnten. Diese Ergebnisse bilden die Grundlage für weitere funktionelle Studien, um die zellulären Interaktionen, die bei entzündlichen Läsionen eine wesentliche Rolle spielen, umfassend zu untersuchen zu können.

1 Introduction

1.1 Multiple sclerosis

Multiple sclerosis (MS) is a chronic autoimmune disease of the central nervous system (CNS) (1). It is the most common non-traumatic cause of neurological disability in younger adults (2). Although the prevalence and incidence of MS are continuously rising (3), the underlying disease mechanism remains uncertain (1).

The pathological hallmarks of MS are focal demyelinating lesions, immune cell infiltration and neurodegeneration. Lesions can be found both in the white matter and the grey matter of the brain and the spinal cord of MS patients (4). They can result in a diverse pattern of clinical signs and symptoms, depending on which structures of the CNS are affected. Most commonly, patients present with monocular visual impairment (optic neuritis), limb weakness (transverse myelitis), double-vision (brain-stem dysfunction) or ataxia (cerebellar lesions) (5, 6). Moreover, lesions can cause dysfunctions of the autonomic nervous system, such as bladder or bowel dysfunction, as well as psychic disorders, such as fatigue or depression (7–9).

In most cases, the first presentation of the disease is the clinically isolated syndrome (CIS). The CIS describes an acute impairment of neurological functions, which is termed ‘attack’ (10). About 50 % of the patients, who had suffered from a CIS, develop a second attack and are then diagnosed with MS. MS manifests in diverse disease entities. Most patients suffer from relapsing-remitting multiple sclerosis (RRMS). This entity is characterized by relapses followed by a symptom-free interval and a (partial) recovery from neurological deficits (remission). However, RRMS can transition to secondary-progressive multiple sclerosis (SPMS). SPMS features a gradual impairment of body functions, sometimes superimposed by relapses. Primary-progressive multiple sclerosis (PPMS) is yet another disease entity which is denoted by a gradual gain of deficits without acute relapses (11).

The treatment and disease management of MS is challenging. So far, there is no cure. However, since the mid-1990s there are more and more (pharmacological) treatment options available (4). Initially, interferons and glatiramer acetate were administered with the aim to reduce the relapse frequency as well as to delay the accumulation of disabilities. Over the time, various therapies have evolved and have been approved. Up till now, the pharmacotherapeutic arsenal spans from classical immunomodulatory agents, such as interferons, glatiramer acetate or dimethyl fumarate, to novel antibodies that specifically interfere with T or B cell function, such as natalizumab or ocrelizumab (12).

1.1.1 Signs and symptoms

Inflammatory lesions in MS can occur in any part of the CNS. Thus, the spectrum of signs and symptoms is broad. It ranges from motor and sensory to visual and autonomic dysfunctions. None of these signs and symptoms are disease-specific. However, Lhermitte’s symptom (neck flection that provokes electrical sensations running down the spine and limbs) and Uhthoff phenomenon (increase of body temperature which is accompanied by worsening of neurological symptoms) are clinical findings highly suspicious of MS (11). Furthermore, visual impairment (as a consequence of optic neuritis) is a frequent initial presentation of MS (13).

Ultimately, during the disease course of MS, patients can accumulate disabilities that originate from relapses followed by an incomplete recovery (as seen in RRMS and SPMS with superimposed relapses) or from a gradual worsening of symptoms (as seen in PPMS or SPMS without superimposed relapses). The Expanded Disability Status Scale (EDSS) is a tool which assesses the extent of MS-related disabilities in patients. It was introduced by Kurtzke in 1983 and has been frequently used as a clinical outcome parameter ever since (14, 15). The EDSS is an ordinal scaled rating system from 0 to 10 with 0.5 increments interval. 0 indicates a normal neurological examination, whereas 10 indicates death due to MS (15). In brief, the individual EDSS value is obtained by assessing the degree of disability in each Functional System (FS). According to Kurtzke, there are 8 FS: pyramidal, cerebellar, brain stem, sensory, bowel and bladder, visual, cerebral or mental and ambulation (14). The higher the degree of disability is within one FS and the more FS are affected, the higher the EDSS.

1.1.2 Epidemiology and risk factors

In 2016, the global estimated MS prevalence was 2,221,188 (95 % uncertainty interval = [2,033,866;2,436,858]). Compared to 1990 the prevalence has increased by 10.4 % (95 % uncertainty interval = [9.1;11.8]). However, MS prevalence estimates per 100,00 individuals were unequally distributed: In North America (164.6), western Europe (127.0) and Australasia (91.1) the prevalence was on average 47.2-fold higher than in eastern sub-Saharan Africa (3.3), central sub-Saharan Africa (2.8) and Oceania (2.0) (16). Thus, there is a tremendously lower prevalence in countries centered around the equator.

The gender ratio is approximately 3/1 (female/male) for RRMS and 1/1 for PPMS. The mean onset of disease is approximately 30 years (RRMS) and 40 years (PPMS), respectively (2, 16–18).

Up till now, no specific trigger of MS has been identified. Nonetheless, multiple risk factors of genetic and environmental nature have been described so far (5).

1.1.2.1 Environmental risk factors

Among all measured and reported environmental risk factors in MS, vitamin D deficiency, obesity (especially in early life), Epstein-Barr virus infection and cigarette smoking are the strongest predictors for the development of MS (19).

Munger *et al.* observed a relative risk to develop MS of 0.67 (95 % CI = [0.40;1.12]) in a study cohort that had higher vitamin D intake when compared to a matched cohort with lower vitamin D intake (20). Furthermore, in another prospective, nested case-control study, Munger *et al.* showed that higher 25-hydroxyvitamin D levels are associated with a lower MS incidence (OR = 0.69, 95 % CI = [0.36;-0.97]) (21). Salzer *et al.* observed similar effects in yet another study population (22). In summary, both ingested and endogenous vitamin D seems to lower the risk to develop MS. However, it remains unclear if this observation is independent from the geographic differences in the MS prevalence. The MS prevalence is associated with latitude. The closer to the equator an individuum lives, the lower his chance of developing MS is. In regions near the equator the UV light is more intense. Vitamin D metabolism critically depends on UV light. Thus, it remains unclear, if the association between low vitamin D levels and the risk of developing MS is confounded by latitude or UV light exposure (19). Swank *et al.* found that the MS prevalence in costal villages was lower when compared

to continental areas in a study cohort in Norway (23). At costal areas, the consumption of fish is higher. Fish is, especially at higher latitudes, an important source of vitamin D. This could on one hand explain Swank *et al.*'s finding and on the other hand support the hypothesis that vitamin D is latitude-independent protective substance (19).

Furthermore, Munger *et al.* observed an association between BMI and the risk of MS in the same study cohort that showed the association between high vitamin D intake or blood levels and the diminished risk to develop MS (24). The relative risk (RR) of women who had a body mass index (BMI) ≥ 30 kg/m^2 at the age of 18 to develop MS was increased (RR = 2.25, 95 % CI = [1.50;3.37]) when compared to women with normal weight. However, older or younger obese women did not have a higher risk. To further investigate if there was an elevated risk of developing MS for obese children, Munger *et al.* conducted a prospective cohort study (25). They observed an association between obesity in childhood and the risk to develop MS.

The prevalence of infectious mononucleosis, caused by Epstein-Barr virus, especially in early childhood, is latitude-dependent, similar to the MS prevalence (19, 26). It is assumed that infections that occur in early life shift the immune response which could increase the risk to develop autoimmunity in future life (27, 28). Indeed, nested case-control studies proved that the EBV nuclear antigen 1 (EBNA-1) antibody titer predicts the risk of developing MS (29–32). Notably, this association is independent from gender and ethnicity (33). However, the increase of the EBNA-1 antibody titer could be confounded by the presence of subclinical MS in these patients. Subclinical MS could provoke a latent immune response that elevates the concentration of EBNA-1 antibodies (among other antibodies). Levin *et al.* addressed this question in the U. S. military study and followed-up seronegative individuals (34). They showed that all individuals who developed MS had their first symptoms after seroconversion, which denotes the EBV infection. Taken together, this proofs that EBV infection (and the EBNA-1 antibody titer) is a risk factor for developing MS.

For the first time, the evidence for the association between cigarette smoking and the risk to develop MS arose from an exploratory study in Israel (35). Further prospective, case-control and population-based studies confirmed the association (36–41). Some studies showed that cigarette smoking has an unequal impact among females and males: the relative risk in men is higher (1.6 – 2.8) when compared to women (1.0 – 1.4) (19). Furthermore, not only the risk of developing MS is higher for smokers, but also the risk of worsening MS symptoms (42) as well as converting from CIS to MS (43) or RRMS to SPMS, respectively (41, 44).

1.1.2.2 Genetic risk factors

Besides environmental risk factors, genetic risk factors are likely to play a role in MS. This hypothesis arises from the fact that individuals who have first-degree relatives being affected have a 2 to 4 % risk to develop multiple sclerosis. In contrast, the natural risk is assumed to be about 0.1 %. The risk of recurrence of MS within families depends on the genetic sharing (45): In monozygotic twins the concordance is 30 – 50 %, 6 % in dizygotic twins and 3 % in siblings (5). Regardless of the MS phenotype, the familial MS prevalence is approximately 13 % (45, 46).

In order to elucidate the relationship between MS risk and genetic profile, genome-wide association studies (GWAS) have been performed. GWAS identified more than 200 genes that

contribute to varying extends to the risk of MS (47). A major share of these genes is associated with the immune system. Most polymorphisms, which were identified in the GWAS, affect genes that encode proteins crucial for immune cell function: *HLA* genes (including *HLA- DRB1*15:01*), *IL2*, *IL17*. *IL-2* and *IL-17* are important cytokines for the regulation of encephalitogenic T cells (48, 49). Other polymorphisms affect cytokines of the innate immunity, e. g. genes that encode proteins that mediate tumor necrosis factor (TNF) (45). Studies showed that *HLA- DRB1*15:01* polymorphisms can interact with environmental risk factors: Cigarette smoking (50), adolescent obesity (51) and EBV infections (52) synergize with the genetic risk due to *HLA- DRB1*15:01* polymorphisms. Likewise, polymorphisms in genes that are involved in vitamin D metabolism (*GC* and *CYP24A1*) can increase the risk to develop MS (53).

1.1.3 Clinical manifestations

MS has various disease entities which reflect the time of onset, degree of disability as well as presence or absence and, if present, temporal sequence of attacks. The diagnostic criteria were defined by the International Panel on Diagnosis of Multiple Sclerosis in the form of the McDonald criteria whose latest version was released in 2017 (10).

The most common disease phenotype of MS is the relapsing-remitting form (RRMS). It affects approximately 85 % of the patients who are diagnosed with MS (17, 54). This phenotype is characterized by an alternation of relapses and remissions. Originally, Jean-Martin Charcot defined a relapse as a focal functional deficit of a white matter tract that lasts for at least 24 hours. It must not have an alternate explanation (55). The histological correlates are inflammatory demyelinating lesions in any part of the CNS (56). The frequency of relapses varies from 0.46 – 1.8 (mean = 1.5) relapses per year (54). However, immunomodulatory treatment can reduce the relapse frequency (57). A relapse is followed by either a complete or partial recovery of neurological functions. Incomplete recoveries might impact the long-term functional outcome of patients with RRMS (56, 58). Although relapses mostly recover spontaneously, there is an increasing body of evidence that an early and aggressive immunosuppressive therapy (e. g. with corticosteroids) can improve the long-term outcome (54, 59). This strategy might reduce the chance of remaining residual neurological deficits after a relapse. The fear of relapses is considered as one of the most burdensome disease features of MS for the patients. Thus, an adequate treatment that aims to reduce the relapse frequency not only preserves body functions but also reinforces the patients' control over the disease (60, 61).

The secondary-progressive phenotype of multiple sclerosis (SPMS) is characterized by a gradual worsening of symptoms, emerging from an initial relapsing-remitting disease course (62). In addition, the response to the anti-inflammatory pharmacotherapy is decreased (63). The median time from the diagnosis to the development of SPMS is 19 years, the mean age of patients is 40 years. SPMS occurs in 75 % of the patients who have been initially diagnosed with RRMS (17). While 12.1 % of the patients convert to SPMS within the first 5 years from diagnosis, 88.9 % have converted after being diagnosed for more than 26 years (64). In addition to the continuous worsening of neurological deficits, relapses can superimpose the disease course. The relapses in SPMS occur more frequently close to the transition point from RRMS to SPMS (17, 18). *Per se*, there are no variables that can predict the disease progression and extend of disability. However, studies have shown that young (65) and female (66) patients are less prone to develop an irreversible disability. Likewise, a longer period between relapses

as well as a lower overall number of relapses might predict a later conversion into SPMS (67). In contrast, T2 hyperintense MRI lesions, whose presence correlate with the disease course in the early disease phase, fail to predict a clinical outcome in the secondary progressive phase. However, T1 hypointense MRI lesions and radiographic signs of atrophy match with the gradual increase of disabilities in SPMS (68, 69).

It is believed that axonal loss plays a crucial role in the MS disease progression, especially in the context of SPMS. MRI and histopathological findings based on electron microscopy of CNS tissue of MS patients revealed that the axonal density reversely correlates with the number of lesions (63, 70). Radiographic signs of spinal cord (71) or brain (72, 73) atrophy correlate with the EDSS score as a surrogate for the degree of disability. In addition, these observations are believed to be an indication for axonal loss to be among the underlaying mechanisms of MS-associated disability (63). In addition, the axonal pathology in SPMS was assessed when N-acetyl aspartic acid (NAA) was measured by magnetic resonance spectroscopy (MRS). NAA is considered as an axon-specific marker. In acute MS stages, there was a reduction of NAA which was reversible (74). However, when looked at chronic lesions, the NAA reduction was also detected in normal-appearing white matter (75, 76). Thus, brain and spinal cord atrophy, which is thought to be secondary to axonal loss, can underlie disease progression.

10 – 15 % of all MS patients show a gradual worsening of symptoms from the time on they are diagnosed (17, 77, 78). This MS phenotype is termed primary-progressive multiple sclerosis (PPMS). PPMS shows a faster progression when compared to SPMS. Superimposed relapses occur in 40 % of the patients (17). The mean age of onset of disease is higher when compared to RRMS (40 years *versus* 30 years) (78). The disabilities predominantly arise from an impaired corticospinal tract and are more severe when compared to RRMS or SPMS (79). Signs of cortical demyelination and an early spinal cord atrophy is are more common in PPMS when compared to RRMS (77). The gender ratio is balanced (78). Predictable factor are unknown so far (17, 80).

1.1.4 Diagnosis

Most patients initially present with an attack. An attack is defined as

> *"a monophasic clinical episode with patient-reported symptoms and objective findings typical of multiple sclerosis, reflecting a focal or multifocal inflammatory demyelinating event in the CNS, developing acutely or subacutely, with a duration of at least 24 h, with or without recovery, and in the absence of fever or infection. Attack, relapse, exacerbation, and (when it is the first episode) clinically isolated syndrome are synonyms." (10)*

The further diagnostic workup for patients suspected of MS encompasses clinical, imaging and laboratory testing. In principle, these tests aim to resolve a dissemination in time and a dissemination in space of MS-specific lesions (and symptoms) according to the revised McDonald criteria (10). The dissemination in space can be inferred from the presence of more than one lesion site (and its topological symptom) or abnormal MRI finding at multiple CNS areas. The lesion sites are defined as juxtacortical, periventricular, infratentorial or spinal (12). If there are lesions in at least two out of four

sites, the criteria of dissemination in space will be fulfilled. The dissemination in time can be inferred from a history of more than one attack or the presence of CSF-specific oligoclonal bands. The presence of oligoclonal bands is a strong predictor of the risk for a second attack, independent from MRI findings (81–84). Additionally, other possible explanations for the clinical presentation must be ruled out (such as infections, vascular or primary neurodegenerative diseases). These aspects are summarized by the revised McDonald Criteria (10).

1.1.5 Treatment and disease management

The treatment of MS is built on three pillars: treating acute attacks, reducing the disease activity with disease-modifying therapies and ameliorating symptoms (2).

In general, disease-modifying therapies encompass immunomodulatory drugs, immunosuppressants and immune reconstitution drugs (1). The goal of the pharmacotherapy with these substances is to reduce the rate of relapses, reduce the number of lesions (as observed by MRI) and, ultimately, delay the overall gain of disability (2). In other words, this strategy aims to achieve 'no evidence of disease activity' (NEDA). NEDA is a scoring system that stratifies the MS disease activity by assessing the absence of clinical (NEDA-1 and -2), radiological (NEDA-3 and -4) and laboratory (NEDA-5) disease parameters (1, 15, 85).

1.1.5.1 Treatment of attacks

Acute attacks are most effectively treated intravenously with corticosteroids such as methylprednisolone (4, 86, 87). However, the long-term benefit (when compared to placebo) is subtle: Beck *et al.* assessed the effect of corticosteroids on the recovery of visual loss due to optic neuritis. Although visual function recovered faster in the corticosteroid group, the visual field, contrast sensitivity and color vision were only slightly better in the treatment group when compared to the placebo group (88). A meta-analysis by Miller *et al.* unraveled that high dose methylprednisolone treatment *versus* placebo achieved a mean increase of the EDSS of 0.76 (89). An escalating treatment option for acute relapses is plasmapheresis (90, 91). This therapy can reduce acute deficits, however, it fails in preventing subsequent disease activity (11).

1.1.5.2 Disease-modifying therapies

The basic idea of disease-modifying therapies is to decelerate disease progression and, ultimately, prolong the relapse-free interval and, thereby, reduce the chance to accumulate neurological deficits over the lifetime. Likewise, it is believed that the conversion from a CIS to MS is delayed when the patient is treated adequately. However, only little is known to which extend these drugs can improve the long-term clinical outcome of patients (11). While interferons, glatiramer acetate, dimethyl fumarate and teriflunomide are considered as milder agents with less (severe) side effects (category I), Fingolimod, ozanimod, ponesimod, siponimod and cladribine (category II) as well as natalizumab, ocrelizumab and alemtuzumab (category III) can more effectively reduce the annualized relapse rate and are therefore used for RRMS patients with more severe disease activity or with therapy failure (12).

Since the mid-1990s there are two substances available for the treatment of RRMS: interferons and glatiramer acetate (4). The CHAMPS, ETOMS and BENEFIT trial showed that the conversion rate (from CIS to MS) can be reduced from 45 – 50 % (placebo group) to 28 – 35 % (intervention group) by the administration of interferon (92–94). However, the long-term outcome is only mildly improved (11). Interferons bear the risk that patients can develop neutralizing antibodies that make a treatment less effective. This phenomenon can be observed in about 5 % of all recipients (95). Glatiramer acetate, dimethyl fumarate as well as teriflunomide are other category I immunomodulatory agents which can reduce the annualized relapse rates of RRMS patients similar to interferons (4, 96, 97). If these treatment approaches fail or the patient initially presents with a severe disease activity, treatment escalation will be justified (12).

Fingolimod, ozanimod, ponesimod and siponimod are sphingosine 1-phosphate receptors that are crucial for lymphocyte trafficking. Therefore, blocking of sphingosine 1-phosphate receptors leads to a reduced infiltration of lymphocytes into the CNS. Fingolimod showed a reduction of the annualized relapse rate of 0.4 when compared to placebo. Moreover, it reduced the cumulative probability of disease progression in a concentration-depended fashion in RRMS patients (from 24.1 % to 17.7 % and 16.6 %, respectively) (98, 99). The effectiveness was superior to interferon treatment (100). Ozanimod, like fingolimod, is a sphingosine 1-phosphate receptor modulator. Cohen *et al.* showed similar effects for ozanimod as previously observed for fingolimod in patients with RRMS (101). Ponesimod is a third sphingosine 1-phosphate receptor modulator approved for RRMS (102). Siponimod, unlike all other sphingosine 1-phopsphate receptor modulators, is also approved for treating SPMS (103). Giovannoni *et al.* reported that cladribine, an immunosuppressant agent which targets specific lymphocyte subpopulations, reduces the annualized relapse rate and prolongs the relapse-free interval in RRMS patients (104).

Natalizumab and ocrelizumab are two monoclonal antibodies that interfere with the migration of lymphocytes into the CNS through an antagonism of the glycoprotein alpha4 integrin (natalizumab) (105, 106) or deplete the B cell repertoire (ocrelizumab) by opsonizing CD20 molecules (107, 108). Despite its great efficacy in reducing the annualized relapse rate, as observed in the AFFIRM (105) and SENTINEL (109) trial, the use of natalizumab is reluctant. If natalizumab inhibits glycoprotein alpha4 integrin, $CD4^+$ T cells cannot migrate into the CNS anymore. Among other functions, $CD4^+$ T cells are crucial to monitor virus infections. Therefore, by decreasing the number of $CD4^+$ T cells in the CNS, the risk of a JC virus reactivation and the development of its associated disease, progressive multifocal leukoencephalopathy (PML), is increased (110). To date there is no evidence that ocrelizumab would bear a significant PML risk compared to other treatments (except of natalizumab). However, it can cause higher susceptibility for infections due to hypogammaglobulinemia, a side effect that has to be monitored closely. Ocrelizumab is administered intravenously in a six-months period. Ofatumumab, a novel monoclonal antibody directed against CD20, is an ocrelizumab-like agent that is administered subcutaneously once per month. It showed a higher reduction in the annualized relapse rate when compared to teriflunomide in the ASCLEPIOS I and ASCLEPIOS II trials and is considered to be an alternative to ocrelizumab to treat patients with highly active RRMS or active SPMS (111). Alemtuzumab is considered as third line therapy if treatment with natalizumab or ocrelizumab fails (12).

So far, ocrelizumab is the only available treatment option for PPMS. Pharmacological treatment options for SPMS encompass interferon beta (if SPMS is superimposed by relapses), siponimod (for active SPMS characterized by clinical or MRI progression) and mitoxantrone (for highly active SPMS leading to significant disabilities within a short interval) (12). Glatiramer acetate and interferons are first line therapy options for patients with CIS (12).

1.1.5.3 Symptoms management

The fact that MS is a burdensome disease, not only for the patients but also for their socioeconomical environment (112), is probability not least based on the severe comorbidities which MS is associated with. Besides sensorimotor dysfunction, MS patients can suffer from bladder dysfunction, neuropathic pain, cognitive impairment, fatigue, anxiety, depression and insomnia (1). Moreover, spasticity is a common problem that approximately 90 % of all MS patients have to face during their lifetime (113). All of these symptoms should be addressed adequately by a multimodal treatment strategy that comprises pharmacological intervention, physiotherapy and psychotherapy (11, 113).

1.1.6 Animal models of multiple sclerosis

Analyzing human tissues, cells or body fluid samples can be valuable puzzle pieces to better understand by which mechanisms diseases are caused or which variables can influence disease progression. However, in the context of MS, the access to human CNS tissue samples is limited. Samples from autopsies and biopsies might not reflect the actual stage of the disease since they are obtained at externally define timepoints. Thus, the use of animal models can be justified.

In experimental autoimmune encephalomyelitis (EAE), an animal model of MS, an autoimmune CNS attack is considered as being responsible for the demyelination and neurodegeneration (114). For that reason, EAE is a widely used model for MS (115, 116). In theory, EAE can be induced in any vertebrate (114). Autoreactive T cells (T_h1, T_h17 $CD4^+$ T cells and CD8 T cells), which are often targeted against myelin epitopes, are required to induce EAE. The formation of autoreactive T cells can be initialized either actively by immunizing animals with antigens or passively by transferring previously engineered autoreactive T cells into the animal (114, 117, 118). For the active immunization either myelin basic protein (MBP), proteolipid protein (PLP) or myelin oligodendrocyte glycoprotein (MOG) can be used. MOG is believed to be the most popular antigen (114) because it reliably leads to a monophasic disease when one-time injected (119) as well as to a prolonged disease when injected with a higher dose or more frequently (120). After 10 – 17 days in the active immunization model and 5 – 7 days in the cell transfer model, the recipient organism develops first disease symptoms (114). Regardless the nature of the disease induction, disease onset is characterized by a perivascular infiltration of mononuclear cells into the white matter (121). At the peak of the disease axons are demyelinated and destructed (122). EAE lesions are observed predominantly in the spinal cord and optic nerve and only sparsely present in the brain (120). Although EAE provides a full spectrum and controllable progress of an immune-mediated demyelinating disease, it comes with limitations: In EAE, $CD4^+$ T cells are the key players that initialize and maintain the disease (123). In contrast, $CD8^+$ T cells and B cells are also dominant cell types that drive neuroinflammation in human pathology (124). Despite the differences between MS and EAE, EAE is believed to be a powerful tool to study disease

mechanisms, to screen for effects of drugs on neuroinflammation and to identify molecules that are critical for neuroinflammatory interactions (125).

1.2 Immunopathology of multiple sclerosis

The strong association of polymorphisms in genes which encode proteins involved in the immune systems suggests that the demyelination and axon damage, as observed in MS, are caused by the organism's own immune system. In recent decades, this hypothesis has been supported by numerous histopathological and experimental studies.

1.2.1 Histopathology

Early disease stages of MS, such as CIS and (early) RRMS, are associated with white matter lesions. These lesions show demyelination, oligodendrocyte loss, reactive gliosis and neuro-axonal degeneration. They are located in the brain, spinal cord and optic nerve, according to the clinical phenotype (45). Despite the precise anatomical (lesion location) and functional relationship, the volume of the lesion only moderately correlates with the severity of disability or cognitive impairment (126, 127). Consequently, it is believed that other mechanisms contribute to the gain of disability, too. Among these, grey matter lesions and normal-appearing white matter (NAWM) damage are suggested to play a crucial role (45).

1.2.1.1 White matter lesions

White matter lesions are found throughout all entities and disease stages of MS. There are different lesion types: active lesions, which are predominantly found under acutely inflamed conditions (e. g. during attacks), and chronic active as well as inactive lesions, which can be detected predominantly in SPMS and PPMS patients (45). Active lesions are comprised of an infiltration of circulating immune cells and (activated) glial cells, such as $CD8^+$ T cells, $CD20^+$ B cells, fewer $CD4^+$ T cells, activated microglia, macrophages and reactive astrocytes. In *post mortem* studies, chronic active lesions accounted for about 30 % of all histopathological lesions (128). They are characterized by a constant subtle open blood-brain barrier and accumulation of macrophages and microglia at the lesion edge while showing a hypocellular lesion center. Furthermore, reparative mechanism seem to fail within these lesion types (128, 129). Inactive lesions lack macrophages and feature a lower density of lymphocytes. However, they contain demyelinated and damaged axons and reactive gliosis (130–134). Despite the abundance of inactive lesions in SPMS and PPMS, active lesions or mixed lesions can make up to 57 % of all lesions in SPMS or PPMS, highlighting a significant contribution of inflammatory processes to the disease progression (45). Consistent with this concept, Luchetti *et al.* showed that mixed active/inactive lesions correlate with disease severity in progressive phenotypes of MS (135).

1.2.1.2 Normal-appearing white matter

Normal-appearing white matter (NAWM) is white matter that macroscopically appears to be normal. However, in MS patients it is characterized by diffuse immune cell infiltrations, neuro-axonal damage and gliosis (131, 136). These changes are observed more frequently in progressive MS entities. Previously, alterations to NAWM were considered to result from a mechanism which occurs secondary

to the initial white matter lesion and axonal damage. However, the correlation of number, size and location of both lesion types is poor (136). Thus, changes to the NAWM is suggested to be an independent histopathological hallmark (137).

1.2.1.3 Grey matter lesions

The earliest stages of MS denote grey matter lesions, preferentially observed in the neocortex and the cerebellum as well as archiocortical and deep grey matter structures (such as the basal ganglia, substantia nigra, and amygdala) (138). Depending on their (microscopic) localization, grey matter lesions are categorized in 3 types. Type I is located at the cortico-subcortical border, involving both grey and white matter. Type II lesions are perivenous lesions that occur exclusively in the grey matter. Type III lesions are subpial lesions that spread inward and are often associated with meningeal inflammation. As for NAWM, grey matter lesions are more widespread in SPMS and PPMS patients, affecting up to 60 % of the cortex (45).

1.2.2 Immune pathophysiology

Histopathological assessment of CNS tissue from MS patients provides strong evidence that the immune system is directly involved in the pathogenesis of MS. Not only cells of CNS resident immunity, represented by microglia and, to a lesser extent, astrocytes, but also peripheral immunity, represented by lymphoid (T and B cells) and myeloid cells (mononuclear phagocytes) are detected in MS lesions (130). Thus, the questions arise how and why these cells are targeted to the CNS, how neuroinflammation is maintained and resolved and, ultimately, how this vicious circle can be disrupted.

1.2.2.1 Autoimmunity

There is evidence that MS is an autoimmune disease. It is suggested that autoreactive T cells can become activated, migrate into the CNS and initiate demyelination accompanied by neuro-axonal damage (139).

The autoimmunity hypothesis is supported by e. g. findings from Pette *et al.* who identified MBP-specific T cells in peripheral blood mononuclear cells (PBMC) from MS patients (140). It is believed that T cells either fail to tolerate self-antigens due to dysfunctional central tolerance mechanisms or that they are skewed in the periphery due to impaired peripheral tolerance mechanisms. Both could trigger an autoimmune response with tissue inflammation (139).

A second piece of evidence arises from a (failed) clinical trial with altered peptide ligands (APL). APLs were designed to stimulate or inhibit T cell receptors (TcR) with the goal to abrogate encephalitogenic T cell function. Unfortunately, the clinical trial with MBP83–99, an APL that mimics MBP, failed in a sense that it led to an exacerbation of previously diagnosed MS (141). Consequently, T cells can be stimulated peripherally against CNS epitopes such as MBP and induce CNS autoimmunity (139).

Experimental autoimmune encephalomyelitis (EAE) denotes major histopathological features of MS (see 1.2.1) and is commonly used as a model to mimic neuroinflammation and immune-induced demyelination (142). In EAE, which is initiated by active immunization with a CNS-specific antigen, such as MBP, MOG or PLP, peripheral myelin-specific autoreactive T cells recognize the antigen as foreign

and expand in lymphoid tissues (143). After their activation in the periphery is completed, they are able to pass the blood-brain barrier and migrate into the CNS. In contrast, unstimulated T cells cannot cross the blood-brain barrier (144). This sequence, from external introduction of the antigen to neuroinflammation, shows that T cells can acquire an autoreactive phenotype which originates in peripheral immune compartments (139).

Taken together, there are several lines of evidence that support the notion that MS is an autoimmune disease triggered by autoreactive T cells. However, T cells are not only responsible for the whole spectrum of the histopathological and clinical phenotype of the disease. They rather initiate a sophisticated cascade of immune reactions involving other lymphoid as well as myeloid and CNS-specific cell types.

1.2.2.2 T cells

As aforementioned, T cells and T cell autoreactivity in particular play a central role in the pathophysiology of MS. Aberrant T cell activation is believed to be a critical trigger for autoreactivity. Aberrant T cell activation can be explained by the following pathophysiological hypotheses.

First, an imbalanced relationship between $CD4^+CD25^+Foxp3^+$ regulatory T (T_{reg}) cell function and CNS-specific effector T cells can lead to an exuberant effector T cell function that can cause neuroinflammation. Classically, $CD4^+CD25^+Foxp3^+$ regulatory T cells can inhibit autoimmunity by mediating effector T cell function and thereby reduce tissue damage (145). Thus, if T_{reg} cell function was impaired, effector T cells could injure tissues (146, 147). Indeed, Viglietta *et al.* and Frisullo *et al.* observed that the abundance and function of $CD4^+CD25^+$ T_{reg} cells was diminished in circulating cells from MS patients (148, 149). Likewise, $CD46^+$ induced type I regulatory cells, $CD39^+$ T_{reg} cells, $IFN\gamma^+$ T_{reg} cells and follicular T_{reg} cells, which are anti-inflammatory T cell subtypes, are less abundant among PBMC in MS patients (150–152).

Second, in contrast to a (functional) reduction of anti-inflammatory T_{reg} cells, the number of pro-inflammatory effector $CD4^+$ T cells, which express IL-17, and $CD8^+$ T cells might be elevated PBMC fractions in MS patients. IL-17-expression $CD4^+$ T cells, also termed T_h17 cells, are able to cross the blood-brain border, damage neurons and recruit more $CD4^+$ T cells in the CNS (153). Kebir *et al.* showed that blood lymphocytes sampled from MS patients are more prone to acquire a T_h17 phenotype. Moreover, Kebir *et al.* identified T cells co-expressing IL-17 and IFNγ in brain tissue of MS patients (154). Thus, skewing $CD4^+$ T cells to a T_h17 phenotype is considered to be a significant contribution to MS pathogenesis (155).

Third, aberrant T cell activation requires antigen presentation. In principle, B cells and myeloid cells are competent to present antigens. However, up till now it is not clear which (peripheral) antigens exhibit the capacity to induce the activation of autoreactive T cells. Potentially, a molecular mimicry between myelin proteins and antigens from microbes could reinforce auto-pathogenicity of T cells (156). Indeed, circulating myeloid cells from MS patients exhibit a pro-inflammatory phenotype (157). Previous studies showed that these cells can express pro-inflammatory cytokines, such as TNF, IL-12, IL-6, IL-23 and IL-1β to a higher extend. These cytokines drive T cell differentiation into pro-inflammatory T_h1 and T_h17 cells (45).

Once aberrantly activated, T cells can cross the blood-brain barrier. The interchange of immune cells between the CNS and peripheral compartments occurs naturally for the sake of immune surveillance. Furthermore, a lymphatic drainage system is established to facilitate the communication between the CNS and the periphery (deep cervical lymph nodes) (158). In MS cells, especially B cells have been shown to migrate from the CNS to the periphery and vice versa (159, 160). In order to pass the blood-brain barrier, T cells must upregulate chemokine receptors, adhesion molecules and other surface proteins (45). However, the knowledge about how T cells enter the CNS is still incomplete (161, 162). It is believed that pro-inflammatory cytokines are predominantly responsible for disrupting the blood-brain barrier and, therefore, are a prerequisite for T cell migration into the CNS (163).

T cells densely accumulate in white matter lesions in the CNS of MS patients (133, 163, 164). They are found in all lesion types (165). The number of $CD8^+$ T cells exceeds the number of $CD4^+$ cells in the lesion (133), nevertheless, the implications of T cell activation in the lesions are not negligible. T cells are believed to initialize lesion formation, because they are found in pre-active lesions (163, 166). Cytokines, which are secreted by T cells, not only enable the T cells to enter the CNS but also equip them with chemotactic properties. In EAE, mRNA which encodes IFNγ and IL-2 is strongly enriched in brain and spinal cord tissue when compared to healthy control (167, 168). IFNγ is predominantly secreted by T_h1 and T_h17 cells (169–171) and can skew microglia and macrophages to a pro-inflammatory phenotype (172, 173). Finally, these activated phagocytes cause demyelination and axonal damage, the major histopathological hallmarks of MS.

Thus, T cells exhibit the ability to recognize encephalitogenic antigens in the periphery, shift to a pro-inflammatory state (T_h1 and T_h17), cross the blood-brain barrier, attract and activate phagocytes and, thereby, induce neuroinflammation.

1.2.2.3 B cells

B cells are believed to contribute to the development of MS relapses. This assumption is based on two pillars: the presence of antibodies which are synthesized an released in the CNS and detectable in the cerebrospinal fluid of MS patients as so-called oligoclonal bands and the effectiveness of therapies which deplete B cells (45). Interestingly, both phenomena are not necessarily linked. Patients who are treated with rituximab, a monoclonal antibody directed against the B cell epitope CD20, still show oligoclonal bands in their CSF, probably produced by long-lived plasma cells that do not express CD20 (174, 175). Thus, B cells must have yet another function besides intrathecal antibody production in MS. B cells isolated from MS patients' PBMC exhibit a more pro-inflammatory profile and lack expression of anti-inflammatory cytokines (176). Aberrant B cell activation in MS patients can skew T cells towards a T_h1 or T_h17 phenotype through TNF secretion in the periphery (177). Likewise, B cells can attract or activate myeloid cells, such as macrophages, through the expression of granulocyte-macrophage colony-stimulating factor (GM-CSF) (178). Indeed, Li *et al.* and Bar-Or *et al.* showed that patients treated with rituximab showed reduced pro-inflammatory myeloid cell responses and lower numbers of pro-inflammatory T_h1 and T_h17 cells (176, 178).

B cells can present antigens in a MHC class II-dependent fashion in autoimmune diseases (179, 180) and MS in particular (181). Although it has not been elucidated yet which antigens significantly

contribute to disease development (182), MBP- and MOG-specific memory B cell populations have been identified in treatment-naïve RRMS patients (183, 184).

Overall, B cells might function as peripheral antigen-presenting cells (APC) and modulators of T cell encephalitogenicity. Thus, they might bridge the gap between the occurrence of autoantigens and T cell-mediated neuroinflammation.

1.2.2.4 Macrophages

Mononuclear phagocytes are cells that are able to phagocytose microscopic structures upon attraction and activation. During development, two distinct phenotypes of mononuclear phagocytes emerge: erythro-myeloid progenitor-derived and hematopoietic stem cell-derived mononuclear phagocytes. Both phenotypes exhibit the ability of self-renewal and, thereby, self-maintenance (185). However, they develop in different embryonic niches. Consequently, once they have colonized their embryonic niches, they develop independently. Erythro-myeloid progenitor-derived mononuclear phagocytes arise from the yolk sac, an extra-embryonic structure during embryogenesis, and give rise to tissue-resident macrophages as well as erythrocytes and megakaryocytes (186–188). Thus, erythro-myeloid progenitor-derived mononuclear phagocytes will become tissue-resident phagocytes, whereas hematopoietic stem cell-derived mononuclear phagocytes will define the monocyte-macrophage paradigm. Tissue-resident phagocytes comprise microglia (CNS), Kupffer cells (liver), Langerhans cells (epidermis) and alveolar macrophages (lung) (189).

In the context of CNS (auto-) immunity, one must distinguish between cells that populate the CNS *per se* (microglia as well as meningeal, perivascular and choroid plexus macrophages) and cells that migrate to the CNS upon attraction and activation (hematopoietic stem cell-derived macrophages). Strong evidence that mononuclear phagocytes in MS lesions result from the infiltration of monocytes into the CNS derives from observations from the EAE model. If monocytes are depleted before the disease onset, EAE onset will be delayed and the clinical score is less severe (190–193). Similarly, if monocytes are depleted after disease onset, the disease progression will be inhibited (194). Furthermore, the clinical severity correlates with the number of infiltrating monocytes (195). However, microglia contribute substantially to disease development and progression, too. Heppner *et al.* demonstrated that the suppression of microglia activation is accompanied by an inhibition of EAE development (196).

In MS lesions, macrophages are the dominant cell population and can be detected in early lesions (197–199). It is believed that macrophages are the key effector cells that cause demyelination and axonal damage. Bitsch *et al.* reported that the level of amyloid precursor protein expression in axons, which was interpreted as a sign of acute axonal damage, correlates with the number of macrophages (and $CD8^+$ T cells) (200). Furthermore, they are at close proximity to damaged axons and phagocytose myelin (165).

Taken together, hematopoietic stem cell-derived mononuclear phagocytes play a crucial role in EAE and, presumably, MS pathogenesis. Their function cannot be replaced by erythro-myeloid progenitor-derived mononuclear phagocytes, such as microglia. Thus, macrophages and microglia must be seen as two independent contributors to CNS autoimmunity.

How do hematopoietic stem cell-derived mononuclear phagocytes (monocytes) migrate to the CNS? C-C chemokine receptor type 2 (CCR2) is a chemokine receptor that preferentially binds its ligand monocyte chemoattractant protein-1 (MCP-1/CCL2) (190). The absence of CCR2 on the surface of monocytes or CCL2 in EAE ameliorates EAE symptoms (201–204). CCR2 is strongly expressed on monocytes with high Ly6C expression ($CCR2^{+}Ly6C^{hi}$ monocytes) (205). The number of $CCR2^{+}Ly6C^{hi}$ monocytes was elevated prior to relapses in a relapsing model of EAE (206). In humans, there are 3 different monocyte phenotypes described based on their CD14 and CD16 expression levels: classical monocytes ($CD14^{++}CD16^{neg}$), non-classical monocytes ($CD14^{+}CD16^{++}$) and intermediate subsets ($CD14^{++}CD16^{+}$) (207). In PBMC of RRMS and PPMS patients the number of non-classical monocytes is increased (208–210). Additionally, they show a higher expression of CCR2 which is low expressed in non-classical monocytes in healthy conditions (208, 211). Moreover, CCL2 can be detected in MS lesions and CSF of MS patients (212–215). Thus, CCR2 and its ligand CCL2 presumably attract monocytes across the blood-brain barrier. Thereby, they might be involved in EAE and MS early disease development and are potential pharmacological targets (190).

1.2.2.5 Macrophage phenotypes in neuroinflammatory lesions

Once monocytes have entered their target tissue, they acquire a new phenotype and are now termed macrophages. This transformation is driven by cytokines. Depending on which cytokines dominate the extracellular environment, monocytes can acquire different phenotypes and thereby adapt to the specific needs of the organism (216). In EAE and MS, macrophages are the predominant cell type that is directly responsible for demyelination and axonal damage. However, they can acquire an alternate phenotype if they adapt to a different set of cytokines. In this context, macrophages are associated with remyelination and tissue repair (217–220).

GM-CSF, IFNγ and TNFα, which are secreted by T cells, polarize macrophages to a pro-inflammatory phenotype (M1 macrophages). This polarization makes macrophages express MHC class II, CD40 and CD86 (221) and secrete IL-6, IL-12p40, IL-1a, IL-1b, iNOS, NO and proteases and denote the early phase of EAE (190, 221, 222). Girvin *et al.* showed that an ablation of the CD40/CD40L signaling pathway ameliorates EAE and decreases the T cells response (223). Thus, attracting T cells to the CNS is one key function of M1 macrophages in EAE. Furthermore, M1 macrophages can directly damage neurons, most likely through the secretion of toxic metabolites (224). Reactive oxygen species (ROS) and reactive nitrogen species (RNS) from M1 macrophages can trigger mitochondrial pathology in axons and lead to axon fragmentation, a phenomenon which is termed focal axonal degeneration (FAD) (225). M1 macrophages not only secrete neurotoxic metabolites but also directly attack neurons at the nodes of Ranvier (226). Taking into consideration that iNOS was detected in phagocytes in chronic active MS lesions (227), acute axonal damage is most prominent at early stages of MS (228) and the extend of axonal damage correlates with the number of macrophages in the MS lesion (200), one can conclude that the concept of M1 macrophage polarization associated with axonal damage, which was established in EAE, can be transferred to MS.

If monocytes or macrophages are exposed to IL-4, IL-10, IL-13, IL-33 and TGF-β, they will acquire an anti-inflammatory phenotype (M2 macrophages). The conversion to M2 macrophages is accompanied by a shift toward anti-inflammatory T cell phenotypes (221, 229). This observation can be explained by a downregulation of MHC class II of M2 macrophages, stimulated by IL-10 in an

autocrine fashion (190). IL-10 dampens the antigen presenting capability of antigen-presenting cells (APC), thus, leading to a reduced T_h1 activity (230). In addition, the toxic effect of the iNOS-induced respiratory burst from M1 macrophages is reversed by the IL-4-dependent expression of Arginase-1 from M2 macrophages (231). Arginase-1 abrogates NO synthesis by depleting its precursor arginine. Furthermore, Arginase-1 promotes the polyamine pathway and thereby drives collagen synthesis which is needed for tissue repair (190, 232). Thus, iNOS and Arginase-1 expression in M1 and M2 macrophages can be interpreted as a mechanism that switches macrophages from a pro-inflammatory state to an anti-inflammatory state and vice versa. Ultimately, M2 macrophages are associated with axonal repair and remyelination. This is supported by cell transfer experiments that showed that M2 macrophages decrease EAE disease severity (233, 234). Moreover, Kotter *et al.* showed that oligodendrocyte precursor cells (OPC) will fail to respond to an acute demyelination and that remyelination will be impaired if macrophages are depleted (235). Miron *et al.* showed that M2 macrophage density was higher in lesions where remyelination was enhanced by parabiotic coupling. Additionally, they identified activin-A as a substance which is release by M2 macrophages and exhibits the ability to reinforce OPC differentiation (217).

The polarization to M1 and M2 macrophages is not static. During the disease progression, from initial lesion expansion to lesion resolution, macrophages change der polarization phenotype from M1 to M2, most likely in response to external stimuli (222). Notably, individual cells switch from M1 to a M2 phenotype rather than a share of cells being replaced by their anti-inflammatory counterparts (222, 236). Locatelli *et al.* and Giles *et al.* elucidated that the microenvironment dictates macrophage polarization. At lesion formation macrophages in the parenchyma show a M1 phenotype whereas macrophages in the meninges exhibit a M2 phenotype (222, 236). This concept is supported by Béchade *et al.* who showed that *NOS2* expression in microglia is inducible by LPS and IFNγ (237).

However, the concept of the existence of M1 and M2 macrophage phenotypes has to be interpreted as a rough simplification since there is more and more evidence arising that further elucidates the complexity of the molecular phenotypes of CNS macrophages. By applying single-cell genomics, Mendiola *et al.* uncovered multiple CNS innate immune cell populations that might convey neurotoxicity in the context of EAE (238). Likewise, Giladi *et al.* identified 8 monocyte-derived subsets at different disease stages of EAE, highlighting the molecular and, eventually, functional diversity of mononuclear phagocytes in neuroinflammation.

Taken together, the function and fate of macrophages in the context of MS and EAE is complex. Macrophages respond to external stimuli (from other immune cells), adapt their phenotype and, thereby, acquire either pro-inflammatory or anti-inflammatory properties. This then causes either demyelination and axonal damage or support remyelination and axonal repair.

1.2.2.6 Microglia

Like macrophages, microglia are mononuclear phagocytes. However, they derive (embryonically) from erythro-myeloid progenitors from the yolk sac and make up the CNS-specific phagocyte population. Their dominant function is to maintain CNS homeostasis (239). Whether microglia are overall beneficial or harmful cells in the context of autoimmunity has not yet been fully unraveled (239, 240). Under various circumstances microglia can get activated. They acquire an amoeboid shape, boost proliferation, increase their motility as well as phagocytosis activity and start to present antigens (239,

241). In MS and EAE, microglia are associated with axonal damage and oligodendrocyte pathology, contain myelin remnants and express MHC class II molecules (241). If microglia function is impaired, EAE symptoms will be less severe (196). Ponomarev *et al.* demonstrated that microglia make up 37 % of all myeloid cells in inflammatory lesions. They claim that microglia, once being activated, can differentiate into macrophages and dendritic cells (242). In contrast, microglia seem to play a substantial role in resolving acute inflammatory lesions. When microglia are activated at an early time during EAE disease progression, the clinical EAE outcome is improved (243). Thus, timing of microglia activation is believed to be crucial for defining their function. Like macrophages (244), myelin phagocytosis might be a stimulus to suppress pro-inflammatory properties of microglia (245). Thus, one can debate if there is a M1 and M2 phenotype for microglia as there is one for macrophages (246).

1.2.2.7 Border-associated macrophages (BAMs)

Yet another entity of CNS-specific mononuclear phagocytes resides at the dura mater, subdural meninges and choroid plexus (247). These non-parenchymal cells are termed border-associated macrophages (BAMs). Recently, it was shown that BAMs exhibit a particular ontogeny, self-renewal capacity as well as transcriptional profile when compared to parenchymal microglia or macrophages (247). Mrdjen *et al.* showed that BAMs can be classified by CD38, Lyve1, MHCII and CCR2 expression. During EAE, the numbers of BAM decrease, which is in line with the overall reduction of tissue-resident macrophages upon infiltration of bone marrow-derived monocytes. However, during EAE BAMs loose their differential surface marker expression profile and uniformly express CD38 and MHCII which is believed to indicate a shift towards a universal activation state (248). Taken together, these findings might indicate that BAM are a third entity, besides tissue-resident and infiltrating phagocytes, that contribute to EAE disease progression.

1.2.3 Mechanisms of immune-mediated tissue damage

Neuronal loss is a major hallmark of multiple sclerosis and EAE. An association study that investigated *post-mortem* histopathological findings and clinical disease courses of MS patients provided evidence that axonal loss has a stronger impact on clinical disease severity than demyelination (249). Accumulation of oxidized phospholipids and DNA strand breaks, which can be observed in active cortical MS lesions, is believed to be an indirect sign of reactive oxygen species (ROS) and reactive nitrogen species (RNS) secreted by macrophages and microglia as highlighted in section 1.2.2.5 (250, 251). In a previous study, externally added oxygen and nitrogen donors were sufficient to induce axonal injury similar to EAE but without signs of demyelination (225).

There is increasing evidence that mitochondria are directly affected by ROS and RNS and that their dysfunction contributes to axonal pathology in MS (250). It is believed that there is an imbalance between the (higher) energy requirements of demyelinated axons and the (lower) energy production due to impaired mitochondria in MS, thus, leading to a state of virtual hypoxia in axons (252). Mitochondrial dysfunction might result from oxidative damage to mtDNA, which is believed to be more susceptible to oxidative stress because of the lack of histones and repair mechanisms, ultimately leading to increased activity of oxidative phosphorylation (OXPHOS), resulting in lower ATP concentrations in injured axons (253–255). The molecular basis of this observation was investigated by Mahad *et al.* who showed that there is a lack of cytochrome c oxidase (COX-1) immunoreactivity in

multiple sclerosis lesions, potentially leading to a global functional deficit of the OXPHOS in axons (256). However, the absolute number of mitochondria was elevated in active and inactive multiple sclerosis lesions, pointing towards a compensatory mechanism to deal with lower OXPHOS efficiency and secondary ATP deprivation (257, 258).

Furthermore, dysfunctional mitochondria in chronic lesions itself are a source of ROS. The liberation of electrons caused by a defective electron transport chain can react with oxygen to ROS. This vicious circle might even enhance the tissue and axonal damage observed in multiple sclerosis (131).

Based on the understanding of the underlying molecular mechanism of ROS-induced axonal pathology induced by mitochondrial dysfunction clinical trials have been carried out with the goal to decrease ROS toxicity and thereby reduce axonal pathology in multiple sclerosis. Vitamins, co-enzymes, creatine, free radical scavengers and hyperbaric oxygen treatments are potential candidates to scavenge the oxidative burst from activated phagocytes in acute lesions and the accumulation of ROS as a result of defective mitochondria (259). The widespread self-medication of over-the-counter antioxidant drugs and substances, such as vitamins and co-enzymes, has not shown to modify the disease course of multiple sclerosis so far. Furthermore, a recent study which has investigated the effect of idebenone, a derivative of co-enzyme Q10 which is approved for the treatment of Leber's hereditary optic neuropathy (LHON), showed no clinical benefits (259–262). However, Lipoic acid (ALA), a free radical scavenger, showed a reduction of whole-brain atrophy and had a discrete impact on the walking performance of PPMS patients (263–265).

However, to understand how inflammation disturbs mitochondrial function and how mitochondrial dysfunction impacts neuronal cell integrity is not fully understood and needs to be further investigated.

2 Outline

Mononuclear phagocytes play a crucial role in lesion formation and lesion alteration in EAE and multiple sclerosis. It is believed that the function of mononuclear phagocytes depends on their polarization state, enabling both destructive and reparative phenotypes (also termed as M1 and M2 macrophages, respectively). A recent study has shown that in EAE the pro-inflammatory phenotype of mononuclear phagocytes characterizes the early stage of the lesion formation whereas the anti-inflammatory state dominates the later time point, associated with an alleviation of symptoms and lesion resolution or astrogliosis formation (222). Interestingly, pro-inflammatory mononuclear phagocytes segue into an anti-inflammatory phenotype on a single-cell level. This raises the question how pro- and anti- inflammatory mononuclear phagocytes are molecularly and functionally defined, which molecular signals enable pro-inflammatory mononuclear phagocytes to acquire an anti-inflammatory phenotype and which molecules do pro- and anti-inflammatory mononuclear phagocyte secrete to communicate with other immune and CNS cells.

We applied cell sorting, quantitative label-free mass spectrometry and RNA sequencing and developed computational techniques to unravel the composition of the cellular signatures of immune cells in EAE and to decipher potential cell-cell communication patterns with a focus on mononuclear phagocytes. Furthermore, we measured the alterations in the proteomes of neuronal mitochondria from EAE compared to healthy controls to further investigate the molecular mechanism of mitochondrial pathology in EAE. In particular, we addressed the following key questions:

1. Which proteins are differentially abundant in polarized macrophages at certain stages of EAE disease progression?
2. Which molecular (functional) features underlie these cells?
3. How are these features conserved on a transcriptome level?
4. How are immune cells and resident CNS cells molecularly equipped to communicate which each other?
5. Which molecular features are altered in the neuronal mitochondrial proteome in EAE compared to healthy controls?

With this large-scale screening approach, we aimed to uncover molecular programs that could potentially be modified by pharmacological interference to alleviate disease severity in EAE and, ultimately, in multiple sclerosis.

3 Materials and methods

3.1 Materials

3.1.1 Buffers and media

Buffers and media were stored, prepared and used according to the manufacturer's recommendations, unless otherwise specified.

Description	Source
Acetate buffer	20 mM sodium acetate, pH 3
Blocking buffer	10 % (w/v) BSA, 10 % FBS (v/v), 10 % (w/v) fish gelatin in PBS
Destain solution	50 % (v/v) methanol, 10 % (v/v) acetic acid in H_2O
EDTA (0.5 M)	0.5 M EDTA in H_2O
Fixation and permeabilization buffer	BD Cytofix/Cytoperm™ Fixation/Permeablization Kit (cat# 554714, Becton Dickinson, Franklin Lakes, New Jersey, USA)
HEPES buffer	20 mM HEPES, 200 mM NaCl in H_20
Imidazole buffer (1 M)	1 M imidazole in H_2O
Imidazole buffer (40 mM)	40 mM imidazole in urea buffer
Imidazole buffer (5 mM)	5 mM imidazole in urea buffer
Immunocapture (IC) buffer	137 mM KCl, 2.5 mM $MgCl_2$, 3 mM KH_2PO_4, 10 mM HEPES, 1 mM EDTA pH 7.40; 1 % (w/v) essentially fatty acid-free BSA, 0.5 x protease inhibitor
LB medium	1 % (w/v) tryptone, 1 % (w/v) NaCl, 0.5 % (w/v) yeast extract in H_20, pH 7.0
Mitochondria isolation buffer	220 mM mannitol, 80 mM sucrose, 10 mM HEPES, 1 mM EDTA pH 7.40, 1 % (w/v) essentially fatty acid-free BSA
Percoll gradient solution	30 % (v/v) Percoll in PBS
Perfusion buffer (histology)	4 % (w/v) paraformaldehyde, 5 IU/ml heparin in 0.1 M phosphate buffer, pH 7.4
Phosphate-buffered saline (PBS)	Dulbecco's Phosphate Buffered Saline, modified, without calcium chloride and magnesium chloride, liquid, sterile-filtered, suitable for cell culture (cat# D8537-500ML, MilliporeSigma, St. Louis, Missouri, USA)
SDS running buffer	NuPAGE™ MOPS SDS Running Buffer (20X) (cat# NP0001, Thermo Fisher Scientific, Waltham, Massachusetts, USA)
SDS sample additive	NuPAGE™ Sample Reducing Agent (10X) (cat# NP0004, Thermo Fisher Scientific, Waltham, Massachusetts, USA)
SDS sample buffer	NuPAGE™ LDS Sample Buffer (4X) (cat# NP0007, Thermo Fisher Scientific, Waltham, Massachusetts, USA)
Solubilization buffer	91 µl 20 mM β-mercaptoethanol in 65 ml urea buffer

Sonification buffer	17.53 g NaCl, 3.55 g Na_2HPO_4, 3.45 g NaH_2PO_4 in 1 l H_20
Tissue digestion buffer	0.8 mg/ml collagenase, 10 mg/ml DNase in PBS
Urea buffer	8 mol/l urea in H_20
Wash buffer	8,5 ml LDAO (N,N-dimethyldodecylamine-N-oxide) in 500 ml sonification buffer

Table 1: Buffers and media.

3.1.2 Reagents and kits

Reagents and kits were stored, prepared and used according to the manufacturer's recommendations, unless otherwise specified.

Description	Source
Acetic acid	Acetic acid, glacial (cat# A6283-100ML, MilliporeSigma, St. Louis, Missouri, USA)
ACK buffer	ACK Lysing Buffer (cat# A1049201, Thermo Fisher Scientific, Waltham, Massachusetts, USA)
Affinity resin	TALON® Metal Affinity Resin (cat# 635606, Takara Bio Inc., Kusatsu, Japan)
Bovine serum albumin (BSA)	Essentially fatty acid-free BSA (cat# A8806-1G, MilliporeSigma, St. Louis, Missouri, USA)
Collagenase	Collagenase A from *Clostridium histolyticum* (cat# 10103578001, MilliporeSigma, St. Louis, Missouri, USA)
Coomassie stain	Bio-Safe™ Coomassie Stain (cat# 1610786, Bio-Rad Laboratories, Inc., Hercules, California, USA)
DAPI	Invitrogen™ DAPI (4',6-Diamidino-2-Phenylindole, Dihydrochloride, cat# Artikelnummer.10184322, Thermo Fisher Scientific, Waltham, Massachusetts, USA)
DNase (MOG)	DNase I, 20,000 units (cat# 18047019, Thermo Fisher Scientific, Waltham, Massachusetts, USA)
DNase (tissue digestion buffer)	DNase I recombinant, RNase-free, 10,000 units (cat# 4716728001, MilliporeSigma, St. Louis, Missouri, USA)
Drop delay beads	BD FACS™ Accudrop Beads (cat# 345249, Becton Dickinson, Franklin Lakes, New Jersey, USA)
Ethylenediaminetetraacetic acid (EDTA)	EDTA, ~0.5 M (cat# 03690, MilliporeSigma, St. Louis, Missouri, USA)
Fc block	TruStain FcX™ (anti-mouse CD16/32) Antibody (cat# 101319, San Diego, California, USA)
Fetal bovine serum (FBS)	Fetal Bovine Serum (cat# F2442-50ML, MilliporeSigma, St. Louis, Missouri, USA)
Fish gelatin	Gelatin from cold water fish skin (cat# G7041-100G, MilliporeSigma, St. Louis, Missouri, USA)
Freud's adjuvant, incomplete	Freund's Adjuvant, Incomplete (cat# F5506-10ML, MilliporeSigma, St. Louis, Missouri, USA)

Heparin	Heparin Natrium Braun 25.000 I.E./5 ml Injektions-/Infusionslösung (PZN/EAN: 15782698 / 4150157826988, B. Braun Melsungen AG, Melsungen)
HEPES	4-(2-Hydroxyethyl)piperazine-1-ethanesulfonic acid (cat# PHG0001-100G, MilliporeSigma, St. Louis, Missouri, USA)
Imidazole	Imidazol (cat# I2399-100G, MilliporeSigma, St. Louis, Missouri, USA)
Isoflurane	Isoflo® *ad us. vet*., Inhalationsanaesthetikum (Zoetis Schweiz GmbH, Delémont, Swiss)
Isopropyl β-D-1-thiogalactopyranoside (IPTG)	IPTG, ≥ 99 % (TLC), ≤ 0.1 % Dioxane (cat# I6758, MilliporeSigma, St. Louis, Missouri, USA)
Kanamycin	Kanamycin sulfate (cat# 60615-5G, MilliporeSigma, St. Louis, Missouri, USA)
Ketamine	Ketamine hydrochloride 10 % (Bela-Pharm GmbH, Vechta, Germany)
Lysozyme	Lysozyme from chicken egg white (cat# L6876-1G, MilliporeSigma, St. Louis, Missouri, USA)
M. tuberculosis H37Ra, heat-inactivated	BD Difco™ Adjuvantien (cat# 231141, Becton Dickinson, Franklin Lakes, New Jersey, USA)
Methanol	Methanol (cat# 34860, MilliporeSigma, St. Louis, Missouri, USA)
mRNA library kit	Collibri™ 3’ mRNA Library Prep Kit for Illumina™ Systems (cat# A38110024, Thermo Fisher Scientific, Waltham, Massachusetts, USA)
N,N-Dimethyldodecylamine-N-oxide (LDAO)	N,N-Dimethyldodecylamine N-oxide (cat# 40234-5G, MilliporeSigma, St. Louis, Missouri, USA)
Na_2HPO_4	Di-Sodium hydrogen phosphate (cat# 1065860500, MilliporeSigma, St. Louis, Missouri, USA)
NaH_2PO_4	Sodium phosphate monobasic (cat# S0751, MilliporeSigma, St. Louis, Missouri, USA)
NaOH	Sodium hydroxide, reagent grade, ≥98%, pellets (anhydrous) (cat# S5881-500G, MilliporeSigma, St. Louis, Missouri, USA)
Paraformaldehyde (PFA)	Paraformaldehyde (cat# 158127-5G, MilliporeSigma, St. Louis, Missouri, USA)
Percoll	Percoll® (cat# P1644-25ML, MilliporeSigma, St. Louis, Missouri, USA)
Pertussis toxin	Pertussis toxin from *Bordetella pertussis* (cat# P7208-50UG, MilliporeSigma, St. Louis, Missouri, USA)
Protein ladder	PageRuler™ Prestained Protein Ladder, 10 to 180 kDa (cat# 26616, Thermo Fisher Scientific, Waltham, Massachusetts, USA)
RNA extraction kit	RNeasy Micro Kit (cat# 74004, QIAGEN, Hilden, Germany)
RNase inhibitor	RNase Inhibitor (cat# N8080119, Thermo Fisher Scientific, Waltham, Massachusetts, USA)
Sodium acetate	Sodium acetate (cat# S2889-250G, MilliporeSigma, St. Louis, Missouri, USA)

Sodium chloride (NaCl)	Sodium chloride (cat# S7653-250G, MilliporeSigma, St. Louis, Missouri, USA)
Triton X-100	Triton™ X-100 (cat# T8787-50ML, MilliporeSigma, St. Louis, Missouri, USA)
Tryptone	Tryptone (cat# T7293-250G, MilliporeSigma, St. Louis, Missouri, USA)
Urea	Urea (cat# U5378-100G, L6876-1G, MilliporeSigma, St. Louis, Missouri, USA)
Viability dye (blue)	SYTOX™ Blue Dead Cell Stain, for flow cytometry (cat# S34857, Thermo Fisher Scientific, Waltham, Massachusetts, USA)
Viability dye (red)	Invitrogen™ LIVE/DEAD™ Fixable Near-IR Dead Cell Stain Kit (cat# L10119, Thermo Fisher Scientific, Waltham, Massachusetts, USA)
Xylazine	Xylariem®, Xylazinehydrochloride 23.3 mg/ml (Serumwerk Bernburg AG, Bernburg, Germany)
Yeast extract	Yeast Extract (cat# Y1625-250G, MilliporeSigma, St. Louis, Missouri, USA)
β-Mercaptoethanol	2-Mercaptoethanol (cat# M6250-10ML, MilliporeSigma, St. Louis, Missouri, USA)

Table 2: Reagents and kits.

3.1.3 Antibodies

Antibodies were stored and used according to the manufacturer's recommendations. If not otherwise stated, antibodies that were used for flow cytometry (Table 3) were diluted 1:200 in the respective buffer.

Description	Source
ACSA-2-APC	ACSA-2 Antibody, anti-mouse, APC, REAfinity™ (cat# 130-116-245, Miltenyi Biotec, Bergisch Gladbach, Germany)
Arginase-1-APC	Arginase 1 Monoclonal Antibody, APC, eBioscience™ (clone# A1exF5, cat# 17-3697-82, Thermo Fisher Scientific, Waltham, Massachusetts, USA)
B220-FITC	FITC Rat Anti-Mouse CD45R/B220 (cat# 553087, clone# RA3-6B2 (RUO), BD Biosciences, Franklin Lakes, New Jersey, USA)
CD11b-APC	APC anti-mouse/human CD11b antibody (clone# M1/70, cat# 101211, Biolegend, San Diego, California, USA)
CD19-PerCP	PerCP anti-mouse CD19 Antibody (clone# 6D5, cat# 115531, Biolegend, San Diego, California, USA)
CD3-APC	APC anti-mouse CD3 antibody (clone# 17A2, cat# 100235, Biolegend, San Diego, California, USA)
CD45-BV786	Brilliant Violet 785™ anti-mouse CD45 antibody (clone# 30-F11, cat# 103149, Biolegend, San Diego, California, USA)

CD4-FITC	FITC anti-mouse CD4 antibody (clone# GK1.5, cat# 100405, Biolegend, San Diego, California, USA)
CD8-PE	PE anti-mouse CD8a antibody (clone# 53-6.7, cat# 100707, Biolegend, San Diego, California, USA)
iNOS-eFluor 450	iNOS Monoclonal Antibody, eFluor 450, eBioscience™ (clone# CXNFT, cat# 48-5920-82, Thermo Fisher Scientific, Waltham, Massachusetts, USA)
Ly6C-PerCP	PerCP anti-mouse Ly-6C antibody (clone# HK1.4, cat# 128027, Biolegend, San Diego, California, USA)
Ly6-G-BV785	Brilliant Violet 785™ anti-mouse Ly-6G antibody (clone# 1A8, cat# 100707, Biolegend, San Diego, Californi127645a, USA)
O4-APC	O4 Antibody, anti-human/mouse/rat, APC (cat# 130-119-155, Miltenyi Biotec, Bergisch Gladbach, Germany)
PDGFRα-PE	PE anti-mouse CD140a antibody (clone# APA5, cat# 135905, Biolegend, San Diego, California, USA)

Table 3: Antibodies for flow cytometry.

Description	Source
goat anti-rabbit-AF647	goat anti-rabbit IgG (H+L) highly cross-adsorbed secondary antibody, Alexa Fluor 647 (cat# A-21245, Thermo Fisher Scientific, Waltham, Massachusetts, USA)
Histone H3	anti-Histone H3 (citrulline R2 + R8 + R17) antibody (cat# ab5103, abcam, Cambridge, UK)
Lactoferrin (LTF)	IHC-plus™ polyclonal rabbit anti-human LF/LTF/Lactoferrin antibody (cat# LS-B11832, Lifespan Biosciences, Seattle, Washington, USA)
Myeloperoxidase (MPO)	human/mouse Myeloperoxidase/MPO antibody (cat# AF3667, R&D systems, Minneapolis, Minnesota, USA)
Neutrophil elastase (ELANE)	anti-Neutrophil Elastase antibody (cat# ab68672, abcam, Cambridge, UK)
S100A8	mouse S100A8 antibody (cat# MAB3059, R&D systems, Minneapolis, Minnesota, USA)
S100A9	mouse S100A9 antibody (cat# AF2065, R&D systems, Minneapolis, Minnesota, USA)

Table 4: Antibodies for immunohistochemistry

3.1.4 Mouse lines

C57BL/6JRj mice were purchased from Janvier Labs (Saint Berthevin Cedex, France). This mouse line was used whenever no genetic labeling was needed.

iNOS-tdTomato-Cre x Arginase-1-YFP (*C.129S4/(B6)-Arg1tm1Lky/j*) mice were crossed inhouse as described in Locatelli *et al.*, Béchade *et al.* and Reese *et al.* (222, 237, 266). This line expresses a red fluorescent protein (tdTomato) under the *iNOS/NOS2* promoter and yellow fluorescent protein (YFP) under the *Arg1* promoter. iNOS and Arginase-1 can be considered as two of the most specific M1 and

M2 macrophage signature proteins (229). Thus, the dual genetic labelling of iNOS and Arginase-1 enables to monitor the polarization state of phagocytes by measuring fluorescence signals. This mouse line and its respective colony was maintained in-house.

Thy-1 YFP-16 (*B6.Cg-Tg(Thy1-YFP)16Jrs/J*) mice were purchased from The Jackson Laboratory (Bar Harbor, Maine, USA). They were used to label, identify and isolate neurons (267). This strain expresses yellow fluorescent protein (YFP) under the *Thy-1* promoter. *Thy-1* (CD90) is predominantly expressed by neurons in the CNS (268). This mouse line and its respective colony was maintained in-house.

MITO-Tag mice (B6.Cg-Gt(ROSA)26Sor$^{tm1(CAG-EGFP)Brsy}$/J) were purchased from The Jackson Laboratory (Bar Harbor, Maine, USA) (269). Mice from this strain were neonatally intraventricularly injected with and in-house synthesized and purified *AAV9.hSyn:iCre* virus to obtain a specific *Cre* expression of *hSyn*-expressing cells (neurons) (270, 271).

3.1.5 Bacteria strains

MOG_{1-125} was expressed in an *E. coli* strain as previously reported by Adelmann *et al.* (272).

3.1.6 Instruments

All instruments were operated according to the manufacturer's recommendations.

Description	Source
Cell sorter	BD FACSAria™ III (Becton Dickinson, Franklin Lakes, New Jersey, USA)
Centrifuges and rotors	Avanti JXN-26 (cat# B38619) equipped with JA-25.50 Fixed-Angle Rotor- Aluminum, 8 x 50 mL, 25,000 rpm, 75,600 x g (cat# 363055) or JA-10 Fixed-Angle Aluminum Rotor- 6 x 500 mL, 10,000 rpm, 17,700 x g (cat# 369687, Beckman Coulter, Brea, California, USA)
	Micro Centrifuge 5417R (cat# 55 69 54175) equipped with Rotor FA-24x2 (cat# 5495500006, Eppendorf AG, Hamburg, Germany)
	Thermo Scientific™ Multifuge™ X3 Centrifuge Series (cat# 10325804) equipped with Thermo Scientific™ TX-1000 4 x 1000mL Swinging Bucket Rotor Body and Buckets (cat# 15133169 and 15163169, Thermo Fisher Scientific, Waltham, Massachusetts, USA)
Confocal microscope	FV1000 confocal system on a BX61 microscope (Olympus, Shinjuku, Japan)
Microfluidic analyzer	2100 Bioanalyzer Instrument (cat# G2939BA, Agilent, Santa Clara, California, USA)
Microvolume spectrophotometer	NanoDrop™ 2000/2000c Spectrophotometers (cat# ND-2000, Thermo Fisher Scientific, Waltham, Massachusetts, USA)
Objectives (confocal microscope)	x10/0.4 (water immersion), x20/0.85 and x60/1.42 (both oil immersion) (Olympus, Shinjuku, Japan)
PCR cycler	Biometra TRIO 48 (cat# 846-x-070-723, Analytik Jena AG, Jena, Germany)

Photometer	Eppendorf BioPhotometer® (Eppendorf AG, Hamburg, Germany)
Power supply	PowerPac Universal Power Supply (cat# 1645070, Bio-Rad Laboratories, Inc., Hercules, California, USA)
SDS-PAGE electrophoresis chamber	Mini Gel Tank (cat# A25977, Thermo Fisher Scientific, Waltham, Massachusetts, USA)
Ultrasonic processor	Ultrasonic processor UP200St (Hielscher Ultrasonics GmbH, Teltow, Germany)

Table 5: Instruments.

3.1.7 Consumables and miscellaneous equipment

Consumables and miscellaneous equipment were used according to the manufacturers' instructions.

Description	Source
Cage, filtertop	EUROSTANDARD TYPE II L (cat# 1284L, Tecniplast, Hohenpeissenberg, Germany)
Cage, sealed top	TYPE II L (cat# 1285L, Tecniplast, Hohenpeissenberg, Germany)
Concentrator	AMICON® Ultra-15 Centrifugal Filters (3 kDa NMWCO, cat# UFC900324, MilliporeSigma, St. Louis, Missouri, USA)
Cover slips	Menzel™ Microscope Coverslips (cat# 11911998, Thermo Fisher Scientific, Waltham, Massachusetts, USA)
Dialysis chamber	Slide-A-Lyzer G2 Dialysis Cassettes 3.5 kDa MWCU, 5 – 15 ml (cat# 87724, Thermo Fisher Scientific, Waltham, Massachusetts, USA)
Food pellet	Mouse, general (cat# V1184-0000, ssniff Spezialitaeten GmbH, Soest, Germany)
Gravity column	TALON® 2 ml Disposable Gravity Column (cat# 635606, Takara Bio Inc., Kusatsu, Japan)
MACS columns	LS columns (cat# 130-042-401, Miltenyi Biotec, Bergisch Gladbach, Germany)
Magnetic beads	µMACS GFP Isolation Kit (cat# 130-091-125, Miltenyi Biotec, Bergisch Gladbach, Germany)
Mesh filter	Falcon® 100 µm Cell Strainer (cat# 352360, Corning, New York, USA)
Microfluidic chips	Agilent DNA 1000 Kit (cat# 5067-1504, Agilent, Santa Clara, California, USA)
Microscopy slides	Epredia™ Microscope Slides, Cut, 1 mm (cat# 12342108, Thermo Fisher Scientific, Waltham, Massachusetts, USA)
Potter-Elvehjem homogenizer (tissue)	WHEATON® Dounce Tissue Grinder, 1 ml (cat# 357538, DWK Life Sciences GmbH, Mainz, Germany)
Protein LoBind® Tubes	Protein LoBind® Tubes, 2.0 ml (cat# 0030108132, Eppendorf AG, Hamburg, Germany)

SDS gel	NuPAGE™ 4 to 12%, Bis-Tris, 1.0 mm, Mini Protein Gel, 12-well (cat# NP0322BOX, Thermo Fisher Scientific, Waltham, Massachusetts, USA)
Winged infusion set	Multifly®-Needle 21 G tube 80 mm (cat# 85.1638.005, Sarsted, Nuembrecht, Germany)

Table 6: Consumables and miscellaneous equipment.

3.1.8 Software

All computational analysis were done with Python (version 3.7), R (version 4.0.2) and Javascript (273, 274). Flow cytometry data were analyzed with Flowing Software (2.5.1, Turku Bioscience, Finland) and Python.

3.2 Methods

3.2.1 Animal husbandry

All animals were socially housed with maximum 5 mice per cage. The cages were located in a room with a 12 h light/dark cycle within a specialized animal facility. The animals were kept either in filtertop cages (no IVC system) or in sealed top cages (IVC system), depending on their location within the animal facility. They were fed with autoclaved food pellets and water *ad libitum*. The cage was changed once a week.

All animal experiments were performed according to general animal welfare principles and approved by the local authorities (Regierung von Oberbayern) and performed according to the respective animal protocol.

3.2.2 Genotyping

PCR-based genotyping of mouse strains was performed according to the suppliers' protocols. Likewise, primers were designed according to the suppliers' protocols and purchased from metabion international AG (Planegg, Germany). The amplicon was analyzed by gel electrophoresis and the resulting bands were compared to the respective positive and negative controls.

3.2.3 Purification of myelin oligodendrocyte glycoprotein

MOG_{1-125}, which is the N-terminal domain of myelin oligodendrocyte glycoprotein, exhibits the capability of inducing EAE when subcutaneously injected with CFA and heat-inactivated *M. tuberculosis H37Ra* (272). MOG_{1-125} was expressed in *E. coli* as a fusion protein with a polyhistidine-tag (MOG_{1-125}-His). The polyhistidine-tag enables the Ni^{2+}-affinity purification of MOG_{1-125}-His.

First an *E. coli* strain which genetically encodes MOG_{1-125}-His was expanded in 4 l LB medium supplemented with 0.1 % (v/v) kanamycin through incubation at 37 °C on a shaker (200 rpm). The optical density at 450 nm of the suspension, which correlates with the number of cells, was monitored photometrically. Once the optical density reached 0.8 – 1.0, the expression of MOG_{1-125}-His was induced by adding 500 µl 1 M IPTG in H_20 per 1 l bacteria culture. After 6 h of expression cells were

harvested by centrifugation (20,000 g, 4 °C, 10 min). The supernatant was discarded and the pellet frozen at -20 °C and thawed the next day.

The following steps were performed on ice or at 4 °C. The pellets were thawed and resuspended in 40 ml sonification buffer supplemented with one spade point lysozyme and 50 µl DNase (20,000 units). The suspension was distributed to two 50 ml tubes. Next, the suspension was treated with ultrasound (60 s duration, 60 % pulse time, 75 % amplitude) using an ultrasonic processor. This was repeated twice. Afterwards, the sample was centrifuged (20,000 g, 4 °C, 20 min) and the supernatant was discarded. The pellets were resuspended in 20 ml wash buffer and homogenized with a Potter-Elvehjem homogenizer (10 strokes) and centrifuged (20,000 g, 4 °C, 20 min). The supernatant was discarded. The homogenization and subsequent centrifugation were done in total 5 times, 3 times with was buffer, then 2 times in sonification buffer, which were added to the pellet after centrifugation, respectively. Optionally, the pellet was frozen after this step. Next, 40 ml solubilization buffer was added to the pellet. The sample was incubated overnight on an orbital shaker (200 rpm).

To prepare the affinity resin for purification of His-tagged proteins, 10 ml affinity resin was mixed with 30 ml sonification buffer and 10 ml urea buffer and centrifuged (10,000 g, 4 °C, 5 min). The supernatant was discarded. The pellet was resuspended in 20 ml sonification buffer with 20 ml urea buffer and centrifuged (10,000 g, 4 °C, 5 min). The supernatant was discarded. The pellet was resuspended in 10 ml sonification buffer with 30 ml urea buffer and centrifuged (10,000 g, 4 °C, 5 min). Finally, the pellet was resuspended in 40 ml urea buffer and centrifuged (10,000 g, 4 °C, 5 min).

The sample that had been incubated over night was centrifuged (20,000 g, 4 °C, 20 min). The supernatant was added to the pellet that resulted from the centrifugation of the affinity resin. The resin-sample suspension was mixed well and incubated overnight on a shaker (200 rpm) to allow binding of His-tagged MOG_{1-125} to the affinity resin. Next, the resin-sample suspension was centrifuged (10,000 g, 4 °C, 5 min) and the supernatant was discarded. The pellet was resuspended in 30 ml urea buffer, incubated for 20 min on a shaker (200 rpm) and centrifuged (10,000 g, 4 °C, 5 min). To wash the resin, this step was repeated twice. Finally, the pellet was resuspended in 20 ml urea buffer.

The suspension was equally distributed to 4 gravity columns. When the liquid had flowed through completely, 10 ml urea buffer was added. Next, 5 ml imidazole buffer (5 mM) was added. The flow throughs were discarded. Finally, the protein was eluted with 10 ml imidazole buffer (40 mM). The flow throughs of all 4 columns were collected and combined.

Next, the sample was dialyzed. Therefore, the sample was injected into a dialysis chamber. the dialysis chamber was put into 5 l acetate buffer and incubated for 24 h at 4 °C. The buffer was exchanged and the dialysis chamber was again incubated for 24 h at 4 °C.

The sample was aspired from the dialysis chamber and concentrated with concentrators (4,000 g, 4 °C, 10 min) until a concentration of approximately 5 g/l was obtained. The concentration was measured with a microvolume spectrophotometer. The correct size of the purified protein and the purity of the sample were determined by SDS-PAGE (see section 3.2.4). Finally, the sample was aliquoted and stored at -20 °C.

3.2.4 Sodium dodecyl sulphate–polyacrylamide gel electrophoresis

Sodium dodecyl sulphate–polyacrylamide gel electrophoresis (SDS-PAGE) was performed based on the protocol described by Laemmli (275). MOG_{1-125}-His samples were 1:10-fold diluted in HEPES buffer and mixed with SDS sample buffer and SDS sample additive according to the manufacturer's guideline. The samples were incubated at 70 °C for 10 min and cooled to 4 °C after. Optionally, if the color of the sample had changed from purple to green, indicating a pH drop, the sample was titrated with 5 M NaOH solution until the color changed back to purple. 20 µl sample was loaded per pocket on a SDS gel. 4 µl protein ladder was loaded into the outermost pockets. The gel was clamped into the SDS-PAGE electrophoresis chamber and the whole system filled with SDS running buffer. Using a power supply, 200 V were applied for 60 min. Then, the gel was released from the mold, briefly washed with H_2O and incubated with Coomassie stain solution for 15 min. Finally, the Coomassie stain solution was replaced by destain solution and incubated for 15 min. The destain solution would eventually have been refreshed until the gel was completely destained. The migration distance of the protein was referred to the protein ladder and, thereby, the protein's size estimated. The purity of the sample was assessed by the number of additional protein bands present in the respective lane.

3.2.5 Experimental autoimmune encephalomyelitis

In order to induce experimental autoimmune encephalomyelitis (EAE) in mice, a modified protocol based on Abdul-Majid *et al.* was applied (276). All mouse lines, which were used for EAE experiments, had a *C57BL/6* genetic background. Female and male mice were both included in the experimental procedure. Mice were anaesthetized with a mixture of ketamine (87 mg/kg body weight) and xylazine (13 mg/kg body weight). The adequate depth of anesthesia was defined by the absence of pain reflexes and loss of muscle tone. The anaesthetized mice were kept on a 37 °C heating pad. 400 µg MOG_{1-125} was emulsified in 250 µl complete Freud's adjuvant (incomplete Freud's adjuvant supplemented with heat-inactivated *M. tuberculosis H37Ra* to a final concentration of 4 mg/ml). 100 µl of the emulsion was injected subcutaneously into each flank and 50 µl of the emulsion was injected subcutaneously into the base of the tail with a 23 G needle. Next, 350 ng pertussis toxin, dissolved in 100 µl PBS, was intraperitoneally administered. Mice were monitored until the anesthesia had weaned off. The time of immunization defined day 0 (0 dpi, days post immunization). At 2 dpi, mice were again intraperitoneally injected with 350 ng pertussis toxin in 100 µl PBS. From 0 dpi on, mice were monitored at least once a day. A motoric, behavioral and incontinence score was obtained daily. Once an animal obtained a score unequal to 0 it was monitored closely (e. g. twice per day) and water and food was directly supplied on the bottom of the cage.

The motoric score is an ordinal scale from 0 to 5 with steps in increments of 0.5, modified after Abdul-Majid *et al.* and Miller *et al.* (276, 277), previously described by Nikić *et al.* (225). The score is defined as follows: 0: absence of symptoms, 0.5: distal tail paralysis, 1.0: full tail paralysis, 1.5: gait insecurity, 2.0: hind limb paraparesis, 2.5: hind limb paraparesis, 3.0: dragging of hind limb(s), 3.5: hind limb paralysis, 4.0 hind limb paralysis and fore limb paresis, 4.5: hind limb paralysis and fore limb paralysis, 5.0: moribund. The behavioral score is based on an ordinal scale from 0 to 2 with steps in increments of 1. It comprises signs of abnormal behavior. Small behavioral abnormalities were defined as at least 1 abnormal finding in the aspects listed at a score of 0. Significant behavioral abnormalities were defined as at least 2 abnormal findings: 0: normal grooming, eating, drinking, nesting, exploring,

1: small behavioral abnormalities, 2: significant behavioral abnormalities. The incontinence score is based on an ordinal scale from 0 to 2 with steps in increments of 1. Incontinence was diagnosed by sticky fur around the genital. Urinary tract infection was diagnosed by the occurrence of blood at the genital and signs of systemic infection (abnormal behavior, freezing, accelerated heart and respiratory rate): 0: no abnormal findings, 1: incontinence, 2: urinary tract infection.

The animal experiment was terminated if the desired time point or severity of the disease progress had been reached or the termination criteria had been met (as defined by the animal protocol).

3.2.6 Cell isolation

To obtain a single cell suspension of cells from the murine CNS, a protocol which was adapted from Martin *et al.* was established (278).

Mice were lethally anaesthetized with isoflurane. The abdomen and the thorax were carefully opened. The pericardium was carefully removed from the heart. The right atrium was incised and the effluent blood collected with a syringe, equipped with a 20 G needle and prefilled with 100 µl 0.5 M EDTA, if needed. The left ventricle was punctuated with a 21 G winged infusion set, connected to a 20 ml syringe which contained 20 ml ice-cold PBS. PBS was injected intracardially with an approximate injection rate of 0.5 ml/s. The perfusion efficiency was monitored by inspecting the discoloration of the liver. Insufficiently perfused mice were excluded from further analyses.

Next, the fur, skin, muscles and bones of the back were dissected to free the spinal column from the surrounding tissue. At the caudal end of the spinal column, the spinal column was cut from the sacrum by cutting at the height of the uppermost insertion of the *Mm. glutei maximi*. At the cranial end, the spinal column was cut at the border to the scull. Next, to isolate the spinal cord from the spinal column, the 21 G needle of the winged infusion set was punctuated into the *Canalis vertebralis* from the caudal cut and pushed approximately 5 mm forward. The spinal column was clamped at the height where the needle was inserted to seal the *Canalis vertebralis* around the inserted needle. Then, pressure was applied by pushing the plunger of the syringe which was connected to the winged infusion set and the 21 G needle until the spinal cord was flushed out of the spinal column at the cranial end. The spinal cord was briefly washed with PBS and kept at 4 °C in PBS.

Next, PBS was replaced by 1 ml tissue digestion buffer and the spinal cord (with the buffer) transferred into a 1 ml Potter-Elvehjem homogenizer and homogenized with 10 strokes. The homogenate was transferred into a plastic tube and incubated at 37 °C for 30 min at 1,400 rpm to allow enzymatic dissociation of the tissue. Then, the enzymatic reaction was stopped by adding 1 % (v/v) 0.5 M EDTA in H_2O and placing the tube on ice for 10 min. The homogenate was passed through a 100 µm mesh filter and, subsequently, diluted in 30 ml ice-cold PBS. The homogenate was centrifuged (300 g, 4 °C, 10 min) and the supernatant was discarded.

The pellet was resuspended in 12 ml 30 % (v/v) Percoll gradient solution and centrifuged (2,500 g, 4 °C, 30 min, minimal acceleration, minimal deceleration, swing-bucket rotor). After the centrifugation, the myelin fraction was layered on top of the aqueous phase. The cells were at the bottom of the tube. The myelin fraction as well as the excessive Percoll gradient solution were carefully sucked away with a Pasteur pipette. The cell pellet was resuspended in the remaining Percoll gradient solution and transferred to a fresh tube. Next, 4 ml ice-cold PBS was added to the cell suspension and centrifuged

(300 g, 4 °C, 10 min). The supernatant was carefully removed and discarded and the cell pellet was resuspended in the appropriate volume of the respective solution that was needed for the further procedure.

3.2.7 Isolation of peripheral blood mononuclear cells

Blood was collected as described in section 3.2.6. All subsequent steps were performed at 4 °C and all solutions were pre-chilled to 4 °C. To remove erythrocytes from the sample, they were lysed with ACK buffer. Therefore, the sample was centrifuged (300 g, 4 °C, 10 min), the supernatant was discarded and the pellet was resuspended in 4 ml ice-cold ACK buffer. The suspension was incubated on ice for 10 min. Then, the sample was centrifuged (300 g, 4 °C, 10 min) and the supernatant discarded and the pellet resuspended in ice-cold PBS. This procedure was repeated until the pellet was discolorized, indicating that all erythrocytes had been lysed. Finally, the pellet was resuspended in the appropriate volume of the respective solution for the further procedure. 10 min before the analysis, viability dye was added to the sample (1:1000).

3.2.8 Cell surface staining

Single cell suspensions were prepared as described in sections 3.2.6 and 3.2.7. Typically, cells were resuspended in 200 µl ice-cold PBS without any additives (to avoid any protein contamination for the subsequent mass spectrometry analysis). Fc block was 1:500-fold diluted and incubated for 15 min at 4 °C to cover Fc receptors and prevent unspecific antibody binding. Then, antibody solutions were directly added to the sample. The dilution was, if not otherwise specified, 1:200. The sample was incubated for 30 min at 4 °C in the dark. Then, the sample was filled up to a total volume of 3 ml with PBS, mixed and centrifuged (300 g, 4 °C, 10 min). The supernatant was discarded and the pellet resuspended in 3 ml PBS and centrifuged (300 g, 4 °C, 10 min). The pellet was resuspended with PBS and the suspension was subjected to further assays. 10 min before the analysis, viability dye was added to the sample (1:1,000).

For bulk RNA sequencing, cells were stained with surface markers, washed and subsequently fixed by incubating the cells in fixations buffer and permeabilized with permeabilization buffer according to the manufacturer's protocol. Then, the intracellular staining was done in permeabilization buffer.

3.2.9 Fluorescence-activated cell sorting

Fluorescence-activated cell sorting (FACS) was performed on an BD FACSAria™ III sorter according to the manufacturer's guidelines. For sorting of lymphocytes, a 100 µm nozzle was used. All other cell types were sorted with a 130 µl nozzle. The system was pre-chilled to 6 °C prior to use. PBS was used as a sheath fluid. Likewise, cells were collected in a Protein LoBind® Tube (Eppendorf) that contained 1 ml ice-cold PBS. The flow-rate was adjusted to 1,000 – 2,000 events/s. Prior use, a drop delay was performed with drop delay beads using the software's automated configuration tool. The sort was performed at 4-way purity.

After sorting the cells, the cell suspension was centrifuged (500 g, 4 °C, 10 min) and the supernatant was discarded. The cell pellet was snap frozen in liquid nitrogen and stored at -80 °C until analysis.

3.2.10 Labeling and gating strategies of different cell types

Only live cells were sorted, indicated by low viability dye uptake (viability dye^{lo}). If mononuclear cells were sorted, events were restricted to a narrow SSC-A/FSC-A gate as shown by Ramesha *et al.* and Martin *et al.* (278, 279). Otherwise, if CNS cells were sorted, the SSC-A/FSC-A gate was set to exclude SSC-A^{lo}/FSC-A^{lo} events. Furthermore, only single cells were sorted. Therefore, only events which matched to a linear fit of the correlation between SSC-H and FSC-H were included.

The gating strategies for sorting of cells for proteomic analyses are shown in detail in Table 7. CD45 is a marker that denotes myeloid as well as lymphoid cells (280). Therefore, it was used to identify immune cells in single cell suspensions from CNS tissues. CD11b is predominantly expressed by myeloid cells (281, 282). Thus, mononuclear phagocytes, which derive from the myeloid lineage, were identified by the expression of CD45 and CD11b (278, 279) and, in the case of macrophages, by the signature enzymes iNOS and Arginase-1 (222). Intermediate expression levels of both CD45 and CD11b (CD45^{med}CD11b^{med}) are believed to denote microglia, in contrast, macrophages highly express CD45 and CD11b (CD45^{hi}CD11b^{hi}) (222, 278). To assess the expression levels of iNOS and Arginase-1, *iNOS-tdTomato-Cre x Arginase-1-YFP* mice were used. iNOS and Arginase-1 are assumed to be specific marker enzymes that distinguish pro-inflammatory M1 macrophages and anti-inflammatory M2 macrophages (229).

Lymphocytes were identified by the expression of CD45 as well as the expression of CD3 (T cell receptor, T cells) (283) and CD19/B220 (B cells) (284), respectively. CD3$^+$ T cells were further characterized by the expression of CD4 (T cell surface protein T4) and CD8 (T cell surface protein T8) (285).

Astrocytes were identified by the expression of astrocyte cell surface antigen-2, ACSA-2 (286). To fluorescently label neurons, the *Thy-1 YFP-16* mouse line was used and YFP$^+$ events were sorted. Oligodendrocytes were identified by the presence of the surface marker O4 (287). O4 predominantly characterizes pre-oligodendrocytes, pre-myelinating and myelinating oligodendrocytes (288–290). Oligodendrocyte precursor cells (OPC) were isolated based on their expression of PDGFRa (290).

For RNA sequencing, cells were extracellularly stained with Ly6-G-BV785 and CD11b-PerCP, fixed, permeabilized and washed and subsequently intracellularly stained with Arginase-1-APC and iNOS-eFluor 450.

All gates for FACS were defined according to the respective fluorescence minus one (FMO) control.

Cell type	Gating strategy
M1 macrophages	CD45^{hi}CD11b^{hi}iNOS$^+$Arginase-1$^-$
M2 macrophages	CD45^{hi}CD11b^{hi}iNOS$^-$Arginase-1$^+$
Monocytes	CD45$^+$CD11b$^+$Ly6C$^-$
Microglia	CD45^{med}CD11b^{med}
CD4$^+$ T cells	CD45$^+$CD3$^+$CD4$^+$CD8$^-$
CD8$^+$ T cells	CD45$^+$CD3$^+$CD4$^-$CD8$^+$
B cells	CD45$^+$CD19$^+$B220$^+$
Astrocytes	ACSA-2$^+$CD45$^-$
Neurons	Thy-1$^+$CD45$^-$

Oligodendrocytes	$O4^+CD45^-$
Oligodendrocyte precursor cells (OPC)	$PDGFR\alpha^+CD45^-$

Table 7: Gating strategy for the targeted cell types in the proteomics screen.

3.2.11 Isolation of neuronal mitochondria

To analyze the neuronal mitochondrial proteomes in EAE, mitochondria were isolated from MITO-Tag mice, which were neonatally injected with AAV9.hSyn:iCre intraventricularly, at peak of disease (EAE onset + 2 d, EAE score > 2) and at remission (EAE onset + 22 d) according to the previously described protocol by Fecher *et al.* and Tai (270, 271). This enabled us to specifically fluorescently label mitochondria from neurons. In brief, the lumbar spinal cord was isolated and homogenized with a Potter-Elvehjem homogenizer in mitochondria isolation buffer. The sample was incubated with nitrogen (800 psi) while stirring (60 rpm, 10 min), protease inhibitor was added, and the sample was centrifuged (600 g, 10 min). The supernatant was filtered through a 30 µm mesh and incubated with anti-GFP antibody-coated magnetic beads (50 µl) for 1 h at 4° C. Next, the sample was precipitated by magnetic-activated cell sorting (MACS) by applying the magnetic beads to a column in a magnetic field which was equilibrated with IP buffer. The column was washed three times with IC buffer and finally the sample were eluted by removing the columns from the magnetic field and flushing the beads out of the column with a plunger. The samples were immediately stored at -20° C. The isolation was established and performed by Dr. Yi-Heng Tai.

3.2.12 Mass spectrometry analysis

Sample preparation and mass spectrometry analysis was performed by the group of Prof. Dr. Felix Meissner at the Department of Proteomics and Signal Transduction, Max Planck Institute of Biochemistry, Munich, Germany. Sample preparation and mass spectrometry measurement was done as described by Karayel *et al.* (291). In brief, frozen cell pellets were lysed by adding sodium deoxycholate (SDC) lysis buffer (1 % SDC in 100 mM Tris, pH 8.4), incubated at 95 °C for 5 minutes and subsequently homogenized by sonication. Samples were diluted to achieve a constant protein concentration and reduced and alkylated with 40 mM CAA and 10 mM TCEP (5 min incubation at 45 °C). Next, proteins were digested with trypsin and LysC (1:100, 37 °C, overnight incubation). Next, peptides were diluted in 1 % trifluoroacetic acid (TFA) in isopropanol and desalted and purified with a reverse phase column (SDB-RPS tips) with 1 % TFA in isopropanol and 0.2 % TFA with 2 % acetonitrile (ACN). To elute the peptides, the columns were washed with 1.25 % ammonium hydroxide in 80 % ACN and dried (SpeedVac vacuum concentrator). Finally, samples were resuspended in 0.2 % TFA with 2 % ACN. Peptides were separated by liquid chromatography (EASY-nLC™ 1200 system, Thermo Fisher Scientific), equipped with a 50-cm reversed-phase column with ReproSil-Pur C18-AQ 1.9 µm resin (Dr. Maisch). The flow rate was 450 nl/min with a buffer system consisting of buffer A (0.1 % formic acid) and buffer B (80 % ACN with 0.1 % formic acid). The chromatography system was coupled to a Q Exactive HF-X mass spectrometer (Thermo Fisher Scientific), operated with the settings described by Karayel *et al*. Spectra were acquired and analyzed in a data-independent fashion using the Spectronaut™ software (Biognosys, Schlieren, Switzerland).

Sample preparation and mass spectrometry analysis of neuronal mitochondria was performed by the group of Prof. Dr. Stefan Lichtenthaler at the German Center for Neurodegenerative Diseases, Munich, Germany. Isolation of neuronal mitochondria was performed by Dr. Tai. Details are described by Tai (271).

3.2.13 RNA sequencing

After cell sorting, cells were washed and resuspended in 100 µl RNA lysis buffer and incubated for 1 h at 56°C. Then, RNA was extracted with the RNeasy Micro Kit (QIAGEN) according to the manufacturer's protocol. RNA was reversely transcribed into cDNA and the cDNA was subsequently purified using an mRNA library kit according to the manufacturer's protocol. The sample purity was assessed on a microfluidic analyzer equipped with a microfluidic chip. Samples were sequence at the Laboratory for Functional Genome Analysis (LAFUGA, LMU Munich). Quality check and demultiplexing was performed within the Galaxy environment. Gene mapping and raw count normalization was done with a customized R script using the library DEseq2 (292). Further computational analyses were performed with specific Python scripts.

3.2.14 Tissue processing and staining

Mice were lethally anaesthetized with isoflurane and transcardially perfused with 20 ml PBS supplemented with 5 IU/ml Heparin and 20 ml 4 % (v/w) paraformaldehyde in PBS. Next, the spinal cord was dissected (laminectomy) and further fixed in 4 % (v/w) paraformaldehyde in PBS for 12 h. The tissue was cryoprotected with 30 % (w/v) sucrose in PBS for 48 h at 4 °C. The caudal part of the lumbar spinal cord was embedded into molds containing a specimen matrix, frozen at -20 °C and cut in 50 µm sections using a cryostat. The sections were washed twice with PBS and permeabilized with 0.1 % (v/v) Triton X-100 in PBS. Unspecific epitope binding was blocked by incubating the sections in blocking buffer for 2 h. The respective primary antibody was diluted in PBS and incubated at 4 °C for 24 h. The sections were washed three times with PBS. The secondary antibody was diluted in PBS and incubated at room temperature for 2 h. The sections were washed three times with PBS. The second washing step was performed with 0.01 % (w/w) DAPI in PBS. The sections were mounted on a microscopy slice, dried, covered with mounting medium and sealed with a cover slip.

3.2.15 Confocal microscopy imaging

Samples were scanned on a FV1000 confocal microscopy system (Olympus) with 20- or 60-fold magnification and recorded as 12-bit images. The excitation and emission filter wavelength were set as depicted in Table 8. The signal amplification was adjusted to control for oversaturation. Secondary antibody only controls were used to assess the background signal. The channels were recorded sequentially. The resolution was 1024 x 1024 pixels.

Channel	Excitation [nm]	Emission filter (bandpass) [nm]
DAPI	405	405 – 435
YFP	488	510 – 540
tdTomato	559	590 – 620

AF647	635	655 – 755

Table 8: Confocal microscopy excitation and emission filter configuration.

3.2.16 Data analysis

Data analysis was performed with custom scripts written in a Python, R and Javascript environments (273, 274).

3.2.16.1 Data clean-up and data imputation

A protein was considered as true positively detected if it showed an expression value in > 1 sample per group (cell type per condition). If the number of expression values per groups was below 1, all values were imputed by random values deriving from a normal distribution characterized by a mean value of a two-fold negative standard deviation drawn from the original dataset and a standard deviation of the 0.3-fold standard deviation of the original dataset to mimic lowermost values in the dataset and avoid zero inflation effects. If the number of valid samples per group was > 1, sequential imputation of missing values was applied individually for each group to substitute missing values. This method showed higher correlation coefficients when artificially deleted values were predicted compared to other techniques (293). To evaluate the precision of the imputation, single imputation techniques and multiple imputation techniques were assessed on a dummy dataset which was designed to exhibit similar features as the original proteomics expression dataset. The prediction precision was assessed by calculating the correlation coefficient between the actual values, which had been deleted, and the substitutes. After imputation of missing values, all values were $\log_2$-transformed.

Raw counts from transcriptomic analyses were replaced by 0 if < 2 data points per group were defined. If a sequence was only detected in 1 (out of 3) sample, all 3 values were excluded from further analysis. Likewise, counts < 10 were excluded from analysis. Raw counts were normalized according to the median ratio method (294). Missing values were imputed using an iterative imputation algorithm.

3.2.16.2 Central tendencies and interval estimates

The mean value and standard deviation were calculated as a measure for the central tendency and interval estimate for parametric variables. For non-parametric variables, the median and the interquartile range were calculated. Quantile-quantile (Q-Q) plots were used to compare a distribution with a standard normal distribution by visual inspection.

3.2.16.3 Effect sizes

To estimate the effect size of the difference between the central tendencies of two groups, Cohen's d was calculated according to the following equation (295, 296). If not otherwise specified, heteroscedasticity and unequal group sizes were assumed:

$$d = \frac{\bar{\mu}_1 - \bar{\mu}_2}{\sqrt{\frac{(n_1 - 1){\sigma_1}^2 + (n_2 - 1){\sigma_2}^2}{n_1 + n_2 - 2}}}$$

where $\bar{\mu}_1$ and $\bar{\mu}_2$ are the mean values from the two independent groups, σ_1 and σ_2 the respective standard deviations and n_1 and n_2 the group sizes. The numerator denotes the difference in means, the denominator denotes the pooled standard deviation which estimates the overall variance by weighted variances of two groups.

3.2.16.4 Statistical hypotheses testing

Statistical hypotheses testing was performed to control for type I errors when null hypotheses were sought to be rejected or accepted.

To test the if two means $\bar{\mu}_1$ and $\bar{\mu}_2$ from two independent and normally distributed samples 1 and 2 were equal, t-statistic test was calculated. The null hypothesis was defined as:

$$H_0: \bar{\mu}_1 = \bar{\mu}_0$$

Normality was assumed if a given share of values could be parameterized by a mean and variance. This was assessed by visual inspection of quantile-quantile plots for samples with a large sample size. Homoscedasticity of samples was assumed if

$$0.5 < \frac{\sigma_1}{\sigma_2} < 2$$

and

$$p < 0.05$$

for

$$H_0: \sigma_1 = \sigma_2$$

calculated by Levene's test with the groups' standard deviation s_1 and s_2. If the groups had been heteroscedastic, Welch's test would have been calculated. If the groups had been homoscedastic, Student's *t* test would have been calculated. When multiple hypotheses were tested, alpha error accumulation was controlled by calculating the false discovery rate (FDR) *q* value by adjusting *p* values according to Benjamini-Hochberg (297).

3.2.16.5 Correlation analyses

To assess the correlation of the expression of certain proteins between samples, the correlation coefficient according to Pearson was calculated for the respective expression matrices. If multiple correlations among $n > 2$ samples were calculated, hierarchical cluster analysis based on the Euclidean distances of the resulting correlation matrix was calculated and visualized by a dendrogram.

3.2.16.6 Data scaling

For data standardization of all values $x_1, x_2, \ldots, x_i$ of the vector *a*, the standard score *z* was calculated as

$$z = \frac{x - \mu}{\sigma}$$

where μ is the mean and *s* is the standard deviation of *a*.

For minimum-maximum (min-max) rescaling of all values x_1, x_2,…,x_i of the vector a, the values x_1', x_2',…,x_i' were calculated as

$$x' = \frac{x - \min(a)}{\max(a) - \min(a)}$$

where *min(a)* and *max(a)* are the minimum and maximum values of the vector *a*.

3.2.16.7 Dimension reduction

To assess the degree of sample similarity, uniform manifold approximation and projection (UMAP) was performed (298). All features/samples of the expression matrix were standardized before the analysis. Likewise, principal component analysis (PCA) was applied as a dimension reduction technique. As for UMAP, the features/samples were standardized before the analysis. The first two principal components (PC1 and PC2) of each feature/sample were plotted in a two-dimensional space and their proportional explained variance reported.

3.2.16.8 Differential protein expression and receiver operating characteristic (ROC) analysis

The differential protein expression was calculated by the fold change between the logarithmic expression levels of two groups. To assess the relationship between any given fold change and the fraction of false-positive observations above this fold change (as defined as the fraction of observations with $q > 0.05$), a receiver-operating characteristic (ROC) analysis was performed. A given fold change cutoff value was assessed by calculating its Euclidean distance to the point (sensitivity = 1|1-specificity = 0) which characterized the maximum sensitivity and specificity.

3.2.17 Gene set enrichment analysis coupled to network analysis (*NezzworGS*) and functional protein-protein interaction network analysis (*FUPPINA*)

To explore high dimensional proteomic or transcriptomic datasets with respect to underlying functional patterns we developed the Python package *Nezzworker* (engeldaniel.com/nezzworker, github.com/engelsdaniel/nezzworker). It is composed of the two classes *NezzworGS* (gene set enrichment analysis coupled to network analysis) and *FUPPINA* (FUnctional Protein-Protein Interaction Network Analysis).

Gene set enrichment analysis is a powerful technique to gain further insights into the biological function of a group of differentially expressed proteins or genes. However, a single gene can belong to more than one gene set. Furthermore, most gene set libraries (such as Reactome, which was used in this study) are hierarchically designed with child gene sets as a subgroup of a respective parent gene set. This means that the differential abundance of a share of proteins or transcripts may result in the enrichment of more than one gene set, although the biological source of the enrichment is the same. Therefore, we designed *NezzworGS*, a novel computational algorithm implemented into the *Nezzworker* Python module that performs gene set enrichment analysis with subsequent network analysis to further explore the relationship of enriched gene sets. Moreover, *NezzworGS* identifies parent-child relationships of gene sets within hierarchically designed gene set libraries.

The *NezzworGS* algorithm performs a gene set enrichment analysis according to Subramaniana *et al.* implemented into a custom computational algorithm with a subsequent network analysis (299). In principle, this algorithm tests to which extent genes from an *a priori* defined gene set are differentially abundant in two groups. Therefore, the normalized enrichment score (NES) was calculated to assess the extent of the difference between the enrichment of genes between two groups. Both the classical as well as the pre-ranked method were used to calculated the NES (299). Because of the explorative nature of this approach, a FDR-adjusted *p* value (*q* value) threshold ≤ 0.25 was defined (299). Alternatively, gene sets were ranked according to their NES as a primary thresholding criterion. Next, the gene set similarity was calculated in an adjacency matrix based on the number of genes that are shared between gene sets (threshold: > 25 % overlap in any of the gene sets). The adjacency matrix was then translated into a weighted network graph with the nodes representing the gene sets and the edges encoding the gene set similarity. The thickness of the edges encoded the number of leading-edge genes shared between two gene sets. The area of the nodes represented the mean (protein or gene) expression based on expression values of all members of the respective gene set. The spatial distribution of the nodes (weight) reflected the similarity of genes sets (regardless if the genes were present in the underlying dataset), calculated as the maximum overlap fraction of two gene sets in an adjacency matrix. In a subsequent analysis all proteins or genes underlying the identified enriched gene sets were individually analyzed with respect to their mean expression and fold change between the two groups. *NezzworGS* automatically calculates centrality measures of the network and identifies network modules. If Reactome is chosen as the underlying gene sets library, *NezzworGS* evaluates the parent-child relationship between enriched gene sets because some gene sets (children) can be (full) subsets of larger gene sets (parents), leading to an overestimation of the biological signature if both are enriched in the analysis.

The *FUPPINA* algorithm performs a functional protein-protein interaction network analysis based on the STRING (Search Tool for the Retrieval of Interacting Genes/Proteins) database which contains information about physical and functional protein-protein interactions (300). First, an adjacency matrix was constructed based on the STRING score that characterized the interaction between each of the proteins to be analyzed. Second, an undirected weighted network graph was constructed from this adjacency matrix. Nodes which were not connected to at least one other node were remove from the network. Network parameters (density, degree of centrality, degree of eigenvector centrality, degree of betweenness centrality, degree of closeness centrality) were calculated and functional hubs within the network were uncovered by extracting network modules. To further investigate the molecular signature of the modules, a gene set enrichment analysis was performed using the Enrichr algorithm according to Chen *et al*., which was implemented into the custom computational workflow (301). In brief, this algorithm assumes a binominal distribution for the chance of a any gene to be mapped to any gene set in relation to a reference (or background) share of genes. The probability for a list of genes not to occur in any given gene set was calculated according to the Fisher exact test. To summarize the results, *p* values deriving from the Fisher exact test were computed. Gene sets with the lowest *p* values were displayed.

Gene set datasets were obtained from the Molecular Signatures Database (MSigDB, version 7.1 and 7.4, https://www.gsea-msigdb.org) and Reactome (Reactome, release 77, https://reactome.org/download-data/, 09/01/2021)

3.2.18 Validation of a novel gene set enrichment analysis coupled to network analysis algorithm (*NezzworGS*)

To test the *NezzworGS* algorithm, we constructed two dummy datasets. The first dummy dataset was an artificial fold change matrix that contained 1000 genes (gene "1" to gene "1000") with fold change values from an evenly spaced list from -1 to 1. The expression values were drawn from a random distribution and min-max normalized. The second dummy dataset was a gene set library which encompassed 19 artificial gene sets, each including a fraction of genes from the fold change and expression matrix. The gene sets were related in terms of genes they share with each other (Table 9). Next, the fold change matrix, the expression matrix and the gene set library were subjected to the *NezzworGS* algorithm.

Gene set	Genes	N genes	Overlap
A1	1 – 50	50	A2: 80 %, A3: 60 %, A4: 40 %, A5: 20 %, A6: 2 %
A2	10 – 60	50	A1: 80 %
A3	20 – 70	50	A2: 80 %, A1: 60 %
A4	30 – 80	50	A3: 80 %, A2: 60 %, A1: 40 %
A5	40 – 90	50	A4: 80 %, A3: 60 %, A2: 40 %, A1: 20 %
A6	50 – 100	50	A5: 80 %, A4: 60 %, A3: 40 %, A2: 20 %, A1: 2 %
B1	950 – 1000	50	B2: 80 %, B3: 60 %, B4: 40 %, B5: 20 %, B6: 2 %
B2	940 – 990	50	B1: 80 %, B3: 80 %, B4: 60 %, B5: 40 %, B6: 20 %
B3	930 – 980 + 700 – 760	110	B1: 27 %, B2: 36 %, B4: 36 %, B5: 27 %, B6: 18 %, B7: 55 %
B4	920 – 970	50	B1: 40 %, B2: 60 %, B3: 80 %, B5: 80 %, B6: 80 %
B5	910 – 960	50	B1: 20 %, B2: 40 %, B3: 60 %, B4: 80 %, B6: 80 %
B6	900 – 950	50	B1: 2 %, B2: 20 %, B3: 40 %, B4 60 %, B5: 80 %
B7	700 – 760 + 800 – 860 (30)	90	B3: 66 %, B8: 33 %
B8	800 – 860 (30)	30	B7: 100 %
C1	500 – 560 (50)	50	none
C2	400 – 475 (5)	50	none
D1	600 – 620 + 1700 – 1720	40	D2: 75 %, D3: 50 %
D2	610 – 630 + 1700 – 1720	40	D1: 75 %, D3: 25 %
D3	600 – 620 + 2700 – 2720	40	D1: 50 %, D2: 25 %

Table 9: Dummy gene sets. The names of the gene sets are arbitrary. The numbers in the column "genes" represent the artificial gene names from a list of genes from "1" to "1000". The overlap is the ratio between the number of genes a gene sets has in common with another gene set and the overall number of genes.

Gene set enrichment analysis revealed the enrichment of 7 gene sets with a normalized enrichment score (NES) < 0 and 12 gene sets with an NES > 0 (Supplement Figure 1). Gene sets which are comprised of genes with a high fold change value showed higher (absolute) NES values compared to gene sets with genes with fold changes close to 0 or to the middle rank, respectively (gene sets C1, C2, D1, D2 and D3).

The main feature of *NezzworGS* is the analysis of the relationships between enriched gene sets identified from a differential expression matrix. Supplement Figure 2 displays the network of enriched gene sets. Gene sets are represented by vertices. The edges encode the fraction of overlapping leading-edge proteins/genes from the analysis, the actual value is encoded by the edge thickness. By visual inspection, the network encompassed 3 subnetworks and 2 vertices without any further connections. The network reflected the overlap between different gene sets: Gene set A1 was connected with gene sets A2 (80 % overlap), A3 (60 % overlap) and A4 (40 % overlap) but neither with gene set A5 (20 % overlap) nor with gene set A6 (2 % overlap), because the latter ones did not meet the filter criterion of a minimum overlap of 25 % (as defined for this analysis). Furthermore, the edge thickness reflected the degree of overlap between the gene sets (the edge between A1 and A2, which showed an overlap of 80 %, was thicker compared to the edge between A1 and A4 with an overlap of 40 %). The *NezzworGS* algorithm computes a weighted network where the spatial distribution of vertices within a (sub-) network is dictated by the gene sets similarity between two vertices, regardless of the number of leading-edge genes they have in common. This feature is best visualized in the subnetwork that encompassed gene sets D1, D2 and D3. Gene set D2 had a higher overlap with D1 (75 %) compared to D3 (25 %), thus, vertices 10 and 8 were further apart compared to 10 and 9. However, if the sizes of two connected gene sets are unequal, the overlaps (defined by the fraction of genes which are members of both gene sets relative to the gene set size) of each of the gene sets are unequal. In this case, the higher overlap is weighted higher to ensure that gene sets which are child gene sets have a closer proximity to their parent gene set. For example, gene set B8 is a full child gene set of gene set B7 (100 % overlap), however, the genes of B8 only make up one third of the whole gene set, while 66 % of the members of B7 are shared with B3. Nevertheless, B8 and B7 showed a closed proximity compared to B3 and B7 to control for the fact that B8 can be considered as a child gene set of B7.

To further characterize the vertices/gene sets within the network, the *NezzworGS* algorithm computes centrality measures of each vertex (Supplement Figure 3). Practically, this shows with how many other gene sets a specific gene set has (leading-edge) genes/proteins in common. Because many gene set libraries are hierarchically designed (with parent-child relationships), a high degree of centrality might indicate that the respective gene set acts as a parent gene set for the connected gene sets. The degree of centrality analysis reveals that gene set B3 has the highest degree of centrality. Indeed, gene set B3 has most connections with a relative high overlap to other vertices (B1: 27 %, B2: 36 %, B4: 36 %, B5: 27 %, B6: 18 %, B7: 55 %). Vertices which are not connected to any other vertex (C1, C2) or which have equal numbers of edges (D1, D2, D3) have (similar) low degrees of centrality.

Yet another feature of *NezzworGS* is to compute the modularity of a network (Supplement Figure 4). This feature allows to identify functionally linked gene sets and functional cores, especially in larger networks.

Besides the above shown features, *NezzworGS* determines the gene set parent-child-relationship of the Reactome gene set library to control for its hierarchical architecture and the potential overestimation of the enrichment of (functionally) similar gene sets.

3.2.19 Validation of a novel functional protein-protein interaction coupled to network analysis algorithm (*FUPPINA*)

As outlines above, gene set enrichment analysis is a powerful computational technique to unravel molecular signatures of differential gene or protein expression matrices. However, most gene set enrichment analysis algorithms require two sets of expression values from different (experimental) conditions and are therefore not suitable for the analysis of a single set of expression values of genes or proteins. A possible solution is to individually review either highly abundant or differentially abundant (between two phenotypes) proteins or transcripts. However, high abundance does not necessarily come along with high biological impact, likewise differential abundance analysis requires at least two conditions. Thus, we developed an algorithm to screen for functional hubs in a set of genes or proteins based on functional protein-protein interaction data (STRING database) and network analysis (functional protein-protein interaction coupled to network analysis, *FUPPINA*).

To test the *FUPPINA* algorithm we created two dummy datasets. First, we randomly drew 500 gene names from a list of all genes listed in the Reactome gene set library (version 7.4, random dataset). Second, we created a list of gene names by randomly choosing 5 gene sets from the Reactome gene set library and extracting their gene name (gene set dataset). If necessary, this list was filled up to 500 gene names with gene names randomly selected from the list of all gene names listed in the Reactome gene set library. The respective expression values were not taken into account and were all set to 1. Next, we subjected both the random datasets and gene set dataset to *FUPPINA*. The functional protein-protein interaction network of the random dataset was composed of 157 genes/nodes with on average 4.92 edges per node with a network density of 0.06 (Supplement Figure 5). Network modules were not clearly distinguishable by visual inspection.

In contrast, the functional protein-protein interaction network of the gene set dataset was composed of a higher number of genes/nodes (258) with a higher average number of edges per node (22.05), likewise, the network density (0.17) and triadic closure (0.93 versus 0.45) was higher (Supplement Figure 6). By visual inspection, the functional protein-protein interaction network of the gene set dataset encompassed clearly distinguishable modules with a low inter-module connectivity.

Taken together, network analysis of functional protein-protein interactions from a gene list which derived from gene sets mirrored the functional relationship of the underlying genes. Network parameters (degree of centrality, density, modularity, triadic closure) pointed towards a tighter network structure when functionally related genes/proteins are analyzed compared to a functional protein-protein interaction network constructed from a list of random gene names. Thus, the functional protein-protein interaction coupled to network analysis (*FUPPINA*) algorithm can be used as a tool to estimate the functional relationship within a set of genes or proteins independent from expression levels. Moreover, it can serve as the basis for further analysis such as gene set enrichment analysis (using the Enrichr algorithm) to obtain deeper insights into the explicit function of genes or proteins underlying the network's modules.

3.2.20 Annotation of proteins

Proteins were annotated as extracellular proteins according to the Cell-Cell Interaction Database (302). Mitochondrial proteins were identified using the MitoCarta2.0 database (303). To map

mitochondrial proteins to each of the five electron transfer chain complexes as well as to the citric acid cycle (TCA), the Kyoto Encyclopedia of Genes and Genomes (KEGG) was used (304–306). Proteins/genes assigned to the Term 'NADH:ubiquinone oxidoreductase, mitochondria', 'NADH dehydrogenase (ubiquinone) Fe-S protein/flavoprotein complex, mitochondria', 'NADH dehydrogenase (ubiquinone) 1 alpha subcomplex', 'NADH dehydrogenase (ubiquinone) 1 beta subcomplex' (complex I), 'Succinate dehydrogenase (ubiquinone)' (complex II); 'Cytochrome bc1 complex respiratory unit', 'Cytochrome bc1 complex' (complex III); 'Cytochrome c oxidase' (complex IV), 'F-type ATPase, eukaryotes', 'V-type ATPase, eukaryotes' (complex V) and 'Citrate cycle (TCA cycle, Krebs cycle)' (TCA) were considered as proteins involved in these metabolic pathways.

3.2.21 Ligand-receptor interaction prediction

To screen for potential ligand-receptor interactions between M1 and M2 macrophages and other immune cells we first annotated proteins (secreted proteins and ligands) in the respective proteomes using databases curated by Efremova *et al.* and Qiao *et al.* (302, 307). Next, ligand-receptor interaction profiles were extracted from these databases and the respective ligands or receptors were identified. An interaction was assumed if the standardized mean expression of the ligand and receptor was > 1. The interactions were visualized with a custom Javascript script.

4 Results

4.1 Mononuclear phagocytes differently express marker proteins at distinct time points during EAE disease progression

In order to analyze how mononuclear phagocytes change their molecular phenotype during EAE disease progression, their abundances and signature protein expression patterns were measured by flow cytometry. Single cells from EAE spinal cords from disease onset and 5 days after onset (5 dpo, days post onset) were stained with fluorescently labeled anti-CD45, anti-CD11b and anti-Ly6C antibodies. *iNOS-tdTomato-Cre x Arginase-1-YFP* mice were used to distinguish between M1 (M^{iNOS}) and M2 ($M^{Arginase\text{-}1}$) macrophages by genetic fluorescent labelling of the respective cells.

The SSC/FSC analysis of the single cell suspensions from the spinal cord from EAE showed that there was a distinct share of events with an approximate mFI (mean fluorescence intensity) in the SSC channel at 25 k and 125 k in the FSC channel (Figure 1, **A**). These events were characterized by high CD45-BV786 fluorescence signals. In control mice, the number of these events was tremendously lower (Supplement Figure 7, **C**). Next, the FI (fluorescence intensities) of CD45-BV786, CD11b-APC and Ly6C-PerCP were measured in the clusters that were characterized by high CD45-BV786 FI levels (Figure 1, **B**, cluster 1, 3 and 4). The majority of events were $CD11b^+$ and characterized by a higher Ly6C-PerCP FI (compared to $CD11b^-$ events). $CD11b^+$ events further subdivided into $CD11b^{hi}CD45^{hi}$ and $CD11b^{med}CD45^{med}$ events (Figure 1, **C**). The number of $CD45^{hi}CD11b^{hi}$ events exceeded 3.5-fold the number of $CD45^{med}CD11b^{med}$ events. The mFI of the Ly6C-PerCP signal of $CD45^{hi}CD11b^{hi}$ events (mFI = 2,314.9, SD = 2,465.6) was 8.1-fold higher compared to $CD45^{med}CD11b^{med}$ events (mFI = 284.2, SD = 143.7). Most CD45-$BV786^+$ events were CD11b-APC^+ (Figure 1, **D** and Table 10). Analysis of the iNOS-tdTomato and Arginase-1-YFP signals revealed, that both signals were exclusively detected in $CD11b^{hi}$ events. $CD11b^{hi}CD45^{hi}$ events were either iNOS-$tdTomato^+$ or Arginase-$1\text{-}YFP^+$, but not $iNOS^+Arginase\text{-}1^+$. However, only few Arginase-YFP^+ events were detected. The ratio of iNOS-$tdTomato^+$ events to Arginase-$1\text{-}YFP^+$ events was 10.5.

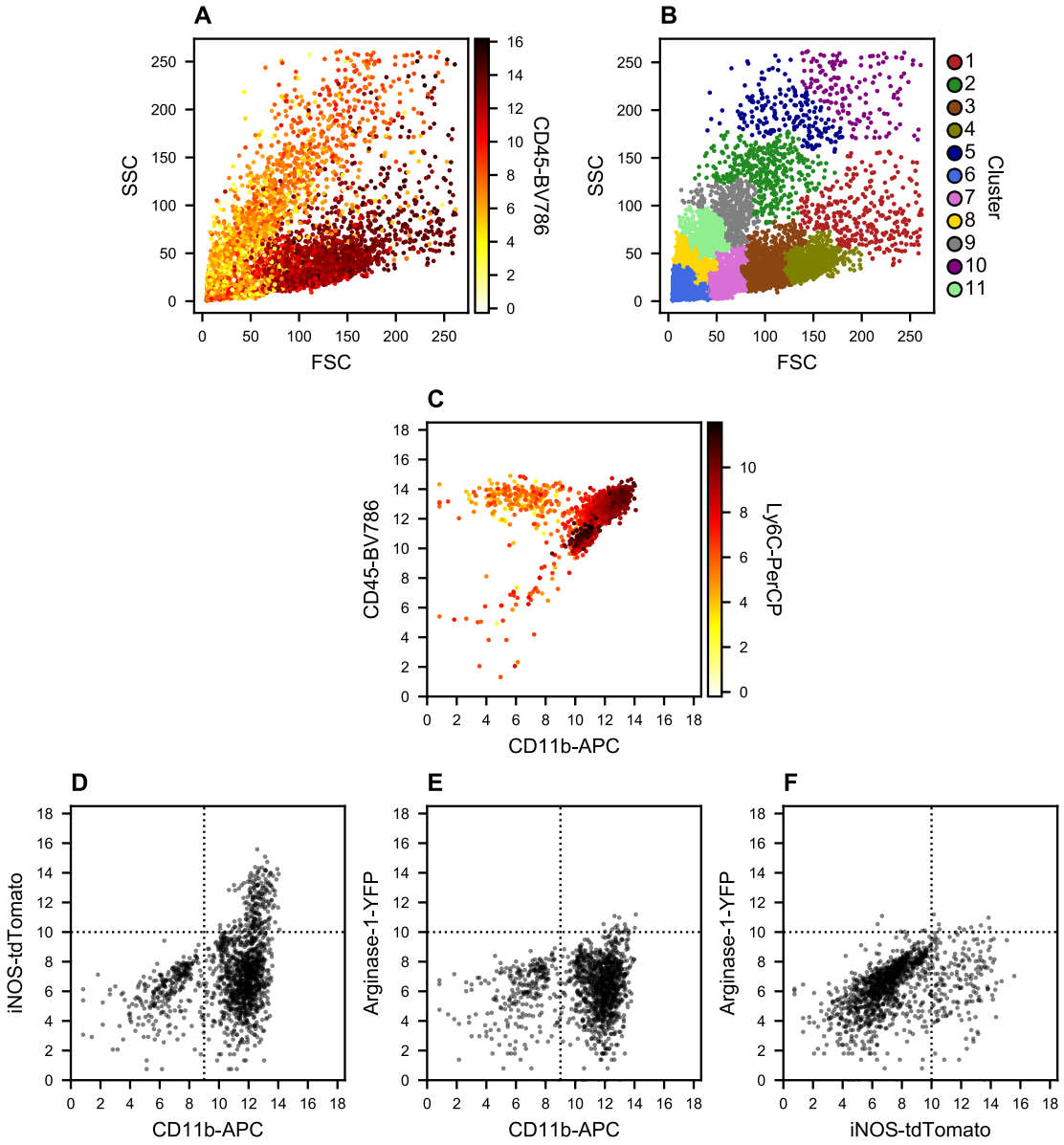

Figure 1: Flow cytometry analysis of cells isolated from EAE spinal cords (onset). Single cell suspensions from spinal cord from EAE mice at disease onset (day with first disease score). **A**: SSC/FSC analysis of all events. Log_2-transformed CD45-BV786 FI is color-coded. **B**: Unsupervised cluster analysis (agglomerative clustering) of events characterized by SSC and FSC. **C**: CD45-BV786 and CD11b-APC FI of $CD45^+$ clusters 1, 3, 4 and 7. Logarithmic Ly6C-PerCP FI is color-coded. **D – F**: iNOS-tdTomato, CD11b-APC and Arginase-1-YFP fluorescence signals in all $CD45^+$ events. iNOS-tdTomato and Arginase-1-YFP signals exclusively occur in CD11b-APC^{hi} events. There were almost none iNOS-tdTomato$^+$Arginase-1-YFP^+ events detected. The horizontal and vertical dotted lines indicate the FI threshold values (signal-to-noise) as defined by FMO controls. SSC and FSC FI were divided by 10^3. All other FI were log_2-transformed. All FI are depicted as area of the signals. Maximum values (oversaturated signals) or minimum values (undersaturated signals) were excluded from the analysis. FI: fluorescence intensity.

Events	Frequency at onset [%] (SD)	Frequency at 5 dpo [%] (SD)	ΔFreq [%]	Cohen's *d* (*p*)
$CD11b^+CD45^+$	58.6 (13.1)	75.6 (5.4)	+17	5.31 (6.6 x 10^{-4})
$CD11b^-CD45^+$	10.3 (4.4)	9.8 (1.6)	-0.5	-0.27 (0.7)
$CD11b^{hi}CD45^{hi}$	43.4 (10.1)	27.1 (5.5)	-16.3	-5.62 (1.3 x 10^{-4})

$CD11b^{lo}CD45^{lo}$	12.4 (4.5)	45.1 (9.3)	32.7	13.03 (6.3 x 10^{-6})
$CD11b^{hi}CD45^{hi}iNOS^{+}Arginase\text{-}1^{-}$	10.5 (4.2)	11.1 (3.5)	0.6	0.30 (0.8)
$CD11b^{hi}CD45^{hi}iNOS^{-}Arginase\text{-}1^{+}$	1.0 (0.6)	10.9 (3.1)	9.9	8.04 (3.6 x 10^{-5})
$CD11b^{hi}CD45^{hi}iNOS^{+}Arginase\text{-}1^{+}$	1.6 (0.6)	8.5 (3.1)	6.8	5.52 (3.8 x 10^{-4})
$CD11b^{hi}CD45^{hi}iNOS^{-}Arginase\text{-}1^{-}$	86.8 (4.0)	69.6 (5.7)	-17.2	-8.01 (1.2 x 10^{-5})
$CD11b^{med}CD45^{med}iNOS^{+}Arginase\text{-}1^{-}$	0.7 (0.5)	0.2 (0.1)	-0.4	-0.71 (1.1 x 10^{-2})
$CD11b^{med}CD45^{med}iNOS^{-}Arginase\text{-}1^{+}$	0.2 (0.6)	3.4 (0.9)	3.1	3.85 (2.4 x 10^{-6})
$CD11b^{med}CD45^{med}iNOS^{+}Arginase\text{-}1^{+}$	0.2 (0.3)	0.2 (0.2)	0.0	-0.06 (0.8)
$CD11b^{med}CD45^{med}iNOS^{-}Arginase\text{-}1^{-}$	98.9 (1.2)	96.2 (1.0)	-2.7	-2.60 (2.3 x 10^{-5})

Table 10: Relative abundances of $CD45^{+}$ events from spinal cords from EAE mice. Single cell suspensions from EAE spinal cords were measured by flow cytometry. CD45-BV786, CD11b-APC, iNOS-tdTomato and Arginase-1-YFP FI (signal area) defined the gates. Frequencies are shown as % (± SD). *p* values result from t statistics for independent and heteroscedastic groups for H_0: $\mu_{Frequency\ at\ onset} = \mu_{Frequency\ at\ 5\ dpo}$. Cohen's *d* was calculated for the comparison between the frequencies at onset and the frequencies at 5 dpo. n_{onset} = 13 mice, $n_{5\ dpo}$ = 8 mice. dpo: days post onset. ΔFreq: Frequency at 5 dpo – Frequency at onset [%].

At 5 dpo, the $CD11b^{hi}CD45^{hi}$/$CD11b^{med}CD45^{med}$ ratio was 5.8-fold lower when compared to onset (0.6 at 5 dpo *versus* 3.5 at onset, Figure 2, **C**, Table 10). As observed at onset, iNOS-tdTomato^{+} and Arginase-1-YFP^{+} events were all CD11b-APC^{hi}. However, in comparison to onset, there were more Arginase-1-YFP^{+} events (from 1.0 % to 10.9 % of all CD45-BV786^{+} events) and more iNOS-tdTomato^{+}Arginase-1-YFP^{+} events (from 1.6 % to 8.5 % of all CD45-BV786^{+} events). The ratio of iNOS-tdTomato^{+} events to Arginase-1-YFP^{+} events was 1.0.

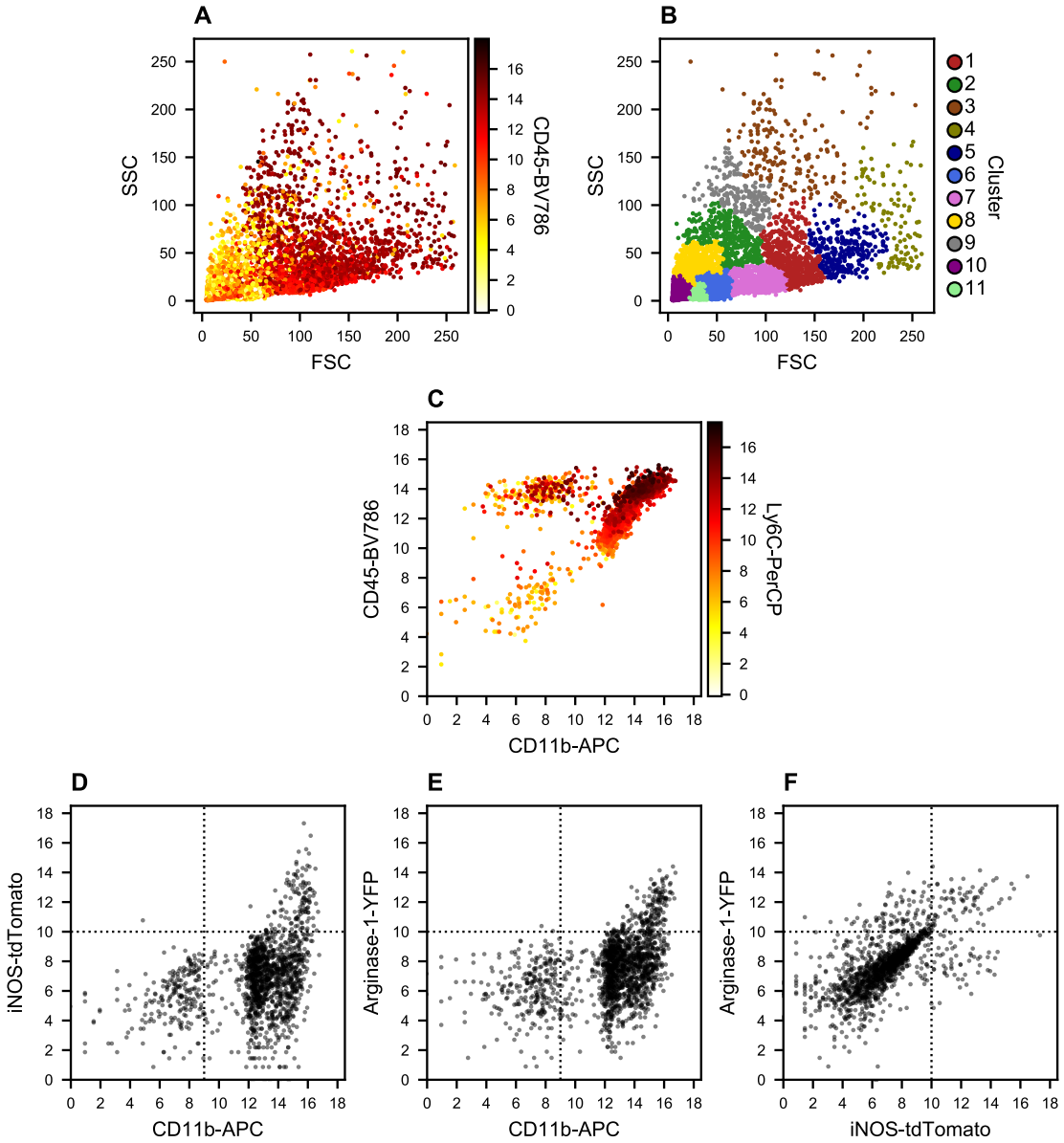

Figure 2: Flow cytometry analysis of cells isolated from EAE spinal cords (5 dpo). Single cell suspensions from spinal cord from EAE mice at 5 days after disease onset (5 dpo). Onset was defined as the day of the occurrence of the first EAE symptom. **A**: SSC/FSC analysis of all events. Log_2-transformed CD45-BV786 FI is color-coded. **B**: Unsupervised cluster analysis (agglomerative clustering) of events characterized by SSC and FSC. **C**: CD45-BV786 and CD11b-APC FI of $CD45^+$ clusters 1, 3, 4, 5, 7 and 9. Logarithmic Ly6C-PerCP FI is color-coded. **D** – **F**: iNOS-tdTomato, CD11b-APC and Arginase-1-YFP fluorescence signals in all $CD45^+$ events. iNOS-tdTomato and Arginase-1-YFP signals exclusively occurred in $CD11b\text{-}APC^{hi}$ events. Some of these events were $iNOS\text{-}tdTomato^+Arginase\text{-}1\text{-}YFP^+$.The horizontal and vertical dotted lines indicate the FI threshold values (signal-to-noise) as defined by FMO controls. SSC-A and FSC-A FI were divided by 10^3. All other FI were log_2-transformed. All FI are depicted as area of signals intensities. Maximum values (oversaturated signals) or minimum values (undersaturated signals) were excluded from the analysis. FI: fluorescence intensity.

Flow cytometry analysis revealed 3 populations of cells which were characterized by CD45, CD11b and Ly6C expression: $CD45^{hi}CD11b^{hi}Ly6C^+$, $CD45^{med}CD11b^{med}Ly6C^+$ and $CD45^{hi}CD11b^-Ly6C^-$ cells. CD11b is a marker protein which is predominantly expressed by myeloid cells. Thus, the majority of $CD45^+$ cells in the EAE spinal cord were myeloid cells. Potentially, the $CD11b^-$ population can be considered as lymphoid cells such as T cells and B cells. As previously characterized, monocyte-derived macrophages express higher levels of CD45 and CD11b compared to microglia (278). Thus, within the myeloid cell population, the $CD45^{hi}CD11b^{hi}$ population reflected macrophages whereas the

$CD45^{med}CD11b^{med}$ population were microglia. Taken together, this showed that at EAE onset the majority of the phagocytes were monocyte-derived macrophages. At 5 dpo the ratio between the number of macrophages and the number of microglia was reduced compared to onset. Moreover, only macrophages – and not microglia – polarized to M1 or M2, respectively (indicated by iNOS and Arginase-1 expression). While the M1 polarization of macrophages dominated at EAE onset, M2 and M1/M2 ($iNOS^+Arginase\text{-}1^+$) cells were approximately as abundant as M1 cells at 5 dpo. These findings were consistent with previous data from Locatelli *et al.* (222).

4.2 Quantitative proteomics measured 8,615 different proteins in 19 different sample types

To identify proteins which might define destructive and reparative phenotypes of mononuclear phagocytes and to better understand their functional role in lesion formation and resolution in EAE, we performed a mass spectrometry proteomic screen in collaboration with the group of Prof. Dr. Felix Meissner. Therefore, M1 (M^{iNOS}) and M2 ($M^{Arginase\text{-}1}$) macrophages as well as microglia, monocytes, T cells, B cells, astrocytes, oligodendrocytes, OPCs and neurons were isolated from the healthy and EAE murine spinal cord, sorted and analyzed by mass spectrometry (see 3.2.10). For simplicity, $CD45^{hi}CD11b^{hi}iNOS^+Arginase\text{-}1^-$ cells are referred to as M1 macrophages whereas $CD45^{hi}CD11b^{hi}iNOS^-Arginase\text{-}1^+$ cells are referred to as M2 macrophages.

4.2.1 The chance of a protein being detected in a sample by mass spectrometry correlated with its abundance

Overall, 19 different sample types were analyzed in this study. Each sample type represented a cell type that was derived either from EAE or healthy spinal cords. At least 3 replicates were analyzed for each sample type, resulting in 85 individual samples (Table 11).

Cell type	Condition	N samples	N proteins	fraction of all identified proteins
M1 macrophages	EAE	8	6,131	0.71
M2 macrophages	EAE	5	6,808	0.79
Monocytes	healthy	5	5,141	0.60
Microglia	EAE	4	6,574	0.76
	healthy	4	5,506	0.64
CD4 T cells	EAE	4	5,649	0.66
	healthy	3	6,127	0.71
CD8 T cells	EAE	3	4,411	0.51
	healthy	4	1,786	0.21
B cells	EAE	4	6,449	0.75
	healthy	4	6,502	0.75
Neurons	EAE	5	3,387	0.39
	healthy	4	3,518	0.41
Astrocytes	EAE	8	3,722	0.43
	healthy	4	4,345	0.50
Oligodendrocytes	EAE	4	5,083	0.59

	healthy	4	3,965	0.46
OPCs	EAE	4	4,729	0.55
	healthy	4	4,645	0.54

Table 11: Characterization of the samples analyzed in the mass spectrometry proteomics screen. The number of all identified proteins was 8,615. A protein was considered to be detected in a sample type (cell type per condition) if it was at least detected in 2 individual samples. N proteins shows the number of proteins which were identified under this premise, % of all identified proteins shows the fraction of all (8,615) proteins.

In total, 8,615 proteins were identified. 1,280 proteins (14.9 %) were present in each of the 19 sample types (in at least 2 sample replicates), 484 (5.6 %) were exclusively detected in 1 sample type (Figure 3, **A**). The number of identified proteins as well as the mean expression levels differed among the cell types (Figure 3, **B**). On average, there were more proteins detected in the immune cell samples, comprised of M1 macrophages, M2 macrophages, monocytes, microglia, CD4 and CD8 T cells and B cells (*Md* = 6,233, *IQR* = [5,197;6,500]), compared to CNS cell samples, encompassing neurons, astrocytes, oligodendrocytes and OPCs (*Md* = 3,961, *IQR* = [3,638;4,625], $p = 2.27 \times 10^{-9}$, Wilcoxon rank-sum test). In contrast, the mean protein expression levels did not differ between immune cell samples and CNS cell samples ($\Delta M = 0.008$, $p = 0.96$, *t* statistics for independent and heteroscedastic groups for H_0: $M_{immune\ cells} = M_{CNS\ cells}$). The distribution of expression values was skewed, predominantly at the upper tail (Figure 3, **C** and **D**).

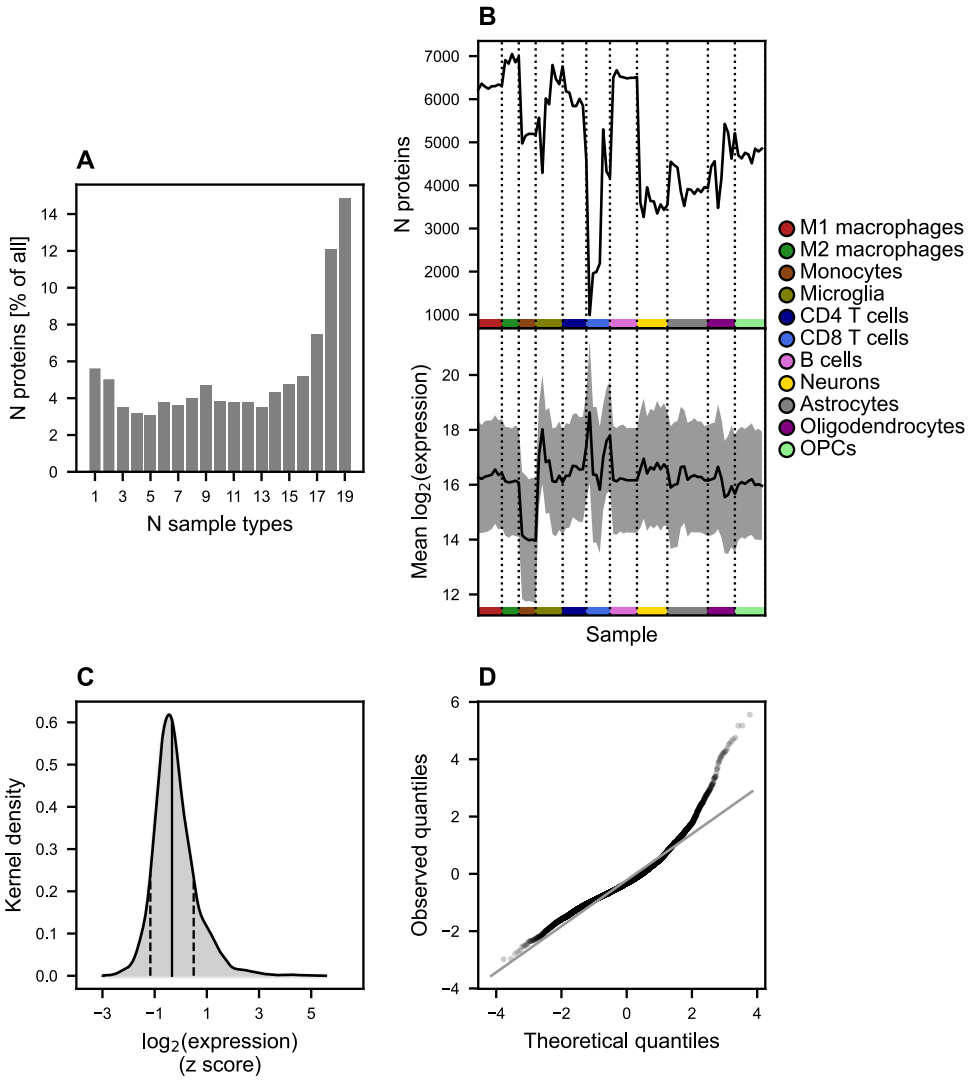

Figure 3: Characterization of expression values in the dataset. 8,615 proteins, which were identified in the mass spectrometry proteomics screen of immune cells and CNS cells, were analyzed with respect to their distribution to the 19 different sample types. **A**: Number of proteins and number of samples in which they could be detected. **B**: Distribution of the number of detected proteins and expression levels according to the cell type (black line: mean expression level, grey area: ± 1 *SD*). **C**: Histogram of the expression level of all detected proteins (solid line: mean expression, dashed line: *SD*). **D**: Quantile-quantile plot of the expression levels of all detected proteins (n = 8,615).

41.63 % of 732,275 data points were missing in the expression matrix. Proteins which were on average lowly expressed were detected in less samples compared to highly expressed proteins (Figure 4, **A**). To test the quantitative association between a protein's expression level and its chance to be detected in a sample, a linear regression model was established with the standardized logarithmic protein expression as the independent variable and the number of samples the protein was detected in as the dependent variable. An increase of the expression level by 1 *SD* was accompanied by an increase of the occurrence of the respective protein in 16 samples. Likewise, proteins that were detected in 1 – 30 samples showed a lower expression level when compared to proteins that were detected in 59 – 85 samples (ΔM = 0.82, Figure 4, **B**). Thus, the lower the protein expression, the lower the chance for a protein to occur in the dataset.

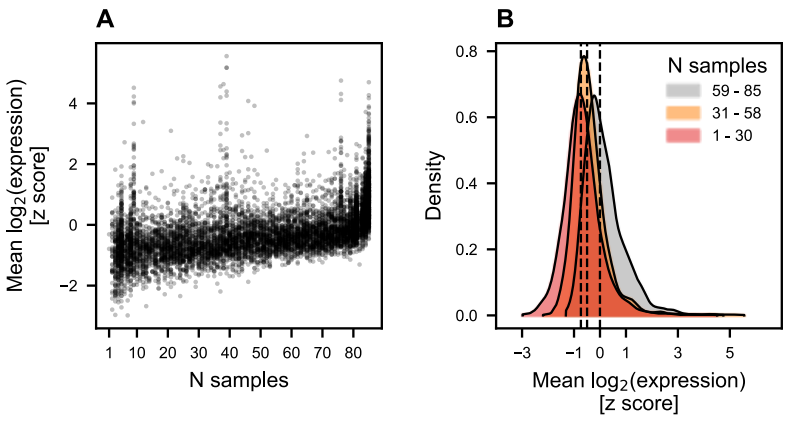

Figure 4: Number of missing expression values and protein expression levels. A: Correlation analysis of the number of samples in which a protein was detected and its mean logarithmic expression (calculated across all samples). Each dot represents an individual protein (n = 8,615 proteins). **B**: Distribution of the mean logarithmic expression values, grouped into categories with different numbers of samples in which the protein was detected (n = 85 samples, the limits that define the categories are arbitrary, dashed lines: mean logarithmic expression values for each category).

4.2.2 A combined imputation technique could replace missing data

To replace missing data and control for the lower probability of proteins with low abundance to be present in the dataset, we compared different imputation approaches with respect to the prediction accuracy of missing data from a test matrix where individual data points had been deleted. The test matrix was designed to mimic the original expression dataset. In principle, the test matrix was an (*n* x *j*) x *k* dimensional matrix where *n* was the number of sample types and *j* the number of replicates of the sample types and *k* the number of identified proteins in the original dataset. The mean expression value of the test matrix was 0, the standard deviation was 2.15, the same as in the original dataset. Each of the *k* expression values of the test matrix were sampled from a standard normal distribution with *SD* = 0.2 to add random noise. Missing values were introduced in a not at random (NAR) fashion: If the mean of the respective sample was low, the chance of excluding this value would be higher. The chance was modelled using a gaussian kernel density estimate function with a mean that was set to -0.82 (derived from the original dataset).

Regression-based (multiple imputation by chained equations, MICE), iterative and k-nearest neighbor (KNN) algorithms were assessed with respect to their prediction accuracy of missing data (Figure 5). In contrast to single value imputation algorithms (Supplement Figure 8), multiple imputation algorithms preserved more precisely the original distribution of the data. The iterative algorithm showed the highest correlation coefficient (for the correlation between original values and imputed values) and only a small downshift of the mean of the imputed data points when compared to the original data points (Figure 5, **B**). However, all multiple imputation algorithms would underestimate the biological relevance of a differential protein expression if the protein was exclusively expressed under one condition (or in one cell type) when compared to a second. Thus, an algorithm was developed that combined single value imputation and multiple imputation algorithms (Figure 5, **D**). If a protein was detected in less than half of the sample replicates (assuming that the protein is lowly expressed or not expressed at all), all expression values (for this particular protein in the respective samples) were imputed by a value drawn from a distribution whose mean was 2 *SD* below the actual mean of the expression value of the protein. The *SD* of this distribution was 0.3-times the *SD* of the

actual *SD* of the expression values of the protein. Next, the remaining missing values were imputed using an iterative approach (as shown in Figure 5, **B**). This imputation technique, which combines regression-based and single value approaches, was used for subsequent analysis in to control for lowly abundant proteins and prevent zero inflation.

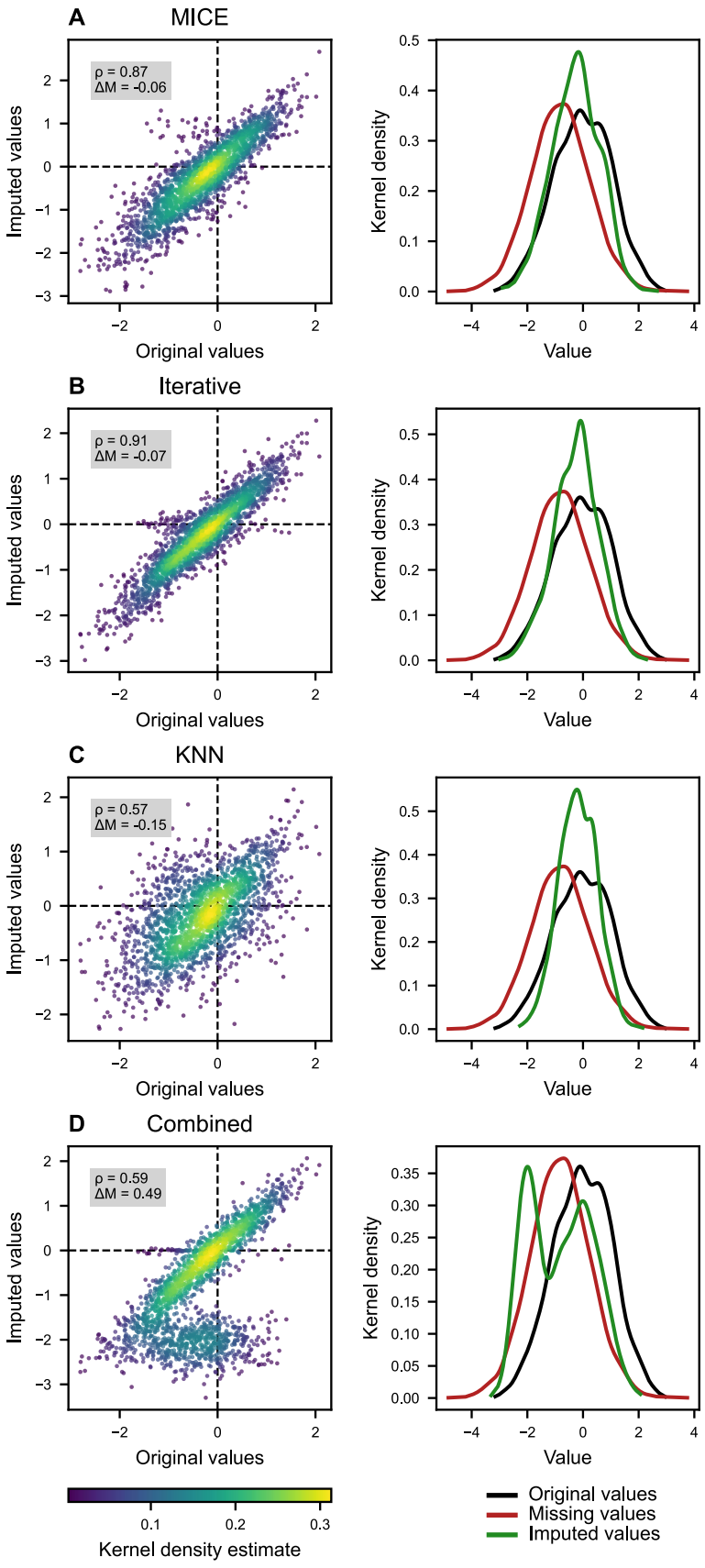

Figure 5: Analysis of the accuracy of multiple and combined imputation algorithms to substitute missing data. Left panels: Correlation between original and imputed values of a test matrix. The probability density function was estimated using Gaussian kernels. Right panels: Distribution of the original, missing and imputed values. **A** – **C**: Different imputation algorithms

applied to a test matrix with missing values mimicking the original dataset. The mean values of each protein in the test matrix were drawn from a standard normal distribution with the mean standard deviation of the protein expression values of the original dataset. **D**: Combination of single imputation and multiple imputation algorithms. (r: Pearson's correlation coefficient, ΔM: difference in mean between original and imputed values, MICE: multiple imputation by chained equations, KNN: k-nearest neighbor).

4.2.3 Dimension reduction techniques revealed the degree of similarity of immune cell and CNS cell proteomes

To assess the similarity of the proteomes, we performed a correlation analysis with subsequent hierarchical cluster analysis and Uniform Manifold Approximation and Projection (UMAP) analysis.

With the exception of one sample (neurons from EAE), correlation analysis revealed a good inter-sample correlation between samples that derive from the same cell type and experimental group. Cluster analysis revealed 2 main clusters (Figure 6). The first cluster was comprised of CNS cell samples (neurons, oligodendrocytes, astrocytes and OPC), the second cluster encompassed all immune cell samples (M1 and M2 macrophages, monocytes, microglia CD4 and CD8 T cells, B cells). The immune cell cluster was subdivided into further clusters, however, there was neither a clear separation between myeloid and lymphatic cells nor between CNS resident and peripheral immune cells. Overall, the experimental group (EAE versus healthy control) was a stronger classifier than the cell type. CNS-specific mononuclear phagocytes (M1 and M2 macrophages as well as microglia) formed a cluster at a low level. Monocytes (from healthy controls) clustered most distantly from M1 and M2 macrophages within the immune cell cluster. Likewise, CD4 and CD8 T cells from EAE showed a lower proximity to macrophages than to their counterparts from healthy controls. B cells from EAE and healthy controls, which were both isolated from PBMC, were the only experimental groups of a specific cell type which showed close proximity in the cluster analysis.

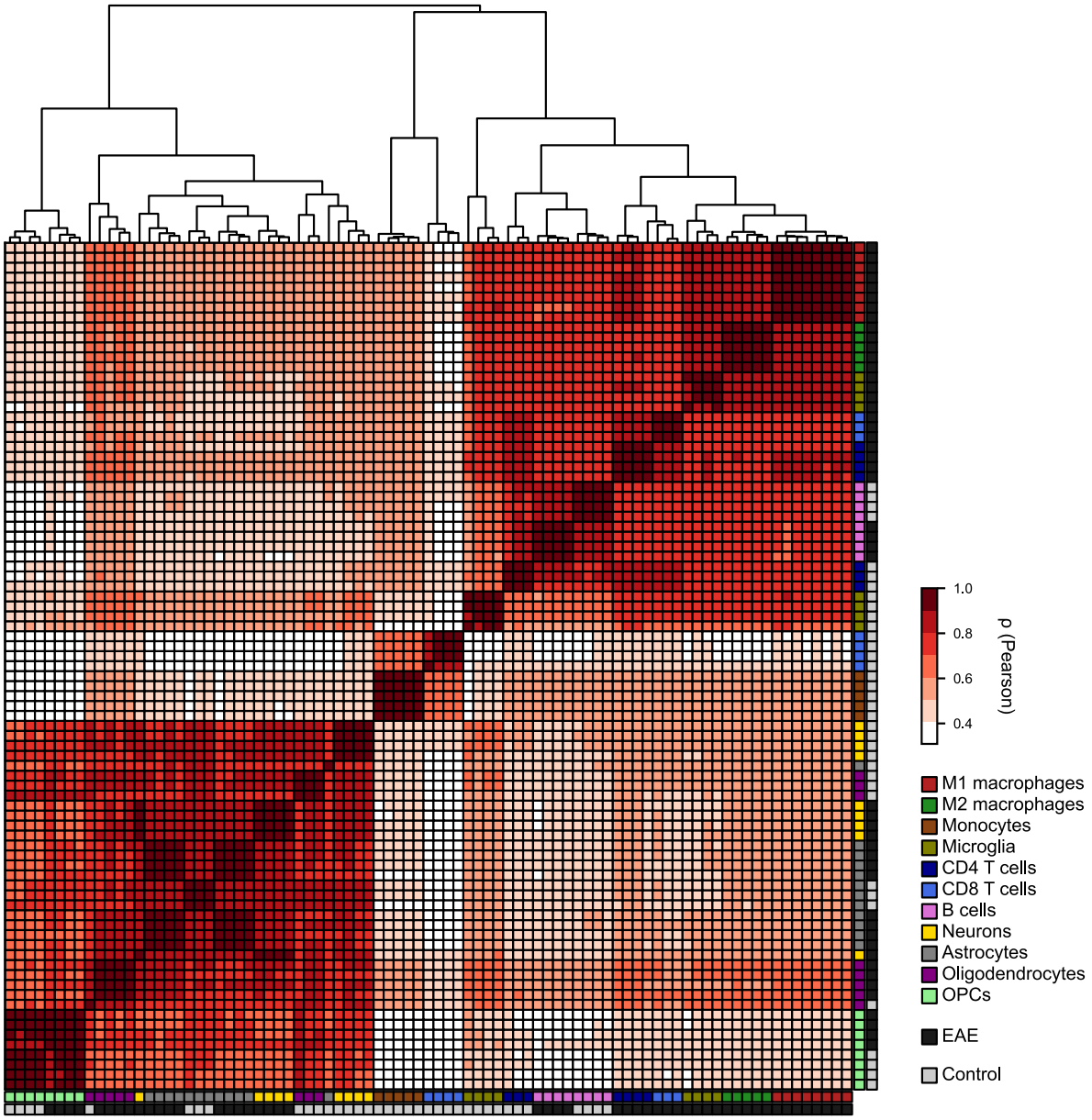

Figure 6: Inter-sample correlation analysis of immune cell and CNS cell proteomes. Color-coded correlation coefficients (Pearson) for each inter-sample correlation. Each sample is defined by the cell type (color) and the experimental condition (greyscale, healthy control or EAE) as indicated with the bars at the edges of the matrix. The dendrogram illustrates the hierarchical cluster analysis based on the Euclidean distances between each feature of the correlation matrix (r: Pearson's correlation coefficient).

In UMAP, phagocytes that were isolated from EAE (M1 and M2 macrophages as well as microglia) formed a cluster that was demarcated from lymphatic cells (CD4 and CD8 T cells and B cells, both from EAE and healthy controls, Figure 7). Monocytes and CD8 T cells from healthy controls were most distinct from all other sample types. Microglia from EAE were closer to M2 macrophages (mean Euclidean distance M_d = 0.88) than to M1 macrophages (M_d = 1.18), whereas microglia from healthy controls shared features of both M1 macrophages (M_d = 2.32) and M2 macrophages (M_d = 2.45) to a comparable extend.

The CNS cells samples showed less tighter clustering, only OPCs were clearly separated from neurons, astrocytes and oligodendrocytes (Figure 7, **C** and **D**). Unlike immune cells, there was no clear clustering of similar cell types.

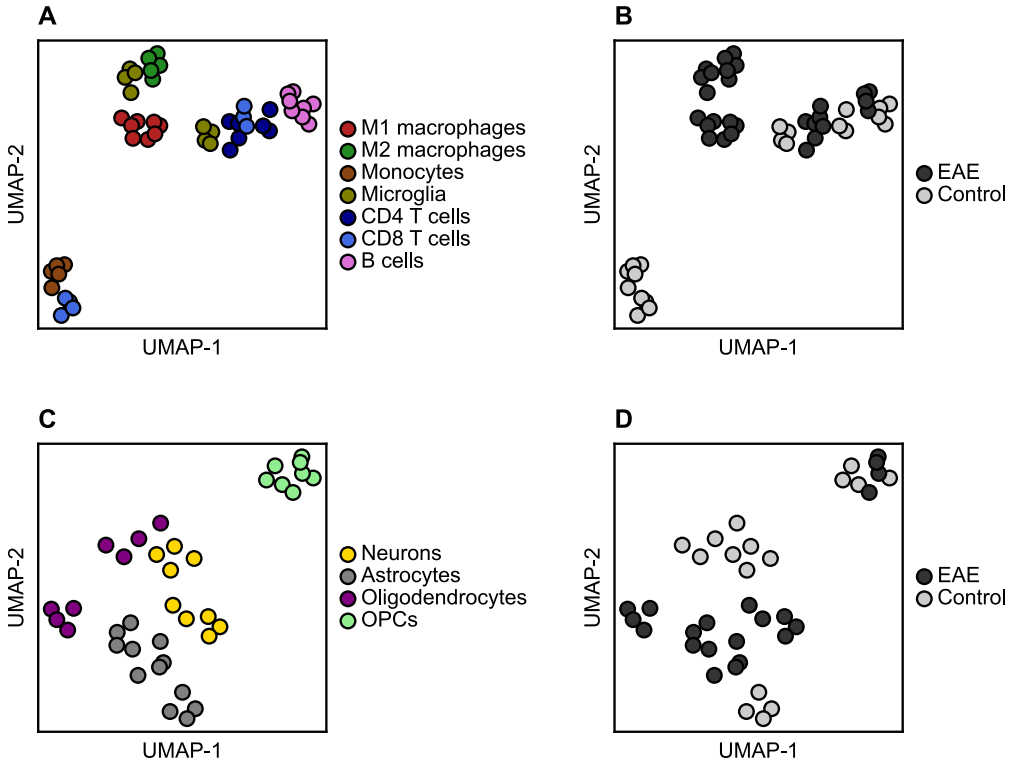

Figure 7: Dimensional reduction of the protein expression matrix. The protein expression matrices of all immune cells and CNS cells samples were standardized and subjected to UMAP. The color code represents the cell type or the experimental condition, respectively (**A** and **B**: immune cells, **C** and **D**: CNS cells).

4.2.4 Analysis of signature protein expression revealed the specificity of the immune cell and CNS cell proteomes

To validate the sample quality on a single protein level, we analyzed the expression levels of the proteins which were targeted for cell sorting. All immune cells were stained with a fluorophore-conjugated anti-CD45 antibody and sorted as $CD45^+$ events. In contrast, CNS cells were sorted as $CD45^-$ events. Overall, the expression of CD45 was higher in immune cells when compared to CNS cells, except of mononuclear phagocytes (M1 and M2 macrophages as well as microglia) which showed similar expression levels of CD45 as some of the CNS cell types (neurons, astrocytes from healthy controls and oligodendrocytes from EAE, $\Delta M_{expression(CD45)} = 4.77$, $p = 1.19 \times 10^{-19}$, Figure 8, **A**). Myeloid cells (M1 and M2 macrophages, microglia and monocytes) showed a higher expression of the myeloid lineage marker CD11b when compared to lymphatic cells (T cells and B cells, $\Delta M_{expression(CD11b)} = 3.63$, $p = 8.47 \times 10^{-7}$). M1 and M2 macrophages were sorted as $CD45^{hi}CD11b^{hi}$ events, whereas microglia were sorted as $CD45^{med}CD11b^{med}$ events. Thus, the expression of CD45 and CD11b in M1 and M2 macrophages was higher compared to microglia ($\Delta M_{expression(CD45)} = 1.09$, $p = 1.74 \times 10^{-4}$ and $\Delta M_{expression(CD11b)} = 0.56$, $p = 3.19 \times 10^{-2}$). To distinguish between M1 and M2 macrophages, we used a transgenic reporter mouse line which expressed tdTomato under a *Nos2* promoter and YFP under a *Arg1* promoter. Indeed, M1

macrophages expressed more iNOS than M2 macrophages ($\Delta M_{expression(iNOS)}$ = 2.74, p = 1.89 x 10^{-5}), whereas the expression of Arginase-1 was higher in M2 macrophages ($\Delta M_{expression(Arginase\text{-}1)}$ = 2.67, p = 3.88 x 10^{-7}). Among all immune cells, CD4 and CD8 T cells expressed highest levels of CD3 ($\Delta M_{expression(CD3D)}$ = 6.36, p = 1.55 x 10^{-21}). Compared to CD8, the CD4 expression was higher in CD4 T cells ($\Delta M_{expression(CD4)}$ = 6.67, p = 5.74 x 10^{-7}), whereas the CD8 expression was higher in CD8 T cells ($\Delta M_{expression(CD8B)}$ = 4.05, p = 6.87 x 10^{-5}), respectively.

The abundance of THY1 was higher in neurons than in all immune cells ($\Delta M_{expression(THY1)}$ = 3.89, p = 6.59 x 10^{-5}), however, when compared to astrocytes, oligodendrocytes and OPCs the expression level was only marginally higher ($\Delta M_{expression(THY1)}$ = 0.56, p = 0.29). The expression of ACSA-2 was high in astrocytes compared to all other CNS samples ($\Delta M_{expression(ACSA\text{-}2)}$ = 1.88, p = 5.38 x 10^{-4}). However, the expression of ACSA-2 in neurons from EAE exceeded the expression of ACSA-2 in astrocytes ($\Delta M_{expression(ACSA\text{-}2)}$ = 0.41, p = 0.27). O4 and PDGFRa, which were used to characterize oligodendrocytes and OPCs, were not detected on proteome level.

Hierarchical cluster analysis based on the Euclidean distance of the signature protein expression matrix revealed a clear distinction between CD4 and CD8 T cells and all other cell types, indicating that the CD3, CD4 and CD8 expression were most specific for T cells (Figure 8, **B**). In the second main cluster (left) all CNS cells, except for OPCs, including microglia from healthy control, clustered together. There was no clear sub-clustering of the individual CNS cell types, indicating that the expression of signature proteins, that were used for cell sorting, could not resolve the cell-type specificity on a proteome level.

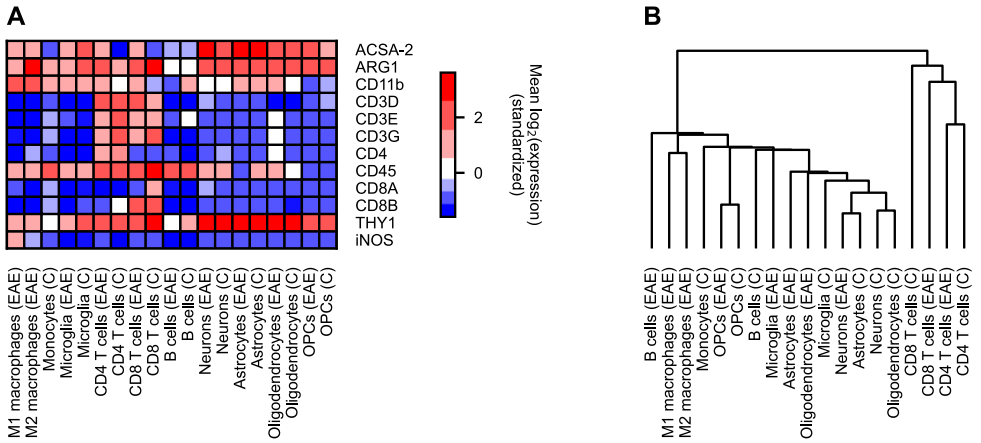

Figure 8: Protein expression of marker proteins of immune and CNS cells. Analysis of the protein expression levels of proteins that were used for cell type identification for cell sorting. **A**: Standardized mean logarithmic expression values were color-coded for visualization. **B**: Column dendrogram showing the hierarchical clustering according to the Euclidean distances between each sample in the expression matrix (C: control, EAE: experimental autoimmune encephalomyelitis).

Monocyte-derived M1 and M2 microglia were sorted according to their CD45 and CD11b expression. Since this identification technique is discussed controversially, we focused on more established markers to distinguish between macrophages and microglia (308, 309). This revealed a clear enrichment of the microglia markers P2RY12, SALL1 and TMEM119, previously proposed as additional signature proteins to discriminate microglia and macrophages (Figure 9). CCR2, a marker that is delineates mononuclear phagocytes from the periphery, was highest expressed in monocytes.

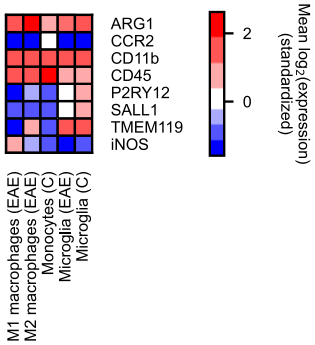

Figure 9: Expression of microglia signature proteins. Standardized mean logarithmic expression values for proteins which distinguish microglia from macrophages were color-coded for visualization (C: control, EAE: experimental autoimmune encephalomyelitis).

To further evaluate the proteome specificity of samples derived from CNS cells, we assessed the expression of signature proteins as previously identified by Cahoy *et al.* (310). This dataset encompasses RNA-seq expression data from murine neurons, astrocytes and oligodendrocytes.

Overall, 16 out of 43 neuronal markers (as described by Cahoy *et al*.) were identified in Thy-1^{+}CD45^{-} cells (neurons) by mass spectrometry. Three (GABRA1, SCG2, SLC12A5) out of these 16 proteins were significantly higher expressed in neurons compared to astrocytes, oligodendrocytes and OPCs. However, the differences in mean logarithmic expression between neurons and all other CNS cell types of these proteins were low ($\Delta M_{expression(\text{GABRA1})} = 0.63$, $\Delta M_{expression(\text{SCG21})} = 0.88$, $\Delta M_{expression(\text{SLC12A5})} = 0.65$) when compared to the differences of signature protein expression between different immune cell types. There was no separation of the neuron samples in the cluster analysis based on the expression of the signature proteins. The following proteins/genes were enriched in the RNA-seq dataset obtained by Cahoy *et al*. but not enriched in neurons in this proteome dataset: Satb2, Nts, Odz2, 9130024F11Rik, Gpr88, Myt1l, 4930544G21Rik, Gabrg2, A930034L06Rik, Plcxd3, Pcsk2, Neurod6, Nov, Prdm8, Glra2, Htr2c, Hs3st2, Crh, A930009L07Rik, Epha7, Dlx1, A130090K04Rik, Gabra5, Efcbp1, Sstr2, Npas4 and Vip.

Twenty Out of the 40 signature genes/proteins, which were analyzed to assess the sample specificity of astrocytes, were detected in the astrocyte proteome. However, only 5 proteins were significantly higher expressed in astrocytes when compared to neurons, oligodendrocytes and OPCs (ALDH1L1, ALDOC, ATP1A2, PLA2G7, SLC25A18). PLA2G7 showed the strongest enrichment in the astrocyte samples ($\Delta M_{expression(PLA2G7)} = 1.54$, $p = 2.24 \times 10^{-3}$). The differences in mean logarithmic expression ($\Delta M_{expression}$) of the other differentially regulated proteins between astrocytes and all other CNS cell types spanned from 0.49 to 1.46. 1500005I02Rik, 2900019G14Rik, AU067665, Bmpr1b, C030045D06Rik, Chrdl1, Cyp4f14, Cyp4f15, Dio2, F3, Fzd2, Gjb6, Gm266, Ppp1r3c, Ppp1r3g, Rfx4, Slc15a2, Tmem166, Ttpa and Vil2, which were additional signature genes as reported by Cahoy *et al.*, could not be detected in the astrocyte proteome. Cluster analysis of the expression matrices of the astrocyte signature proteins revealed no clear differentiation between astrocytes and other CNS cell types.

18 proteins out of 41 candidates from Cahoy *et al*. were detected in the oligodendrocyte proteome. 4 of them were significantly enriched in oligodendrocytes when compared to neurons, astrocytes and OPCs (EVI2A, MBP, MOBP and PLA2G4A). Myelin basic protein (MBP) showed the

highest differential protein expression ($\Delta M_{expression(MBP)}$ = 1.86, p = 5.16 x 10^{-2}). Besides myelin basic protein, proteolipid protein 1 (PLP1) was the only other myelin protein that was enriched in the oligodendrocyte samples ($\Delta M_{expression(PLP1)}$ = 1.18, p = 0.13, from t statistics for independent samples). Ugt8a, AI314604, 9630013A20Rik, 9530066K23ik, A330104H05Rik, Edg8, 1700047M11Rik, A230069A22Rik, Gja12, Gal3st1, Erbb3, Tmem10, Elovl7, 6330530A05Rik, Sgk2, Fa2h, Gm98, Il23a, Srpk3, Plxnb3, Trf, Plekhh1, Mal, Gpr62, Adamts4, signature genes identified by Cahoy *et al*., were not present in the oligodendrocyte expression dataset. Cluster analysis based on the expression of oligodendrocyte signature proteins indicated that CNS cells which derive from the same experimental group (EAE or control) are more similar than same CNS cell types from different experimental groups.

Taken together, only a small fraction of known CNS cell signature proteins were (specifically) enriched in the respective proteomes. Thus, we obtained no cell type-specific resolution for the CNS cell proteomes. However, when compared to the immune cell proteomes, the CNS cell proteomes were highly specific in terms of the expression of neuronal (neurofilament light polypeptide, NEFL) and synaptic (synaptosomal-associated protein, SNAP25) markers, astrocyte markers (10-formyltetrahydrofolate dehydrogenase, ALDH1L1 and astrocyte cell surface antigen-2, ACSA-2/ATP1A2/ATP1B2) and myelin proteins (myelin basic protein, MBP and myelin proteolipid protein 1, PLP1).

4.2.5 Differential protein abundance analysis of M1 versus M2 macrophages

One of the main goals of this study was to elucidate the molecular signature of M1 and M2 macrophages. Therefore, we first analyzed the differential protein expression of M1 and M2 macrophages to screen for up- and downregulated proteins in each polarization state. Differential protein expression was defined as an at least 1.5-fold change in (logarithmic) protein expression level with $q \leq 0.05$ (FDR-adjusted p value derived from t statistics for independent samples with homoscedasticity). We performed a receiver operating characteristic (ROC) analysis to validate this premise (Figure 10). This showed that a fold change of 1.5 indicated a sufficient specificity and sensitivity (Figure 10, **B**) and, thus, was set as the lower threshold for the definition of differentially expressed proteins.

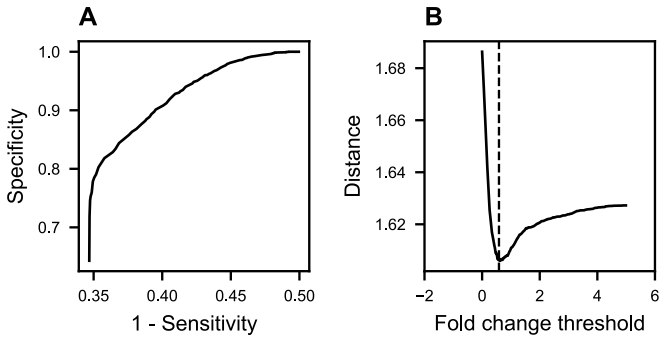

Figure 10: Receiver operating characteristic (ROC) analysis of fold change thresholds for the differential protein expression analysis. A: Correlation between specificity and sensitivity for different fold change thresholds for the analysis of the differential protein expression of M1 and M2 macrophages. Fold change was defined as the difference in the mean logarithmic protein expression levels. The specificity was calculated as the fraction of identified proteins above a certain fold change threshold that met the criteria $q \leq 0.05$ (FDR-adjusted p value from t statistics for independent samples with

homoscedasticity). Sensitivity was defined as the fraction of proteins with $q \leq 0.05$ whose fold change exceeded the given threshold. **B**: Euclidean distance to P(x|y) in the Cartesian space of **A**, where x is the minimum value of 1-sensitivity and y is the maximum of the specificity, calculated for fold change thresholds reaching from 0 to 5 (dashed line: fold change threshold = $\log_2(1.5) = 0.58$).

Overall, 1,525 proteins (17.70 % of all identified proteins in the M1 and M2 proteomes) were differentially expressed in the M1 and M2 macrophage proteomes, 614 were higher abundant in M1 macrophages, 911 in M2 macrophages (Figure 11, **A**). The mean logarithmic fold change of proteins that were upregulated in M1 macrophages ($M_{\log_2}(M_1) = 1.42$) was higher when compared to the mean fold change of proteins which were enriched in M2 macrophages ($M_{\log_2}(M_2) = 1.98$). The 50 most extreme differentially enriched proteins are displayed in Figure 11, **B** and **C**.

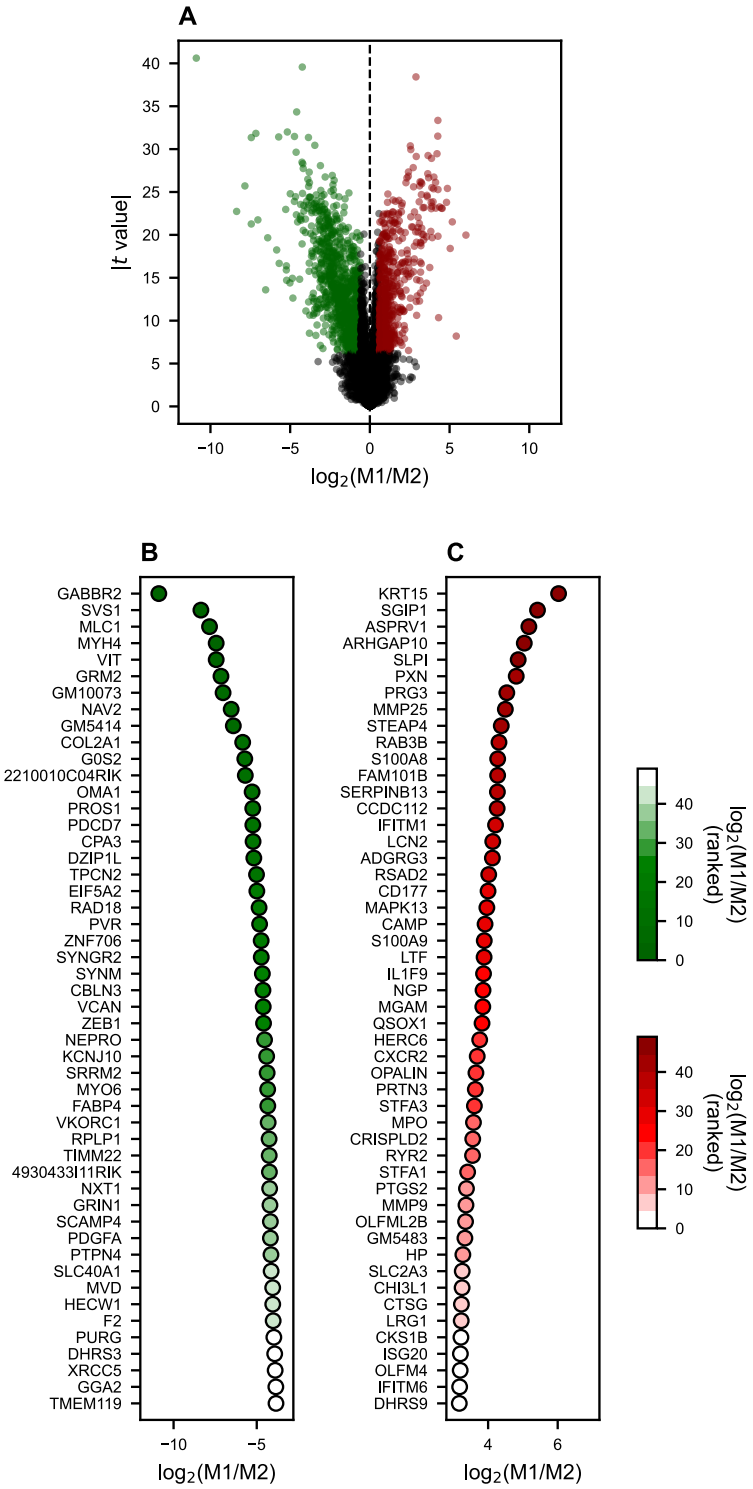

Figure 11: Differential protein expression of M1 and M2 macrophages. A: Logarithmic fold change (FC) differential expression ($M_{(\text{M1 expression level})} - M_{(\text{M2 expression level})}$) of all detected proteins and their respective *t* value (green: upregulated in M2 macrophages with $\log_2(\text{FC}) \leq \log_2(1.5)$ and $q \leq 0.05$, red: upregulated in M1 macrophages with $\log_2(\text{FC}) \geq \log_2(1.5)$ and $q \leq 0.05$, from FDR-adjusted *p* values from *t* statistics for independent samples with group homoscedasticity). **B** and **C**: Top 50 differentially regulated proteins in M2 macrophages (**B**) and M1 macrophages (**C**, green and red: color-coded ranked fold changes, $n_{M1} = 8$, $n_{M2} = 5$).

4.2.6 Gene set enrichment analysis coupled to network analysis revealed molecular signatures of M1 macrophage and M2 macrophage proteomes

To identify molecular patterns underlying differential protein expression in M1 and M2 macrophages, we performed gene set enrichment analysis coupled to network analysis (*NezzworGS* algorithm). First, proteins which were enriched in M1 and M2 macrophages were filtered according to the above defined criteria. For this analysis, the Reactome gene set library (version 7.4, filtered for mouse gene sets) was used as a reference database.

The analysis revealed the enrichment of 94 gene sets with a normalized enrichment score (NES) from -1.51 (most extremely enriched in M2 macrophages) to 2.92 (most extremely enriched in M1 macrophages, Figure 12). After filtering according to statistical testing of the enrichment ($p \leq 0.25$), 17 gene sets were identified to be enriched in M1 and M2 macrophages, respectively. The non-conservative statistical filtering was applied because of pre-filtering of the input expression matrix as well as the explorative nature of this analysis. The identified gene sets were further analyzed by network analysis based on similarity of the gene sets (as defined as the number of genes they have in common) and the number of leading-edge proteins.

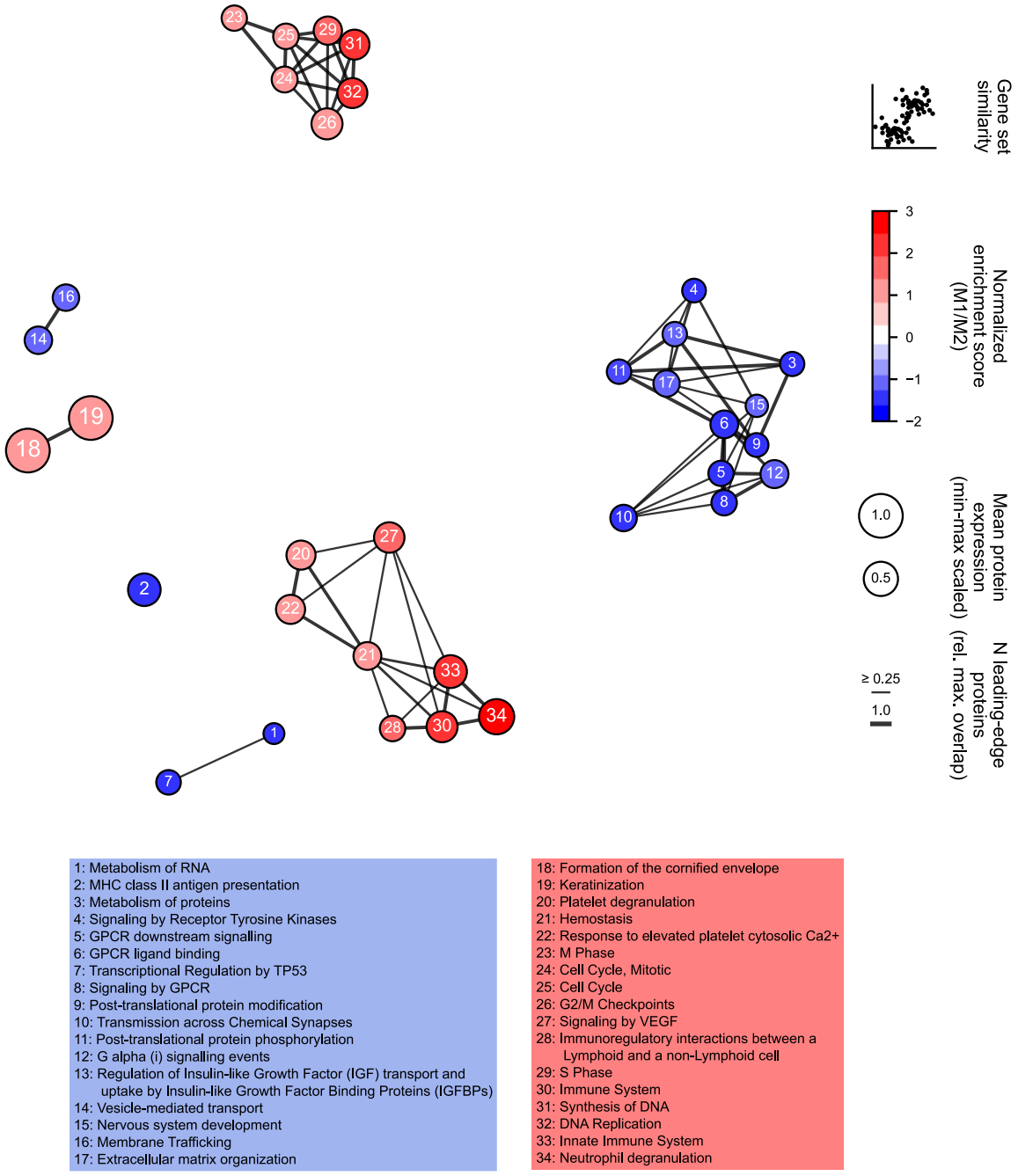

Figure 12: Gene set enrichment network analysis (Reactome) of M1 and M2 proteomes. Proteins which were significantly differently abundant in M1 versus M2 macrophages (|FC| > 1.5 and $q \leq 0.05$) were subjected to gene set enrichment analysis (GSEA, Reactome). Gene sets are displayed as red (enriched in M1 macrophages) and blue (enriched in M2 macrophages) nodes. The normalized enrichment score (NES) is color-coded (NES > 0: enriched in M1 macrophages, NES < 0: enriched in M2 macrophages). The area of each node represents the mean protein expression of the gene sets' underlying proteins. The thickness of edges represents the fraction of leading-edge proteins which two gene sets have in common (the highest fraction of the two gene sets was taken into account). The spatial distribution in the Cartesian space encodes the similarity of two gene sets as defined by the number of genes/proteins they share.

The most enriched gene sets in M1 macrophages were "Neutrophil degranulation" (34, NES = 2.92), "Innate Immune System" (33, NES = 2.25), "DNA Replication" (32, NES = 2.08), "Synthesis of DNA" (31, NES = 2.07) and "Immune system" (30, NES = 1.95, Figure 12). In contrast, M2 macrophages showed an enrichment of the gene sets "Metabolism of RNA" (1, NES = -1.52), "MHC

class II antigen presentation" (2, NES = -1.42), "Metabolism of proteins" (3, NES = -1.41), "Signaling by Receptor Tyrosine Kinases" (4, NES = -1.39) and "GPCR downstream signaling" (5, NES = -1.34).

Modularity analysis revealed that the network was comprised of 8 modules (Supplement Figure 9). Each module represents a subnetwork of gene sets, which share a significant amount of genes and, therefore, might display a functional cluster within the M1 and M2 macrophage proteome. Modularity class 4 showed gene sets enriched in M1 macrophages, which were related to immune cell activation and cytokine metabolism (module of gene sets 20, 21, 22, 27, 28, 30, 33 and 34). Likewise, module 3 and module 5 were comprised of gene sets enriched in M1 macrophages. Module 5 (gene sets 18 and 19) showed gene sets related to keratinization/cornified envelope which is essential for building up physical (membrane) barriers. Module 3 was predominantly characterized by gene sets related to cell proliferation and DNA replication (gene sets 23, 24, 25, 26, 29, 31, 32). Module 1 encompassed one M2-macrophage-enriched gene set ("MHC class II antigen presentation") which did not share a significant fraction of leading-edge proteins with other gene sets and was therefore not connected with other nodes within the network. Modularity class 7 (gene sets 3, 4, 9, 11, 13, 15 and 17) was comprised of metabolism-related gene sets and the gene set "Extracellular matrix organization". Modularity class 2 (gene sets 5, 6, 8, 10 and 12) was built of gene sets related to G-protein coupled signaling (e. g. "GPCR downstream signaling", "GPCR ligand binding" and "Signaling by GPCR"), neuronal proteins (e. g. "Transmission across Chemical Synapses" and "Nervous system development").

The analysis of the parent-child hierarchy of the enriched Reactome gene sets revealed 3 pedigrees within the M2 macrophage-enriched gene sets (Figure 13). The parent gene sets ("Metabolism of proteins", "Signaling by GPCR" and "Vesicle-mediated transport") partially reflect the gene-set-relationships identified by modularity analysis (modularity classes 7, 2 and 8). Likewise, the parent gene sets of the gene sets enriched in M1 macrophages mirror the modules in the network analysis ("Keratinization", "Response to elevated platelet cytosolic Ca2+", "Cell cycle" and "Immune system"; modularity class 5, 4 and 3).

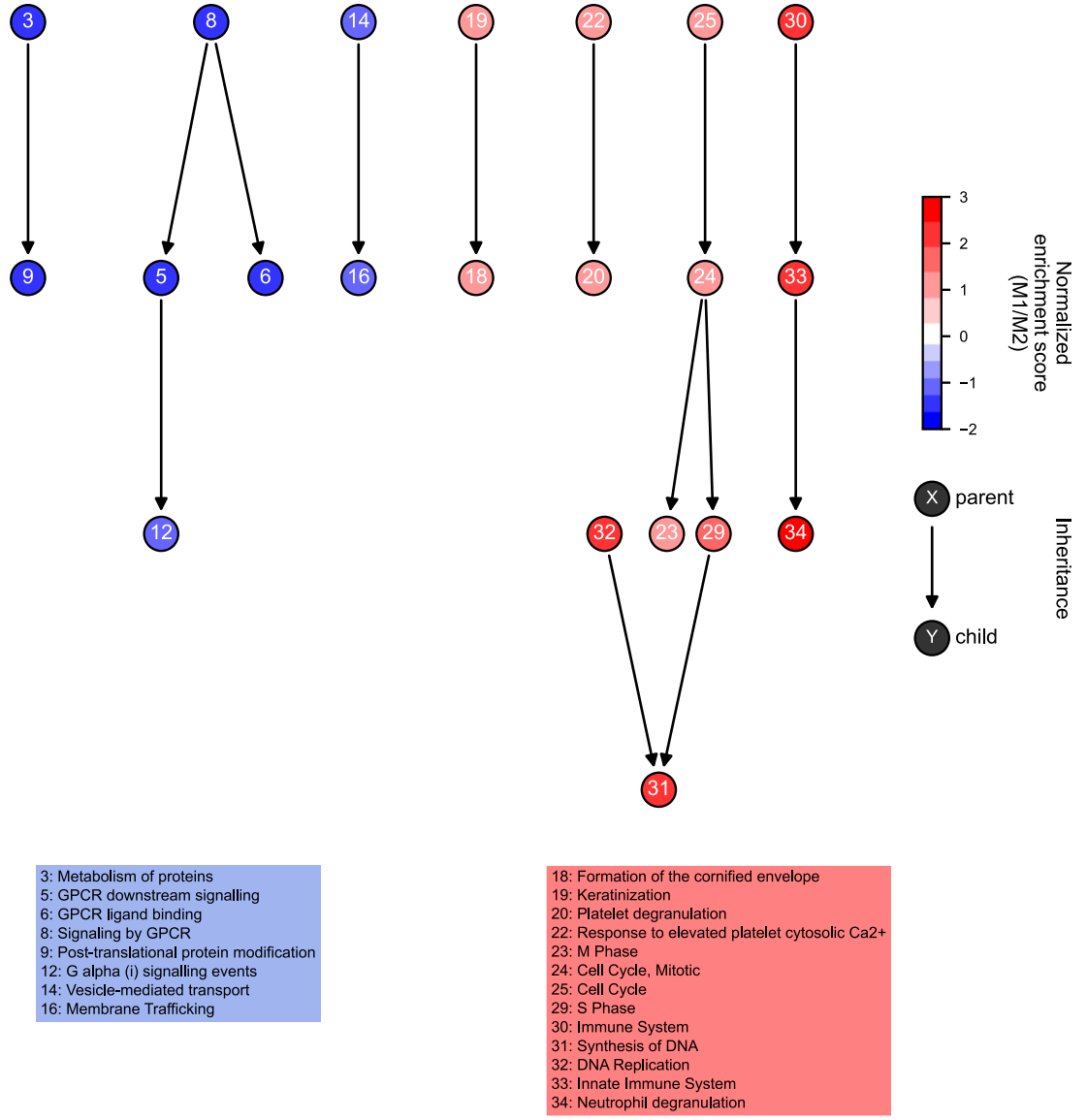

Figure 13: Pedigree analysis of Reactome gene sets identified in the M1 and M2 macrophage proteomes. Hierarchical relationship of gene sets. Gene sets from the gene set enrichment analysis of the M1 and M2 macrophage proteomes which are related in the Reactome gene set database are displayed as nodes. Edges indicate their relationship. Genes underlying a child gene set are members of the parent gene set as well. The normalized enrichment score is color-coded.

Taken together, the M1 macrophage proteome showed an enrichment of gene sets related to immune cell signaling, proliferation and keratinization, whereas gene sets related to G protein-coupled signaling, neuronal system, extracellular matrix organization and MHC II-dependent antigen presentation were enriched in the M2 macrophage proteome.

We hypothesized that the differential protein expression analysis and gene set enrichment analysis were potentially confounded by (protein) contaminants that were enriched during the cell isolation process, especially taking into account the enrichment of gene sets related to extracellular matrix and neuronal system. Thus, we performed RNA sequencing to measure if the enrichment of specific proteins and gene sets is also mirrored on transcription level (with contributions from Lea Merkel). Therefore, $CD45^+CD11b^+Ly6G^-Nos2^+$ (M1) and $CD45^+CD11b^+Ly6G^-Arginase\text{-}1^+$ (M2) cells from

the EAE spinal cord were isolated and sorted at onset and onset + 1 d (M1) as well as onset + 4 d (M2). 6,924 transcripts of 8,615 proteins (80.4 %) of the whole respective proteome could be identified (Figure 14, **A**). However, the correlation between the M1-M2 fold change RNA expression and the M1-M2 fold change protein expression was low ($r = 0.14$, $p = 1.75 \times 10^{-32}$ for H0: $r \neq 0$, Figure 14, **B**). In contrast to the proteome, transcripts of the signature enzyme Arginase-1 (*Arg1*) were not differently enriched in M2 cells, however, *Nos2* showed a clear enrichment in M1 cells (Supplement Figure 10). Based on previous studies, which compared cellular transcriptomes and proteomes, RNA levels only partially predict changes on protein level. As outlined by Hoogendijk *et al.*, this might also depend on the experimental setup and activation or proliferation state of a cell being analyzed (311). The discrepancy between RNA and protein levels in our study is pronounced when looked at *Arg1*/Arginase-1 levels. In contrast to the protein levels, the analysis of the RNA levels in M1 and M2 macrophages could not segregate both polarization states. This might also result from different half-lives of *Nos2*/iNOS and *Arg1*/Arginase-1 RNA and protein molecules.

To identify candidates which are enriched in M1 and M2 macrophages both on protein as well as on RNA level, we computed a correlation analysis for different sum of ranks cutoff values (Supplement Figure 11). Thereby, 1676 transcripts/proteins (863 uppermost and lowermost regulated candidates) showed a correlation coefficient $r \geq 0.9$. The 55 most enriched transcripts/proteins in M1 and M2 macrophages, respectively, are shown in Figure 14.

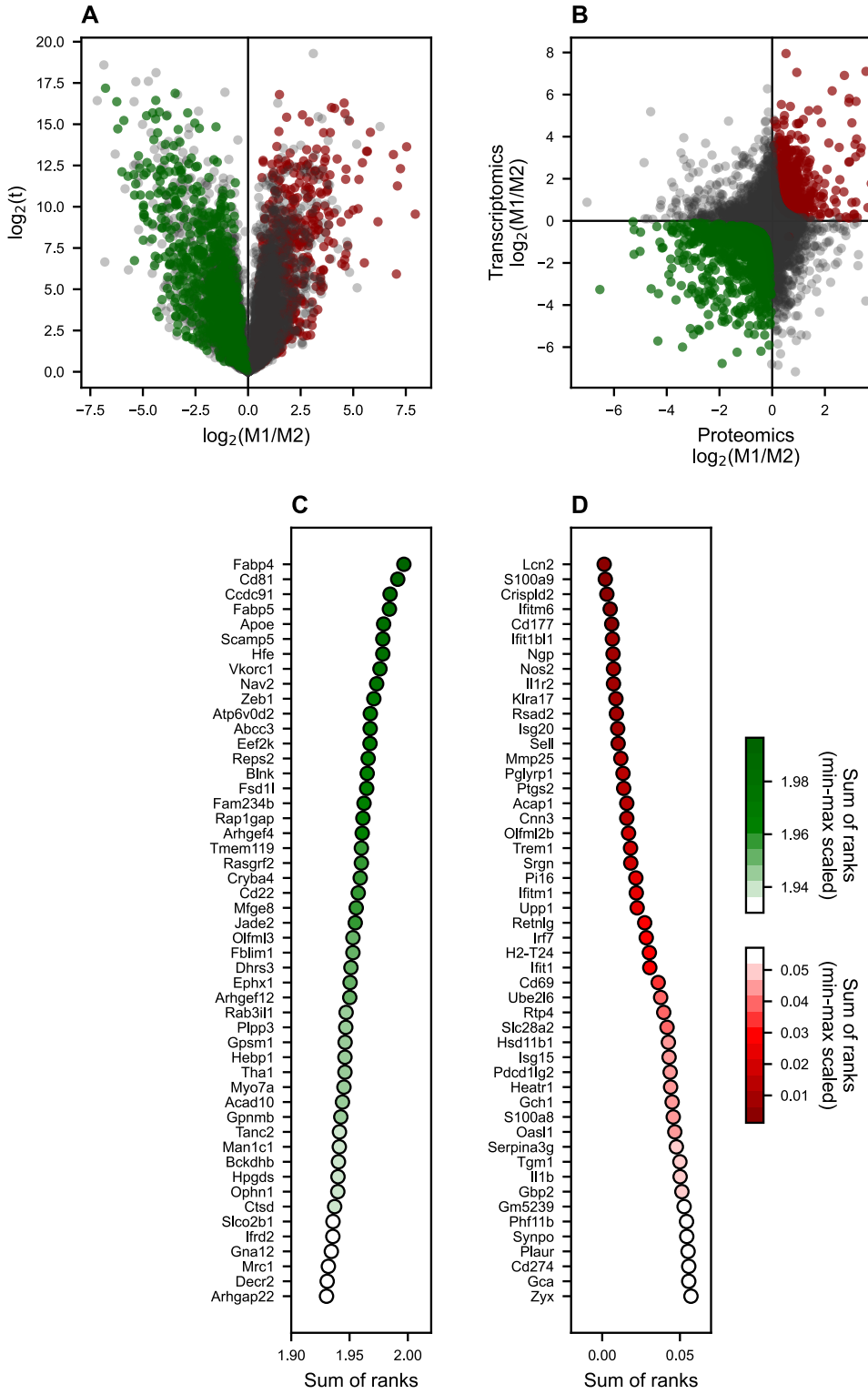

Figure 14: Transcriptome-proteome correlation. A: Logarithmic fold change of the genes expressed in M1 and M2 and their *t* values (calculated from a two-sided t-test for independent groups with homoscedasticity). Transcripts which were also detected on protein level were color-coded (red: enriched in M1 macrophages, green: enriched in M2 macrophages). **B**: Logarithmic fold changes (M1/M2) of the gene expression and protein expression. Green and red indicate the genes/proteins which showed a correlation coefficient $r \geq 0.9$. **C** and **D**: 55 most extremely enriched genes/proteins in M2 (**C**) or M1 (**D**) macrophages. The sum of (min-max scaled) ranks is calculated by adding the (min-max scaled) ranks of the respective $\log_2$(M1/M2) fold change derived from transcriptomics and proteomics. The smaller the sum of ranks, the more enriched a candidate was both on a transcriptomic and proteomic level in M1 macrophages. The higher the sum of ranks, the more the candidate was enriched in M2 macrophages on a transcriptomic and proteomic level simultaneously.

Next, we analyzed the gene set enrichment of the M1 and M2 macrophage transcriptome to test if there are functional clusters that are conserved both in the proteome and transcriptome. Therefore, the RNA expression matrix was filtered for relevantly differentially abundant transcripts ($|FC| > 1.5$ and $q \leq 0.05$), and subjected to gene set enrichment analysis coupled to network analysis (*NezzworGS* algorithm, Figure 15). Overall, 74 gene sets were enriched in the M1 and M2 transcriptome, however, only 23 gene sets passed the filter criterion ($p \leq 0.25$). Among those, 11 gene sets were enriched in the M2 macrophage transcriptome (NES < 0) and 12 gene sets were enriched in the M1 macrophage transcriptome (NES > 0).

Subsequent network analysis with modularity analysis revealed two modules which encompassed most of the enriched gene sets. With the exception of gene sets 2, 5, 10 and 11, all M2 macrophage-enriched gene sets shared a significant number of leading-edge genes and were therefore connected in the network. Within this module, gene sets 6, 7 and 9 shared most of the underlying genes. These gene sets were related to neuronal development. Likewise, gene set 1 and 8 were strongly related, both gene sets encompassed transcripts related to G protein-coupled signaling. Moreover, the gene sets “CDC42 GTPase cycle” and “Extracellular matrix organization” were identified in this module. With the exception of gene set 12 (“Class A/1 (Rhodopsin-like receptors)”), all M1 macrophage-enriched gene sets were found within one module. M1 macrophage-enriched gene sets were predominantly related to (intracellular) signaling pathways such as mitogen-activated protein kinase (MAPK), WNT and PI3K/Akt signaling as well as “Signaling by Interleukins”.

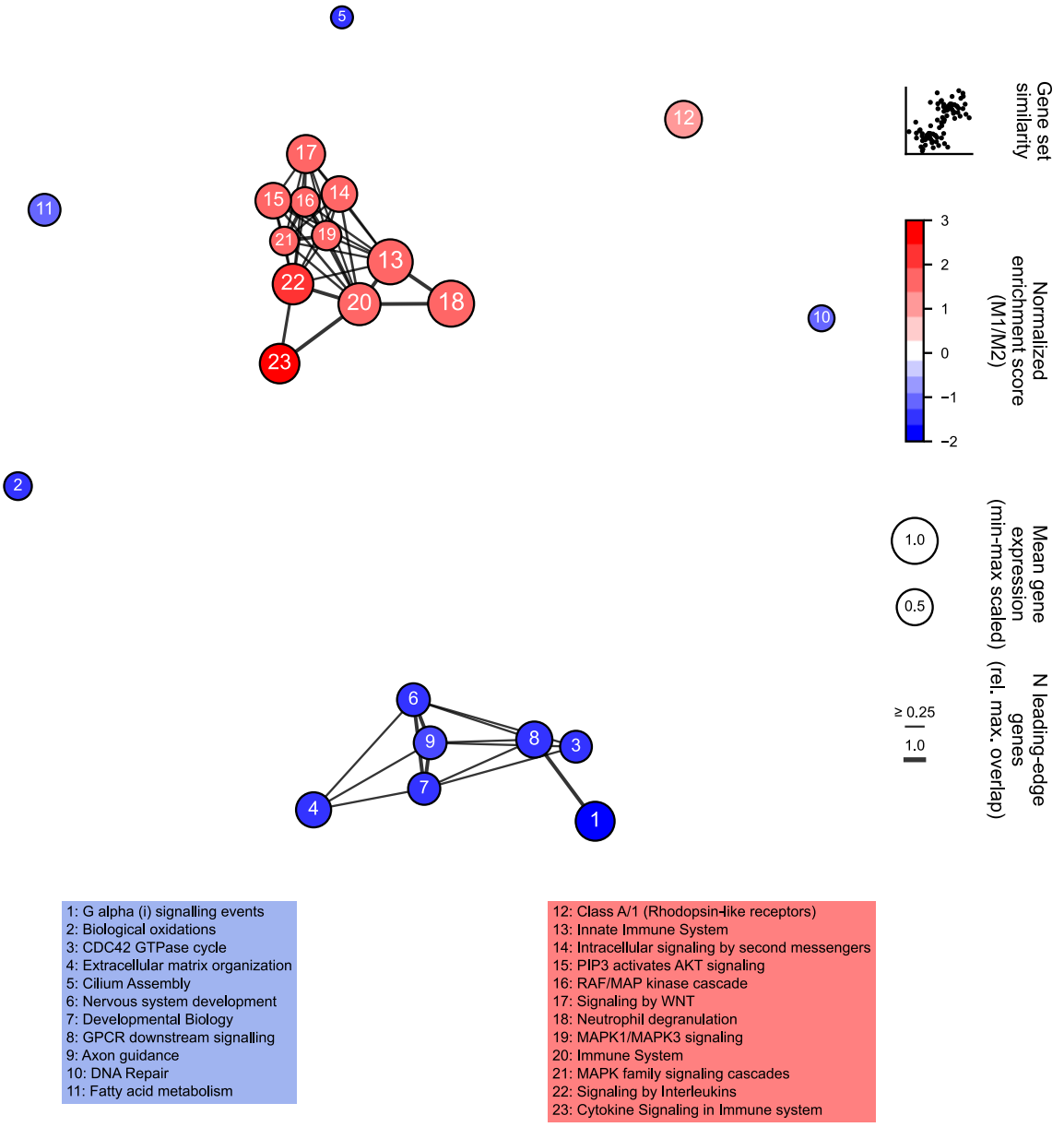

Figure 15: Gene set enrichment network analysis (Reactome) of M1 and M2 transcriptomes. Transcripts which were significantly differently abundant in M1 versus M2 macrophages ($|FC| > 1.5$ and $q \leq 0.05$) were subjected to gene set enrichment analysis (GSEA, Reactome). Gene sets are displayed as red (enriched in M1 macrophages) and blue (enriched in M2 macrophages) nodes. The normalized enrichment score (NES) is color-coded (NES > 0: enriched in M1 macrophages, NES < 0: enriched in M2 macrophages). The area of each node represents the mean expression of the gene sets' underlying transcripts. The thickness of edges represents the fraction of leading-edge genes which two gene sets have in common (the highest fraction of the two gene sets was taken into account). The spatial distribution in the Cartesian space encodes the similarity of two gene sets as defined by the number of genes/proteins they share.

The enrichment of gene sets related to G protein-coupled signaling, neuronal pathways as well as (immune cell) signaling such as MAPK and PI3K/Akt signaling was also mirrored when looked into parent-child relationships of enriched gene sets (Figure 16). In M2 macrophages, the gene sets "GPCR downstream signaling" and "Developmental biology" (the latter one further branches into "Nervous system development") were identified as gene sets with the highest hierarchy. Accordingly, the gene sets "Immune System", "Intracellular signaling by second messengers" and "MAPK family signaling cascades" were the gene sets with highest hierarchy enriched in M1 macrophages.

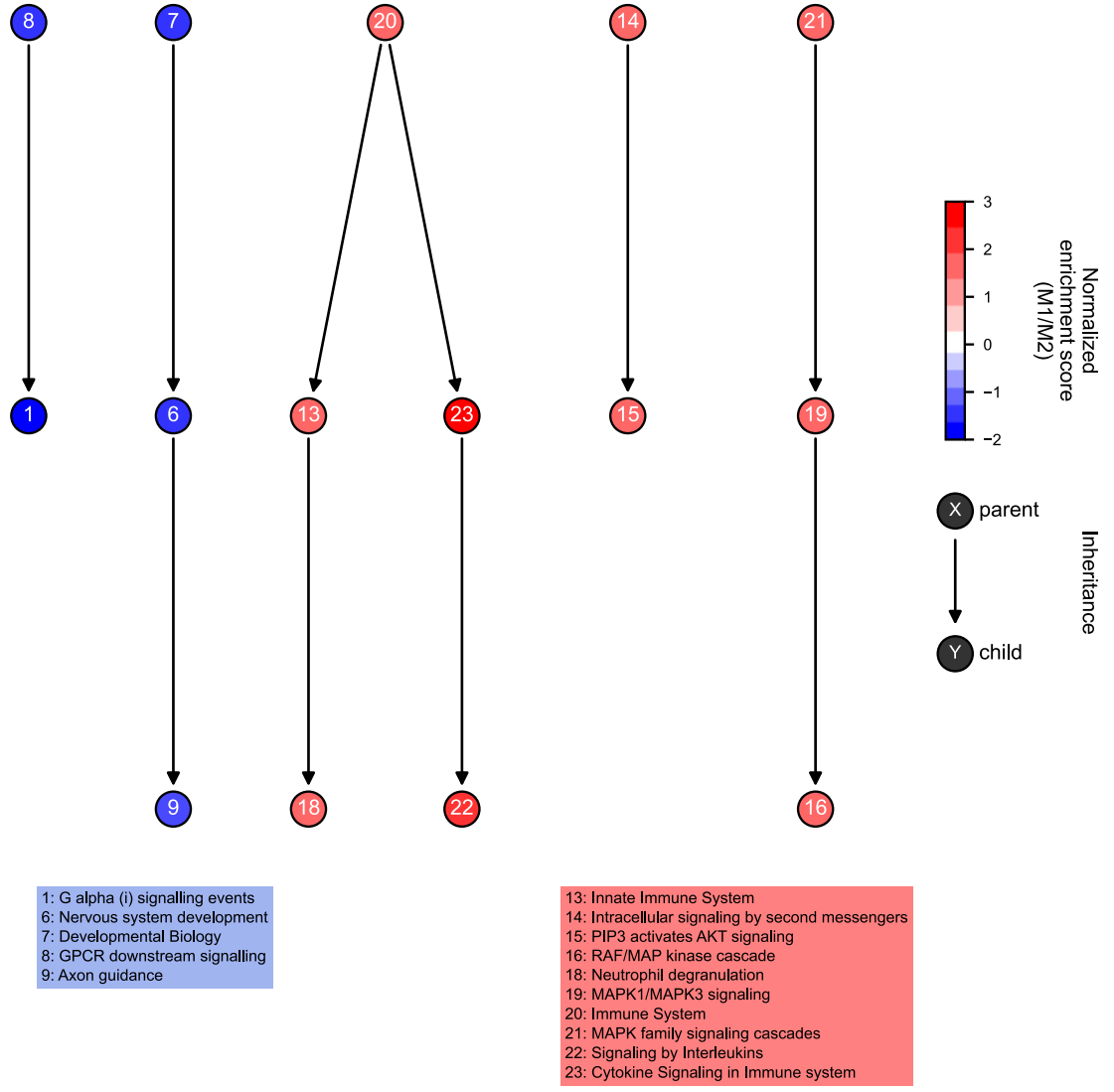

Figure 16: Pedigree analysis of Reactome gene sets identified in the M1 and M2 macrophage transcriptomes. Hierarchical relationship of gene sets. Gene sets from the gene set enrichment analysis of the M1 and M2 macrophage transcriptomes which are related in the Reactome gene set database are displayed as nodes. Edges indicate their relationship. Genes underlying a child gene set are members of the parent gene set as well. The normalized enrichment score is color-coded.

Taken together, we applied *NezzworGS*, a novel computational algorithm that combines gene set enrichment analysis with network analysis, which enabled us to explore potential molecular signatures of M1 and M2 macrophages in depth. Overall, gene sets enriched in M2 macrophages (extracellular matrix organization, neuronal development, MHC II-associated antigen presentation and G protein-coupled receptor signaling) were conserved, on both proteome and transcriptome level, although the correlation between the abundance of single proteins and transcripts was low. In M1 macrophages, gene sets related to immune cell signaling could be detected both on protein and transcript levels. However, there was no clear overlap of proliferation-associated gene sets (as detected in the M1 macrophage proteome) or gene sets related to PIP3/Akt, MAPK or WNT signaling (as detected in the M1 macrophage transcriptome).

4.2.7 Time-dependent transcriptomic alterations in M1 and M2 macrophages

The previously shown analyses were based on differentially abundant proteins or transcripts derived from M1 macrophages which were isolated from EAE onset and M2 macrophages which were isolated 5 days after EAE onset. Consequently, longer exposure of cells to environmental signals within the tissue can have an impact on the molecular phenotype of these cells, regardless the transition of M1 macrophages into M2 macrophages as previously observed by Locatelli *et al.* (222). To address this, we analyzed the transcriptomic signature of M1 and M2 macrophages from an early and late time point during EAE disease course. First, we estimated the transcriptome similarity of M1 ($iNOS^+Arginase\text{-}1^-$), M2 ($iNOS^-Arginase\text{-}1^+$), M0 ($iNOS^-Arginase\text{-}1^-$) and M12 ($iNOS^+Arginase\text{-}1^+$) macrophages at different time points during EAE disease progression (onset + 1 d and onset + 4 d). Based on the gene expression matrix, UMAP analysis revealed that the majority of transcripts are similarly abundant in different polarization phenotypes (M1, M2, M0 and M12) and time points (onset + 1 d and onset + 4 d, Figure 17). To test how the differential abundance of transcripts could translate into a functional signature of these cells, we applied the *NezzworGS* algorithm to the transcriptome subset that mapped to cluster 1 which showed highest variability in gene expression among different polarization states and time points.

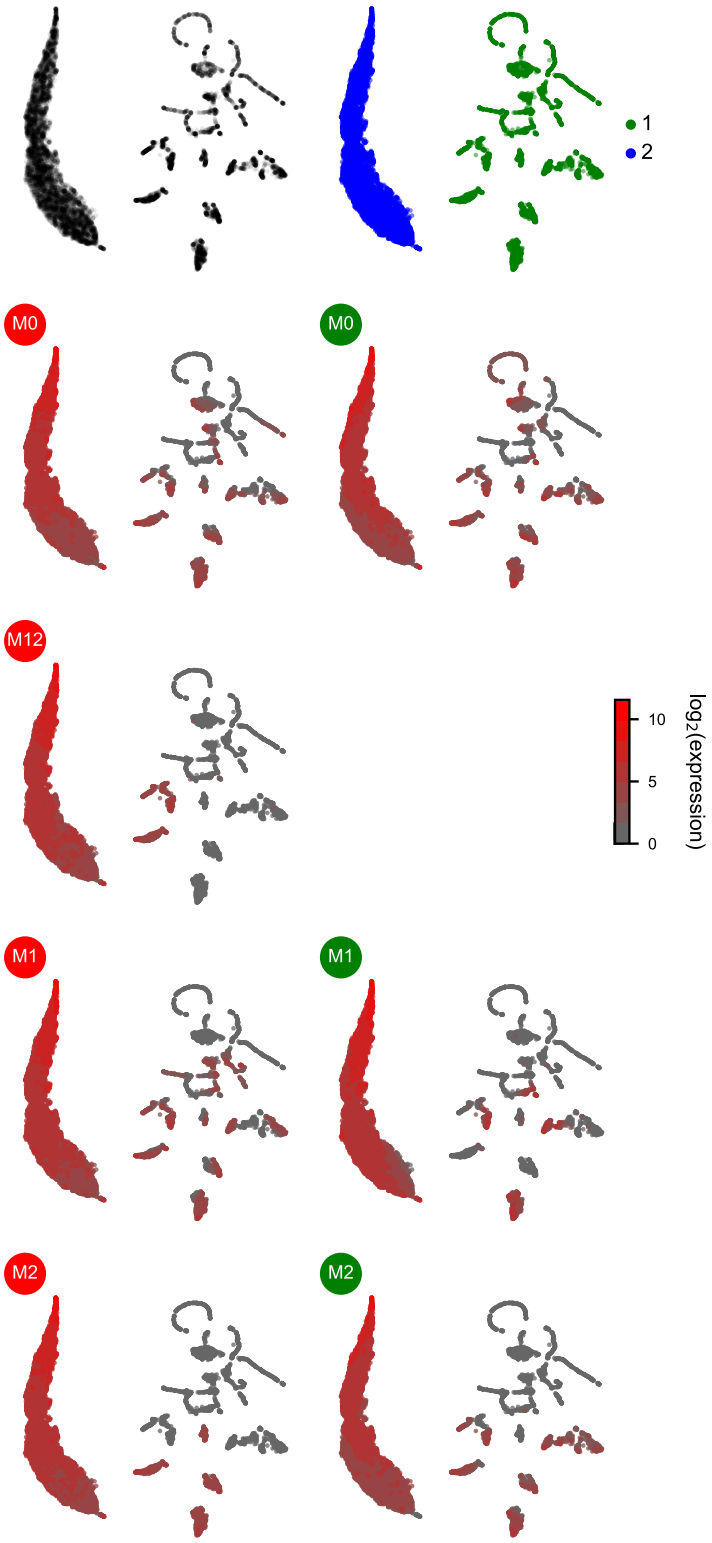

Figure 17: UMAP analysis of M1, M2, M0 and M12 macrophages at different time points during EAE disease progression. Normalized gene expression matrix subjected to UMAP (left upper plot) and balanced iterative reducing and clustering using hierarchies (right upper plot) analysis. Different macrophage polarization states were analyzed at different time points (red: EAE onset + 1 d, green: EAE onset + 4 d). The mean logarithmic gene expression for each condition (macrophage polarization type per time point) was color-coded. M12 macrophages at EAE onset + 4 d were excluded from further analysis because of low cell count.

The previously identified gene sets characterizing M1 macrophages (as opposed to M2 macrophages) related to immune cell signaling and MAPK as well as PI3K/Akt signaling were not identified when M1 macrophages from EAE onset + 1 d were compared to M1 macrophages from EAE onset + 4 d (Figure 18). Thus, these signaling pathways are likely a time-independent signature of M1 macrophages. In contrast, gene sets related to proliferation and DNA replication as well as WNT signaling were enriched at EAE onset + 1 d (compared to EAE onset + 4 d), indicating that cell proliferation and WNT signaling are prominent features of M1 macrophages at lesion formation and are less dominant at later time points during EAE disease progression. GTPase-related gene sets showed the highest NES at EAE onset + 4 d as well as the highest mean expression of the underlying transcripts, indicating a dominant role at later time points of EAE.

In contrast to M1 macrophages, gene set enrichment analysis of M2 macrophages from EAE onset + 1 d and EAE onset + 4 d showed enriched gene sets only at EAE onset + 4 d (Figure 19). This share of gene sets encompassed gene sets related to extracellular matrix organization, G protein-coupled receptor signaling and neuronal genes as previously identified in the M2 macrophage proteome and transcriptome (when compared to M1 macrophages).

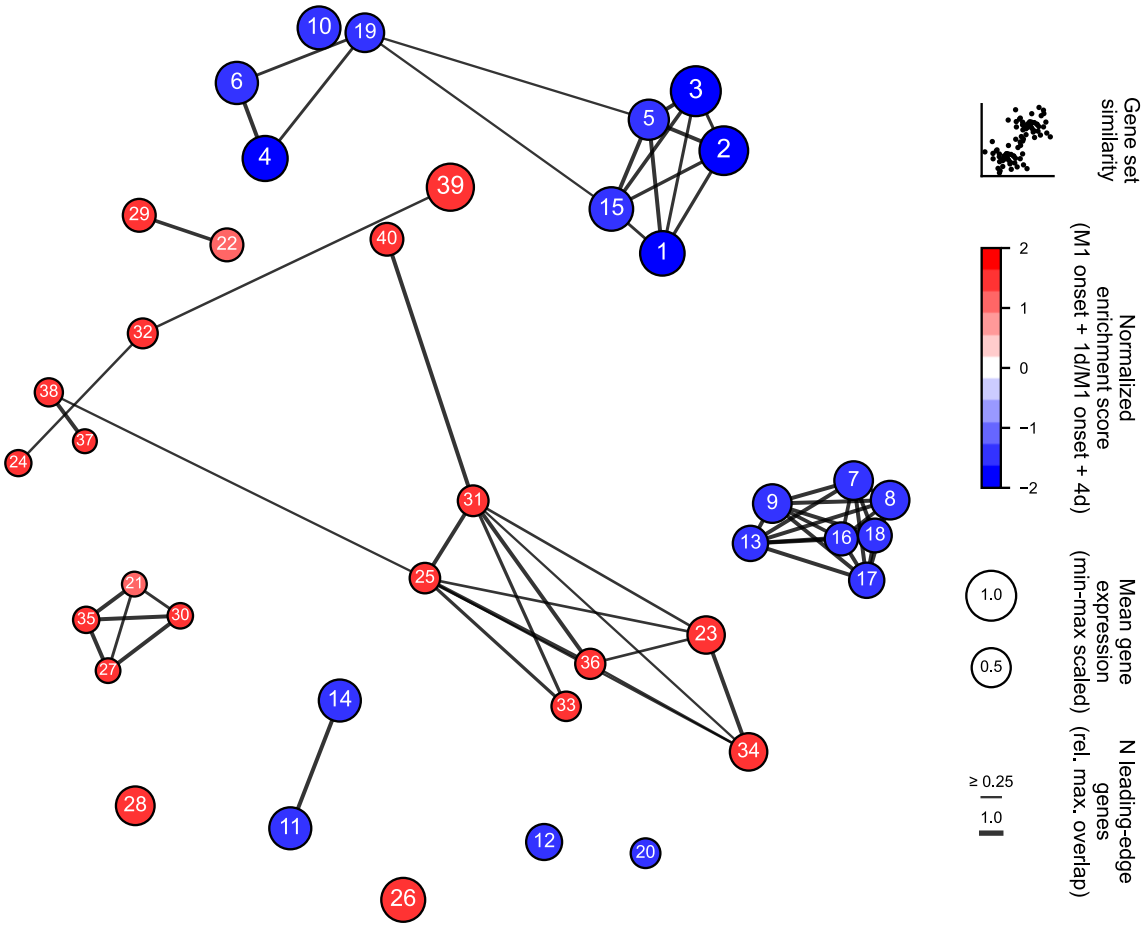

1: RHOA GTPase cycle
2: CDC42 GTPase cycle
3: RAC3 GTPase cycle
4: COPI-dependent Golgi-to-ER retrograde traffic
5: RHO GTPase cycle
6: Golgi-to-ER retrograde transport
7: Centrosome maturation
8: Recruitment of NuMA to mitotic centrosomes
9: Recruitment of mitotic centrosome proteins and complexes
10: Metabolism of nucleotides
11: Response to elevated platelet cytosolic Ca2+
12: G alpha (s) signalling events
13: G2/M Transition
14: Platelet degranulation
15: RAC1 GTPase cycle
16: Regulation of PLK1 Activity at G2/M Transition
17: Mitotic G2-G2/M phases
18: AURKA Activation by TPX2
19: Factors involved in megakaryocyte development and platelet production
20: Nonhomologous End-Joining (NHEJ)

21: G1/S Transition
22: Respiratory electron transport
23: Peroxisomal protein import
24: Regulation of TP53 Activity through Phosphorylation
25: Post-translational protein modification
26: Ion channel transport
27: S Phase
28: Peptide ligand-binding receptors
29: Respiratory electron transport, ATP synthesis by chemiosmotic coupling, and heat production by uncoupling proteins.
30: Synthesis of DNA
31: Metabolism of proteins
32: Transcriptional Regulation by TP53
33: Transport to the Golgi and subsequent modification
34: Protein localization
35: DNA Replication
36: Protein ubiquitination
37: Signaling by WNT
38: TCF dependent signaling in response to WNT
39: RNA polymerase II transcribes snRNA genes
40: Translation

Figure 18: Gene set enrichment network analysis (Reactome) of the transcriptomes of M1 macrophages at EAE onset + 1 d and onset + 4 d. Transcripts were pre-filtered according to their clustering in the UMAP analysis of the expression matrix of M1, M2, M0 and M12 macrophages at relapse and remission of EAE and subjected to gene set enrichment analysis (GSEA, Reactome). Gene sets are displayed as red (enriched at relapse) and blue (enriched at remission) nodes. The normalized enrichment score (NES) is color-coded (NES > 0: enriched at relapse, NES < 0: enriched at remission). The area of each node represents the mean expression of the gene sets' underlying transcripts. The thickness of edges represents the fraction of leading-edge genes which two gene sets have in common (the highest fraction of the two gene sets was taken into account). The spatial distribution in the Cartesian space encodes the similarity of two gene sets as defined by the number of genes/proteins they share

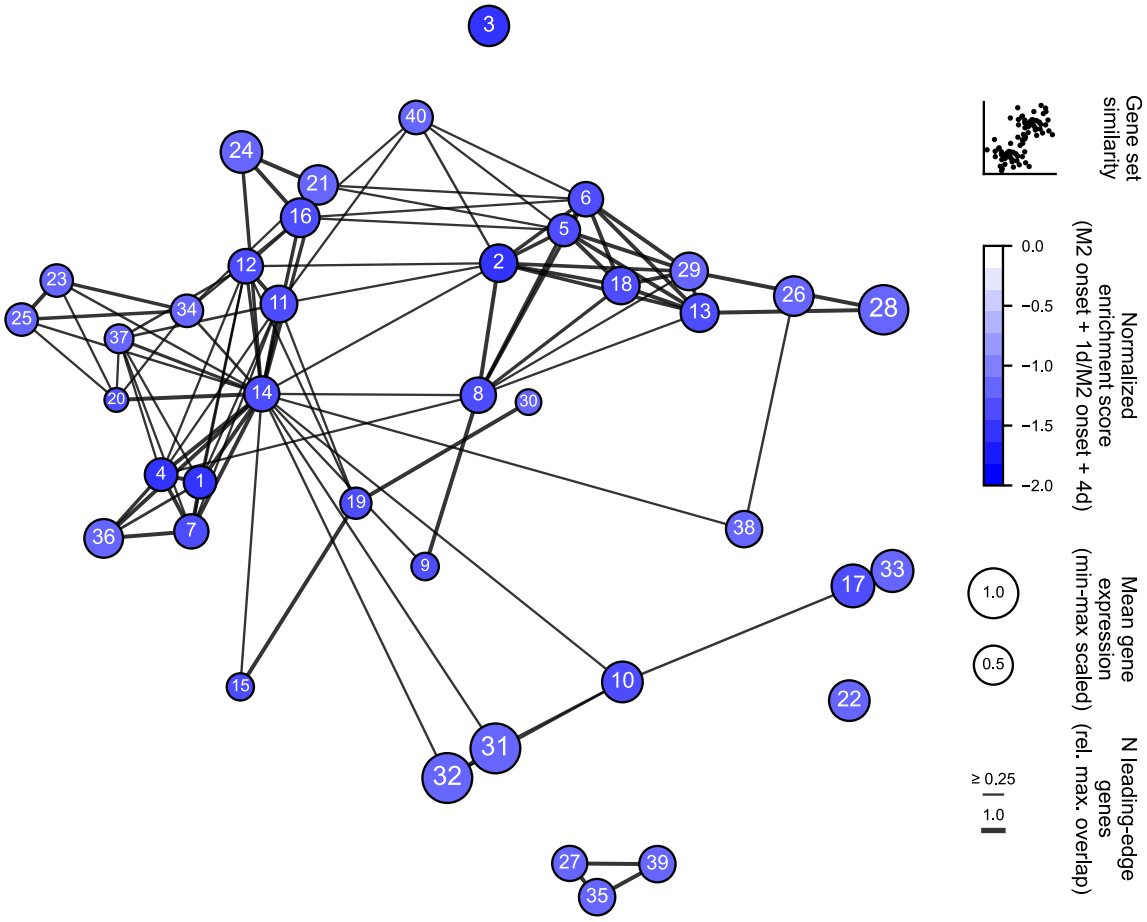

1: G alpha (i) signalling events
2: Factors involved in megakaryocyte development and platelet production
3: Extracellular matrix organization
4: GPCR downstream signalling
5: COPI-dependent Golgi-to-ER retrograde traffic
6: Golgi-to-ER retrograde transport
7: Signaling by GPCR
8: Hemostasis
9: Platelet activation, signaling and aggregation
10: Cellular Senescence
11: Signaling by Hedgehog
12: Hedgehog 'off' state
13: Membrane Trafficking
14: Signal Transduction
15: Ion channel transport
16: Signaling by Rho GTPases, Miro GTPases and RHOBTB3
17: RNA polymerase II transcribes snRNA genes
18: Intra-Golgi and retrograde Golgi-to-ER traffic
19: Transport of small molecules
20: Signaling by Receptor Tyrosine Kinases
21: Signaling by Rho GTPases
22: Biological oxidations
23: Axon guidance
24: RHO GTPase cycle
25: Nervous system development
26: Fatty acid metabolism
27: Nonsense Mediated Decay (NMD) independent of the Exon Junction Complex (EJC)
28: Rab regulation of trafficking
29: Vesicle-mediated transport
30: SLC-mediated transmembrane transport
31: Chromatin modifying enzymes
32: Chromatin organization
33: DNA Repair
34: Developmental Biology
35: Nonsense-Mediated Decay (NMD)
36: GPCR ligand binding
37: Intracellular signaling by second messengers
38: Peroxisomal protein import
39: Nonsense Mediated Decay (NMD) enhanced by the Exon Junction Complex (EJC)
40: Cilium Assembly

Figure 19: Gene set enrichment network analysis (Reactome) of the transcriptomes of M2 macrophages at EAE onset + 1 d and onset + 4 d. Transcripts were pre-filtered according to their clustering in the UMAP analysis of the expression matrix of M1, M2, M0 and M12 macrophages at onset + 1 d and onset + 4 d of EAE and subjected to gene set enrichment analysis (GSEA, Reactome). Gene sets are displayed as red (enriched at onset + 1 d) and blue (enriched at onset + 4 d) nodes. The normalized enrichment score (NES) is color-coded (NES > 0: enriched at onset + 1 d, NES < 0: enriched at onset + 4 d). The area of each node represents the mean expression of the gene sets' underlying transcripts. The thickness of edges represents the fraction of leading-edge genes which two gene sets have in common (the highest fraction of the two gene sets was taken into account). The spatial distribution in the Cartesian space encodes the similarity of two gene sets as defined by the number of genes/proteins they share.

These findings suggest that M2 macrophages develop their molecular signature over time while M1 macrophages change their molecular signature from a proliferation-associated profile at early stages of the disease to a more versatile functional palette during disease progression.

4.2.8 Leading-edge analysis of proteins and transcripts from gene sets enriched in the M1 and M2 macrophage proteome and transcriptome

Our previous finding suggested that gene sets related to G protein-coupled receptor signaling, nervous system, extracellular matrix (all enriched in M2 macrophages) as well as immune cell signaling (enriched in M1 macrophages) significantly contributed to the proteomic and transcriptomic phenotype of M1 and M2 macrophages in EAE. Next, we analyzed the contribution of single proteins and transcripts to the expression of these phenotypes.

Single protein analysis of leading-edge proteins from gene set analysis revealed that the two most differentially abundant proteins in the gene set "GPCR downstream signaling", which was enriched in M2 macrophages, are the neurotransmitter receptors gamma-aminobutyric acid type B receptor subunit 2 (GABBR2) and metabotropic glutamate receptor 2 (GRM2, Figure 20). However, they were not detected on transcript level, although gene set enrichment analysis of M1 versus M2 macrophage transcriptomes showed an enrichment of neuronal-related gene sets in M2 macrophages. The discrepancy between the proteome and transcriptome in terms of fold changes between M1 and M2 macrophages was observed not only for the gene set "GPCR downstream signaling" but also other differentially enriched gene sets, although the overall gene set or related gene sets were conserved in both the proteome and transcriptome. This implies that the proteomic and transcriptomic phenotype of M1 and M2 macrophages has a considerable overlap, however, the differential abundance of individual proteins and their respective transcripts does not necessarily need to overlap.

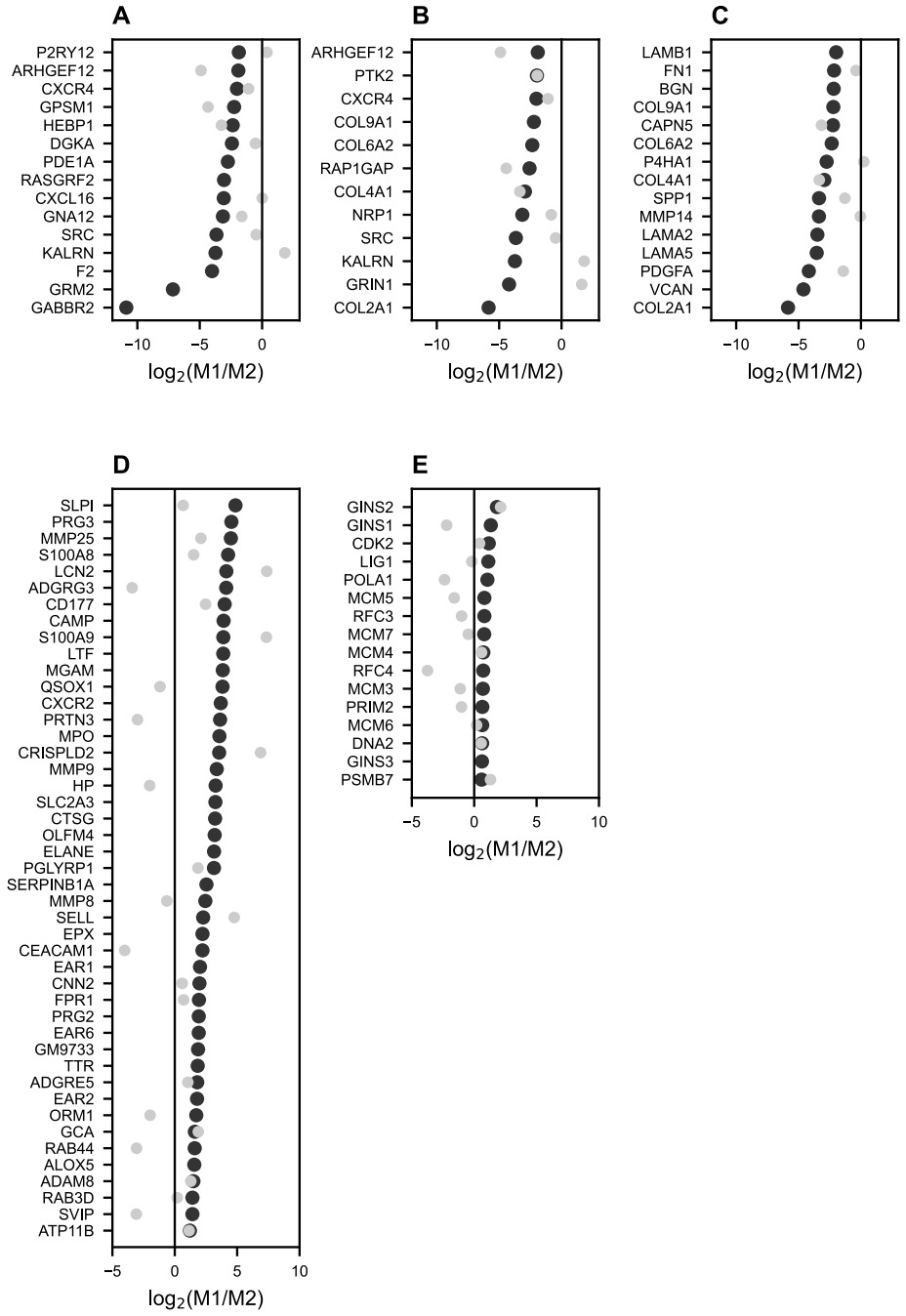

Figure 20: Leading-edge proteins from gene sets enriched in the M1 and M2 macrophage proteomes. Logarithmic differential protein abundance (black) and transcript abundance (grey) of leading-edge proteins from gene sets enriched in M2 macrophages (**A**: "GPCR downstream signaling", **B**: "Nervous system development", **C**: "Extracellular matrix organization") and M1 macrophages (**D**: "Immune System", **E**: "DNA Replication").

Taken together, gene set enrichment analysis coupled to network analysis of proteomes and transcriptomes of differently polarized macrophages at different time points during EAE disease course revealed that M2 macrophages acquire a molecular signature over time which encompasses gene sets related to G protein-coupled receptor signaling, neuronal development-related proteins/genes and extracellular matrix organization. Notably, since these gene sets are conserved in the proteome and transcriptome, it is rather unlikely that their enrichment in the proteome results from a contamination of extracellular proteins or proteins from other cell types such as neurons. M1 macrophages showed

an enrichment of proliferation-related gene sets, both, in the proteome and transcriptome. The analysis of the temporal change of the molecular signature of M1 macrophages in the transcriptome revealed that these gene sets dominate the initial phase of EAE disease progression. However, this finding does not necessarily imply that macrophages indeed proliferate in the inflamed CNS tissue. The molecular signature might also be a remnant from the proliferation state of the cells or the underlying genes/proteins are shared for other functions during neuroinflammation.

4.2.9 Functional protein-protein interaction network analysis revealed functional hubs of extracellular proteins within the M1 and M2 macrophage proteomes

In the previous analysis we characterized the molecular phenotype of M1 and M2 macrophages during EAE disease progression. This analysis identified gene sets related to immune cell signaling and proliferation enriched in M1 macrophages. On the other hand, gene sets related to G protein-coupled receptor signaling, extracellular matrix organization and neuronal development were enriched in M2 macrophages. We hypothesized that the function of M1 and M2 macrophages in the context of CNS inflammation is eventually conveyed by the proteins which they secrete. These secreted proteins might then either induced further pro-inflammatory cascades (of other immune cells or CNS target cells) and contribute to tissue destruction or reinforce intra- and extracellular programs related to tissue repair and maintenance. To screen for molecular functional hubs of extracellular proteins within the M1 and M2 macrophage proteomes on single-protein level, we applied a newly developed computational algorithm based on functional protein-protein interaction mapping of single proteins coupled to network analysis with subsequent gene set enrichment analysis (*FUPPINA* class of the Python module *Nezzworker*).

First, we filtered the M1 and M2 macrophage proteome for extracellular proteins. Overall, 114 proteins of the 614 proteins which were enriched in the M1 macrophage proteome (18.57 %) were annotated as extracellular proteins, according to the Cell-Cell Interaction Database (302). The M2 macrophage proteome exhibited 122 proteins (13.39 %) which were annotated as extracellular proteins. Next, the functional relationships between the extracellular proteins were assessed by analyzing their functional protein-protein interaction as defined by the STRING database (300). In the M1 proteome, 64 proteins (out of 68) showed at least one interaction to another protein and were connected to the main network (Figure 21). The network was composed of 64 vertices which were connected by 266 edges. The network's density was 0.13 (where 0 is a network without any edge and 1 a network with $\frac{n \cdot (n-1)}{2}$ edges where n is the number of vertices). There was no correlation between the degree of centrality and protein expression level on single protein level ($r = 0.13$, $p = 0.29$, Pearson correlation with p for H_0: $r \neq 0$).

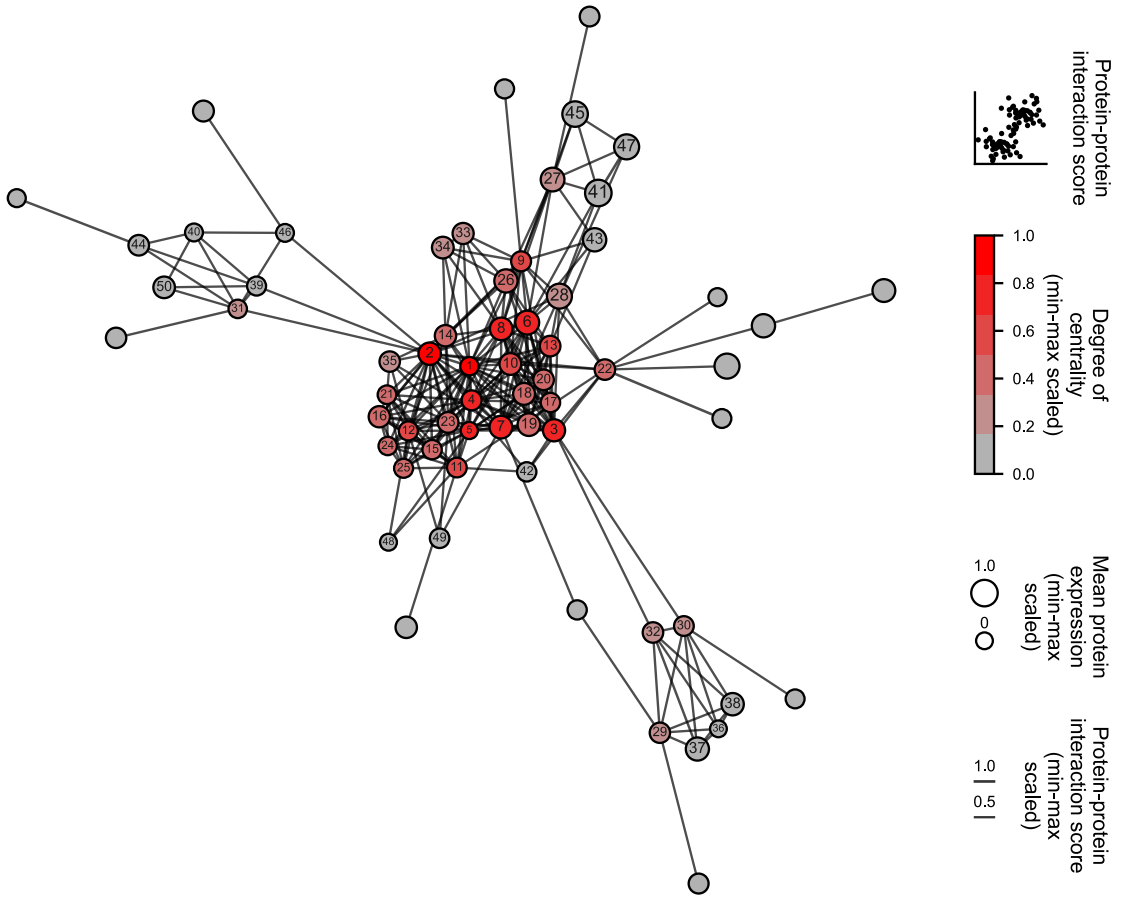

Figure 21: Functional protein-protein interaction network analysis (*FUPPINA*) for M1 macrophage extracellular proteins. Vertices represent proteins which were annotated as extracellular proteins. The degree of centrality is color-coded, the area of a vertex encodes the (min-max scaled) protein expression. Edges display the interaction between two proteins. The edge thickness as well as the spatial distribution in the Cartesian space encode the (min-max scaled) STRING score. The 50 proteins with the highest degree of centrality were annotated (n = 64).

In the M2 macrophage proteome 102 extracellular proteins (out of 108) showed at least one functional protein-protein interaction to another protein (Figure 22). The 102 vertices were connected via 341 interactions (edges). The network density was 0.06. There was no correlation between the degree of centrality and the expression level of the proteins in the network ($r = 0.15$, $p = 0.12$, Pearson correlation with p for H_0: $r \neq 0$).

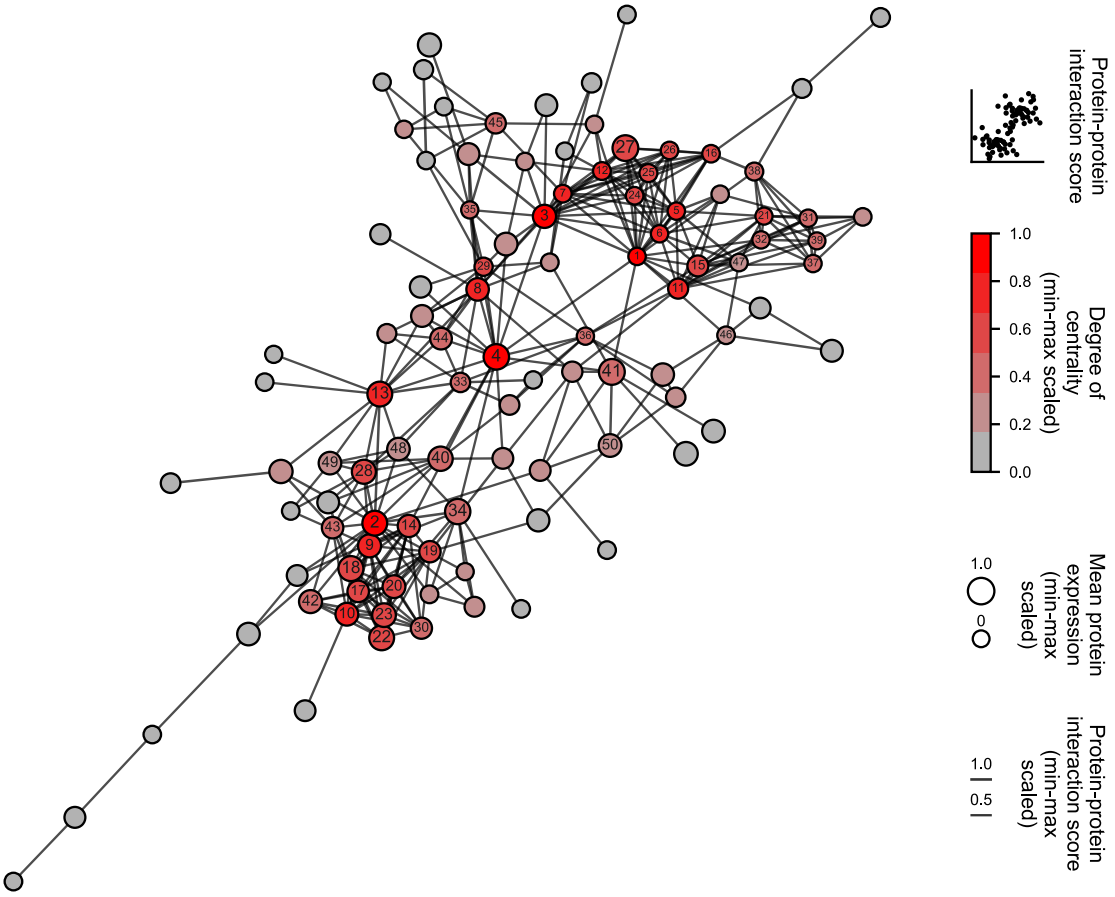

Figure 22: Functional protein-protein interaction network for M2 macrophage extracellular proteins. Vertices represent proteins which were annotated as extracellular proteins. The degree of centrality is color-coded, the area of a vertex encodes the (min-max scaled) protein expression. Edges display the interaction between two proteins. The edge thickness as well as the spatial distribution in the Cartesian space encode the (min-max scaled) STRING score. 6 proteins without any connection to the main network were excluded from the analysis (n = 102).

Next, we compared the two networks to gain deeper insights into the functional diversity of macrophage extracellular proteins. Overall, the M1 macrophage functional protein-protein interaction network of extracellular proteins showed a higher mean degree of centrality, mean degree of eigenvector centrality, mean betweenness centrality and mean closeness centrality compared to the M2 macrophage functional protein-protein interaction network of extracellular proteins (Figure 23). Similarly, the average number of edges per node was higher in the M1 network (4.16 versus 3.34). Taken together, the denser the network (indicated by higher mean centrality metric and a higher number of edges per node), the more proteins functionally interact with each other which can be interpreted as a higher degree of functional relatedness of proteins. Because of higher centrality metrics and a higher average number of edges per node, there are more functional protein-protein interactions among M1 extracellular proteins compared to M2 extracellular proteins.

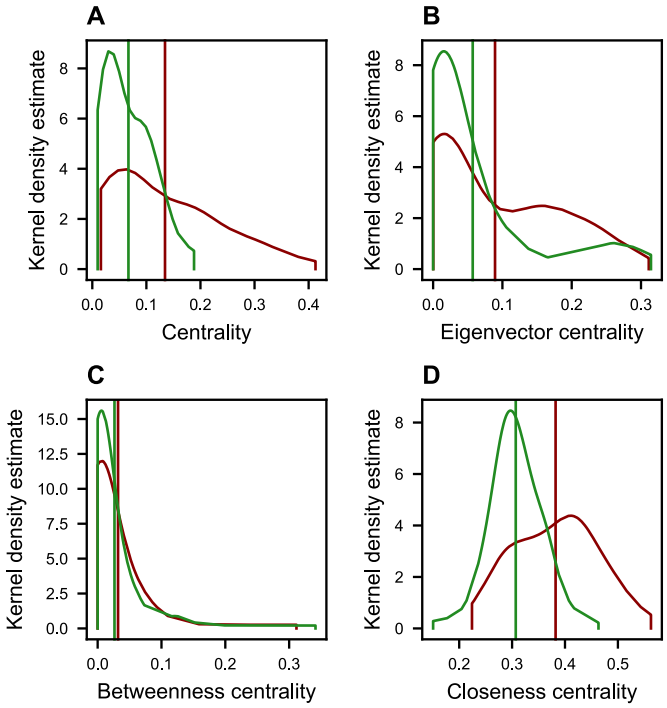

Figure 23: Metrics of the M1 and M2 macrophage extracellular proteins functional protein-protein interaction networks. Histograms of the vertex metrics of the M1 (red) and M2 (green) macrophage extracellular proteins networks. The vertical lines indicate the respective mean value for each feature (**A**: degree of centrality, **B**: degree of eigenvector centrality, **C**: degree of betweenness centrality, **D**: degree of closeness centrality, $n_{M1} = 64$, $n_{M2} = 102$).

By visual inspection both networks displayed multiple subnetworks. A subnetwork is characterized by a high local density (higher number of edges per nodes) and, thus, might indicate a functional hub within the whole network. To further explore these subnetworks, we computed the modularity of each network. The functional protein-protein interaction network of M1 macrophage extracellular proteins showed 4 modularity classes (Figure 24). Nine proteins, which were connected in modularity class 1, showed the highest density. The modularity classes 1 and 3 were clearly separated from the core of the (whole) network which was built up by the modularity classes 2 and 4.

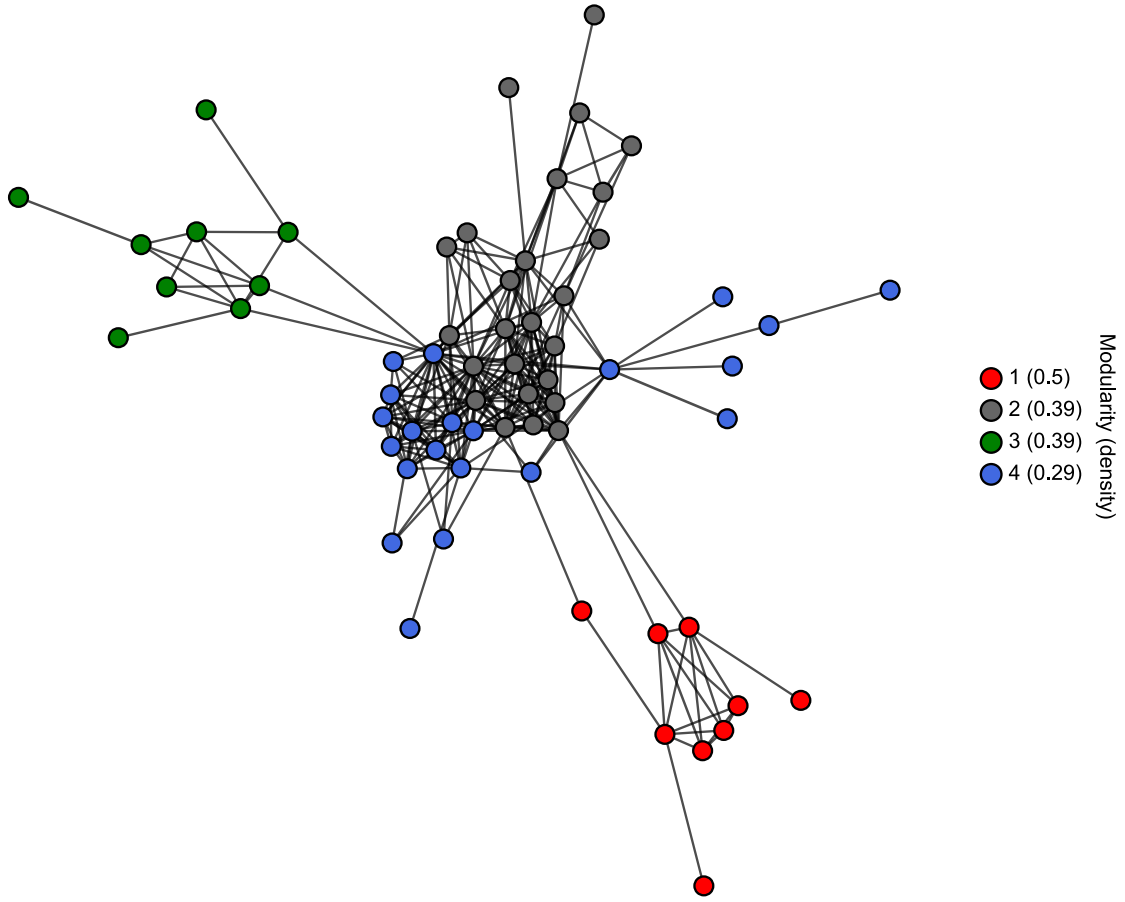

Figure 24: Modularity analysis of the M1 macrophage extracellular proteins functional protein-protein interaction network. Vertices represent proteins which were annotated as extracellular proteins. The modularity class is color-coded. Edges display the interaction between two proteins. The edge thickness as well as the spatial distribution in the Cartesian space encode the (min-max scaled) STRING score.

Next, we assessed the enrichment of Reactome gene sets within each modularity class to get further insights into the molecular phenotypes of the share of proteins that build up the modularity classes. To precisely estimate which gene sets are enriched in each share of proteins (within a module), we implemented the Enrichr algorithm into the network analysis to test the gene set enrichment of a given share of genes/proteins in relation to a share of (control) baseline genes/proteins (301). We set the whole M1 and M2 macrophage proteome as baseline and computed the enrichment of gene sets within one network module. Modularity class 1 showed an enrichment of 2 gene sets ("Neutrophil degranulation" and 'Innate immune system"), Modularity class 3 showed more enriched gene sets, however, those gene sets were only based on the enrichment of 4 different proteins (FAS, NCAM1, SELL and SPN) with a relative strong contribution of FAS to the enrichment of 6 (out of 10) gene sets. In contrast, modularity classes 2 and 4 showed an enrichment of gene sets related to pro-inflammatory signaling pathways (modularity class 4) and tissue damaging pathways (modularity class 2, e. g. "Degradation of the extracellular matrix", "Collagen degradation" and "Extracellular matrix organization"). Furthermore, this modularity class revealed an enrichment of the TLR ligands S100A8 and S100A9 in the extracellular M1 macrophage proteome. Taken into account the spatial orientation of the modules within the main network, FAS-related gene sets (modularity class 3) and immune

system-related gene sets (modularity class 1) were comprised of proteins which did not show any connection with each other, thus, pointing towards different functions within the share of M1 macrophage extracellular proteins. In contrast, gene sets which derived from modularity class 2 and 4 (extracellular matrix-related and immune cell signaling-related) encompassed proteins which functionally interacted with each other.

Modularity class	Gene set	*q* value	Proteins
1	Neutrophil degranulation	< 0.001	ADAM8, CD177, AGPAT2, MCEMP1, PLAUR
	Innate immune system	< 0.001	ADAM8, CD177, AGPAT2, MCEMP1, LBP, PLAUR
2	Degradation of the extracellular matrix	< 0.001	MMP8, CTSG, MMP9, ELANE
	Extracellular matrix organization	< 0.001	CTSG, MMP8, TTR, ELANE, MMP9
	Collagen degradation	< 0.001	MMP8, ELANE, MMP9
	Regulation of TLR by endogenous ligand	0.006	S100A8, S100A9
	IRAK4 deficiency TLR2/4	0.006	S100A8, S100A9
	RHO GTPases activate NAPDH oxidases	0.008	S100A8, S100A9
	Infection with mycobacterium tuberculosis	0.012	LTF, CTSG
	Diseases of immune system	0.014	S100A8, S100A9
	Amyloid fiber formation	0.016	LTF, TTR
	Signaling by interleukins	0.041	PRTN3, CTSG, LCN2, MMP9
3	FasL/CD95L signaling	0.018	FAS
	Cell surface interactions at the vascular wall	0.018	SELL, SPN
	Tp53 regulates transcription of death receptors and ligands	0.02	FAS
	Regulation by c-FLIP	0.027	FAS
	Caspase activation via death receptors in the presence of ligand	0.039	FAS
	Signal transduction by L1	0.048	NCAM1
	RIPK1 mediated regulated necrosis	0.048	FAS
	NCAM1 interactions	0.048	NCAM1
	Caspase activation via extrinsic apoptotic signaling pathway	0.048	FAS
	Basigin interactions	0.048	SPN
4	Binding and uptake of ligands by scavenger receptors	0.012	HPX, ALB
	Amyloid fiber formation	0.012	SNCA, APP
	Interleukin 1 family signaling	0.012	IL1B, IL1R2, APP
	Interferon alpha/beta signaling	0.02	ISG15, IFITM3
	Signaling by interleukins	0.023	IL1B, IL1R2, APP, PTGS2
	Transport of organic anions	0.023	ALB
	Innate immune system	0.032	IL1B, APP, ISG15, TREM1, PPBP, SERPING1
	DDX58/IFIH1-mediated induction of interferon alpha beta	0.036	APP, ISG15
	Interleukin 4 and interleukin 13 signaling	0.037	IL1B, PTGS2
	Synthesis of 15-eicosatetraenoic acid derivatives	0.04	PTGS2

Table 12: Modularity-class-wise gene set enrichment analysis of the M1 macrophage extracellular proteins functional protein-protein interaction network.

Modularity analysis of the M2 macrophage extracellular proteins functional protein-protein interaction network revealed 4 modularity classes (Figure 25). Modularity class 3 and 4 showed the highest density (0.26 and 0.21, respectively). Vertices of these modularity classes were clearly spatially separated.

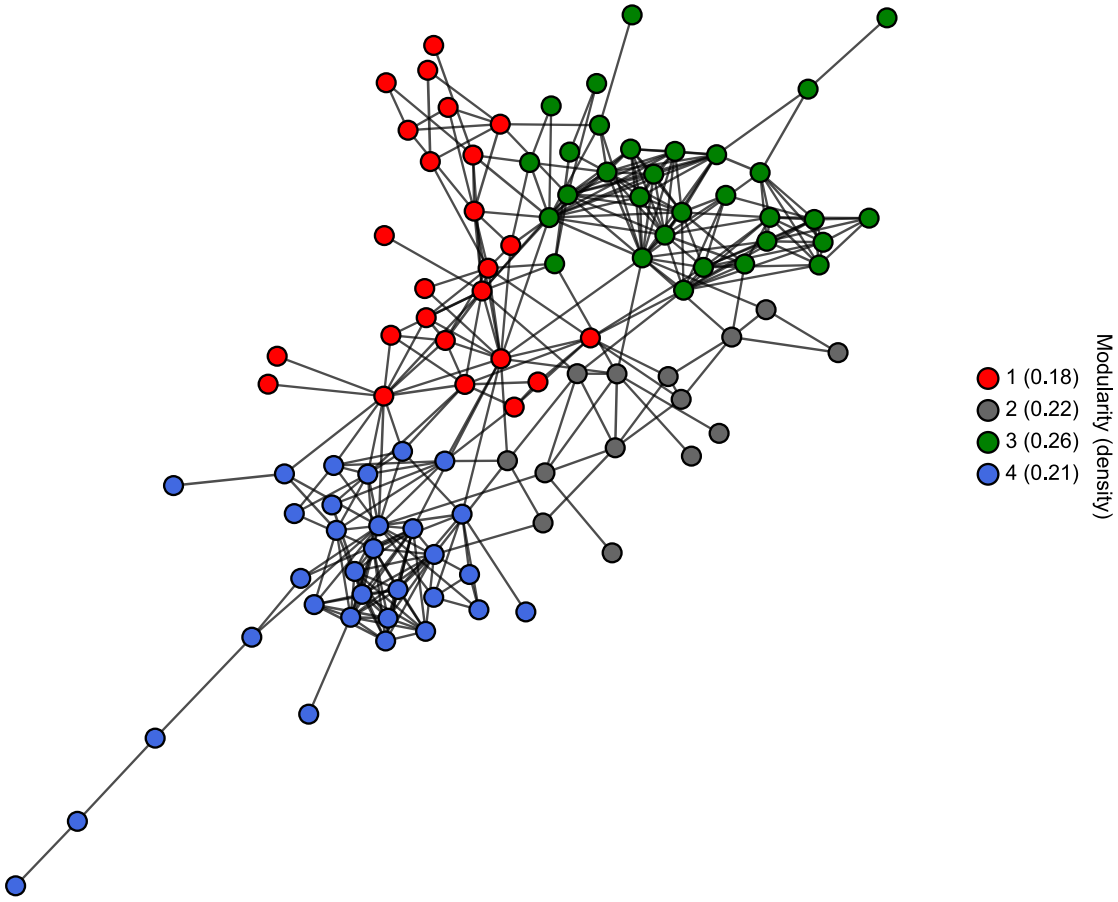

Figure 25: Modularity analysis of the M2 macrophage extracellular proteins functional protein-protein interaction network. Vertices represent proteins which were annotated as extracellular proteins. The modularity class is color-coded. Edges display the interaction between two proteins. The edge thickness as well as the spatial distribution in the Cartesian space encode the (min-max scaled) STRING score.

Gene set enrichment analysis of proteins underlying these modularity classes indicated that proteins with modularity class 3 are associated with tissue repair and biomolecule synthesis (Table 13). In contrast, modularity class 4 showed proteins associated with proteolytic extracellular matrix degradation (cathepsins), comparable to modularity class 2 of the M1 macrophage extracellular proteins functional protein-protein interaction network. Furthermore, cathepsin D (CTSD) showed a high degree of centrality, thus, it might function as a central hub for the tissue degrading function of M2 macrophages. Modularity class 1 was comprised of proteins involved in cell-cell signaling and complement cascades. Notably, these proteins exhibited both pro- (e. g. CXCL16, C1QA, TLRs) and anti-inflammatory (e. g. CX3CL1, IL10RB) functions. C1QA and CD68 showed the highest degrees of centrality in this modularity class and were both highly expressed in the M2 macrophage proteome.

Modularity class	Gene set	*q* value	Proteins
1	Immunoregulatory interactions between a lymphoid and a non-lymphoid cell	0.004	CD200R1, CD200, SIGLEC1
	Toll-like receptor cascades	0.004	CTSS, TLR3, TLR8, TLR7
	Chemokine receptors bind chemokines	0.004	CXCL16, CX3CL1
	Innate immune system	0.006	C1QB, CTSS, TLR3, C1QC, TLR7, C1QA, TLR8, CD68
	Interleukin 10 signaling	0.013	IL10RB, CD80
	Adaptive immune system	0.013	CD200R1, MRC1, CD80, CD200, SIGLEC1, CTSS
	Binding and uptake of ligands by scavenger receptors	0.015	MSR1, LRP1
	Peptide ligand binding receptors	0.019	CXCL16, CX3CL1
	Signaling by GPCR	0.019	GRM2, CXCL16, CX3CL1, GABBR2
	Class A/1 (Rhodopsin-like receptors)	0.028	CXCL16, CX3CL1
2	Nicotinate metabolism	0.006	CD38, NT5E
	Innate immune system	0.008	IGF2R, CD4, CD93, GAA, ANPEP, LGALS3
	Alpha defensins	0.032	CD4
	Pyrimidine catabolism	0.038	NT5E
	PTK6 promotes HIF1A stabilization	0.038	GPNMB
	LTC4-CYSLTR-mediated IL4 production	0.038	GGT1
	Defensins	0.038	CD4
	Cargo recognition for clathrin-mediated endocytosis	0.038	IGF2R, CD4
	Glycogen storage diseases	0.044	GAA
	RUNX1 regulates transcription of genes involved in differentiation of myeloid cells	0.049	LGALS3
3	Hemostasis	0.023	MERTK, AHSG, PROS1, F2, ITGAV
	Defective factor VIII causes Hemophilia A	0.025	F2
	Anchoring fibril formation	0.025	COL4A1
	Crosslinking of collagen fibrils	0.025	COL4A1
	Chylomicron clearance	0.025	APOE
	RUNX3 regulates immune response and cell migration	0.031	SPP1
	Assembly of active LPL and LIPC lipase complexes	0.031	APOA4
	HDL remodeling	0.042	APOE
	N-glycan antennae elongation	0.042	MGAT4A
	Metabolism of carbohydrates	0.043	B4GALT7, BGN, VCAN
4	Peptide hormone metabolism	0.017	CTSD, CTSZ
	Toll-like receptor cascades	0.018	CTSB, LGMN, CTSL
	Attachment and entry	0.019	CTSL
	Extracellular matrix organization	0.022	CTSB, CTSD, CTSL
	Endosomal vacuolar pathway	0.024	CTSL
	Biosynthesis of the N-glycan precursor (dolichol lipid-linked oligosaccharide, LLO) and transfer to a nascent protein	0.024	GLB1, CTSA
	COPII mediated vesicle transport	0.027	CTSZ, FOLR1
	RUNX1 regulates transcription of genes involved in differentiation of keratinocytes	0.028	CTSL
	Vitamin D (calciferol) metabolism	0.028	LGMN

	Trans-golgi network vesicle budding	0.035	GNS, CTSZ

Table 13: Modularity-class-wise gene set enrichment analysis of the M2 macrophage extracellular proteins functional protein-protein interaction network.

Taken together, compared to the functional protein-protein interaction network of M1 macrophage extracellular proteins, the M2 macrophage extracellular proteins functional protein-protein interaction network was looser and less interconnected, indicated by lower values of centrality measures, less edges per vertex and a lower triadic closure (0.52 versus 0.58). This might indicate that extracellular proteins in the M1 macrophage proteome share a more directed molecular phenotype when compared to the extracellular proteins of the M2 proteome. On the other hand, the multi-centric M2 macrophage network might indicate a higher functional diversity of M2 macrophages. This conclusion is supported by the enrichment of genes sets within the share of M2 macrophage extracellular proteins that point towards both tissue degrading and tissue repair mechanism. Notably, the modularity class 2 of the M1 macrophage extracellular proteins functional protein-protein interaction network contained proteins which were associated with the formation of (neutrophil) extracellular traps, such as MPO, ELANE, CTSG, LTF, CAMP, the matrix metalloproteinases MMP9, MMP8 as well as S100A8 and S100A9 (312, 313). Moreover, MMP8, MMP9, LTF, ELANE and MPO were among the 10 vertices with the highest degree of centrality in the network.

Classically, extracellular trap proteins are predominantly expressed by neutrophils. To evaluate our finding which suggests that these proteins are also expressed by macrophages at an early EAE stage, we assessed the protein expression of histone H3, LTF, MPO, ELANE, S100A8 and S100A9 in histological sections from EAE disease onset + 5 d using an *iNOS tdTomato Cre x Arginase-1 YFP* transgenic mouse line to allow the spatial mapping of fluorescent signals with M^{iNOS} (M1) and $M^{Arginase-1}$ (M2) macrophages (Figure 26). At EAE disease onset there was no immunoreactive protein detectable. At EAE onset + 5 d S100A8 signals and M^{iNOS} (M1) macrophages showed and overlay compared to $M^{Arginase-1}$ (M2) macrophages. However, Histone H3, LTF, MPO, ELANE and S100A9 signals were not co-localized with neither the YFP nor the tdTomato signal. Likewise, given the fact that all proteins are secreted proteins, there was no clear spatial relationship of the signals to the location of M^{iNOS} (M1) and $M^{Arginase-1}$ (M2) macrophages. There was no extracellular DNA (DAPI-positive) detectable. Notably, S100a8 and S100a9 were two of the most strongly enriched transcripts in the M1 transcriptome (S100a8: $\log_2(FC) = 2.08$, $q = 2.78 \times 10^{-2}$; S100a9: $\log_2(FC) = 7.42$, $q = 6.80 \times 10^{-3}$). However, considering the even higher protein expression by neutrophils, a cellular assignment of the investigated proteins to macrophages by fluorescent microscopy might be unprecise.

Taken together, by applying *FUPPINA* we identified various proteins which are functionally related to each other. The analysis of single candidates revealed an enrichment of proteins related to extracellular traps in the M1 macrophage proteome. However, histological analysis could not resolve the cell type specificity within EAE lesions. Moreover, analysis of the gene sets underlying the proteins that are functionally related could identify proteins which might be responsible for tissue destructive and reparative properties of M1 and M2 macrophages, respectively.

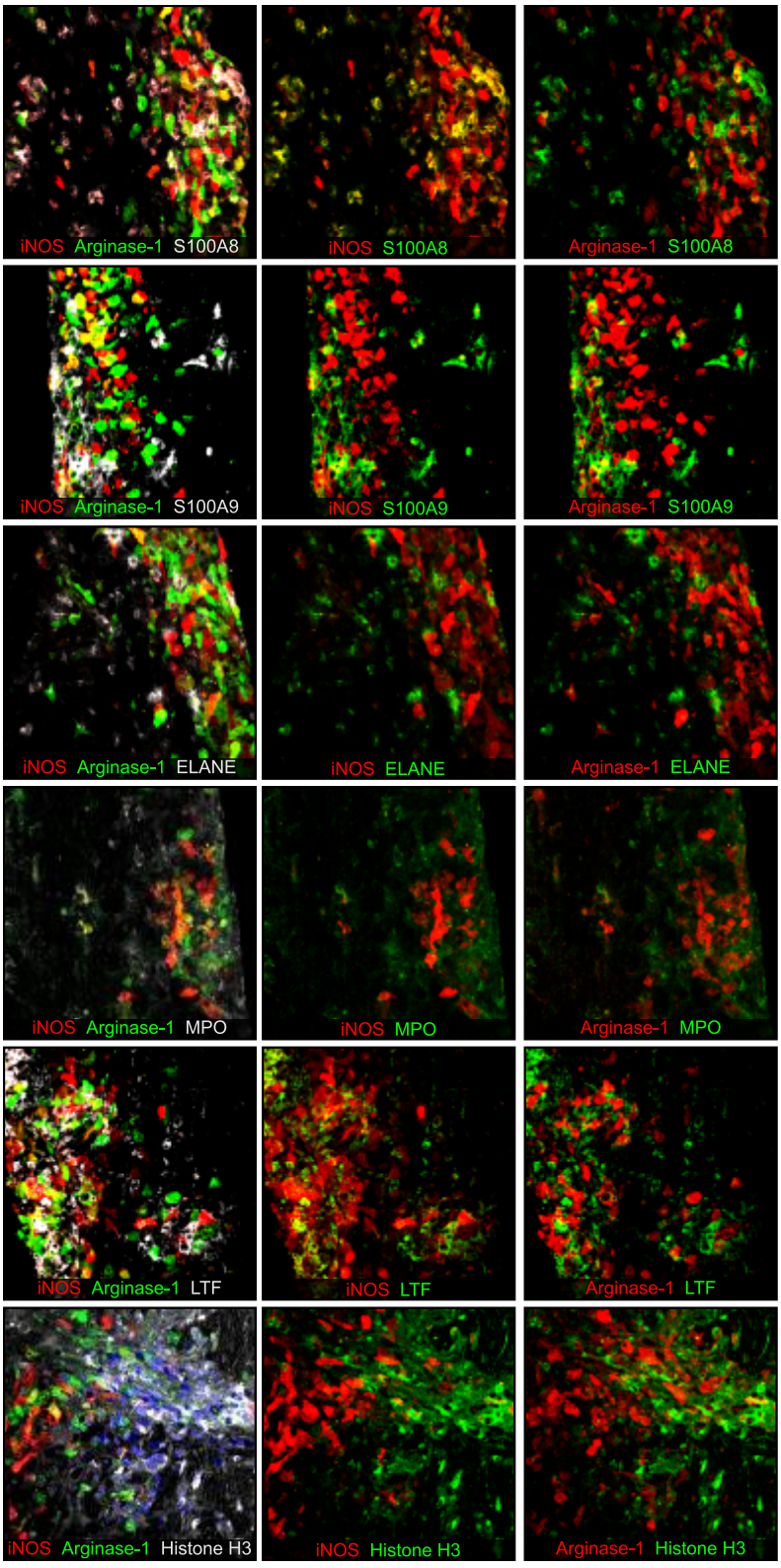

Figure 26: Histological analysis of the expression of MET-associated proteins. Immunofluorescence microscopy of 50 µm lumbar spinal cord sections from an *iNOS tdTomato Cre x Arginase-1 YFP* transgenic mouse at EAE onset + 5 d stained with antibodies targeting MET-associated proteins. The section with the histone H3 staining was also stained with DAPI (blue) to assess the extracellular DNA content.

4.2.10 Ligand-receptor interactions

To further investigate the molecular function of secreted proteins of M1 and M2 macrophages, we assessed the ligand-receptor interactions between M1 and M2 macrophages and other immune cell types. Therefore, proteins which were annotated as ligands and receptors (based on the CellPhoneDB and Cell-Cell Interaction Database) were extracted from the expression matrix (302, 307). A biologically meaningful interaction was assumed if the expression level of both receptor and ligand exceeded the mean expression (of all cell types) of the respective protein by 1 SD.

4.2.10.1 M1 and M2 macrophage ligands

Under the aforementioned assumptions, the M1 macrophage proteome contained 50 proteins which were identified as ligands (Figure 27). 109 of their respective receptors were detected in B cells, CD4 and CD8 T cells, and microglia.

Overall, these ligands and receptors could interact via 344 interactions that were distributed unequally among different cell types: M1 macrophage ligands showed most interactions with receptors enriched in T cells (CD4 T cells: 35 receptors/85 interactions, CD8 T cells: 34 receptors/120 interactions), followed by microglia (23 receptors/47 interactions) and B cells (17 receptors/39 interactions).

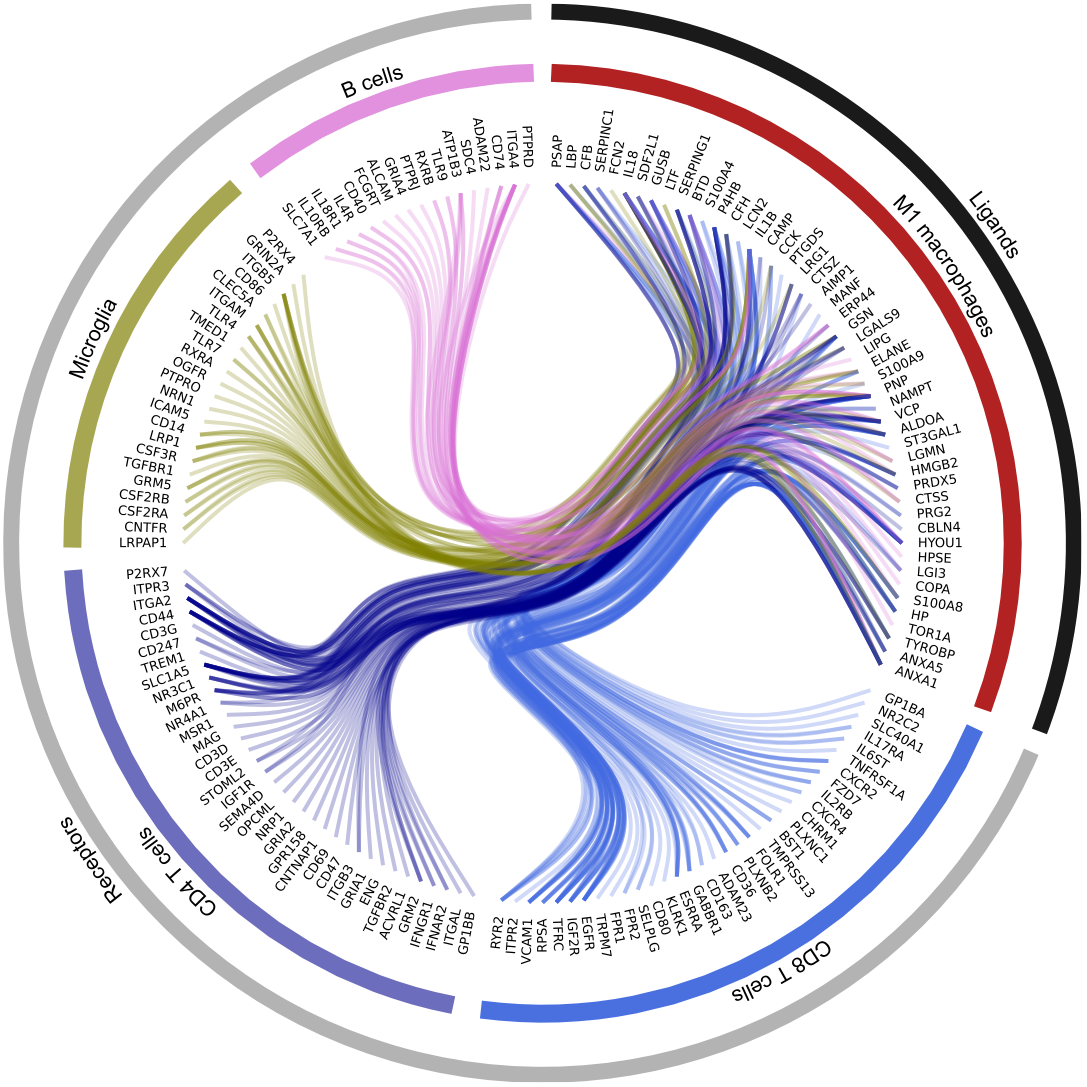

Figure 27: M1 macrophage ligand-receptor interactions. Hierarchical edge bundling of proteins which were annotated as ligands and receptors and which were at least 1 SD higher abundant in the M1 macrophage proteome than the mean abundance of all other immune cell types. Proteins are displayed as ligand-receptor interaction partners. Proteins were annotated according to the CellPhoneDB (Efremova *et al.*) and the Cell-Cell Interaction Database (Qiao *et al.*), respectively (302, 307).

Overall, 51 proteins of the M2 macrophage proteome could be identified as ligands with an abundance exceeding 1 SD of the mean abundance among all cell types (Figure 28). These proteins could interact with 94 receptors found on T cells, B cells, and microglia. Overall, we found 337 possible interactions. The (quantitative) distribution of the ligand-receptor interactions between M2 macrophages and the respective other cell type was comparable with M1 macrophages (CD4 T cells: 78 interactions, CD8 T cells: 116 interactions, B cells: 44 interactions, microglia: 42 interactions).

Overall, the M2 macrophage proteome shared 30 ligands with the M1 macrophage proteome. Among the 27 ligands specific to the M2 macrophage proteome (as compared to the M1 proteome), PTP1 (13 interactions), CTS1 and DPP (both 11 interactions) as well as MFI and SIAE (both 9 interactions) were the ligands with most receptor interactions. Most receptors of the (specific) M2 macrophage ligands were expressed by CD4 and CD8 T cells, however, CD4 and CD8 T cells did not share common receptors to these ligands but rather showed individual enrichments patterns. CD44 and M6PR were the receptors that were capable of recognizing most of the ligands which were

specifically secreted by M2 macrophages (in contrast to M1 macrophages). CD44 could recognize its ligands SPP1, DPP7, SIAE, PTP1 and MIF, whereas M6PR is capable of binding DPP7, SIAE and PTP1. 3 out of these ligands (DPP7, SIAE and PTP1) could function as signals for both the communication between M2 macrophages and CD4 T cells through the binding of IGF2R (DPP7, SIAE and PTP1) as well as CD8 T cells through VCAM1 (PTP1).

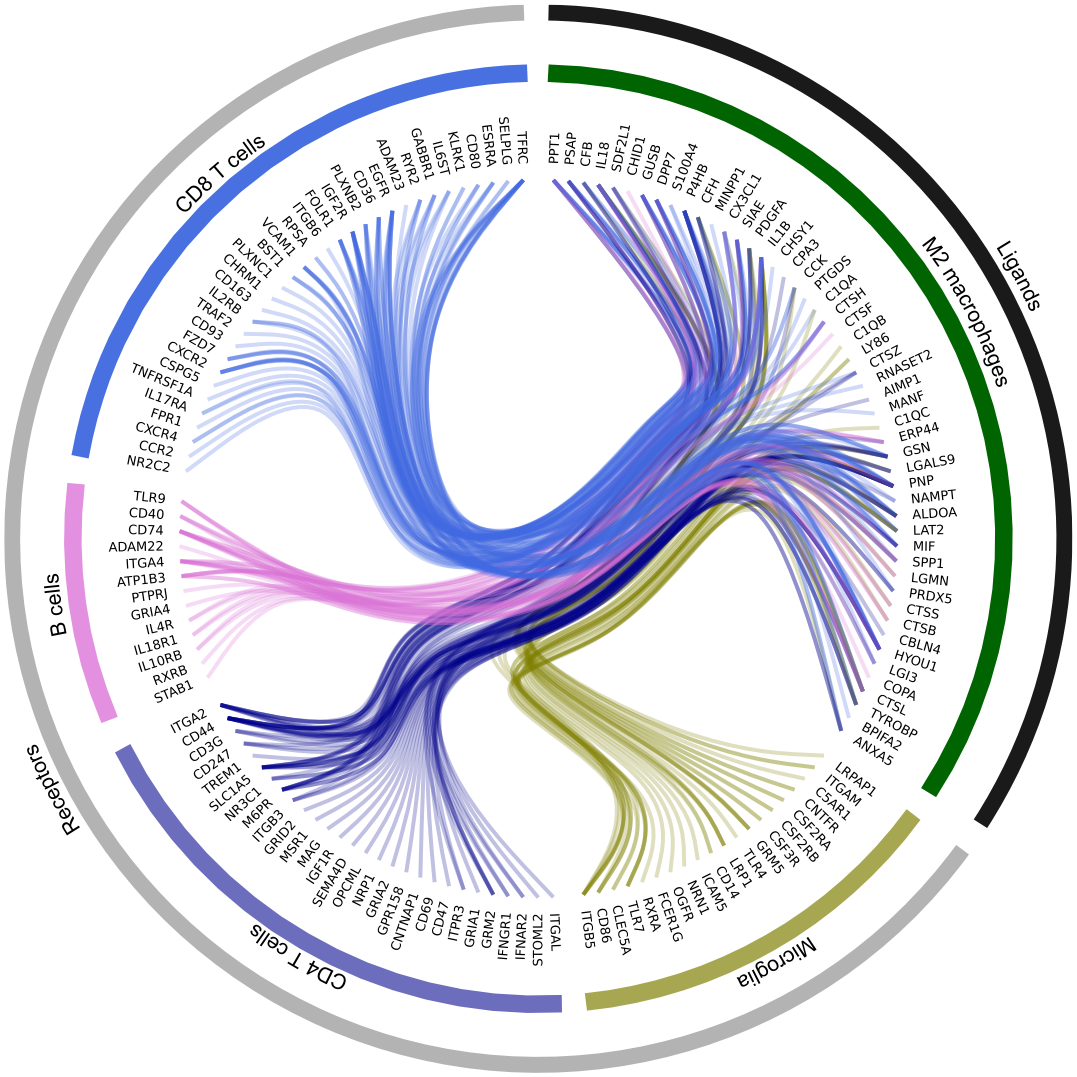

Figure 28: M2 macrophage ligand-receptor interactions. Hierarchical edge bundling of proteins which were annotated as ligands and receptors and which were at least 1 SD higher abundant in the M2 macrophage proteome than the mean abundance of all cell types. Proteins are displayed as ligand-receptor interaction partners. Proteins were annotated according to the CellPhoneDB (Efremova *et al.*) and the Cell-Cell Interaction Database (Qiao *et al.*), respectively (302, 307).

To gain deeper insights into the differential signaling of M1 and M2 macrophages with other immune cells, the 10 most enriched ligands were analyzed with respect to the expression of their respective receptors (Figure 29). 64 receptors of these ligands were detected in the proteomes of microglia, T and B cells. The majority of the receptors were specific to signals deriving from either M1 or M2 macrophages, however, 14 receptors could recognize molecules from both M1 and M2 macrophages.

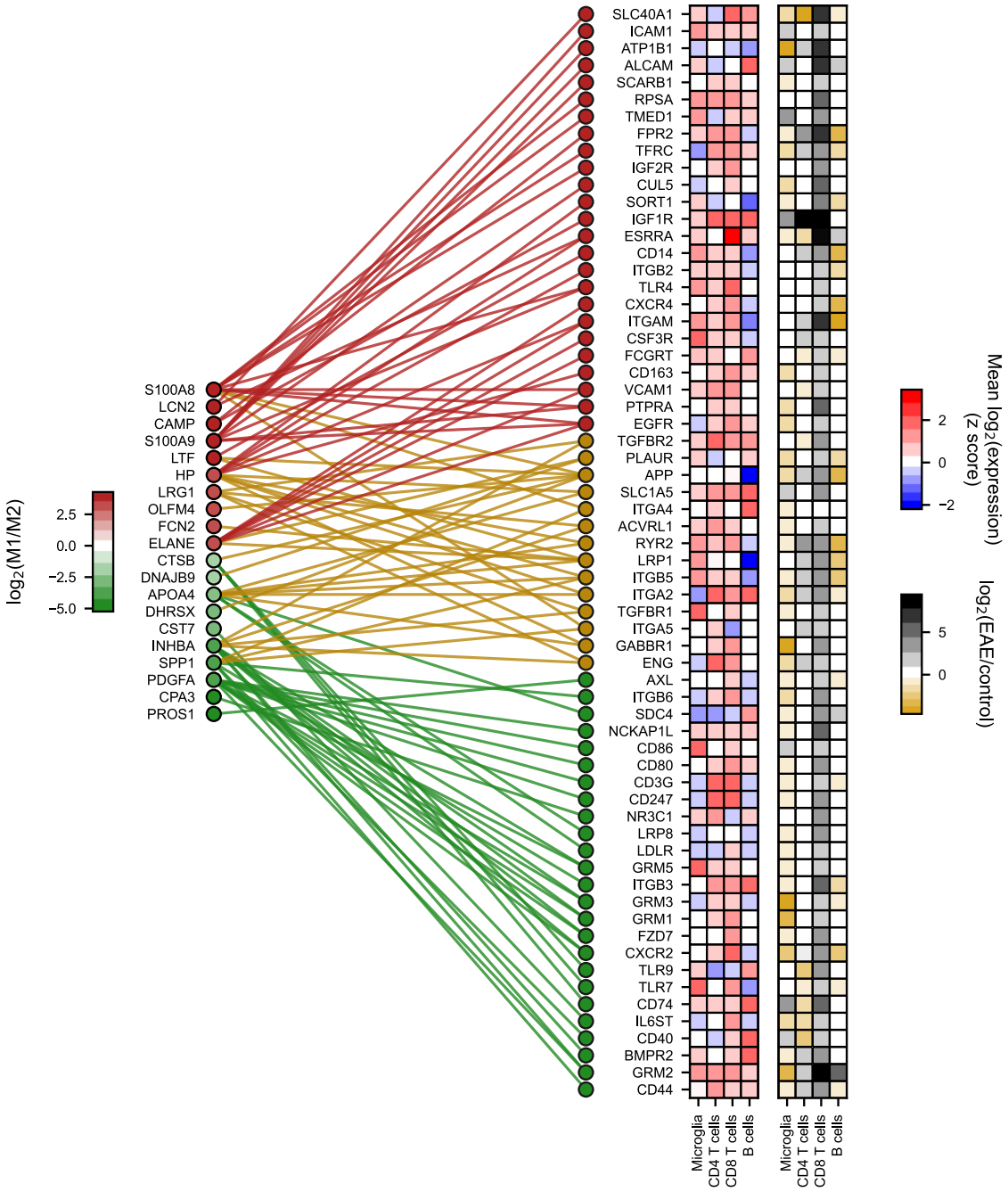

Figure 29: Specific M1 and M2 macrophage ligand-receptor interactions. Analysis of the 20 most differentially enriched ligands in M1 and M2 macrophages (left: M1 and M2 macrophage ligands with color-coded $\log_2$(M1/M2) differential expression) and their receptors (right). The edges indicate the ligand-receptor interactions. The color of the receptors and edges encode the ligand specificity (red: ligands from M1 macrophages, green: ligands from M2 macrophages, yellow: ligands from both M1 and M2 macrophages). Heatmaps indicate the standardized mean logarithmic protein expression in EAE (right, red/blue) and the logarithmic fold change between the protein abundance in EAE and healthy control (left, black/yellow).

Overall, T cells expressed the respective receptors most, indicating their capability of recognizing M1 and M2 macrophage ligands best (Figure 30). In particular, the receptors of M1 macrophages and M2 macrophage ligands were most abundant on CD4 T cells, whereas the receptors recognizing both ligands from M1 and M2 macrophages were highest abundant in CD8 T cells. Microglia showed the highest receptor abundance for ligands from M1 macrophages and lowest abundance for ligands from M2 macrophages.

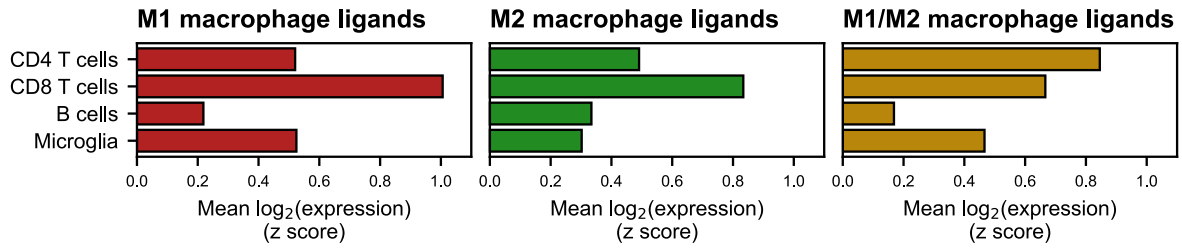

Figure 30: Mean receptor expression of immune cells. Mean logarithmic expression of the receptors for ligands from M1 and M2 macrophages (red and green) and from both M1 and M2 macrophages (orange).

The most differentially abundant ligand (in the M1 macrophage proteome compared to the M2 macrophage proteome) was S100A8. ligand-receptor analysis revealed a possible interaction with the surface proteins VCAM1, PTPRA, EGFR, TLR4, TFRL, IGF2R, RPSA and TMED1. Because S100A8 forms a heterodimer with S100A9, the ligand-receptor interactions of S100A8 and S100A9 partially overlapped (PTPRA, EGFR, TLR4).

The most abundant receptor in this analysis was the steroid hormone receptor ERR1 (ESRRA) in the CD8 T cell proteome which could recognize the neutrophil gelatinase-associated lipocalin (LCN2) and haptoglobin (HP) as ligands from M1 macrophages. Compared to CD8 T cells, the abundance of ESRRA in CD4 T cells was much lower.

Transforming growth factor beta receptor (TGFBR) was found to be expressed on microglia as well as B and T cells (TGFBR2 on all of these cells, TGFBR1 higher on microglia) in EAE. TGFBR1 and TGFBR2 could recognize ligands which were found both in the M1 (LRG1) and M2 macrophage proteome (INHBA).

4.2.10.2 M1 and M2 macrophage receptors

To better understand how M1 and M2 macrophages can receive extracellular signals, the distributions of receptor molecules in the M1 and M2 macrophage proteomes were analyzed. Therefore, proteins which are annotated as receptors according to the CellPhoneDB (Efremova *et al.*) and the Cell-Cell Interaction Database (Qiao *et al.*) were filtered (302, 307). Overall, 222 receptors could be detected in the M1 and M2 macrophage proteomes. 19 of these receptors were enriched in the M1 macrophage proteome ($\log_2(FC) > \log_2(1.5)$ and $q \leq 0.05$, Figure 31, **A** and **B**), whereas 35 receptors were enriched in the M2 macrophage proteome ($\log_2(FC) < \log_2(1.5)$ and $q \leq 0.05$). 168 receptors were not differentially distributed between the M1 and M2 proteomes ($|\log_2(FC)| < \log_2(1.5)$ or $q > 0.05$, Benjamini-Hochberg-adjusted *p* values from independent *t* statistics with homoscedasticity).

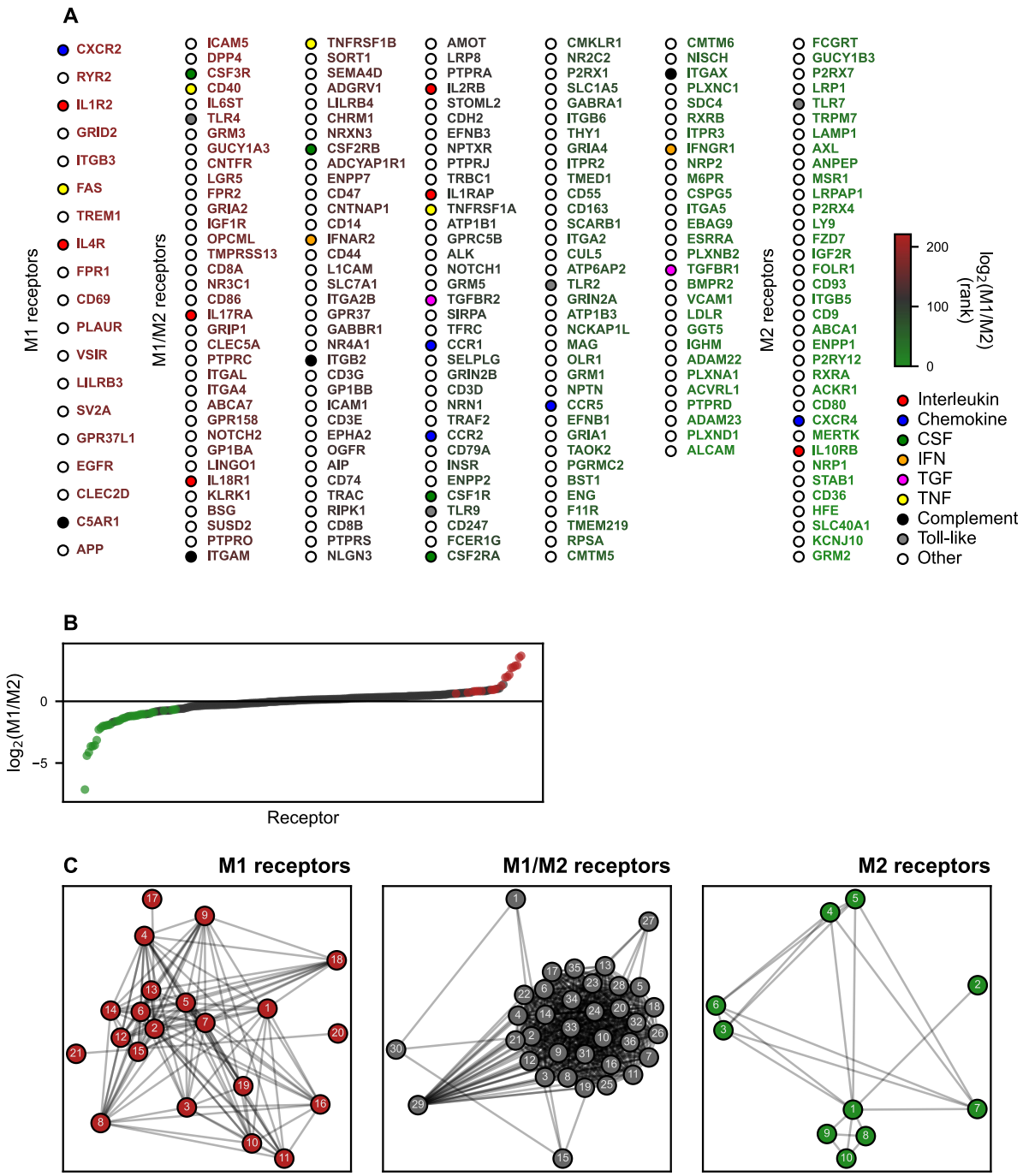

Figure 31: M1 and M2 macrophage receptors. A: Analysis of the differential protein abundance of receptors in the M1 and M2 proteomes. Different types of immune cell receptors are indicated by a colored dot. The logarithmic fold change (M1/M2 protein abundance) is color-coded. The annotation 'M1 receptors' and 'M2 receptors' is based on a FC- and *q* value-cutoff ($|\log_2(FC)| > \log_2(1.5)$ and $q \leq 0.05$). 'M1/M2 receptors' do not meet either of one or both criteria. **B**: Distribution of receptors in the M1 and M2 proteomes. Specific M1 and M2 receptors (based on FC and *q* value as described before) are colored in red (M1) and green (M2), respectively. **C**: Gene set enrichment analysis (GSEA, Reactome) of M1, M2 and M1/M2 receptors with subsequent weighted network analysis. The nodes represent gene sets, edges indicate if two nodes/gene sets share at least one gene/protein. The network's weight is based on the number of common genes. Gene sets were only considered as enriched if OR > 0 and q ≤ 0.05 with the odds ratio OR and the FDR-adjusted *p* value *q* deriving from Fisher's exact test. Ligands and receptors were identified according to the CellPhoneDB (Efremova *et al.*) and the Cell-Cell Interaction Database (Qiao *et al.*), respectively (302, 307) (CSF: colony-stimulating factor, IFN: interferon, TGF: transforming growth factor, TNF: tumor necrosis factor; **M1 macrophage receptors GSEA network**: 1: Adaptive Immune System, 2: Signal Transduction, 3: DAP12 interactions, 4: Hemostasis, 5: Innate Immune System, 6: Signaling by GPCR, 7: Immune System, 8: Response to elevated platelet cytosolic Ca^{2+}, 9: Platelet degranulation, 10: Cell surface interactions at the vascular wall, 11: L1CAM interactions, 12: GPCR ligand binding, 13: G alpha (i) signaling events, 14: Class A/1 (Rhodopsin-like receptors), 15: Peptide ligand-binding

receptors, 16: Signal transduction by L1, 17: FasL/ CD95L signaling, 18: Formyl peptide receptors bind formyl peptides and many other ligands, 19: Immunoregulatory interactions between a Lymphoid and a non-Lymphoid cell, 20: Toxicity of botulinum toxin type F (BoNT/F), 21: Toxicity of botulinum toxin type D (BoNT/D); **M1/M2 macrophage receptors GSEA network**: 1: G alpha (i) signaling events, 2: Signaling by GPCR, 3: FCERI mediated MAPK activation, 4: NCAM signaling for neurite out-growth, 5: Interleukin-3, 5 and GM-CSF signaling, 6: Signaling to ERKs, 7: Interleukin-2 signaling, 8: Signaling to RAS, 9: Interleukin receptor SHC signaling, 10: Signaling by Leptin, 11: Prolonged ERK activation events, 12: Frs2-mediated activation, 13: ARMS-mediated activation, 14: Signaling to p38 via RIT and RIN, 15: G alpha (q) signaling events, 16: FRS-mediated FGFR4 signaling, 17: FRS-mediated FGFR3 signaling, 18: FRS-mediated FGFR2 signaling, 19: FRS-mediated FGFR1 signaling, 20: IRS-mediated signaling, 21: MAPK family signaling cascades, 22: RAF/MAP kinase cascade, 23: GRB2 events in EGFR signaling, 24: SHC1 events in EGFR signaling, 25: SOS-mediated signaling, 26: SHC1 events in ERBB4 signaling, 27: Signaling by the B Cell Receptor (BCR), 28: Signaling by Insulin receptor, 29: EPH-Ephrin signaling, 30: GPCR ligand binding, 31: IGF1R signaling cascade, 32: IRS-related events triggered by IGF1R, 33: Signaling by Type 1 Insulin-like Growth Factor 1 Receptor (IGF1R), 34: Insulin receptor signaling cascade, 35: MAPK1/MAPK3 signaling, 36: Signaling by ERBB4; **M2 macrophage receptors GSEA network**: 1: Hemostasis, 2: GPCR ligand binding, 3: Vesicle-mediated transport, 4: Regulation of lipid metabolism by Peroxisome proliferator-activated receptor alpha (PPARa), 5: PPARa activates gene expression, 6: Binding and Uptake of Ligands by Scavenger Receptors, 7: Cross-presentation of particulate exogenous antigens (phagosomes), 8: Platelet homeostasis, 9: Platelet calcium homeostasis, 10: Elevation of cytosolic Ca^{2+} levels).

Overall, the M1 and M2 macrophage proteomes contained members of various receptor families. Among those, interleukin receptors were detected in both the M1 and M2 macrophage proteome. The interleukin receptors IL1R2 and IL4R were relatively enriched in M1 macrophages, whereas IL10RB was enriched in M2 macrophages. IL17RA and IL18R1, two receptors that can recognize pro-inflammatory cytokines IL-17 and IL-18, both showed a logarithmic M1/M2 fold change > 0 (IL17RA: $\log_2(FC) = 0.59$, $q = 0.23$; IL18R1: $\log_2(FC) = 0.47$, $q = 0.15$). IL1RAP and IL2RB, which bind the pro-inflammatory molecules IL-1 and IL-2, were equally enriched in M1 and M2 macrophages (IL1RAP: $\log_2(FC) = 0.15$, $q = 0.84$; IL2RB: $\log_2(FC) = 0.19$, $q = 0.69$). IL10RB was the only interleukin receptor that was significantly enriched in M2 macrophages ($\log_2(FC) = -2.29$, $q = 2.51 \times 10^{-4}$). Notably, IL-10, the ligand of the IL10RB, showed anti-inflammatory properties (314).

Furthermore, the M1 and M2 proteomes contained the chemokine receptors CCR1, CCR2, CCR5, CXCR2 and CXCR4. However, only CXCR2 and CXCR4 were differentially enriched in M1 (CXCR2: $\log_2(FC) = 3.69$, $q = 2.00 \times 10^{-6}$) and M2 macrophages ($\log_2(FC) = -2.02$, $q = 2.97 \times 10^{-2}$), respectively. CCR1, CCR2 and CCR5 showed no enrichment, neither in M1 nor M2 macrophages (CCR1: $\log_2(FC) = 0.11$, $q = 0.83$, CCR2: $\log_2(FC) = 0.05$, $q = 0.93$, CCR5: $\log_2(FC) = -0.26$, $q = 0.67$). The atypical chemokine receptor 1 ACKR1 was enriched in the M2 proteome ($\log_2(FC) = -1.94$, $q = 7.47 \times 10^{-4}$).

The alpha and beta subunit of the granulocyte-macrophage colony-stimulating factor receptor (GM-CSF/CSF2RA and CSF2RB) the macrophage colony-stimulating factor receptor (M-CSF/CSF1R) as well as the granulocyte colony-stimulating factor receptor (G-CSF/CSF3R) were expressed by macrophages. However, none of these receptors was significantly enriched in either of the proteomes.

From the interferon-alpha/beta receptor, which contains the 2 subunits IFNAR1 and IFNAR2, only subunit 2 (IFNAR2) was detected in the macrophage proteomes. Moreover, interferon gamma receptor 1 (IFNGR1) was detected. However, none of these receptors (subunits) were significantly enriched in either of the proteomes (IFNAR2: $\log_2(FC) = 0.35$, $q = 0.23$, IFNGR1: $\log_2(FC) = -0.40$, $q = 0.44$).

Likewise, transforming growth factor receptors were not enriched in either the M1 or the M2 macrophage proteome (TGFBR1: $\log_2(FC) = -0.63$, $q = 8.45 \times 10^{-2}$, TGFBR2: $\log_2(FC) = 0.13$, $q = 0.84$).

Within the tumor necrosis factor receptor superfamily, the Fas receptor (FAS) was highly enriched in the M1 macrophage proteome when compared to the M2 macrophage proteome ($\log_2(FC) = 2.72$, $q = 1.0 \times 10^{-6}$). Other members of the tumor necrosis factor receptor superfamily could be detected in

both the M1 and M2 macrophage proteomes (CD40, TNFRSF1A and TNFRSF1B). All of them showed a relative enrichment in the M1 macrophage proteome (FC > 0), however, none of them was significantly enriched (CD40: $\log_2(FC) = 0.92$, $q = 7.34 \times 10^{-2}$, TNFRSF1A: $\log_2(FC) = 0.15$, $q = 0.82$, TNFRSF1B: $\log_2(FC) = 0.43$, $q = 0.19$)

Moreover, we analyzed the expression of the macrophage-specific complement receptors CR3 and CR4 as well as the complement component 3a receptor 1 (C3AR1) and the complement component 5a receptor 1 (C5AR1/CD88). CR3 and CR4 are both members of the b2-integrin family. Both share the common b2 chain CD18 (ITGB2). In addition, CR3 is completed by CD11b (ITGAM), whereas CR4 functions together with CD11c (ITGAX), respectively (315). CR3 was higher enriched in M1 macrophages when compared to M2 macrophages, however the fold change was below the threshold of $\log_2(1.5)$ (ITGB2: $\log_2(FC) = 0.31$, $q = 1.17 \times 10^{-2}$; ITGAM: $\log_2(FC) = 0.44$, $q = 8.89 \times 10^{-3}$). In contrast, the abundance of ITGAX (as a part of CR4) was slightly higher in M2 macrophages ($\log_2(FC) = -0.34$, $q = 0.14$). The complement component 3a receptor 1 (C3AR1) was neither detected in the M1 macrophage proteome, nor in the M2 macrophage proteome. However, the complement component 5a receptor 1 (C5AR1) was more abundant in the M1 macrophage proteome ($\log_2(FC) = 0.70$, $q = 1.40 \times 10^{-2}$, Benjamini-Hochberg-adjusted *p* values from independent *t* statistics with homoscedasticity).

Next, we performed a gene set enrichment analysis (GSEA) of the M1, M2 and M1/M2 macrophage receptors (Figure 31, **C**). In the M1 macrophage proteome, 21 gene sets were enriched. Of those, 8 gene sets formed a tight module (2, 5, 6, 7, 12, 13, 14, 15). This cluster was comprised of gene sets associated with immune system-related G protein-coupled receptor signal transmission. Further, it encompassed gene sets pointing towards aspects of cell-cell-communication ('Immunoregulatory interactions between a Lymphoid and a non-Lymphoid cell'). In contrast, only 10 gene sets derived from the M2 macrophage-enriched receptor expression. These gene sets grouped in 3 clusters. The first cluster (gene sets 3 and 6) pointed towards an anti-inflammatory/tissue clearance function (e. g. 'Vesicle-mediated transport' and 'Binding and Uptake of Ligands by Scavenger Receptors'). The second cluster (gene sets 4 and 5) was associated with lipid uptake and lipid-induced signaling ('Regulation of lipid metabolism by Peroxisome proliferator-activated receptor alpha (PPARa)' and 'PPARa activates gene expression'). The third cluster (gene sets 1, 8, 9 and 10) was pointing towards homeostasis maintaining. Furthermore, the M2 macrophage receptor profile exhibited properties of antigen presentation ('Cross-presentation of particulate exogenous antigens (phagosomes)'). Gen sets which were enriched in the share of receptors that were equally abundant in M1 and M2 macrophages (M1/M2 receptors) reflected the versatility of different receptors types in both proteomes (e. g. interleukin signaling, CSF signaling). In addition, the gene sets encompassed genes/proteins which provides insights into the intracellular signal transduction. A large fraction of gene sets was associated with MAP/RAS, ERK, FRC signaling.

Next, we aimed to investigate how ligands from other immune cells could be recognized by macrophages. Therefore, we analyzed potential ligand-receptor interactions between immune receptors (interleukin, chemokine, CSF, interferon, TGF, TNF and complement receptors) in the M1 and M2 macrophage proteomes and their respective ligands detected in CD4 and CD8 T cells, B cells and microglia (Figure 32). Overall, 51 ligands could be identified in the proteomes of CD4 T cells, CD8 T cells, B cells and microglia for 28 immune cell receptors in M1 and M2 macrophages. The majority of

ligands (n = 31) was specific to receptors which were characterized by FC > 0, indicating an enrichment in the M1 macrophage proteome. 19 ligands could bind receptors which were enriched in both the M1 macrophage and M2 macrophage proteome. In contrast, one ligand (ARL8B) was able to bind only one receptor that was enriched in M2 macrophages (TGFBR1).

Overall, CD8 T cells showed the highest mean fold change of the EAE versus healthy control protein expression of all ligands showed in Figure 32 (CD8 T cells: mean $\log_2$(FC) = 3.24, CD4 T cells: mean $\log_2$(FC) = 0.63, B cells: mean $\log_2$(FC) = -0.77, microglia: mean $\log_2$(FC) = -0.58). Interleukin-16 (IL16) was among the ligands with the highest fold change in CD8 T cells ($\log_2$(FC) = 7.59, q = 8.50 x 10^{-5}). It was also highly abundant in B cells but without any significant difference between EAE and healthy control B cells. Interleukin-1a, interleukin-1b and interleukin-18 (IL1A, IL1B and IL18) were highly abundant in the microglia proteome compared to CD4 T cells, CD8 T cells and B cells. All three ligands were higher abundant in EAE compared to healthy control (IL1A: $\log_2$(FC) = 1.79, q = 8.83 x 10^{-2}; IL1B: $\log_2$(FC) = 2.91, q = 2.87 x 10^{-2}, IL18: $\log_2$(FC) = 1.82, q = 3.82 x 10^{-2}). Besides in microglia, interleukin-1a, interleukin-1b and interleukin-18 were detected with a higher abundance in CD4 and CD8 T cells compared to B cells. Interleukin-14 (TXLNA/IL14) was almost equally abundant in CD4 T cells, CD8 T cells and microglia. In CD8 T cells it was highly enriched in EAE when compared to healthy control ($\log_2$(FC) = 4.34, q = 3.50 x 10^{-5}). Likewise, the fold change of interleukin-1b was significantly differentially abundant in EAE versus healthy control in CD8 T cells ($\log_2$(FC) = 3.06, q = 9.12 x 10^{-3}). All other detected interleukins (interleukin-1a, interleukin-14, interleukin-16, interleukin-18) were unchanged in CD4 T cells and B cells. Notably, all detected interleukins in lymphocytes and microglia could bind to both receptors predominantly expressed in M1 macrophages (FC > 0) as well as M2 macrophages (FC < 0). Interleukin-1 receptor antagonist (IL1RN) was mainly detected in microglia and less abundant in EAE when compared to healthy control.

Besides interleukins, C-C motif, C-X-C motif and C-X3-C motif chemokine ligands were detected in the immune cell proteomes as possible ligands of M1 and M2 macrophage receptors. CCL4 was detected with a higher abundance in T cells compared to B cells and microglia. CCL5 was detected in both T and B cells with comparable amounts. Likewise, CXCL4 (PF4) was highly abundant in lymphocytes when compared to microglia. In contrast, microglia showed a higher protein level of CXCL4 when compared to lymphocytes. When compared to healthy control, the protein level of CCL4 was elevated in EAE in CD8 T cells ($\log_2$(FC) = 2.77, q = 1.20 x 10^{-3}) and reduced in microglia ($\log_2$(FC) = -1.37, q = 5.26 x 10^{-2}). Likewise, the CCL5 protein amount in EAE in CD8 T cells was higher when compared to healthy control ($\log_2$(FC) = 1.32, q = 5.12 x 10^{-2}), whereas in microglia it was diminished ($\log_2$(FC) = -1.05, q = 6.42 x 10^{-2}). CXCL4 (PF4) was higher abundant in lymphocytes than in microglia. It showed a lower abundance in B cells from EAE compared to the healthy control ($\log_2$(FC) = -1.31, q = 6.53 x 10^{-3}). In contrast, CX3CL1 showed the highest protein amount in microglia and was lower abundant in EAE compared to healthy control ($\log_2$(FC) = -2.03, q = 5.26 x 10^{-2}). Furthermore, it was elevated in EAE in CD8 T cells, however, with a low protein amount in both EAE and healthy control ($\log_2$(FC) = 2.34, q = 2.37 x 10^{-4}).

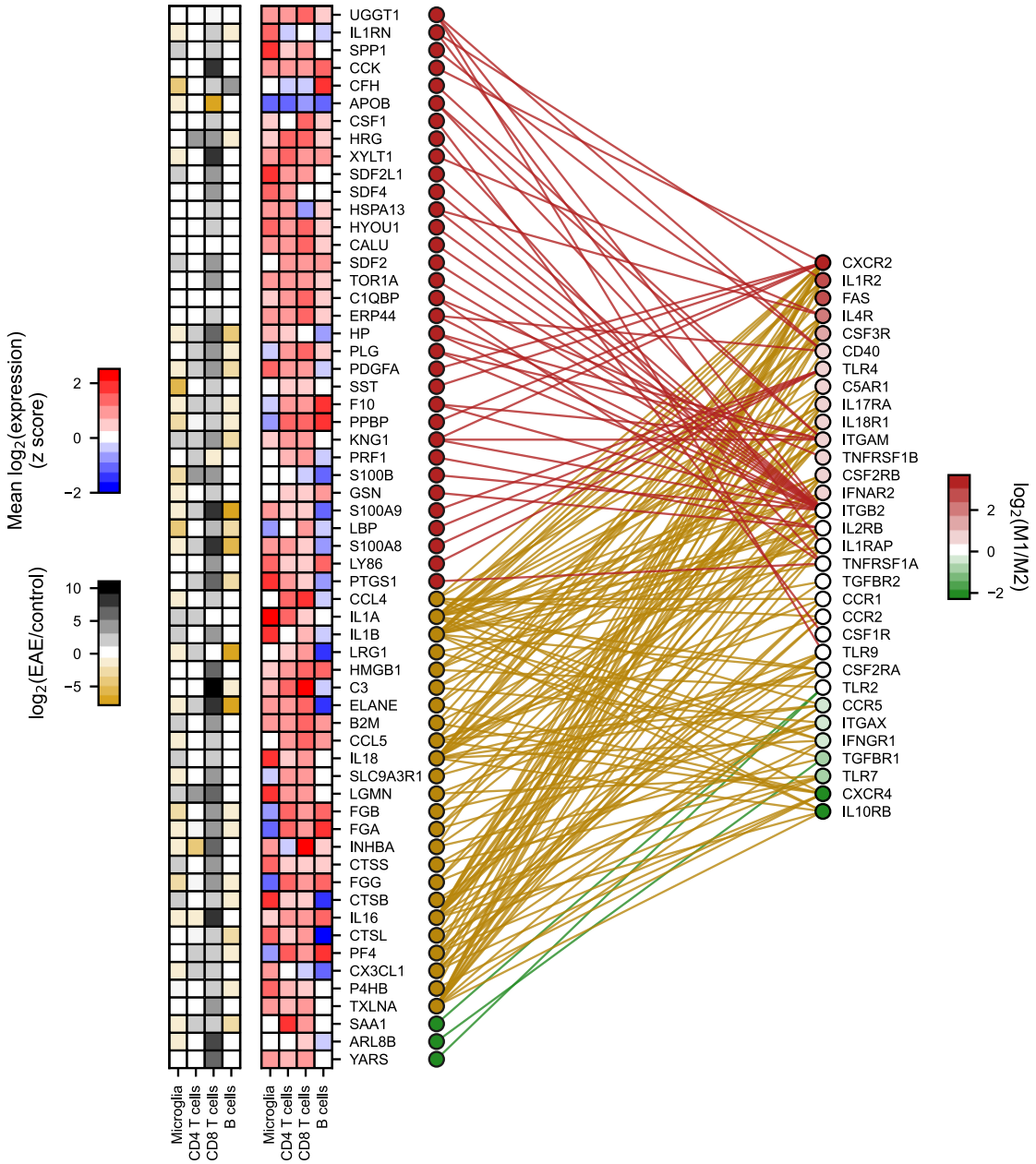

Figure 32: Ligand-receptor interaction between ligands from CD4 T cells, CD8 T cells, B cells and microglia and M1 and M2 macrophage immune receptors. Interleukin, chemokine, CSF, interferon, TGF, TNF and complement receptors which were detected in the M1 and M2 macrophage proteome (right). Their fold change (M1/M2) is color-coded. The respective ligands are shown on the left, ligand-receptor interactions are indicated by connecting lines. The color of the ligand and connecting line encodes the M1- and M2-binding specificity (red: ligand only binds receptors with FC > 0, green: ligand only binds receptors with FC < 0, yellow: receptor binds both receptors with FC > 0 and receptors with FC < 0. Heatmaps indicate the standardized mean logarithmic protein expression in EAE (right, red/blue) and the logarithmic fold change between the protein abundance in EAE and healthy control (left, black/yellow).

4.3 Differential protein expression in neuronal mitochondria from EAE and healthy control

Reactive oxygen species (ROS) and reactive nitrogen species (RNS) are important effector molecules of the inflammatory response of (tissue) macrophages (316). Exposure of axons to oxidative stress can occur during the disease course of neuroinflammatory diseases and is discussed to alter axonal mitochondrial function (317). To further investigate the molecular mechanism of mitochondrial dysfunction in neuroinflammation, we assessed proteomic changes during the disease course of EAE.

We isolated mitochondria from EAE and healthy controls and analyzed them by quantitative mass spectrometry (in collaboration with Dr. Tai and Prof. Dr. Lichtenthaler). In total, 3356 proteins could be detected (Figure 33, **A**). 804 of those (23.96 %) were annotated as mitochondrial proteins as defined by the MitoCarta2.0 database which encompasses 1158 mitochondrial proteins (303). Thus, 69.43 % of the mitochondrial proteome (802 out of 1158 proteins) was covered by this analysis. The abundance of mitochondrial proteins was higher compared to non-mitochondrial proteins (Figure 33, **B**). The analysis of the distribution of the logarithmic expression levels of the proteins by histogram and quantile-quantile analysis revealed normally distributed protein amounts (Figure 33, **C** and **D**).

To analyze the degree of the overall sample/proteome similarity, a principal component analysis (PCA) was performed (Figure 33, **E**). The majority of the variance could be explained by principal component 1 (PC1, 35 %), principal component 2 (PC2) could explain 20 % of the variance. Furthermore, PC1 segregated samples which derived from EAE or healthy controls. In addition, EAE and control samples could be distinguished by correlation analysis. Furthermore, neither the correlation analysis nor the principal component analysis showed any evidence for a sample to be an outlier (Supplement Figure 12).

Next, the differentially enriched proteins were assessed by calculating the fold change of the abundance levels of the proteins between both experimental groups (EAE and healthy control) and subsequent statistical testing. The threshold value of the fold change was set to $\log_2(1.5)$. Besides the subjective biological meaningfulness, this threshold did not undermine controlling the false discovery rate evaluated by statistical testing (Figure 33, **F** and **G**). Under this assumption, 595 proteins were differentially abundant (Figure 33, **H**). 497 different proteins were higher abundant in the neuronal mitochondrial proteome from EAE, 98 proteins were lower abundant in EAE compared to healthy controls.

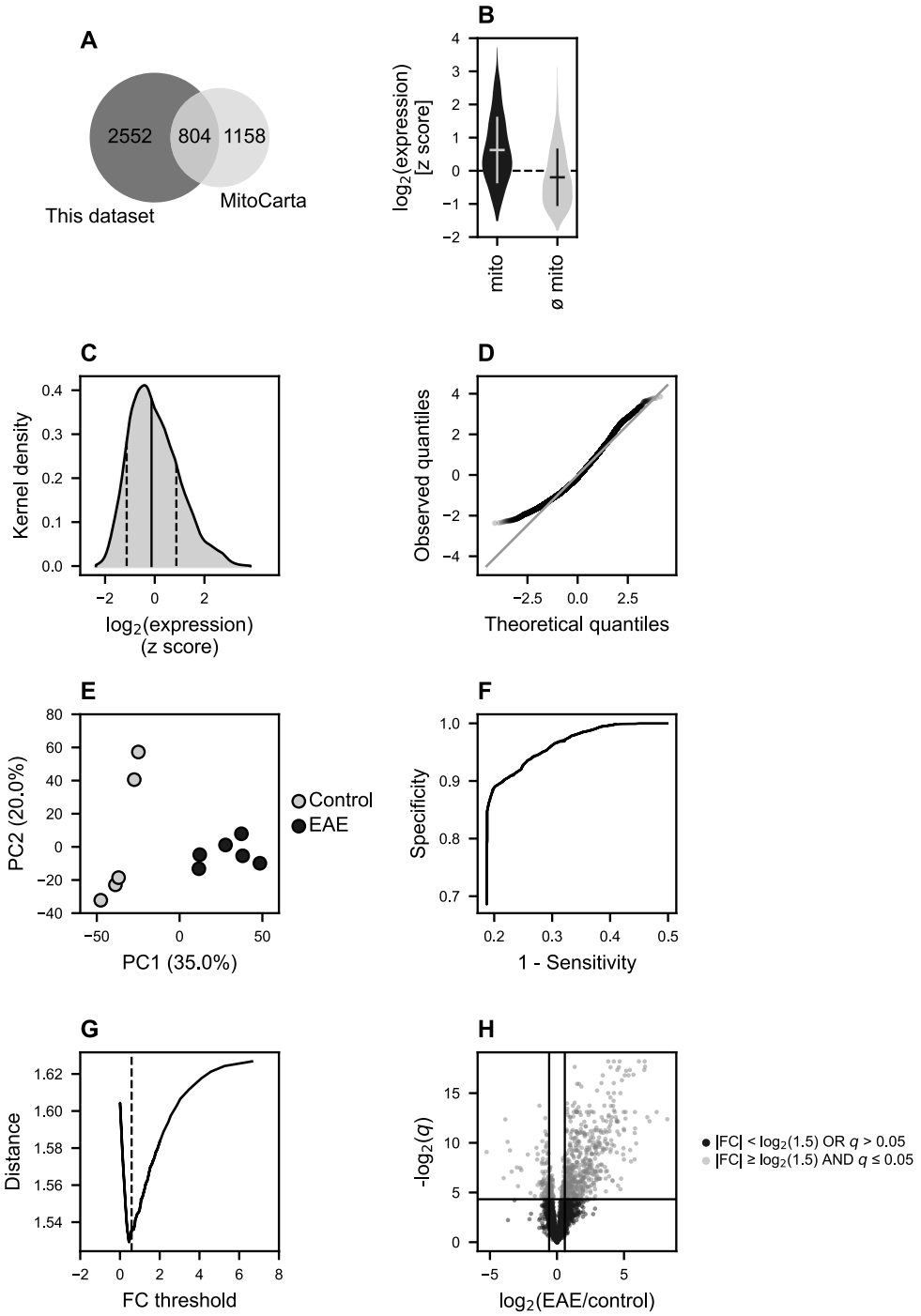

Figure 33: Characterization of the neuronal mitochondrial proteomes from EAE and healthy control. A: Number of mitochondrial proteins identified in the neuronal mitochondrial proteome. A protein was annotated as "mitochondrial" according to MitoCarta2.0 (303). **B**: Analysis of the abundance of mitochondrial and non-mitochondrial proteins in the mitochondrial proteomes of neurons from EAE and healthy controls. Violin plot with kernel density estimates, horizontal lines display mean values, vertical lines indicate mean ± SD. **C**: Distribution of the standardized logarithmic expression values (LFQ) of all proteins in all samples (n = 36,916). Vertical solid line displays the mean value, dashed lines indicate the upper and lower SD around the mean. **D**: Quantile-quantile plot of the standardized logarithmic expression values of all proteins in all samples (n = 36,916). **E**: Principal component analysis (PCA) of all samples from EAE and healthy controls. The first two principal components (PC1 and PC2) were visualized and the respective variance which they explain is shown. **F**: Correlation between specificity and sensitivity for different fold change thresholds for the analysis of the differential protein levels in mitochondria from EAE and healthy control neurons. Fold change was defined as the difference in mean logarithmic protein expression levels. Specificity was calculated as the fraction of identified proteins above a certain fold change threshold that met the criteria $q \leq 0.05$ (FDR-adjusted p value from t statistics for independent samples with homoscedasticity). Sensitivity was defined as the fraction of proteins with $q \leq 0.05$ whose fold change exceeded the given threshold. **G**: Euclidean distance to

P(x|y) in the Cartesian space of **F**, where x is the minimum value of 1-sensitivity and y is the maximum of the specificity, calculated for fold change thresholds reaching from 0 to 5 (dashed line: fold change threshold = $\log_2(1.5) = 0.58$). **H**: Logarithmic fold change between EAE and healthy control of all detected proteins and respective negative logarithmic *q* values (Benjamini-Hochberg-adjusted *p* values from independent *t* statistics with homoscedasticity). Vertical lines indicate fold change thresholds (-1.5 and 1.5), horizontal line indicate *q* value threshold ($q \leq 0.05$).

4.3.1 Gene set enrichment analysis coupled to network analysis of the neuronal mitochondrial proteome

To investigate alterations in the molecular signature in the proteome of neuronal mitochondria in EAE, we performed gene set enrichment analysis with subsequent network analysis (*NezzworGS* algorithm). This revealed an enrichment of 28 gene sets in EAE or healthy control neuronal mitochondria (Figure 34). 14 gene sets were enriched in the healthy control neuronal mitochondrial proteome (normalized enrichment score < 0), whereas 14 gene sets were enriched in EAE neuronal mitochondria (normalized enrichment score > 0). Overall, the mean protein expression of proteins underlying gene sets which were enriched in the proteome of neuronal mitochondrial from the healthy control was lower compared to the mean protein expression of proteins from neuronal mitochondria from EAE. Gene sets enriched in the mitochondrial proteome in EAE were represented in 3 modules in the network analysis (modules 1, 3 and 5, Supplement Figure 13). These modules were comprised of gene sets related to (mitochondrial) translation (module 3) and signal transduction as well as immune response (module 5). The gene set “Peroxisomal protein import” was not connected to any of the other nodes (module 1). Gene sets enriched in the mitochondrial proteome of healthy controls (modules 2 and 4) were mostly related to energy metabolism.

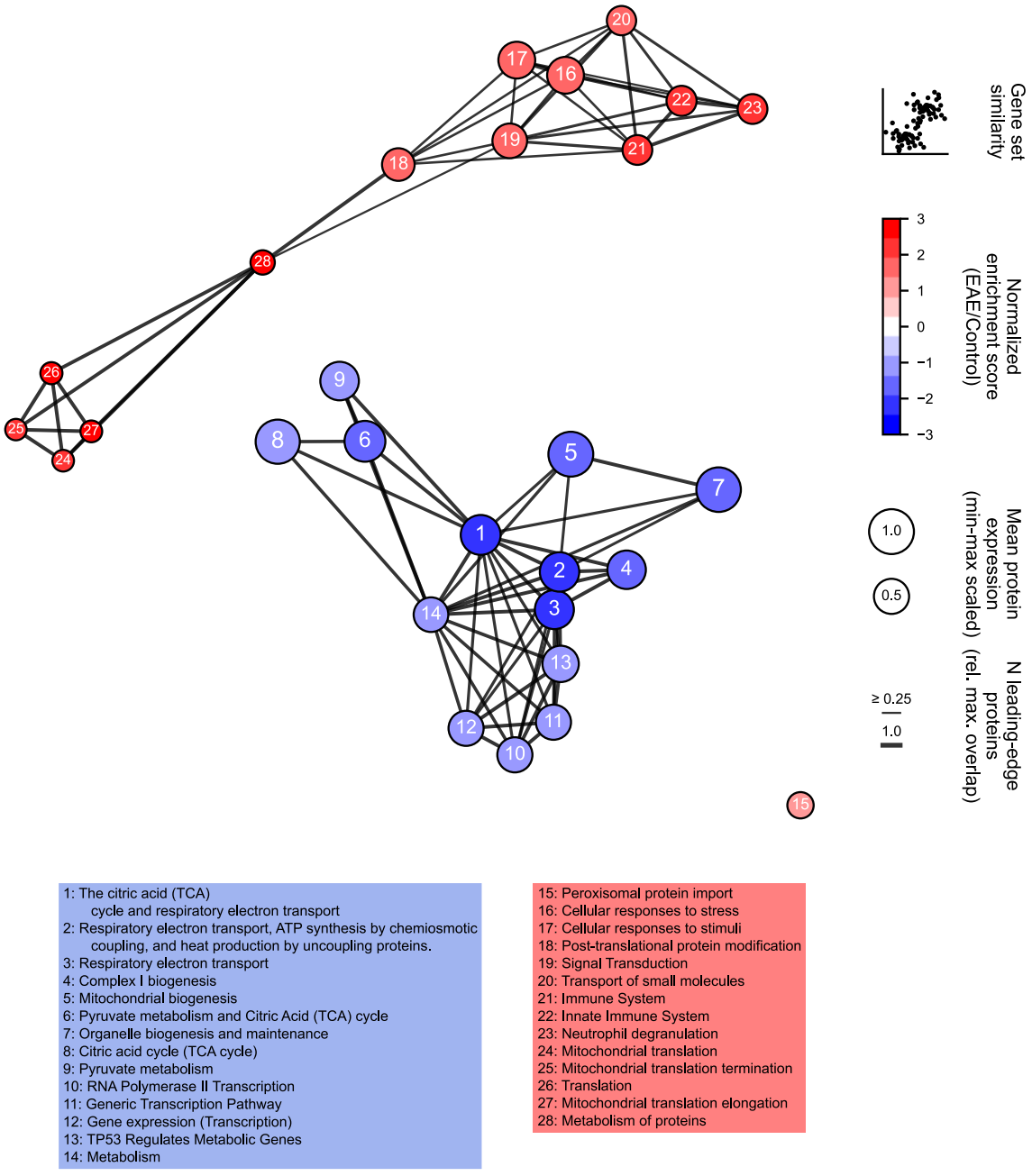

Figure 34: Gene set enrichment analysis (Reactome) of the neuronal mitochondria proteome in EAE and healthy control. Mitochondrial proteins (according to MitoCarta2.0) which were enriched ($|FC| > 1.5$ and $q \leq 0.05$) were subjected to *NezzworGS* analysis. Nodes display gene sets and edges indicate the number of leading-edge proteins which two gene sets have in common. The area of the node encodes the mean protein expression of the proteins assigned to the respective gene set. The color of the node displays the normalized enrichment score. The spatial distribution of the nodes encodes the similarity of gene sets. The thickness of edges represents the fraction of leading-edge proteins two gene sets have in common (the highest fraction of the two gene sets was taken into account).

The node/gene set with the highest degree of centrality and gene set size in this cluster encompassed proteins involved in the citric acid cycle and respiratory electron transport (Supplement Figure 14, Figure 34). Other linked gene sets were e. g. “Respiratory Electron Transport, ATP Synthesis by Chemiosmotic Coupling and Heat Production by Uncoupling Proteins”, “Respiratory Electron Transport”, “Pyruvate Metabolism and Citric Acid TCA Cycle” and “Citric Acid Cycle TCA Cycle”. To further elucidate the relationship between the gene sets associated with mitochondrial energy

metabolism we performed a gene set hierarchy analysis (Supplement Figure 15). This revealed 4 gene sets with highest hierarchy enriched in both the EAE and healthy control neuronal mitochondria proteome. In the healthy control neuronal mitochondria proteome, 2 out of 4 were related to energy metabolism ("The citric acid (TCA) cycle and respiratory electron transport" and "Pyruvate metabolism and Citric Acid (TCA) cycle"). The analysis of the child nodes revealed that proteins involved in pyruvate metabolism/citric acid cycle and, separately, respiratory chain were enriched in healthy neuronal mitochondria when compared to EAE, thus showing a global downregulation of the mitochondria energy metabolism in EAE.

To further validate the findings derived from gene set enrichment analysis, we analyzed the protein expression levels of the proteins underlying the respective gene sets which were previously identified. This revealed that the fold change of the expression levels between the neuronal mitochondrial proteome of EAE and the neuronal mitochondrial proteome of healthy control was low (Figure 35). However, there was a difference in the absolute expression levels of the proteins with respect to their assignment to the respective gene set. Proteins assigned to gene sets which were enriched in the control neuronal mitochondrial proteome were more abundant ($M_{expression\ (z\ score)}$ = 1.19) compared to proteins assigned to gene sets enriched in the EAE neuronal mitochondrial proteome ($M_{expression\ (z\ score)}$ = 0.66). Members of the gene set "Citric Acid Cycle TCA Cycle" showed the highest mean standardized expression level (2.15).

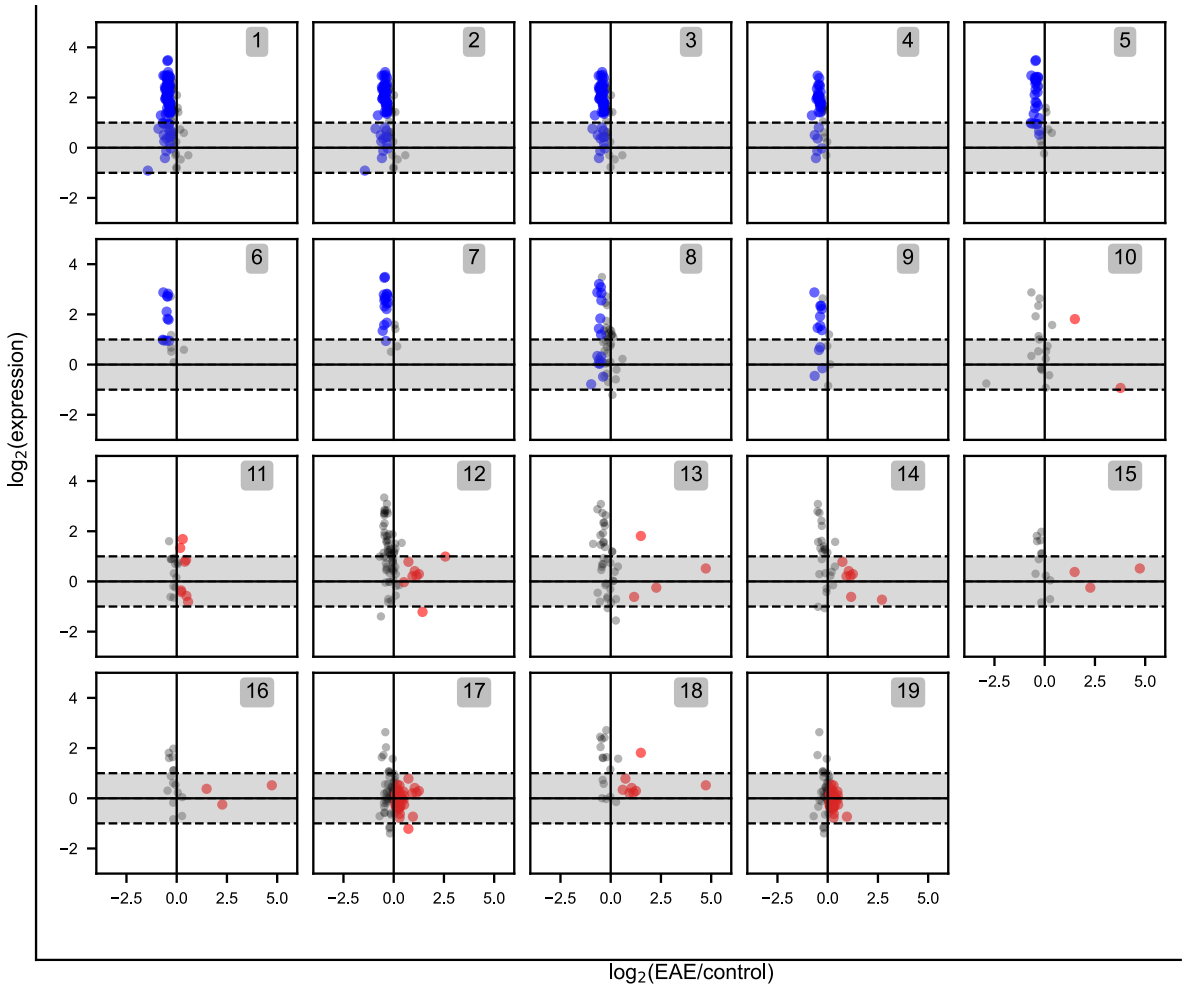

Figure 35: Expression analysis of proteins underlying the enriched gene sets from gene set enrichment analysis based on differentially expressed proteins in neuronal mitochondria from EAE and healthy control. Logarithmic fold change (EAE/control) and mean logarithmic standardized expression values for each protein are shown. Proteins which were identified as leading-edge proteins were color-coded (red: FC > 0, blue: FC < 0). Vertical lines indicate FC = 0, the horizontal lines mark the upper and lower SD (1: The citric acid (TCA) cycle and respiratory electron transport, 2: Respiratory electron transport, ATP synthesis by chemiosmotic coupling, and heat production by uncoupling proteins., 3: Respiratory electron transport, 4: Complex I biogenesis, 5: Mitochondrial biogenesis, 6: Pyruvate metabolism and Citric Acid (TCA) cycle, 7: Organelle biogenesis and maintenance, 8: Citric acid cycle (TCA cycle), 9: Pyruvate metabolism, 10: RNA Polymerase II Transcription, 11: Generic Transcription Pathway, 12: Gene expression (Transcription), 13: TP53 Regulates Metabolic Genes, 14: Metabolism, 15: Peroxisomal protein import, 16: Cellular responses to stress, 17: Cellular responses to stimuli, 18: Post-translational protein modification, 19: Signal Transduction, 20: Transport of small molecules, 21: Immune System, 22: Innate Immune System, 23: Neutrophil degranulation, 24: Mitochondrial translation, 25: Mitochondrial translation termination, 26: Translation, 27: Mitochondrial translation elongation, 28: Metabolism of proteins, $n_{EAE} = 6$, $n_{control} = 5$).

With the exception of 3 proteins (SUCLG2, SDHC and IDH2) all members of the gene set “Citric Acid Cycle TCA Cycle“ showed a negative logarithmic fold change, indicating their enrichment in healthy control neuronal mitochondria compared to EAE (Figure 36).

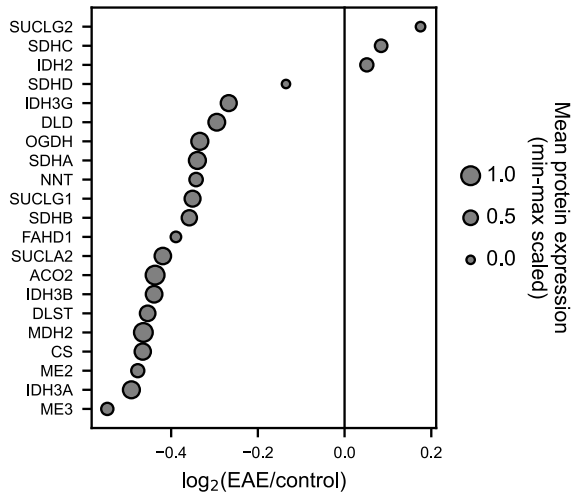

Figure 36: Differential abundance of proteins assigned to the gene set 'Citric Acid Cycle TCA Cycle'. Logarithmic fold change (EAE/control) of the expression level between neuronal mitochondria from EAE and healthy control. The area of the dot represents the min-max scaled mean protein expression (n_{EAE} = 6, $n_{control}$ = 5).

To validate this finding, we performed histological analysis of the abundance of IDH3 and MDH2 (lower abundant in EAE compared to healthy control in our proteomics screen) as well as IDH2 (higher abundant in EAE, Figure 37, experiment performed by Dr. Tai). IDH3A and MDH2 showed a more than 50 % reduction of the normalized fluorescence intensity, indicating a lower protein abundance in EAE when compared to healthy control. In contrast, IDH2 showed a slight increase in normalized fluorescence intensity, indicating an increase in the protein amount in EAE. These findings were in line with the results obtained from the proteomic analysis and highlight a mitochondrial energy deficit in EAE.

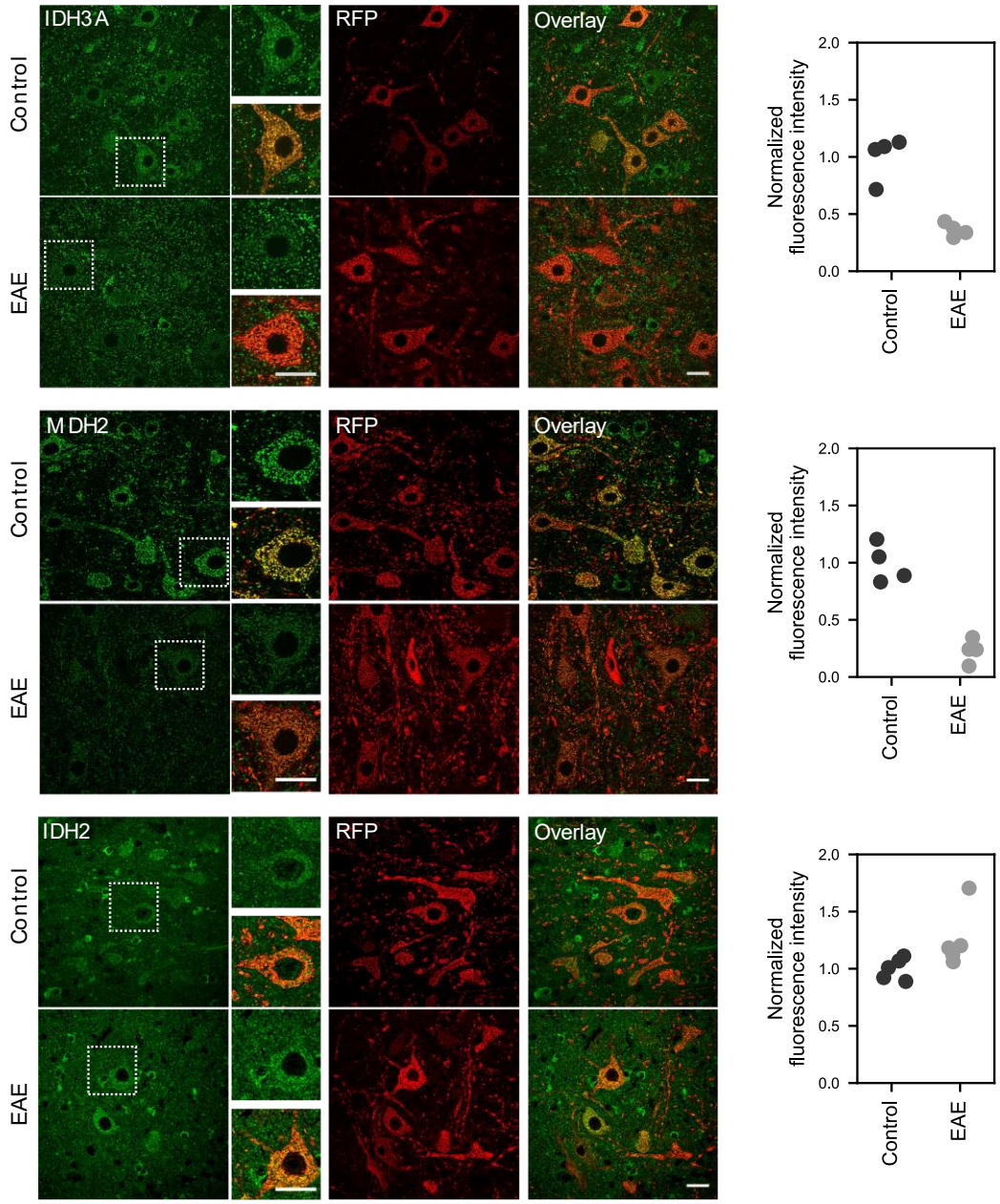

Figure 37: Histological analysis of IDH3, MDH2 and IDH2 expression in neuronal mitochondria in EAE and healthy controls (data from Tai *et al.*). Confocal microscopy images from histological staining of the mitochondrial proteins IDH3, MDH2 and IDH2 (green channel). Tissue was obtained from EAE and healthy controls of Thy1-mitoRFP mice (red channel: transgenic labeling of mitochondria). Normalized fluorescence intensities (per individual mouse) were measured to compare protein abundance between EAE and healthy controls. Data taken from Tai *et al.* (318).

Next, we aimed to understand how the expression of these proteins is altered at a later time point of the disease course, eventually mimicking the remission phase of multiple sclerosis. Thus, we analyzed the proteomes of neuronal mitochondrial at a later time point during the disease course (remission). We observed a clear distinction between the proteomes from the relapse phase (EAE onset + 2 d) and the remission phase (EAE onset + 22 d, Supplement Figure 16). Analysis of the overall differential protein abundance at relapse and remission revealed a reduction of the fold change (EAE versus healthy control) at remission for proteins assigned to gene sets that were downregulated at the relapse phase (Figure 38). This indicates that in the downregulation of mitochondrial energy metabolism dominates the initial phase of EAE and resolves during the recovery phase of the disease.

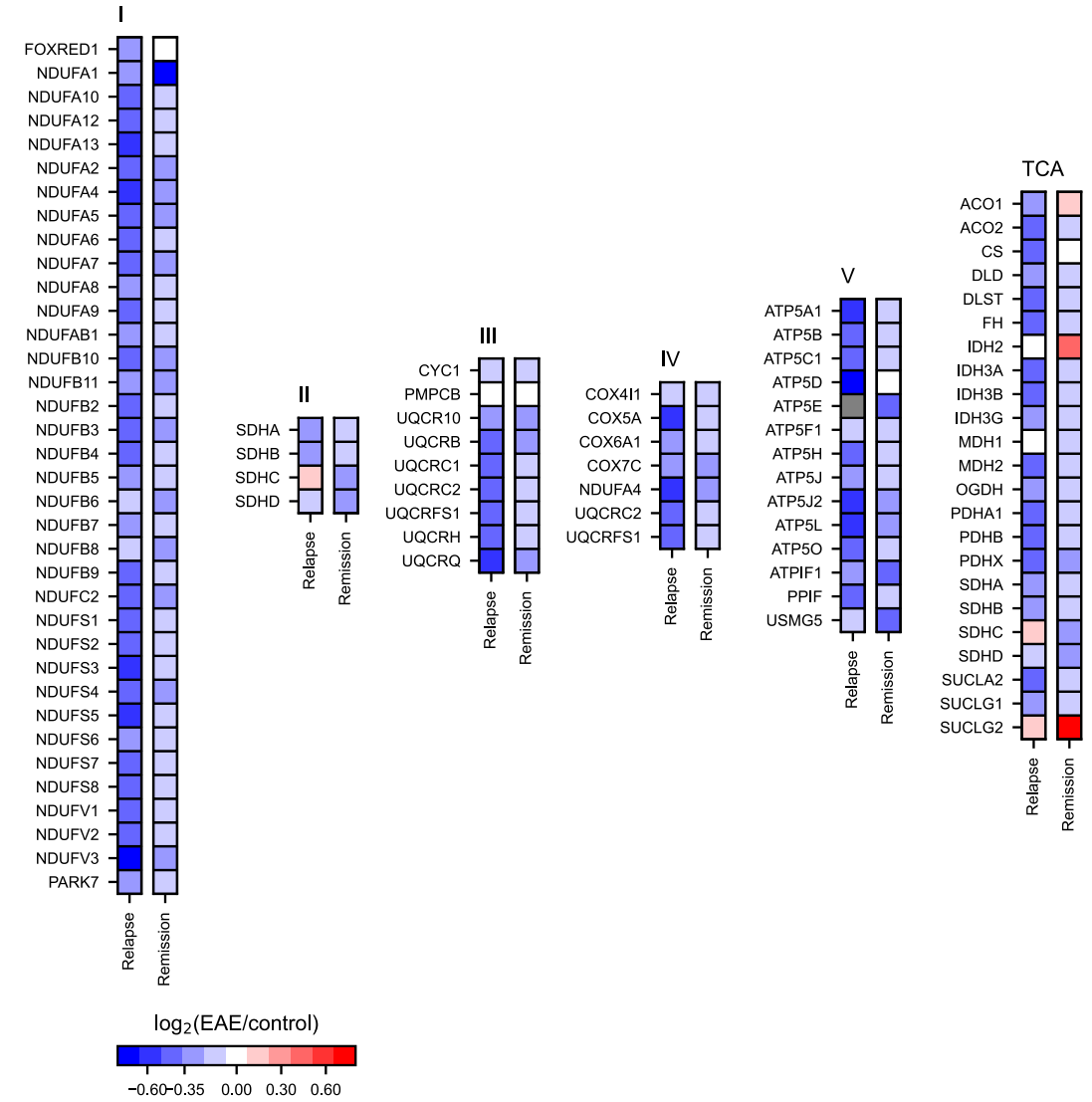

Figure 38: Logarithmic fold change of electron transport chain and citric acid cycle proteins at EAE relapse and remission. Proteins were selected from the neuronal mitochondrial proteomes from either the relapse or remission phase according to the Kyoto Encyclopedia of Genes and Genomes (KEGG) database and their fold changes (EAE/control) were calculated ($n_{EAE\text{-}relapse}$ = 6, $n_{control\text{-}relapse}$ = 5, $n_{EAE\text{-}remission}$ = 4, $n_{control\text{-}remission}$ = 5, grey: not detected).

5 Discussion

In this study I performed a large-scale proteomics screen, complemented by transcriptomic analyses and followed by computational analyses to elucidate the molecular signatures and intercellular communication pathways of mononuclear phagocytes as well as immune cells and CNS cells in experimental autoimmune encephalomyelitis (EAE), an animal model of multiple sclerosis. To address this, I used a transgenic mouse model that expressed fluorescent proteins under a *Nos2* (iNOS) and *Arg1* (Arginase-1) promoter which enabled us to identify and sort M1 (M^{iNOS}) and M2 ($M^{Arginase\text{-}1}$) macrophages at an early (onset + 1 d) and late (onset + 4/5 d) time point during the disease course of EAE and analyze their proteomes and transcriptomes with mass spectrometry and next-generation sequencing, respectively. Furthermore, we measured proteomic alterations in neuronal mitochondria in the context of EAE. To allow for refined computational analysis of the macrophage and mitochondria proteomics data sets I further designed a novel analytical tool, *Nezzworker*, which combines gene set enrichment analysis (*NezzworGS*) and functional protein-protein interaction analysis (*FUPPINA*) with network analysis.

5.1 Mononuclear phagocytes in CNS autoimmunity

The concept of pro-inflammatory, so-called classically activated macrophages (M1) and anti-inflammatory, alternatively activated macrophages (M2), has arisen over the past decades. It alludes to the T_h1/T_h2 paradigm of T cells (319, 320). However, there is strong evidence that the concepts of M1/M2 and T_h1/T_h2 are not only terminologically related but share a functional analogy in terms of mediating pro-inflammatory or anti-inflammatory immune cell activation. IFN-γ, which is secreted by T_h1 cells, can induce macrophage activation and thereby promote a pro-inflammatory phenotype (M1). In contrast, IL-4, IL-5 and IL-10, which are cytokines secreted by T_h2 cells, can dampen macrophage activation and, thus, play a major role in the emergence of an anti-inflammatory phenotype of macrophages (M2) (320, 321). A central metabolic hub in the polarization of macrophages is L-arginine. Depending on the extracellular stimuli (from T cells), macrophages induce a distinct metabolic pathway to synthesize either nitric oxide (NO), an important effector molecule for host defense, or L-ornithine and urea (322). The production of these molecules depends on their common substrate L-arginine and the execution of specialized intracellular programs which in the end result in the expression of inducible nitric oxide synthase (iNOS) after IFN-γ stimulation or Arginase-1 (Arg-1) resulting from stimulation with IL-4, IL-5 and IL-10 (320). Notably, already in the early 1990s, NO had been discussed not only to play a role in killing pathogens but also in autoimmune disorders (323). NO was found at higher concentration in MS lesions. Furthermore, indirect evidence of an excessive NO production in individuals suffering from MS exist since they showed higher levels of the NO oxidation products nitrate and nitrite in body fluids (324–330). Nitric oxide was even discussed as a disease activity marker (325, 326). Moreover, NO and reactive oxygen species in general are believed to be a major cause of oligodendrocyte dysfunction and demyelination, axonal pathology and the disruption of the blood-brain barrier (331, 332). This suggests that NO-producing macrophages play a major role in MS. However, anti-NO or anti-iNOS trials have not been successful so far, most likely because of the additional immunomodulatory effects that accompany the detrimental effects of NO (331). In contrast to the apparent toxic effect of NO from M1 macrophages, there is no clearly defined metabolite that

could explain the anti-inflammatory effect of M2 macrophages. L-ornithine and urea, which are the products of the reaction catalyzed by arginase-1, can rather be seen as the result of a compensatory mechanism to reduce the toxic effect of M1 macrophages. Through the conversion of L-arginine to L-ornithine and urea, the substrate to produce NO is depleted and, thereby, the toxic and pro-inflammatory function of M1 macrophages is attenuated (333). Taken together, our transgenic model that utilized genetically encoded fluorescent marker proteins to enable the detection of iNOS- and L-arginase-expressing cells, combined with further antibody-based immunophenotyping of extracellular epitopes is a powerful tool to monitor the polarization phenotype of macrophages.

Macrophages play a key role in autoimmunity and can be detected in tissue samples or body fluids of inflamed organs. It was shown that the M1/M2 ratio can correlate with disease severity and, moreover, cell transfer experiments indicated that M2 macrophages are associated with the amelioration of an autoimmune disease model (334). In multiple sclerosis macrophages, in addition to other myeloid cells such as microglia, are considered as the immediate effector cell population because of their capability to phagocytose and secrete reactive oxygen species (335, 336). Indeed, studies in EAE have proven macrophages' indispensability in disease development. When myeloid cells or, in particular, CX_3CR1^+ cells, were depleted, EAE disease course was mitigated and, in the case of CX_3CR1^+ cell depletion, neither demyelination nor axonal damage could be detected (196, 336, 337). However, taking into account that macrophages can acquire different polarization states and, thereby, fulfill different tasks within the context of autoimmunity, it is obvious that shifting the macrophage polarization state towards an M2 phenotype could also have a positive effect on disease progression. Unfortunately, further insights cannot be simply derived from human pathology since defining the macrophage polarization in MS lesions remains challenging due to a limitation of sample availability at specific time points during the disease course. In an autopsy study Vogel *et al.* identified two macrophage subsets within MS lesions (338). One subset showed an M1-like phenotype, another subset, which accounted for approximately 70 % of the $CD40^+$ macrophages, showed an intermediate activation status. This large fraction of macrophages, that did not show a clear M1 or M2 signature, points towards the oversimplification criticism of the M1-M2 concept of macrophage polarization, especially when looked at the human tissues. However, one must consider that post-mortem studies might reflect histopathological changes which have been acquired, altered and potentially resolved, potentially over decades. In addition, it remains unclear if the different molecular phenotypes of macrophages reflect an *a priori* feature of monocyte-derived macrophages that is required and responsible for their pathogenicity or if the polarization phenotype reflects primarily an effector state as an adaption to further external stimuli, e. g. secreted by T cells. Thus, EAE is a powerful tool to study the temporal and spatial progress of macrophage polarization and, furthermore, to track effects derived from interventional studies. Indeed, previous studies have made contributions to better understand the link between macrophage polarization and EAE disease progression (or resolution). Mikita *et al.* showed that the EAE disease severity could be ameliorated by administering *in vitro* M2 polarized macrophages (339). Weng *et al.* found out that a pharmacological modification of the EAE disease course by lenalidomide is associated with an increase in the fraction of M2 cells ($F4/80^+CD206^+$) (340). Likewise, Liu *et al.* observed a shift from M1 to M2 macrophages after the administration the selective Rho kinase inhibitor Fasudil (indicated by a reduction of CD16/32, iNOS, IL-12, TLR4 and CD40 and an increase in CD206, Arginase-1, IL-10 and CD14 in the spleen), potentially mediated by T cells, accompanied by a reduction of inflammatory cytokines (229). Moreover, there is evidence that a

skewed M1/M2 ratio towards the M2 phenotype potentially reinforces remyelination of axons. Butovsky *et al.* first showed that microglia pretreated with IL-4, which induces a M2 phenotype, could enhance oligodendrogenesis and alleviate clinical symptoms of EAE (341). It was later shown that remyelination was accompanied by a M1-to-M2 shift and that M2-conditioned media could enhance remyelination in a demyelination model (217). However, a major drawback of all of these studies is the inconsistent use of signature proteins and genes to determine the polarization phenotype which makes comparability and adaptation difficult.

The M1 and M2 proteomes measured in this study derive from a specific phagocyte population from the (inflamed) EAE spinal cord at different time points. Notably, these M1 and M2 populations are only a minority that co-occurred with e. g. non-polarized infiltrating macrophages (as defined by the absence of iNOS/*Nos2* and Arginase-1/*Arg1* expression in $CD45^{hi}CD11b^{hi}$ cells in the EAE spinal cord) and microglia (as defined by $CD45^{med}CD11b^{med}$ cells). However, we have specifically chosen to analyze these cells because of a previous study which has characterized this transgenic model in the context of EAE with respect to spatial and temporal changes in the polarization phenotype. This study revealed that the M2 phenotype in this model emerges in many cases from the M1 phenotype on a single cell level over the disease course of EAE (222). Thus, the alteration in the M1 and M2 macrophage proteomes can be interpreted rather as a change in protein expression on a single-cell level after time than a characterization of two proteomes that define two cell subtypes co-existing in EAE or emerging over the disease course.

We could identify 17.70 % of the macrophage proteome being different between M1 and M2 macrophages. As a comparison, CD4 T cells differed by 12.35 % of all proteins in their proteomes, microglia by 33.57 % (EAE versus healthy control). Interestingly, microglia (from EAE) and M2 macrophage proteomes showed the greatest similarity in terms of differential enrichment of proteins. The similarity of the M2 macrophage and microglia proteomes was also mirrored in the UMAP analysis where M2 macrophage samples showed a greater proximity to EAE microglia than to samples from M1 macrophages or microglia from healthy controls. Indeed, previous studies showed that microglia, like M2 macrophages, have an anti-inflammatory and immune modulatory function. Ajami *et al*. showed that the recruitment of monocyte-derived macrophages is crucial for EAE induction, however, microglia alone were not able to induce neuroinflammation on their own (195). Furthermore, activation of triggering receptor expressed on myeloid cells-2 (TREM2) induced myelin clearance by microglia, highlighting their importance in the context of disease amelioration (342). However, TREM2 was not detected in this study. Finally, microglia might enhance remyelination through secretion of molecules that support oligodendrocyte differentiation (217).

5.2 Molecular signatures of M1 and M2 macrophages

One of the main objectives of this study was to better understand which cellular programs differentially polarized macrophages execute in the context of neuroinflammation. Therefore, we designed and applied a computational algorithm that performs gene set enrichment analysis and subsequent network analysis (*NezzworGS*) of the M1 and M2 macrophage proteome. The differential enrichment of gene sets within the M1 and M2 macrophage proteomes mirrored the inflammatory and tissue reparative function of the respective polarization state: Gene sets related to proliferation and immune cell signaling were upregulated in the M1 macrophage proteome, whereas gene sets

related to the interaction of cells with the extracellular matrix, potentially reflecting the clearance of debris and regenerative properties, were upregulated in the M2 macrophage proteome. Indeed, in the gene set “Extracellular matrix organization” the most enriched protein in M2 macrophages was collagen type II alpha I (COL2A1). A major concert related to this finding was contamination of the sample by sticky extracellular matrix fragments. However, the detection of collagen transcripts and the enrichment of the gene set “Extracellular matrix organization” in the M2 macrophage transcriptome makes a contamination unlikely. There is further evidence that macrophages are directly linked to collagen metabolism: It was previously reported that M1-like activation of macrophages could decrease the secretion of collagens, whereas M2-like activation increased the amount of collagen (343). This strengthens the hypothesis that the high abundance of extracellular matrix proteins as observed in our study mirrors a phagocyte phenotype which promotes tissue repair. However, it remains unclear if collagen synthesis *per se* is beneficial to restore functional deficits in EAE or if the increase in gliosis is thereby promoted which might introduce further obstacles for the neuronal plasticity.

Moreover, the M2 macrophage proteome showed an upregulation of gene sets related to the nervous system and G protein-coupled receptor signaling. As for the enrichment of the gene set “Extracellular matrix organization” there was the concern of a possible contamination of the proteomes by neuronal proteins attached to M2 macrophages during the isolation process. However, these gene sets were also enriched in the M2 macrophage transcriptome which makes a contamination unlikely. The enrichment of these gene sets (on proteome level) was dominated by a high abundance of the gamma-aminobutyric acid type B receptor subunit 2 (GABA-B-R2/GABBR2). GABA-B receptor 2 belongs to the GABA-B receptor superfamily, which encompasses G-protein-coupled receptors as opposed to the GABA-A receptor superfamily, which are ion channels. Thus, GABA-B receptors are metabotropic receptors, whereas GABA-A receptors are ionotropic receptors (344). The high protein abundance of GABA-B-R2 detected in the M2 macrophage proteome may result either from upregulation of the receptor in M2 macrophages or from phagocytosis of synapses which contain GABA-B-R2 (because GABA-B-R2 was not detected on transcript level). To date, there are no studies which have investigated the role of GABA-B-R2 in phagocyte function in particular. However, GABAergic signaling has recently been discussed in the context of phagocyte pathogen defense. Bhandage *et al.* showed that mononuclear phagocytes secrete GABA when being exposed to *T. gondii* and *N. caninum* and express multiple GABA-A-R subunits as well as enzymes involved in GABA synthesis (345). Another study confirmed the RNA expression of GABA-A-R subunits in human peripheral monocytes (346). However, both studies only observed RNA expression levels in peripheral (murine and human) mononuclear phagocytes (dendritic cells and monocytes) with no link to (neuro-) inflammation. Thus, these observations cannot be applied without restriction to the properties of infiltrating macrophages in the context of EAE and multiple sclerosis. In contrast, Bhat *et al.* explored the effect of GABAergic signaling on EAE (347). They could show that pharmacologically enhancing GABAergic signaling was accompanied by an amelioration of EAE. Potentially, the positive GABAergic signaling effect results from the modulation of phagocyte polarization. Indeed, Januzi *et al.* showed that the activity of the M1 marker NFκB as well as COX-2 and iNOS levels in RAW264.7 cells and TNFα levels in alveolar macrophages from mice pre-treated with LPS were decreased upon treatment with muscimol, a GABA-A receptor agonist (348). This study points towards the involvement if GABA signaling in the polarization of macrophages towards a M2 phenotype. Taken together, recent findings

proved that GABAergic signaling might play a role in phagocyte function and polarization. Likewise, there is evidence that modulating GABAergic signaling in EAE can positively influence the disease course. So far, only GABA-A receptor signaling was observed in these contexts. Our study raises the question to which extent the GABA-B2 receptor signaling pathway might play a role in phagocyte-mediated neuroinflammation and (CNS-specific) phagocyte polarization. What speaks against this assumption is that we have only detected GABA-B-R2 in M2 macrophages but not in M1 macrophages, however, previous studies would suggest that GABA signaling has an influence on diminishing the pro-inflammatory properties of macrophages (348). Thus, if GABA-B-R2 played a role in phagocyte polarization towards M2, it would likely be detectable also in M1 macrophages under the assumption that M2 macrophages arise from M1 macrophages (222).

We observed an enrichment of proteins related to immune cell function and proliferation-associated proteins in the M1 macrophage proteome. However, it remains unclear if infiltrating (bone marrow-derived) macrophages in fact proliferate in the inflamed tissue or if this molecular signature is a remnant from a previous developmental phase. There is evidence that microglia independently from macrophages undergo self-renewal through proliferation during the disease course of EAE (195). Eventually, the sorted and analyzed macrophages ($CD45^{hi}CD11b^{hi}$) in our study are mixed with activated microglia. Moreover, it remains unclear if the underlying proteins of the proliferation-associated gene sets are in fact driving proliferation or are also responsible for shaping the pro-inflammatory M1-like phenotype of these cells.

Although the enrichment of inflammatory-related gene sets points towards high abundance of proteins related to pro-inflammatory functions, only few classical cytokines were found in our proteome analysis. Eventually, this is due to technical limitations of the experimental procedure since only a minority of secreted proteins could be captured by this experimental approach. However, the analysis of the expression of receptors in the M1 and M2 macrophage proteomes revealed a clear enrichment of inflammation-related receptors in the M1 macrophage proteome (e. g. CXCR2, IL-2R2, FAS, IL-4R, C5AR1). It has been shown that these receptors play a crucial role in (auto-) inflammatory diseases and that their modulation can alter the disease course (349–351). Moreover, we identified proteins in the M1 macrophage proteome which are related to immune cell modulation. Such a receptor, which is highly abundant in M1 macrophages, is V-domain Ig suppressor of T cell activation (VISTA/VSIR). This receptor has been previously found as a key immune checkpoint expressed by T cells and myeloid cells, including myeloid-derived suppressor cells (352). Indeed, VISTA blockade by monoclonal antibodies was associated with an exacerbation of EAE (353). On the other hand, VISTA agonism can prevent immune-mediated conditions such as graft-versus-host-disease (354). Thus, tackling VISTA could be a potential pharmacological target for the immunomodulation in autoinflammatory conditions such as EAE and multiple sclerosis. Since the expression of VISTA is relatively high at the initial phase of the disease, the antagonism might force the shift of tissue macrophages from a pro-inflammatory state towards a reparative function. Another immune checkpoint modulator, which was found to be enriched in the M1 macrophage proteome, is LILRB3 (leukocyte immunoglobulin-like receptor). LILRB3 belongs to a subgroup of 5 inhibitory leukocyte immunoglobulin-like receptors (355). Yeboah *et al.* showed that agonistic LILRB3 antibodies skew human monocytes to a M2-like phenotype, indicating the immunomodulatory function of LILRB3. Thus,

similar to VISTA, LILRB3 could be a potential druggable target to shift pro-inflammatory macrophages to a less harmful phenotype in the context of neuroinflammation.

As opposed to the proteomic signature of M1 and M2 macrophages, transcriptomics revealed insights into possible signaling pathways that promote the acquisition of different macrophage phenotypes. In the M1 macrophage transcriptome (but not in the respective proteome) we observed an enrichment of gene sets related to the WNT signaling as well as PI3K/Akt signaling pathway. Interestingly, these pathways promote the transition of pro-inflammatory macrophages to alternatively activated macrophages (356–358). This possible functional impact is further supported by the fact that the gene set related to WNT signaling dominated the early phase of EAE and was not enriched at the remission phase.

PI3K/Akt signaling as well as MAPK signaling pathways, which were enriched in our transcriptomic analysis of M1 macrophages, were also enriched in previous analyses by Orecchioni *et al.*, both in *in vivo* M1-like macrophages (PI3K/Akt and MAPK signaling) and *in vitro* stimulated (IFN-γ + LPS, MAPK signaling) macrophages (359). Furthermore, they found an enrichment of transcripts related to Toll-like receptor 4 (*Tlr4*) downstream signaling which is in line with our finding.

5.3 Functional protein-protein interaction analysis of extracellular proteins within the M1 and M2 macrophage proteome

Most analytical techniques to assess functional patterns of biological processes from omics studies are based on differential gene/protein expression. This includes single gene/protein identification as well as gene set enrichment analysis or dimensional reduction and clustering algorithms. However, molecular signatures do not have to be determined by highly (differentially) abundant genes or proteins only but can also manifest through the interaction between various genes or proteins. Likewise, depending on the experimental or observational method, there are not always two clearly defined groups from which a differential gene/protein expression matrix can be derived from. Therefore, we developed a novel computational technique that combines functional protein-protein interaction network analysis with gene set enrichment analysis (*FUPPINA*). Previous studies have already implemented network analyses into the workflow of gene set enrichment analysis and showed benefits of this technique (360, 361).

We investigated the functional protein-protein interaction networks of extracellular proteins of the M1 and M2 macrophage proteome. The goal was to identify protein-protein interaction subnetworks with distinct functions that could unravel further features of M1 and M2 macrophages. We identified and explored these subnetworks within large networks with help of topological network variables (density and modularity). Furthermore, *FUPPINA* allows to correlate protein expression levels with the degree of centrality of a protein. We observed no correlation between these variables, neither for M1 macrophage extracellular proteins nor M2 macrophage extracellular proteins. This indicates that network analysis is a powerful tool to screen for proteins or genes within a proteome or transcriptome regardless their expression values because since even low abundant proteins can have a large impact on cellular function if they are embedded into a larger functional network. To complement this technique, the Enrichr algorithm was implemented into the *FUPPINA* computational workflow. This allowed us to seek for gene sets within subnetworks without taking gene or protein

abundance into account (as compared to the classical rank-based gene set enrichment analysis algorithm) (301).

Overall, the M1 macrophage functional protein-protein interaction network was denser compared to the M2 macrophage functional protein-protein interaction network, thus, more proteins interacted with each other in the M1 macrophages extracellular proteome compares to M2 macrophages. This observation can be interpreted as an indicator for a more directed cellular program of M1 macrophages where protein subnetworks closely functionally collaborate to express a certain cellular phenotype. The gene set enrichment analysis of the modules with the highest network density revealed the pro-inflammatory feature of M1 macrophages. This finding is in line with the gene set enrichment analysis of the whole M1 macrophage proteome.

To further dissect the functions of M1 and M2 macrophages and we wanted to explore which extracellular proteins within the M1 and M2 macrophage proteome function as signals and mediators for tissue damage (M1 macrophages) and tissue repair (M2 macrophages). The M1 macrophage extracellular protein network showed 4 modules. While 2 modules encompassed proteins related to immune cell signaling, one module (module 2) contained proteins which play a role in the formation of extracellular traps, subsumed under the gene sets “Degradation of the extracellular matrix” and “Extracellular matrix organization” (312, 313, 362–365). Extracellular traps (ETs) were first described in 2004 by Brinkmann *et al.* as a host defense mechanism of neutrophils (366). These neutrophil extracellular traps (NETs) are membrane-less extracellular structures composed of DNA and proteins (neutrophil elastase, cathepsin G, myeloperoxidase, lactoferrin, gelatinase as well as histones). Because of their sticky properties, NETs are believed to immobilize pathogens to ultimately facilitate their killing. Besides antimicrobial function, extracellular traps have been observed in the context of autoimmune disorders such as systemic lupus erythematosus and ANCA-associated vasculitis (367, 368). Moreover, extracellular traps are not only ejected by neutrophils but also monocytes and macrophages (369). There were several proteins enriched in the M1 macrophage proteome which belong to the family of ET-associated proteins (myeloperoxidase, neutrophil elastase, cathepsin G, lactoferrin, cathelicidin, the matrix metalloproteinases MMP9, MMP8 and MMP12 as well as S100A8 and S100A9).

MPO (myeloperoxidase) and ELANE (neutrophil elastase) are considered as neutrophil signature proteins, thus, a major concern of the assumption that macrophage extracellular traps play a critical role in lesion formation at an early stage of the disease course as promoted by our findings is a possible contamination of the sorted $CD45^{+}CD11b^{+}$ cells by neutrophils. However, MPO and ELANE have been detected in extracellular traps ejected by macrophages in other studies (370, 371). With immunofluorescence microscopy of EAE tissues and RNA sequencing we did not gain further significant comprehensive insights into the potential contribution of METs to the molecular mechanism of the disease development. It remains unclear if this is due to technical limitations associated with the investigation of extracellular proteins or due to a contamination by neutrophils that migrate to the spinal cord early during disease development. However, we obtained strong evidence for S100A8/S100A9 being involved in the molecular signature of M1 macrophages, judged by proteomic and transcriptomic as well as histological analyses. Notably both candidates were strongly enriched in M1 macrophages at disease onset (on a protein and RNA level) and were still detected at onset + 5 d in histological sections in inflammatory spinal cord lesions. S100A8 and S100A9 can form a heterodimer

in phagocytes and neutrophils and sense calcium to facilitate cytoskeleton rearrangement (372). Under inflammatory conditions S100A/S100A9 is secreted and may function as an immunomodulatory signal. It may serve as a biomarker for autoimmune disorders since its concentration was elevated in the serum of systemic lupus erythematosus patients and correlated with disease activity (373). A similar study found that S100A8/S100A9 correlated with clinical, radiological and serum inflammation markers in rheumatoid arthritis patients (374). S100A9 is also a druggable target. Quinoline-3-carboxamides bind to S100A9 in a zinc- and calcium-dependent fashion (375). Interestingly, laquinimod, a quinoline-3-carboxamide derivative, could prevent the development of EAE and abolish immune cell infiltration into the murine spinal cord (376). This finding has led to multiple clinical trials assessing the efficacy of laquinimod for the treatment of RRMS and PPMS (377–379). Although the drug showed promising effects in terms of MRI lesions and annual relapse rates, the European Medicines Agency (EMA) refused the marketing authorization due to higher incidences of malignancies and embryotoxic or fetotoxic effects which were observed in the animal model (379).

5.4 Ligand-receptor interactions

As outlined in a previous study, the local environment of phagocytes in EAE is critical for acquiring their phenotype (222). Locatelli *et al.* showed that M^{iNOS} (M1) macrophages are found predominantly in the spinal cord parenchyma during initial lesions stages, whereas $M^{Arginase}$ (M2) macrophages are located at the meninges at initial stages of disease and lesion development. During disease progression, M^{iNOS} (M1) macrophages can switch their phenotype to $M^{Arginase}$ (M2) macrophages. *In vitro* studies showed that macrophage polarization is triggered by various cytokines from other immune cells or moieties from pathogens (380, 381). Taken together, macrophage polarization is a complex orchestration of the interplay of different immune cell types. Thus, we aimed to analyze with which molecular signals M1 and M2 macrophages in EAE can communicate with other cell types. We screened for enriched ligands in the proteome of a cell type of interest and screened for the enrichment of the corresponding receptor in the proteomes of other cell types. However, the individual CNS cell samples did not show a specific signature protein enrichment with respect to the cell type. Thus, one cannot assume cell-specificity for the CNS cell proteomes. However, the immune cells showed a clear differential enrichment of the corresponding proteins. Thus, our main focus was to determine which ligand-receptor interactions between macrophages and other myeloid and lymphatic immune cells play a role in EAE.

We identified S100A8, LCN2, CAMP, S100A9, LTF, HP, LRG1, OLFM4, FCN2 and ELANE as the most differentially enriched ligands in the M1 macrophage proteome. The S100A8/S100A9 heterodimer is a signal complex that promote pro-inflammatory functions of myeloid cells. It was shown that binding of S100A8/S100A9 to toll-like receptor 4 (TLR4) is a crucial interaction to mediate the pro-inflammatory stimulus (382, 383). In the context of neuroinflammation, Reynolds *et al.* showed that TLR4 on CD4 T cells is crucial for EAE disease development (384). In our study high abundances of TLR4 were detected in the macrophage, microglia and T cell proteomes. Both M1 and M2 macrophages were equipped with TLR4, however, there was a non-significant tendency towards higher expression in M1 macrophages. Thus, the secretion of S100A8/S100A9 may serve both as a paracrine and autocrine stimulus to promote pro-inflammatory immune cell functions. Since TLR4 was lower abundant in the M2 macrophage proteome, the S100A8/S100A9-TLR4 interaction is potentially a mechanism that

promotes the shift from M1 to M2 macrophages by downregulating TLR4 expression. Indeed, TLR4 expression seemed to be linked to macrophage polarization. Previous studies by Sauer *et al.* and Orr *et al.* pointed out that TLR4 is higher expressed in M1 macrophages and that TLR4 deficiency facilitates the polarization to M2 macrophages, presumably via the IRF/STAT pathway (380, 385, 386). In contrast, interleukin-10 receptor (IL-10R) has the ability to reverse the intracellular signaling which was initiated by TLR4 (380). IL-10R was highly enriched in the M2 macrophage proteome in our study. Likewise, IL-1α, IL-1β, IL-14 (alpha-taxilin, TXLNA) and IL-18, which are ligands that can bind to IL-10R, were detected, predominantly in microglia and T cells. Notably, IL-1α, IL-1β and IL-18 were enriched in EAE, whereas IL-14 and IL-16 were not changed or even more abundant in microglia and T cells in healthy controls. Thus, the differential expression of TLR4 and IL-10R in macrophages could sense signals sent from microglia and T cells to promote the pro-inflammatory (TLR4) state or to facilitate the transition towards an anti-inflammatory phenotype (IL-10R). However, it remains unclear which factors regulate the expression of TLR4 and IL-10R. Since there are both high protein levels of the ligand (S100A8/S100A9) and the receptor (TLR4) in M1 macrophages, one could assume that the TLR4 stimulation rather reflects an autocrine mechanism, whereas the IL-10R stimulation is potentially a result of T cell-macrophage or microglia-macrophage interactions.

The ligand-receptor interaction between leucine-rich alpha-2-glycoprotein (LRG1), which was enriched in the M1 macrophage proteome, inhibin beta A (INHBA), enriched in the M2 macrophage proteome and TGF-b receptor 2, which was highly abundant in the CD4 T cell proteome might be crucial for the differentiation of T_h17 cells. It was shown that leucine-rich alpha 2 glycoprotein induces T_h17 differentiation in naïve CD4 T cells by stimulating TGF-β-Smad2 signaling (387). Thus, LRG1 secreted by M1 macrophages could promote further pro-inflammatory T cell response. In contrast, M2 macrophages could dampen this signaling through inhibiting TGF-b receptors by inhibin beta A (388). However it is unclear if such a mechanism contributed to neuroinflammation because it was shown that TGF-b signaling in general has anti-inflammatory effects (389). Probably, the initial ligand (whether it is TGF-b or LRG1) and local cytokine environment paves the way for one or the other receptor response.

Our analyses suggest that macrophages use distinct pathways when communicating with CD4 and CD8 T cells. Judged by the number of possible ligand-receptor interactions as well as the abundance of receptors, the M1 macrophage-CD8 T cell interaction was more pronounced than the M1-macrophage-CD4 T cell interaction. The most abundant receptor on CD8 T cells was estrogen-related receptor alpha (ESRRA). A possible ligand to this receptor is Lipocalin-2 (LCN2). Lipocalin-2 was detected in both the ligand-receptor analysis of M1 macrophages as well as the functional protein-protein interaction network. Furthermore, Lipocalin-2 showed the highest sum of ranks in the comprehensive proteome-transcriptome analysis, indicating a strong enrichment in the M1 macrophage proteome as well as transcriptome. LCN2 is known to be increased in the spinal cord after EAE induction as well as spinal cord injury, potentially secreted by microglia and astrocytes (390, 391). Moreover, *Lcn2*-deficient mice showed a milder EAE disease course, therefore, it is believed to play a major role in EAE (391). An *in vitro* study showed that LCN2, which was added to cultured hippocampal neurons, impaired spine mobility and maturation and led to spine retraction (392). LCN2 not only impaired spine constitution but also inhibited myelination *in vitro* (393). Furthermore, LCN2 was found in the CSF of PPMS patients, its concentration correlated with the neurofilament light concentration as a biomarker for neuronal

impairment (393). Thus, LCN2 might be a key mediator of demyelination and spine pathology in MS. Our study shows that M1 macrophages are potentially a main source of LCN2, which might contribute to tissue damage as well as regulate adaptive immune responses through binding to receptors on CD8 T cells.

The most strongly enriched ligand in the M2 macrophage proteome was vitamin K-dependent protein S (PROS1). Together with its receptor AXL receptor tyrosine kinase (AXL), which was also specifically enriched in the M2 macrophage proteome compared to the M1 macrophage proteome, this ligand-receptor signaling mechanism can inhibit M1 macrophage polarization as shown in a previous study by Ubil *et al.* (394). Thus, PROS1-AXL co-expression in macrophages might maintain an anti-inflammatory phenotype in EAE through autocrine stimulation.

5.5 Mitochondrial pathology

One of the tissue consequences of the infiltration of macrophages is the emergence of axonal damage in neuroinflammatory lesions (225). Axonal pathology is widely discussed to correlate with functional deficits of MS patients and to be a potential underlying mechanism for the transmission from RRMS to SPMS (395–398). The causal link between immune cells infiltration and axonal loss is not fully understood. However, oxidative stress caused by ROS release of immune cells and enhanced by secondary mitochondrial dysfunction is believed to be a major contributor to the axonal pathology in MS and EAE (399). It was shown that mitochondrial pathology is an early sign of axonal pathology in EAE and MS (225). To further explore the underlying molecular mechanisms when mitochondria are exposed to ROS we measured neuronal mitochondrial proteomes using specific fluorescent transgenic labeling techniques combined with MACS (270). We showed that proteins related to energy metabolism (TCA cycle and OXPHOS) were less abundant in the proteome of EAE neuronal mitochondria when compared to healthy controls. We further showed that the downregulation of most of the proteins related to mitochondrial energy metabolism was restored after the initial phase of the disease resolved. Similar results were obtained from *post mortem* transcriptome analyses from MS patients from Dutta *et al.* who observed a decrease of respiratory chain complex I and III transcripts in the MS motor cortex (400). Likewise, Rosenkranz *et al.* observed a de-regulation of gene transcripts in neurons in EAE related to energy metabolism and electron transfer chain in particular (401).

We observed a lower abundance of both TCA cycle and OXPHOS proteins in EAE compared to healthy control in our study. It remains unclear if the lower abundance of proteins from both pathways is functionally linked or can be seen as two individual mechanisms. Possibly, TCA cycle is predominantly affected and the loss of OXPHOS proteins is secondary due to lack of reduction equivalents. To address this, we overexpressed IDH3A by viral transduction and assessed possible shifts in energy metabolism by measuring the ADP-to-ATP ratio *in vivo* in EAE (318). Indeed, axons which were transduced with IDH3A showed higher ATP levels. This indicates that OXPHOS function can be partially restored by enhancing TCA function in EAE, highlighting TCA as a possible pharmacological target for neuroinflammatory diseases.

Furthermore, it remains unclear whether the lower abundance of proteins related to TCA cycle and OXPHOS in EAE results from exposure to damaging molecules, such as ROS, or from a compensatory mechanism that aims to escape the vicious circle of ROS production characterized by

enhanced ROS production due to damaged mitochondria (131). Recently, proliferator-activated receptor gamma coactivator 1- alpha (PGC-1a) has been identified as a regulator of energy metabolism in EAE which bears the ability to ameliorate EAE severity when overexpressed in murine neurons (401). If the downregulation of mitochondrial energy metabolism was an escape mechanism from further ROS damage with subsequent liberation of free electrons and radical formation, overexpression of PGC-1a and the associated restoration of OXHPHOS integrity would rather cause further worsening of neuronal impairment and increase EAE severity. Taken together, these findings provide evidence that mitochondrial energy metabolism in EAE is rather compromised than regulated.

5.6 Limitations of this study

To identify and allow sorting of M1 and M2 macrophages in EAE we used a transgenic mouse model. A limitation of this model, however, is the indirect measurement of iNOS and Arginase-1 protein expression through the expression of fluorescent proteins regulated by the *Nos2* and *Arg1* promoter. The potential difference between the half-lives of the fluorescent proteins and the actual iNOS and Arginase-1 proteins can result in a mismatch between the fluorescent labeling and the metabolic state of a cell. Likewise, RNA sequencing revealed that the *Arg1* transcript levels were as high in sorted $CD45^+CD11b^+Ly6G^-iNOS^+$ (M1) cells as in $CD45^+CD11b^+Ly6G^-Arginase\text{-}1^+$ (M2) cells, whereas the *Nos2* transcript levels reflected the actual distribution of the protein levels among M1 and M2 cells. However, in the sorted *Nos2*-$tdTomato^+$ and *Arg1*-YFP^+ cells iNOS and Arginase-1 were clearly differentially enriched in the respective proteomes, increasing the reliability of this model, but also emphasizing the potential poor transcriptome-proteome correlation.

In this study we used iNOS and Arginase-1 expression as the only marker enzymes to distinguish between M1 and M2 macrophage phenotypes. However, there is increasing evidence that parenchymal CNS myeloid cells and macrophages in particular show a high transcriptional complexity and diversity (238, 402, 403). Thus, the identified differentially abundant proteins, genes and gene sets reflect molecular signatures that are either shared by a heterogenous group of cells (all expressing either iNOS or Arginase-1) or are highly expressed in a subgroup of these cells, not necessarily reflecting the molecular signature of other coexisting macrophage popoulations.

We faced technical limitations regarding the sorting of CNS cells. Except of microglia, none of the resident CNS cell proteomes (neurons, astrocytes, oligodendrocytes, OPCs) showed a specific signature with respect to previously characterized protein or RNA expression data. It is likely that the dense physical interaction of these cells within the CNS tissue makes dissociation of the cells (while maintaining their integrity) impossible. A recently developed technique based on bio-orthogonal noncanonical amino acid tagging (BONCAT), cell type-specific Cre expression and mass spectrometry could circumvent this limitation (404). Therefore, Cre is expressed under a cell type-specific promoter which further enables the cells to express a variant methionyl-tRNA synthetase (MetRS) that allows the incorporation of the methionine surrogate azidonorleucine (ANL) into nascent polypeptides. After that, isotopic peptides, which derive from a specific cell type, can be identified and whole proteomes of a certain cell type can by analyzed.

5.7 Outlook

In the past two decades specific cell-targeting pharmacotherapies in multiple sclerosis have emerged. According to their mode of action, they can be divided into two groups: antibodies and small molecules. Rituximab/ocrelizumab, natalizumab and alemtuzumab are monoclonal antibodies which inhibit T cell (natalizumab and alemtuzumab) and B cell (rituximab/ocrelizumab) function. The sphingosine 1-phosphate receptor modulators fingolimod, ozanimod and siponimod as well as glatiramer acetate are small molecules that interfere with T cell function. Notably, although belonging to treatment category II and III, their side effects are controllable, presumably because of their targeted mode of action. One could hypothesize that not only altering T and B cell function but also addressing myeloid cells like mononuclear phagocytes might mitigate the disease course of multiple sclerosis. However, so far, none of the approved drugs primarily target these cells. In principle, depletion of monocytes or macrophages (under experimental conditions) was associated with amelioration of EAE as shown in previous studies (192, 193). Moreover, analogous to the function of integrin alpha 4 in T cells, motile sperm domain-containing protein 2 (MOSPD2) was identified to regulate monocyte migration (405). Furthermore, targeting MOSPD2 with inhibiting antibodies could ameliorate EAE (406). However, depleting monocytes (systemically or locally in the CNS) raises concerns about severe side effects. Thus, targeting phagocyte polarization rather than phagocyte migration might circumvent this concern. Indeed, there are promising agents which have shown to modulate macrophage function in EAE, for example by shifting their polarization from a pro-inflammatory phenotype (M1) to an anti-inflammatory phenotype (M2) (308). Additionally, assuming that phagocytes have not only destructive functions but also reparative effects, remaining phagocytes' migration function intact but altering their polarization might be more beneficial overall. Taken together, mononuclear phagocytes in general and monocyte-derived macrophages in particular are promising pharmacological targets for future drug development for multiple sclerosis.

In this study we have identified possible druggable targets, both, on macrophages but also other immune cells, that build a communication pathway between macrophages and other immune cells in the inflamed CNS. However, further functional testing is necessary to narrow down hypotheses and identify promising targets for directed therapeutical approaches for multiple sclerosis and other neuroinflammatory diseases.

List of figures

List of tables

List of abbreviations

$\bar{\mu}$	mean
µ	micro
ACK	ammonium-chloride-potassium
APC	antigen-presenting cell
APC	allophycocyanin
B cell	B lymphocyte
CD	cluster of differentiation
CI	confidence interval
CSF	cerebrospinal fluid
CSF	colony-stimulating factor
DAPI	4’,6-diamidino-2-phenylindole
dpi	days post immunization
dpo	days post onset
EAE	experimental autoimmune encephalomyelitis
EBNA-1	Epstein–Barr virus nuclear antigen 1
EBV	Epstein-Barr virus
EDSS	expanded disability status scale
EDTA	ethylenediaminetetraacetic acid
EMA	European Medicines Agency
FACS	fluorescence-activated cell sorting
FAD	focal axonal degeneration
FC	fold change
FI	fluorescence intensity
FMO	fluorescence minus one
FS	functional system
FSC	forward scatter
FSC-A	forward scatter (area)
FSC-H	forward scatter (height)
g	standard acceleration due to gravity
g	grams
GM-CSF	granulocyte-macrophage colony-stimulating factor
GWAS	gene-wide association studies
h	hours
H_0	null hypothesis
HLA	human leukocyte antigen
IFN	interferon
IL	interleukin
iNOS	inducible nitric oxide synthase
IVC	individually ventilated cage
k	kilo
KEGG	Kyoto Encyclopedia of Genes and Genomes
l	liter
LDAO	N,N-dimethyldodecylamine-N-oxide

Ly6C	lymphocyte antigen 6 complex locus 6C1
Ly6G	lymphocyte antigen 6 complex locus G6D
M1	pro-inflammatory macrophages
M2	anti-inflammatory macrophages
MACS	magnetic-activated cell sorting
MBP	myelin basic protein
M-CSF	macrophage colony-stimulating factor
mFI	mean fluorescence intensity
MHC	major histocompatibility complex
min	minutes
MOG	myelin oligodendrocyte glycoprotein
MRI	magnetic resonance imaging
MRS	magnetic resonance spectroscopy
MS	multiple sclerosis
n	nano
NAA	N-acetylaspartic acid
NAWM	normal appearing white matter
NEDA	no evidence of disease activity
NO	nitric oxide
OCB	oligoclonal bands
OPC	oligodendrocyte precursor cells
OR	odds ratio
OXPHOS	oxidative phosphorylation
p value	probability value
PAGE	polyacrylamide gel electrophoresis
PLP	myelin proteolipid protein
PPMS	primary progressive multiple sclerosis
q	FDR-adjusted *p* value
receiver operating characteristic	ROC
RNS	reactive nitrogen species
ROS	reactive oxygen species
rpm	rotations per minute
RRMS	relapsing-remitting multiple sclerosis
s	seconds
SD	standard deviation
SDS	sodium dodecyl sulphate
SPMS	secondary progressive multiple sclerosis
SSC	sideward scatter
SSC-A	sideward scatter (area)
SSC-H	sideward scatter (height)
STRING	Search Tool for the Retrieval of Interacting Genes/Proteins
T cell	T lymphocyte
TCA	tricarboxylic acid
TCR	T cell receptor
TGF	transforming growth factor

TGF-β	transforming growth factor beta
T_h	T helper cell
TNF	tumor necrosis factor
TNF	tumor necrosis factor
TNFα	tumor necrosis factor alpha
T_{reg}	regulatory T cells
YFP	yellow fluorescent protein
n	sample size
σ	standard deviation

References

1. **Dobson R, Giovannoni G**. Multiple sclerosis – a review. *Eur J Neurol*. 2019;26(1):27–40. doi:10.1111/ene.13819

2. **Hauser SL, Cree BAC**. Treatment of Multiple Sclerosis: A Review. Vol. 133, American Journal of Medicine. 2020. p. 1380-1390.e2. doi:10.1016/j.amjmed.2020.05.049

3. **Browne P, Chandraratna D, Angood C, Tremlett H, Baker C, Taylor B V., et al.** Atlas of multiple sclerosis 2013: A growing global problem with widespread inequity. Vol. 83, Neurology. 2014. p. 1022–4. doi:10.1212/WNL.0000000000000768

4. **Huang WJ, Chen WW, Zhang X**. Multiple sclerosis: Pathology, diagnosis and treatments (review). Experimental and Therapeutic Medicine. 2017. doi:10.3892/etm.2017.4410

5. **Reich DS, Lucchinetti CF, Calabresi PA**. Multiple Sclerosis. Longo DL, editor. *N Engl J Med*. 2018;378(2):169–80. doi:10.1056/NEJMra1401483

6. **Brownlee WJ, Hardy TA, Fazekas F, Miller DH**. Diagnosis of multiple sclerosis: progress and challenges. *Lancet*. 2017;389(10076):1336–46. doi:10.1016/S0140-6736(16)30959-X

7. **Merkelbach S, Haensch CA, Hemmer B, Koehler J, König NH, Ziemssen T**. Multiple sclerosis and the autonomic nervous system. In: Journal of Neurology. 2006. doi:10.1007/s00415-006-1105-z

8. **Brenner P, Piehl F**. Fatigue and depression in multiple sclerosis: pharmacological and non-pharmacological interventions. Vol. 134, Acta Neurologica Scandinavica. 2016. p. 47–54. doi:10.1111/ane.12648

9. **Boeschoten RE, Braamse AMJ, Beekman ATF, Cuijpers P, van Oppen P, Dekker J, et al.** Prevalence of depression and anxiety in Multiple Sclerosis: A systematic review and meta-analysis. *J Neurol Sci*. 2017;372:331–41. doi:10.1016/j.jns.2016.11.067

10. **Thompson AJ, Banwell BL, Barkhof F, Carroll WM, Coetzee T, Comi G, et al.** Diagnosis of multiple sclerosis: 2017 revisions of the McDonald criteria. *Lancet Neurol*. 2018;17(2):162–73. doi:10.1016/S1474-4422(17)30470-2

11. **Compston A, Coles A**. Multiple sclerosis. *Lancet*. 2008;372(9648):1502–17. doi:10.1016/S0140-6736(08)61620-7

12. **Hemmer B, Bayas A, Faßhauer E, Flachenecker P**. Diagnose und Therapie der Multiplen Sklerose, Neuromyelitis-optica-Spektrum-Erkrankungen und MOG-IgG-assoziierten Erkrankungen, S2k-Leitlinie. Deutsche Gesellschaft für Neurologie (Hrsg.), Leitlinien für Diagnostik und Therapie in der Neurologie. 2021.

13. **Yamout BI, Alroughani R**. Multiple Sclerosis. *Semin Neurol*. 2018;38(2):212–25. doi:10.1055/s-0038-1649502

14. **Kurtzke JF**. Rating neurologic impairment in multiple sclerosis: An expanded disability status scale (EDSS). *Neurology*. 1983;33(11):1444–52. doi:10.1212/wnl.33.11.1444

15. **Inojosa H, Schriefer D, Ziemssen T**. Clinical outcome measures in multiple sclerosis: A review. Vol. 19, Autoimmunity Reviews. 2020. p. 102512. doi:10.1016/j.autrev.2020.102512

16. **Wallin MT, Culpepper WJ, Nichols E, Bhutta ZA, Gebrehiwot TT, Hay SI, et al.** Global, regional, and national burden of multiple sclerosis 1990–2016: a systematic analysis for the Global Burden of Disease Study 2016. *Lancet Neurol*. 2019;18(3):269–85. doi:10.1016/S1474-4422(18)30443-5

17. **Kamm CP, Uitdehaag BM, Polman CH**. Multiple Sclerosis: Current Knowledge and Future Outlook. *Eur Neurol*. 2014;72(3–4):132–41. doi:10.1159/000360528

18. **Confavreux C, Vukusic S**. Natural history of multiple sclerosis: A unifying concept. *Brain*. 2006;129(3):606–16. doi:10.1093/brain/awl007

19. **Ascherio A, Munger KL**. Epidemiology of Multiple Sclerosis: From Risk Factors to Prevention--An Update. Vol. 36, Seminars in Neurology. 2016. p. 103–14. doi:10.1055/s-0036-1579693

20. **Munger KL, Zhang SM, O'Reilly E, Hernán MA, Olek MJ, Willett WC, et al.** Vitamin D intake and incidence of multiple sclerosis. *Neurology*. 2004;62(1):60–5. doi:10.1212/01.WNL.0000101723.79681.38

21. **Munger KL, Levin LI, Hollis BW, Howard NS, Ascherio A**. Serum 25-hydroxyvitamin D levels and risk of multiple sclerosis. *J Am Med Assoc*. 2006;296(23):2832–8. doi:10.1001/jama.296.23.2832

22. **Salzer J, Hallmans G, Nyström M, Stenlund H, Wadell G, Sundström P**. VitaminDas a protective factor in multiple sclerosis. *Neurology*. 2012;79(21):2140–5. doi:10.1212/WNL.0b013e3182752ea8

23. **Swank RL, Lerstad O, Strøm A, Backer J**. Multiple Sclerosis in Rural Norway. *N Engl J Med*. 1952;246(19):721–8. doi:10.1056/nejm195205082461901

24. **Munger KL, Chitnis T, Ascherio A**. Body size and risk of MS in two cohorts of US women. *Neurology*. 2009;73(19):1543–50. doi:10.1212/WNL.0b013e3181c0d6e0

25. **Munger KL, Bentzen J, Laursen B, Stenager E, Koch-Henriksen N, Sørensen TIA, et al.** Childhood body mass index and multiple sclerosis risk: A long-term cohort study. *Mult Scler J*. 2013;19(10):1323–9. doi:10.1177/1352458513483889

26. **Warner HB, Carp RI**. Multiple Sclerosis and Epstein-Barr virus. Vol. 318, The Lancet. 1981. p. 1290. doi:10.1016/S0140-6736(81)91527-0

27. **Sewell DL, Reinke EK, Hogan LH, Sandor M, Fabry Z**. Immunoregulation of CNS autoimmunity by helminth and mycobacterial infections. In: Immunology Letters. 2002. p. 101–10. doi:10.1016/S0165-2478(02)00025-1

28. **Bach J-F**. The Effect of Infections on Susceptibility to Autoimmune and Allergic Diseases. *N Engl J Med*. 2002;347(12):911–20. doi:10.1056/nejmra020100

29. **DeLorenze GN, Munger KL, Lennette ET, Orentreich N, Vogelman JH, Ascherio A**. Epstein-Barr virus and multiple sclerosis: Evidence of association from a prospective study with long-term follow-up. *Arch Neurol*. 2006;63(6):839–44. doi:10.1001/archneur.63.6.noc50328

30. **Sundström P, Juto P, Wadell G, Hallmans G, Svenningsson A, Nyström L, et al.** An altered immune response to Epstein-Barr virus in multiple sclerosis: A prospective study. *Neurology*. 2004;62(12):2277–82. doi:10.1212/01.WNL.0000130496.51156.D7

31. **Ascherio A, Munger KL, Lennette ET, Spiegelman D, Hernán MA, Olek MJ, et al.** Epstein-Barr virus antibodies and risk of multiple sclerosis: A prospective study. *J Am Med Assoc*. 2001;286(24):3083–8. doi:10.1001/jama.286.24.3083

32. **Levin LI, Munger KL, Rubertone M V., Peck CA, Lennette ET, Spiegelman D, et al.** Temporal relationship between elevation of Epstein-Barr virus antibody titers and initial onset of neurological symptoms in multiple sclerosis. *J Am Med Assoc*. 2005;293(20):2496–500. doi:10.1001/jama.293.20.2496

33. **Munger KL, Levin LI, O'Reilly EJ, Falk KI, Ascherio A**. Anti-Epstein-Barr virus antibodies as serological markers of multiple sclerosis: A prospective study among United States military personnel. *Mult Scler J*. 2011;17(10):1185–93. doi:10.1177/1352458511408991

34. **Levin LI, Munger KL, O'Reilly EJ, Falk KI, Ascherio A**. Primary infection with the Epstein-Barr virus and risk of multiple sclerosis. *Ann Neurol*. 2010;67(6):824–30. doi:10.1002/ana.21978

35. **Bäärnhielm M, Olsson T, Alfredsson L**. Fatty fish intake is associated with decreased occurrence of multiple sclerosis. *Mult Scler J*. 2014;20(6):726–32. doi:10.1177/1352458513509508

36. **Ghadirian P, Dadgostar B, Azani R, Maisonneuve P**. A case-control study of the association between socio-demographic, lifestyle and medical history factors and multiple sclerosis. *Can J Public Heal*. 2001;92(4):281–5. doi:10.1007/bf03404961

37. **Sundström P, Nyström L**. Smoking worsens the prognosis in multiple sclerosis. *Mult Scler*. 2008;14(8):1031–5. doi:10.1177/1352458508093615

38. **Hedström AK, Bäärnhielm M, Olsson T, Alfredsson L**. Tobacco smoking, but not Swedish snuff use, increases the risk of multiple sclerosis. *Neurology*. 2009;73(9):696–701. doi:10.1212/WNL.0b013e3181b59c40

39. **Ramagopalan S V., Lee JD, Yee IM, Guimond C, Traboulsee AL, Ebers GC, et al.** Association of smoking with risk of multiple sclerosis: A population-based study. *J Neurol*. 2013;260(7):1778–81. doi:10.1007/s00415-013-6873-7

40. **Riise T, Nortvedt MW, Ascherio A**. Smoking is a risk factor for multiple sclerosis. *Neurology*. 2003;61(8):1122–4. doi:10.1212/01.WNL.0000081305.66687.D2

41. **Hernán MA, Jick SS, Logroscino G, Olek MJ, Ascherio A, Jick H**. Cigarette smoking and the progression of multiple sclerosis. *Brain*. 2005;128(6):1461–5. doi:10.1093/brain/awh471

42. **Emre M, Decker C**. Effects of Cigarette Smoking on Motor Functions in Patients With Multiple Sclerosis. *Arch Neurol*. 1992;49(12):1243–7. doi:10.1001/archneur.1992.00530360041015

43. **Di Pauli F, Reindl M, Ehling R, Schautzer F, Gneiss C, Lutterotti A, et al.** Smoking is a risk factor for early conversion to clinically definite multiple sclerosis. *Mult Scler*. 2008;14(8):1026–30. doi:10.1177/1352458508093679

44. **Healy BC, Ali EN, Guttmann CRG, Chitnis T, Glanz BI, Buckle G, et al.** Smoking and disease progression in multiple sclerosis. *Arch Neurol*. 2009;66(7):858–64. doi:10.1001/archneurol.2009.122

45. **Filippi M, Bar-Or A, Piehl F, Preziosa P, Solari A, Vukusic S, et al.** Multiple sclerosis. *Nat Rev Dis Prim*. 2018;4(1):43. doi:10.1038/s41572-018-0041-4

46. **Harirchian MH, Fatehi F, Sarraf P, Honarvar NM, Bitarafan S**. Worldwide prevalence of familial multiple sclerosis: A systematic review and meta-analysis. Vol. 20, Multiple Sclerosis and Related Disorders. 2018. p. 43–7. doi:10.1016/j.msard.2017.12.015

47. **Hillert J, Masterman T**. The genetics of multiple sclerosis. In: Handbook of Multiple Sclerosis, Third Edition. 2001. p. 33–65. doi:10.15586/codon.multiplesclerosis.2017.ch1

48. **Lückel C, Picard F, Raifer H, Campos Carrascosa L, Guralnik A, Zhang Y, et al.** IL-17+ CD8+ T cell suppression by dimethyl fumarate associates with clinical response in multiple sclerosis. *Nat Commun*. 2019;10(1):5722. doi:10.1038/s41467-019-13731-z

49. **Pope BJ, Sharma V, Boland M, Meador W, Bridges SL, Raman C**. IL-2 enhances IFNγ signals in subpopulations of T and B lymphocytes from treatment naive relapsing remitting multiple sclerosis (RRMS) patients. *J Immunol*. 2018;200(1 Supplement).

50. **Hedström AK, Sundqvist E, Bäärnhielm M, Nordin N, Hillert J, Kockum I, et al.** Smoking and two human leukocyte antigen genes interact to increase the risk for multiple sclerosis. *Brain*. 2011;134(3):653–64. doi:10.1093/brain/awq371

51. **Hedström AK, Bomfim IL, Barcellos L, Gianfrancesco M, Schaefer C, Kockum I, et al.** Interaction between adolescent obesity and HLA risk genes in the etiology of multiple sclerosis. *Neurology*. 2014;82(10):865–72. doi:10.1212/WNL.0000000000000203

52. **Sundqvist E, Sundström P, Lindén M, Hedström AK, Aloisi F, Hillert J, et al.** Epstein-Barr virus and multiple sclerosis: Interaction with HLA. *Genes Immun*. 2012;13(1):14–20. doi:10.1038/gene.2011.42

53. **Olsson T, Barcellos LF, Alfredsson L**. Interactions between genetic, lifestyle and environmental risk factors for multiple sclerosis. Vol. 13, Nature Reviews Neurology. 2016. p. 26–36. doi:10.1038/nrneurol.2016.187

54. **Nazareth TA, Rava AR, Polyakov JL, Banfe EN, Waltrip RW, Zerkowski KB, et al.** Relapse prevalence, symptoms, and health care engagement: patient insights from the Multiple Sclerosis in America 2017 survey. *Mult Scler Relat Disord*. 2018;26:219–34. doi:10.1016/j.msard.2018.09.002

55. **Charcot J**. Lectures on the diseases of the nervous system, delivered at La Salpêtrière. Vol. 60, The British and Foreign Medico-Chirurgical Review. 1877.

56. **Goodin DS, Frohman EM, Garmany GP, Halper J, Likosky WH, Lublin FD, et al.** Disease modifying therapies in multiple sclerosis: Report of the therapeutics and technology assessment subcommittee of the American academy of neurology and the MS council for clinical practice guidelines. *Neurology*. 2002;58(2):169–78. doi:10.1212/WNL.58.2.169

57. **Derfuss T, Ontaneda D, Nicholas J, Meng X, Hawker K**. Relapse rates in patients with multiple sclerosis treated with fingolimod: Subgroup analyses of pooled data from three phase 3 trials. *Mult Scler Relat Disord*. 2016;8:124–30. doi:10.1016/j.msard.2016.05.015

58. **Repovic P, Lublin FD**. Treatment of Multiple Sclerosis Exacerbations. Vol. 29, Neurologic Clinics. 2011. p. 389–400. doi:10.1016/j.ncl.2010.12.012

59. **Stoppe M, Busch M, Krizek L, Then Bergh F**. Outcome of MS relapses in the era of disease-modifying therapy. *BMC Neurol*. 2017;17(1):151. doi:10.1186/s12883-017-0927-x

60. **Berkovich RR**. Acute Multiple Sclerosis Relapse. Vol. 22, CONTINUUM Lifelong Learning in Neurology. 2016. p. 799–814. doi:10.1212/CON.0000000000000330

61. **Berkovich R**. Treatment of Acute Relapses in Multiple Sclerosis. Vol. 10, Neurotherapeutics. 2013. p. 97–105. doi:10.1007/s13311-012-0160-7

62. **Lublin FD, Reingold SC, Cohen JA, Cutter GR, Sørensen PS, Thompson AJ, et al.** Defining the clinical course of multiple sclerosis: The 2013 revisions. Vol. 83, Neurology. 2014. p. 278–86. doi:10.1212/WNL.0000000000000560

63. **Bjartmar C, Yin X, Trapp BD**. Axonal pathology in myelin disorders. *J Neurocytol*. 1999;28(4–5):383–95. doi:10.1023/a:1007010205037

64. **Weinshenker BG, Bass B, Rice GPA, Noseworthy J, Carriere W, Baskerville J, et al.** The natural history of multiple sclerosis: A geographically based study: I. Clinical course and disability. *Brain*. 1989;112(1):133–46. doi:10.1093/brain/112.1.133

65. **Trojano M, Avolio C, Manzari C, Calo A, De Robertis F, Serio G, et al.** Multivariate analysis of predictive factors of multiple sclerosis course with a validated method to assess clinical events. *J Neurol Neurosurg Psychiatry*. 1995;58(3):300–6. doi:10.1136/jnnp.58.3.300

66. **Runmarker B, Andersson C, Odén A, Andersen O**. Prediction of outcome in multiple sclerosis based on multivariate models. *J Neurol*. 1994;241(10):597–604. doi:10.1007/BF00920623

67. **Confavreux C, Aimard G, Devic M**. Course and prognosis of multiple sclerosis assessed by the computerized data processing of 349 patients. *Brain*. 1980;103(2):281–300. doi:10.1093/brain/103.2.281

68. **Trojano M, Paolicelli D, Bellacosa A, Cataldo S**. The transition from relapsing-remitting MS to irreversible disability: Clinical evaluation. Vol. 24, Neurological Sciences. 2003. p. s268–70. doi:10.1007/s10072-003-0171-6

69. **Brex PA, Ciccarelli O, O'Riordan JI, Sailer M, Thompson AJ, Miller DH**. A Longitudinal Study of Abnormalities on MRI and Disability from Multiple Sclerosis. *N Engl J Med*. 2002;346(3):158–64. doi:10.1056/nejmoa011341

70. **Barnes D, Munro PMG, Youl BD, Prineas JW, Mcdonald WI**. The longstanding ms lesion. *Brain*. 1991;114(3):1271–80. doi:10.1093/brain/114.3.1271

71. **Losseff NA, Webb SL, O'Riordan JI, Page R, Wang L, Barker GJ, et al.** Spinal cord atrophy and disability in multiple sclerosis. A new reproducible and sensitive MRI method with potential to monitor disease progression. *Brain*. 1996;119(3):701–8. doi:10.1093/brain/119.3.701

72. **Bakshi R, Dandamudi VSR, Neema M, De C, Bermel RA**. Measurement of brain and spinal cord atrophy by magnetic resonance imaging as a tool to monitor multiple sclerosis. Vol. 15, Journal of Neuroimaging. 2005. doi:10.1177/1051228405283901

73. **Losseff NA, Wang L, Lai HM, Yoo DS, Gawne-Cain ML, McDonald WI, et al.** Progressive cerebral atrophy in multiple sclerosis A serial MRI study. *Brain*. 1996;119(6):2009–19.

doi:10.1093/brain/119.6.2009

74. **Davie CA, Hawkins CP, Barker GJ, Brennan A, Tofts PS, Miller DH, et al.** Serial proton magnetic resonance spectroscopy in acute multiple sclerosis lesions. *Brain*. 1994;117(1):49–58. doi:10.1093/brain/117.1.49

75. **Fu L, Matthews PM, De Stefano N, Worsley KJ, Narayanan S, Francis GS, et al.** Imaging axonal damage of normal-appearing white matter in multiple sclerosis. *Brain*. 1998;121(1):103–13. doi:10.1093/brain/121.1.103

76. **Narayanan S, Fu L, Pioro E, De Stefano N, Collins DL, Francis GS, et al.** Imaging of axonal damage in multiple sclerosis: Spatial distribution of magnetic resonance imaging lesions. *Ann Neurol*. 1997;41(3):385–91. doi:10.1002/ana.410410314

77. **Miller DH, Leary SM**. Primary-progressive multiple sclerosis. *Lancet Neurol*. 2007;6(10):903–12. doi:10.1016/S1474-4422(07)70243-0

78. **Tremlett H, Paty D, Devonshire V**. The natural history of primary progressive MS in British Columbia, Canada. *Neurology*. 2005;65(12):1919–23. doi:10.1212/01.wnl.0000188880.17038.1d

79. **Kremenchutzky M, Rice GPA, Baskerville J, Wingerchuk DM, Ebers GC**. The natural history of multiple sclerosis: A geographically based study 9: Observations on the progressive phase of the disease. *Brain*. 2006;129(3):584–94. doi:10.1093/brain/awh721

80. **Vukusic S, Confavreux C**. Natural history of multiple sclerosis: Risk factors and prognostic indicators. Vol. 20, Current Opinion in Neurology. 2007. p. 269–74. doi:10.1097/WCO.0b013e32812583ad

81. **Tintoré M, Rovira A, Brieva L, Grivé E, Jardí R, Borrás C, et al.** Isolated demyelinating syndromes: comparison of CSF oligoclonal bands and different MR imaging criteria to predict conversion to CDMS. *Mult Scler J*. 2001;7(6):359–63. doi:10.1177/135245850100700603

82. **Tintoré M, Rovira A, Río J, Tur C, Pelayo R, Nos C, et al.** Do oligoclonal bands add information to MRI in first attacks of multiple sclerosis? *Neurology*. 2008;70(13 PART 2):1079–83. doi:10.1212/01.wnl.0000280576.73609.c6

83. **Andreadou E, Chatzipanagiotou S, Constantinides VC, Rombos A, Stamboulis E, Nicolaou C**. Prevalence of cerebrospinal fluid oligoclonal IgG bands in Greek patients with clinically isolated syndrome and multiple sclerosis. *Clin Neurol Neurosurg*. 2013;115(10):2094–8. doi:10.1016/j.clineuro.2013.07.026

84. **Dobson R, Ramagopalan S, Davis A, Giovannoni G**. Cerebrospinal fluid oligoclonal bands in multiple sclerosis and clinically isolated syndromes: A meta-analysis of prevalence, prognosis and effect of latitude. *J Neurol Neurosurg Psychiatry*. 2013;84(8):909–14. doi:10.1136/jnnp-2012-304695

85. **Giovannoni G, Turner B, Gnanapavan S, Offiah C, Schmierer K, Marta M**. Is it time to target no evident disease activity (NEDA) in multiple sclerosis? Vol. 4, Multiple Sclerosis and Related Disorders. 2015. p. 329–33. doi:10.1016/j.msard.2015.04.006

86. **Wiendl H, Toyka K V., Rieckmann P, Gold R, Hartung H-P, Hohlfeld R**. Basic and escalating immunomodulatory treatments in multiple sclerosis: Current therapeutic

recommendations. *J Neurol*. 2008;255(10):1449–63. doi:10.1007/s00415-008-0061-1

87. **Grauer O, Offenhäusser M, Schmidt J, Toyka K V., Gold R**. Glucocorticosteroid therapy in optic neuritis and multiple sclerosis: Evidence from clinical studies and practical recommendations. Vol. 72, Nervenarzt. 2001. p. 577–89. doi:10.1007/s001150170057

88. **Beck RW, Cleary PA, Anderson MM, Keltner JL, Shults WT, Kaufman DI, et al.** A Randomized, Controlled Trial of Corticosteroids in the Treatment of Acute Optic Neuritis. *N Engl J Med*. 1992;326(9):581–8. doi:10.1056/nejm199202273260901

89. **Miller DM, Weinstock-Guttman B, Béthoux F, Lee J-C, Beck G, Block V, et al.** A meta-analysis of methylprednisolone in recovery from multiple sclerosis exacerbations. *Mult Scler J*. 2000;6(4):267–73. doi:10.1177/135245850000600408

90. **Weinshenker BG, O'Brien PC, Petterson TM, Noseworthy JH, Lucchinetti CF, Dodick DW, et al.** A randomized trial of plasma exchange in acute central nervous system inflammatory demyelinating disease. *Ann Neurol*. 1999;46(6):878–86. doi:10.1002/1531-8249(199912)46:6<878::AID-ANA10>3.0.CO;2-Q

91. **Keegan M, Pineda AA, McClelland RL, Darby CH, Rodriguez M, Weinshenker BG**. Plasma exchange for severe attacks of CNS demyelination: Predictors of response. *Neurology*. 2002;58(1):143–8. doi:10.1212/wnl.58.1.143

92. **Jacobs LD, Beck RW, Simon JH, Kinkel RP, Brownscheidle CM, Murray TJ, et al.** Intramuscular Interferon Beta-1A Therapy Initiated during a First Demyelinating Event in Multiple Sclerosis. *N Engl J Med*. 2000;343(13):898–904. doi:10.1056/nejm200009283431301

93. **Comi G, Filippi M, Barkhof F, Durelli L, Edan G, Fernández O, et al.** Effect of early interferon treatment on conversion to definite multiple sclerosis: A randomised study. *Lancet*. 2001;357(9268):1576–82. doi:10.1016/S0140-6736(00)04725-5

94. **Kappos L, Freedman MS, Polman CH, Edan G, Hartung HP, Miller DH, et al.** Effect of early versus delayed interferon beta-1b treatment on disability after a first clinical event suggestive of multiple sclerosis: a 3-year follow-up analysis of the BENEFIT study. *Lancet*. 2007;370(9585):389–97. doi:10.1016/S0140-6736(07)61194-5

95. **Kappos L, Clanet M, Sandberg-Wollheim M, Radue EW, Hartung HP, Hohlfeld R, et al.** Neutralizing antibodies and efficacy of interferon β-1a: A 4-year controlled study. *Neurology*. 2005;65(1):40–7. doi:10.1212/01.wnl.0000171747.59767.5c

96. **Fox RJ, Miller DH, Phillips JT, Hutchinson M, Havrdova E, Kita M, et al.** Placebo-Controlled Phase 3 Study of Oral BG-12 or Glatiramer in Multiple Sclerosis. *N Engl J Med*. 2012;367(12):1087–97. doi:10.1056/nejmoa1206328

97. **O'Connor P, Wolinsky JS, Confavreux C, Comi G, Kappos L, Olsson TP, et al.** Randomized Trial of Oral Teriflunomide for Relapsing Multiple Sclerosis. *N Engl J Med*. 2011;365(14):1293–303. doi:10.1056/nejmoa1014656

98. **Kappos L, Radue E-W, O'Connor P, Polman C, Hohlfeld R, Calabresi P, et al.** A Placebo-Controlled Trial of Oral Fingolimod in Relapsing Multiple Sclerosis. *N Engl J Med*. 2010;362(5):387–401. doi:10.1056/nejmoa0909494

99. **Kappos L, Antel J, Comi G, Montalban X, O'Connor P, Polman CH, et al.** Oral Fingolimod (FTY720) for Relapsing Multiple Sclerosis. *N Engl J Med*. 2006;355(11):1124–40.

doi:10.1056/nejmoa052643

100. **Cohen JA, Barkhof F, Comi G, Hartung H-P, Khatri BO, Montalban X, et al.** Oral Fingolimod or Intramuscular Interferon for Relapsing Multiple Sclerosis. *N Engl J Med*. 2010;362(5):402–15. doi:10.1056/nejmoa0907839

101. **Cohen JA, Comi G, Selmaj KW, Bar-Or A, Arnold DL, Steinman L, et al.** Safety and efficacy of ozanimod versus interferon beta-1a in relapsing multiple sclerosis (RADIANCE): a multicentre, randomised, 24-month, phase 3 trial. *Lancet Neurol*. 2019;18(11):1021–33. doi:10.1016/S1474-4422(19)30238-8

102. **Kappos L, Fox RJ, Burcklen M, Freedman MS, Havrdová EK, Hennessy B, et al.** Ponesimod Compared With Teriflunomide in Patients With Relapsing Multiple Sclerosis in the Active-Comparator Phase 3 OPTIMUM Study: A Randomized Clinical Trial. *JAMA Neurol*. 2021;78(5):558–67. doi:10.1001/JAMANEUROL.2021.0405

103. **Kappos L, Bar-Or A, Cree BAC, Fox RJ, Giovannoni G, Gold R, et al.** Siponimod versus placebo in secondary progressive multiple sclerosis (EXPAND): a double-blind, randomised, phase 3 study. *Lancet*. 2018;391(10127):1263–73. doi:10.1016/S0140-6736(18)30475-6

104. **Giovannoni G, Comi G, Cook S, Rammohan K, Rieckmann P, Sørensen PS, et al.** A Placebo-Controlled Trial of Oral Cladribine for Relapsing Multiple Sclerosis. *N Engl J Med*. 2010;362(5):416–26. doi:10.1056/nejmoa0902533

105. **Polman CH, O'Connor PW, Havrdova E, Hutchinson M, Kappos L, Miller DH, et al.** A Randomized, Placebo-Controlled Trial of Natalizumab for Relapsing Multiple Sclerosis. *N Engl J Med*. 2006;354(9):899–910. doi:10.1056/nejmoa044397

106. **Miller DH, Khan OA, Sheremata WA, Blumhardt LD, Rice GPA, Libonati MA, et al.** A Controlled Trial of Natalizumab for Relapsing Multiple Sclerosis. *N Engl J Med*. 2003;348(1):15–23. doi:10.1056/nejmoa020696

107. **Hauser SL, Bar-Or A, Comi G, Giovannoni G, Hartung H-P, Hemmer B, et al.** Ocrelizumab versus Interferon Beta-1a in Relapsing Multiple Sclerosis. *N Engl J Med*. 2017;376(3):221–34. doi:10.1056/nejmoa1601277

108. **Montalban X, Hauser SL, Kappos L, Arnold DL, Bar-Or A, Comi G, et al.** Ocrelizumab versus Placebo in Primary Progressive Multiple Sclerosis. *N Engl J Med*. 2017;376(3):209–20. doi:10.1056/NEJMoa1606468

109. **Rudick RA, Stuart WH, Calabresi PA, Confavreux C, Galetta SL, Radue E-W, et al.** Natalizumab plus Interferon Beta-1a for Relapsing Multiple Sclerosis. *N Engl J Med*. 2006;354(9):911–23. doi:10.1056/nejmoa044396

110. **Knier B, Hemmer B, Korn T**. Novel monoclonal antibodies for therapy of multiple sclerosis. Vol. 14, Expert Opinion on Biological Therapy. 2014. p. 503–13. doi:10.1517/14712598.2014.887676

111. **Hauser SL, Bar-Or A, Cohen JA, Comi G, Correale J, Coyle PK, et al.** Ofatumumab versus Teriflunomide in Multiple Sclerosis. *https://doi.org/101056/NEJMoa1917246*. 2020;383(6):546–57. doi:10.1056/NEJMOA1917246

112. **Jennum P, Wanscher B, Frederiksen J, Kjellberg J**. The socioeconomic consequences of multiple sclerosis: A controlled national study. *Eur Neuropsychopharmacol*.

2012;22(1):36–43. doi:10.1016/j.euroneuro.2011.05.001

113. **Jo JCC, Airas L, Bartholome E, Grigoriadis N, Mattle H, Oreja Guevara C, et al.** Symptomatic therapy in multiple sclerosis: A review for a multimodal approach in clinical practice. Vol. 4, Therapeutic Advances in Neurological Disorders. 2011. p. 139–68. doi:10.1177/1756285611403646

114. **Sanabria-Castro A, Flores-Díaz M, Alape-Girón A**. Biological models in multiple sclerosis. Vol. 98, Journal of Neuroscience Research. 2020. p. 491–508. doi:10.1002/jnr.24528

115. **Burrows DJ, McGown A, Jain SA, De Felice M, Ramesh TM, Sharrack B, et al.** Animal models of multiple sclerosis: From rodents to zebrafish. Vol. 25, Multiple Sclerosis Journal. 2019. p. 306–24. doi:10.1177/1352458518805246

116. **Lassmann H, Bradl M**. Multiple sclerosis: experimental models and reality. Vol. 133, Acta Neuropathologica. 2017. p. 223–44. doi:10.1007/s00401-016-1631-4

117. **Stromnes IM, Goverman JM**. Active induction of experimental allergic encephalomyelitis. *Nat Protoc*. 2006;1(4):1810–9. doi:10.1038/nprot.2006.285

118. **Baker D, Amor S**. Experimental autoimmune encephalomyelitis is a good model of multiple sclerosis if used wisely. Vol. 3, Multiple Sclerosis and Related Disorders. 2014. p. 555–64. doi:10.1016/j.msard.2014.05.002

119. **Delarasse C, Smith P, Baker D, Amor S**. Novel pathogenic epitopes of myelin oligodendrocyte glycoprotein induce experimental autoimmune encephalomyelitis in C57BL/6 mice. *Immunology*. 2013;140(4):456–64. doi:10.1111/imm.12155

120. **Constantinescu CS, Farooqi N, O'Brien K, Gran B**. Experimental autoimmune encephalomyelitis (EAE) as a model for multiple sclerosis (MS). Vol. 164, British Journal of Pharmacology. 2011. p. 1079–106. doi:10.1111/j.1476-5381.2011.01302.x

121. **Kipp M, Van Der Star B, Vogel DYS, Puentes F, Van Der Valk P, Baker D, et al.** Experimental in vivo and in vitro models of multiple sclerosis: EAE and beyond. Vol. 1, Multiple Sclerosis and Related Disorders. 2012. p. 15–28. doi:10.1016/j.msard.2011.09.002

122. **Herrero-Herranz E, Pardo LA, Gold R, Linker RA**. Pattern of axonal injury in murine myelin oligodendrocyte glycoprotein induced experimental autoimmune encephalomyelitis: Implications for multiple sclerosis. *Neurobiol Dis*. 2008;30(2):162–73. doi:10.1016/j.nbd.2008.01.001

123. **'t Hart BA, Gran B, Weissert R**. EAE: Imperfect but useful models of multiple sclerosis. Vol. 17, Trends in Molecular Medicine. 2011. p. 119–25. doi:10.1016/j.molmed.2010.11.006

124. **Barnett MH, Prineas JW**. Relapsing and Remitting Multiple Sclerosis: Pathology of the Newly Forming Lesion. *Ann Neurol*. 2004;55(4):458–68. doi:10.1002/ana.20016

125. **Lovett-Racke AE**. Contribution of EAE to understanding and treating multiple sclerosis. *J Neuroimmunol*. 2017;304:40–2. doi:10.1016/j.jneuroim.2016.08.013

126. **Sormani MP, Rovaris M, Comi G, Filippi M**. A reassessment of the plateauing relationship between T2 lesion load and disability in MS. *Neurology*. 2009;73(19):1538–42. doi:10.1212/WNL.0b013e3181c06679

127. **Rocca MA, Amato MP, De Stefano N, Enzinger C, Geurts JJ, Penner IK, et al.** Clinical and imaging assessment of cognitive dysfunction in multiple sclerosis. Vol. 14, The Lancet Neurology. 2015. p. 302–17. doi:10.1016/S1474-4422(14)70250-9

128. **Absinta M, Sati P, Masuzzo F, Nair G, Sethi V, Kolb H, et al.** Association of Chronic Active Multiple Sclerosis Lesions With Disability In Vivo. *JAMA Neurol*. 2019;76(12):1474. doi:10.1001/JAMANEUROL.2019.2399

129. **Kuhlmann T, Ludwin S, Prat A, Antel J, Brück W, Lassmann H**. An updated histological classification system for multiple sclerosis lesions. *Acta Neuropathol*. doi:10.1007/s00401-016-1653-y

130. **Lassmann H, Van Horssen J, Mahad D**. Progressive multiple sclerosis: Pathology and pathogenesis. Vol. 8, Nature Reviews Neurology. 2012. p. 647–56. doi:10.1038/nrneurol.2012.168

131. **Mahad DH, Trapp BD, Lassmann H**. Pathological mechanisms in progressive multiple sclerosis. Vol. 14, The Lancet Neurology. 2015. p. 183–93. doi:10.1016/S1474-4422(14)70256-X

132. **Prineas JW, Kwon EE, Cho ES, Sharer LR, Barnett MH, Oleszak EL, et al.** Immunopathology of secondary-progressive multiple sclerosis. *Ann Neurol*. 2001;50(5):646–57. doi:10.1002/ana.1255

133. **Machado-Santos J, Saji E, Tröscher AR, Paunovic M, Liblau R, Gabriely G, et al.** The compartmentalized inflammatory response in the multiple sclerosis brain is composed of tissue-resident CD8+ T lymphocytes and B cells. *Brain*. 2018;141(7):2066–82. doi:10.1093/brain/awy151

134. **Frischer JM, Weigand SD, Guo Y, Kale N, Parisi JE, Pirko I, et al.** Clinical and pathological insights into the dynamic nature of the white matter multiple sclerosis plaque. *Ann Neurol*. 2015;78(5):710–21. doi:10.1002/ana.24497

135. **Luchetti S, Fransen NL, van Eden CG, Ramaglia V, Mason M, Huitinga I**. Progressive multiple sclerosis patients show substantial lesion activity that correlates with clinical disease severity and sex: a retrospective autopsy cohort analysis. *Acta Neuropathol*. 2018;135(4):511–28. doi:10.1007/s00401-018-1818-y

136. **Kutzelnigg A, Lucchinetti CF, Stadelmann C, Brück W, Rauschka H, Bergmann M, et al.** Cortical demyelination and diffuse white matter injury in multiple sclerosis. *Brain*. 2005;128(11):2705–12. doi:10.1093/brain/awh641

137. **Evangelou N, DeLuca GC, Owens T, Esiri MM**. Pathological study of spinal cord atrophy in multiple sclerosis suggests limited role of local lesions. *Brain*. 2005;128(1):29–34. doi:10.1093/brain/awh323

138. **Klaver R, De Vries HE, Schenk GJ, Geurts JJG**. Grey matter damage in multiple sclerosis A pathology perspective. In: Prion. 2013. p. 66–75. doi:10.4161/pri.23499

139. **Korn T**. Pathophysiology of multiple sclerosis. Vol. 255, Journal of Neurology. 2008. p. 2–6. doi:10.1007/s00415-008-6001-2

140. **Pette M, Fujita K, Kitze B, Whitaker JN, Albert E, Kappos L, et al.** Myelin basic protein-specific T lymphocyte lines from ms patients and healthy individuals. *Neurology*. 1990;40(11):1770–6. doi:10.1212/wnl.40.11.1770

141. **Bielekova B, Goodwin B, Richert N, Cortese I, Kondo T, Afshar G, et al.** Encephalitogenic potential of the myelin basic protein peptide (amino acids 83-99) in multiple sclerosis: Results of a phase II clinical trial with an altered peptide ligand. *Nat Med*. 2000;6(10):1167–75. doi:10.1038/80516

142. **Gold R, Linington C, Lassmann H**. Understanding pathogenesis and therapy of multiple sclerosis via animal models: 70 Years of merits and culprits in experimental autoimmune encephalomyelitis research. Vol. 129, Brain. 2006. p. 1953–71. doi:10.1093/brain/awl075

143. **Wekerle H, Kojima K, Lannes-Vieira J, Lassmann H, Linington C**. Animal models. In: Annals of Neurology. 1994. doi:10.1002/ana.410360714

144. **Flügel A, Berkowicz T, Ritter T, Labeur M, Jenne DE, Li Z, et al.** Migratory Activity and Functional Changes of Green Fluorescent Effector Cells before and during Experimental Autoimmune Encephalomyelitis. *Immunity*. 2001;14(5):547–60. doi:10.1016/S1074-7613(01)00143-1

145. **Bettelli E, Carrier Y, Gao W, Korn T, Strom TB, Oukka M, et al.** Reciprocal developmental pathways for the generation of pathogenic effector TH17 and regulatory T cells. *Nature*. 2006;441(7090):235–8. doi:10.1038/nature04753

146. **Kaskow BJ, Baecher-Allan C**. Effector t cells in multiple sclerosis. *Cold Spring Harb Perspect Med*. 2018;8(4). doi:10.1101/cshperspect.a029025

147. **Kitz A, Singer E, Hafler D**. Regulatory T Cells: From Discovery to Autoimmunity. Vol. 8, Cold Spring Harbor perspectives in medicine. 2018. doi:10.1101/cshperspect.a029041

148. **Viglietta V, Baecher-Allan C, Weiner HL, Hafler DA**. Loss of Functional Suppression by CD4+CD25+ Regulatory T Cells in Patients with Multiple Sclerosis. *J Exp Med*. 2004;199(7):971–9. doi:10.1084/jem.20031579

149. **Frisullo G, Nociti V, Iorio R, Patanella AK, Caggiula M, Marti A, et al.** Regulatory T cells fail to suppress CD4+T-bet+ T cells in relapsing multiple sclerosis patients. *Immunology*. 2009;127(3):418–28. doi:10.1111/j.1365-2567.2008.02963.x

150. **Astier AL, Meiffren G, Freeman S, Hafler DA**. Alterations in CD46-mediated Tr1 regulatory T cells in patients with multiple sclerosis. *J Clin Invest*. 2006;116(12):3252–7. doi:10.1172/JCI29251

151. **Fletcher JM, Lonergan R, Costelloe L, Kinsella K, Moran B, O'Farrelly C, et al.** CD39 + Foxp3 + Regulatory T Cells Suppress Pathogenic Th17 Cells and Are Impaired in Multiple Sclerosis . *J Immunol*. 2009;183(11):7602–10. doi:10.4049/jimmunol.0901881

152. **Dhaeze T, Peelen E, Hombrouck A, Peeters L, Van Wijmeersch B, Lemkens N, et al.** Circulating Follicular Regulatory T Cells Are Defective in Multiple Sclerosis. *J Immunol*. 2015;195(3):832–40. doi:10.4049/jimmunol.1500759

153. **Kebir H, Kreymborg K, Ifergan I, Dodelet-Devillers A, Cayrol R, Bernard M, et al.** Human TH17 lymphocytes promote blood-brain barrier disruption and central nervous system inflammation. *Nat Med*. 2007;13(10):1173–5. doi:10.1038/nm1651

154. **Kebir H, Ifergan I, Alvarez JI, Bernard M, Poirier J, Arbour N, et al.** Preferential recruitment of interferon-γ-expressing TH17 cells in multiple sclerosis. *Ann Neurol*. 2009;66(3):390–402. doi:10.1002/ana.21748

155. **Van Langelaar J, Van Der Vuurst De Vries RM, Janssen M, Wierenga-Wolf AF, Spilt IM, Siepman TA, et al.** T helper 17.1 cells associate with multiple sclerosis disease activity: Perspectives for early intervention. Vol. 141, Brain. 2018. p. 1334–49. doi:10.1093/brain/awy069

156. **Cavallo S**. Immune-mediated genesis of multiple sclerosis. Vol. 3, Journal of Translational Autoimmunity. 2020. p. 100039. doi:10.1016/j.jtauto.2020.100039

157. **Moore CS, Rao VTS, Durafourt BA, Bedell BJ, Ludwin SK, Bar-Or A, et al.** MiR-155 as a multiple sclerosis-relevant regulator of myeloid cell polarization. *Ann Neurol*. 2013;74(5):709–20. doi:10.1002/ana.23967

158. **Louveau A, Smirnov I, Keyes TJ, Eccles JD, Rouhani SJ, Peske JD, et al.** Structural and functional features of central nervous system lymphatic vessels. *Nature*. 2015;523(7560):337–41. doi:10.1038/nature14432

159. **Palanichamy A, Apeltsin L, Kuo TC, Sirota M, Wang S, Pitts SJ, et al.** Immunoglobulin class-switched B cells form an active immune axis between CNS and periphery in multiple sclerosis. *Sci Transl Med*. 2014;6(248). doi:10.1126/scitranslmed.3008930

160. **Stern JNH, Yaari G, Vander Heiden JA, Church G, Donahue WF, Hintzen RQ, et al.** B cells populating the multiple sclerosis brain mature in the draining cervical lymph nodes. *Sci Transl Med*. 2014;6(248). doi:10.1126/scitranslmed.3008879

161. **Larochelle C, Lécuyer MA, Alvarez JI, Charabati M, Saint-Laurent O, Ghannam S, et al.** Melanoma cell adhesion molecule-positive CD8 T lymphocytes mediate central nervous system inflammation. *Ann Neurol*. 2015;78(1):39–53. doi:10.1002/ana.24415

162. **Sonar SA, Lal G**. Differentiation and transmigration of CD4 T cells in neuroinflammation and autoimmunity. Vol. 8, Frontiers in Immunology. 2017. p. 29. doi:10.3389/fimmu.2017.01695

163. **van Langelaar J, Rijvers L, Smolders J, van Luijn MM**. B and T Cells Driving Multiple Sclerosis: Identity, Mechanisms and Potential Triggers. Vol. 11, Frontiers in Immunology. 2020. doi:10.3389/fimmu.2020.00760

164. **Frischer JM, Bramow S, Dal-Bianco A, Lucchinetti CF, Rauschka H, Schmidbauer M, et al.** The relation between inflammation and neurodegeneration in multiple sclerosis brains. *Brain*. 2009;132(5):1175–89. doi:10.1093/brain/awp070

165. **Lucchinetti C, Brück W, Parisi J, Scheithauer B, Rodriguez M, Lassmann H**. Heterogeneity of multiple sclerosis lesions: Implications for the pathogenesis of demyelination. *Ann Neurol*. 2000;47(6):707–17. doi:10.1002/1531-8249(200006)47:6<707::AID-ANA3>3.0.CO;2-Q

166. **Ramaglia V, Sheikh-Mohamed S, Legg K, Park C, Rojas OL, Zandee S, et al.** Multiplexed imaging of immune cells in staged multiple sclerosis lesions by mass cytometry. *Elife*. 2019;8. doi:10.7554/eLife.48051

167. **Renno T, Lin JY, Piccirillo C, Antel J, Owens T**. Cytokine production by cells in cerebrospinal fluid during experimental allergic encephalomyelitis in SJL/J mice. *J Neuroimmunol*. 1994;49(1–2):1–7. doi:10.1016/0165-5728(94)90174-0

168. **Olsson T**. Cytokines in neuroinflammatory disease: role of myelin autoreactive T cell production of interferon-gamma. *J Neuroimmunol*. 1992;40(2–3):211–8.

doi:10.1016/0165-5728(92)90135-8

169. **Kurschus FC, Croxford AL, P. Heinen A, Wörtge S, Ielo D, Waisman A**. Genetic proof for the transient nature of the Th17 phenotype. *Eur J Immunol*. 2010;40(12):3336–46. doi:10.1002/eji.201040755

170. **Hirota K, Duarte JH, Veldhoen M, Hornsby E, Li Y, Cua DJ, et al.** Fate mapping of IL-17-producing T cells in inflammatory responses. *Nat Immunol*. 2011;12(3):255–63. doi:10.1038/ni.1993

171. **Loos J, Schmaul S, Noll TM, Paterka M, Schillner M, Löffel JT, et al.** Functional characteristics of Th1, Th17, and ex-Th17 cells in EAE revealed by intravital two-photon microscopy. *J Neuroinflammation*. 2020;17(1):357. doi:10.1186/s12974-020-02021-x

172. **Bsibsi M, Peferoen LAN, Holtman IR, Nacken PJ, Gerritsen WH, Witte ME, et al.** Demyelination during multiple sclerosis is associated with combined activation of microglia/macrophages by IFN-γ and alpha B-crystallin. *Acta Neuropathol*. 2014;128(2):215–29. doi:10.1007/s00401-014-1317-8

173. **Perry VH, Holmes C**. Microglial priming in neurodegenerative disease. Vol. 10, Nature Reviews Neurology. 2014. p. 217–24. doi:10.1038/nrneurol.2014.38

174. **Cross AH, Stark JL, Lauber J, Ramsbottom MJ, Lyons JA**. Rituximab reduces B cells and T cells in cerebrospinal fluid of multiple sclerosis patients. *J Neuroimmunol*. 2006;180(1–2):63–70. doi:10.1016/j.jneuroim.2006.06.029

175. **Piccio L, Naismith RT, Trinkaus K, Klein RS, Parks BJ, Lyons JA, et al.** Changes in B- and T-lymphocyte and chemokine levels with rituximab treatment in multiple sclerosis. *Arch Neurol*. 2010;67(6):707–14. doi:10.1001/archneurol.2010.99

176. **Bar-Or A, Fawaz L, Fan B, Darlington PJ, Rieger A, Ghorayeb C, et al.** Abnormal B-cell cytokine responses a trigger of T-cell-mediated disease in MS? *Ann Neurol*. 2010;67(4):452–61. doi:10.1002/ana.21939

177. **Duddy M, Niino M, Adatia F, Hebert S, Freedman M, Atkins H, et al.** Distinct Effector Cytokine Profiles of Memory and Naive Human B Cell Subsets and Implication in Multiple Sclerosis. *J Immunol*. 2007;178(10):6092–9. doi:10.4049/jimmunol.178.10.6092

178. **Li R, Rezk A, Miyazaki Y, Hilgenberg E, Touil H, Shen P, et al.** Proinflammatory GM-CSF-producing B cells in multiple sclerosis and B cell depletion therapy. *Sci Transl Med*. 2015;7(310). doi:10.1126/scitranslmed.aab4176

179. **Milich DR, Chen M, Schödel F, Peterson DL, Jones JE, Hughes JL**. Role of B cells in antigen presentation of the hepatitis B core. *Proc Natl Acad Sci U S A*. 1997;94(26):14648–53. doi:10.1073/pnas.94.26.14648

180. **Li R, Rezk A, Li H, Gommerman JL, Prat A, Bar-Or A**. Antibody-Independent Function of Human B Cells Contributes to Antifungal T Cell Responses. *J Immunol*. 2017;198(8):3245–54. doi:10.4049/jimmunol.1601572

181. **Molnarfi N, Schulze-Topphoff U, Weber MS, Patarroyo JC, Prod'homme T, Varrin-Doyer M, et al.** MHC class II–dependent B cell APC function is required for induction of CNS autoimmunity independent of myelin-specific antibodies. *J Exp Med*. 2013;210(13):2921–37. doi:10.1084/jem.20130699

182. **Gharibi T, Babaloo Z, Hosseini A, Marofi F, Ebrahimi-kalan A, Jahandideh S, et al.** The role of B cells in the immunopathogenesis of multiple sclerosis. *Immunology*. 2020;160(4):325–35. doi:10.1111/imm.13198

183. **Harp CT, Lovett-Racke AE, Racke MK, Frohman EM, Monson NL**. Impact of myelin-specific antigen presenting B cells on T cell activation in multiple sclerosis. *Clin Immunol*. 2008;128(3):382–91. doi:10.1016/j.clim.2008.05.002

184. **Harp CT, Ireland S, Davis LS, Remington G, Cassidy B, Cravens PD, et al.** Memory B cells from a subset of treatment-naïve relapsing-remitting multiple sclerosis patients elicit CD4+ T-cell proliferation and IFN-γ production in response to myelin basic protein and myelin oligodendrocyte glycoprotein. *Eur J Immunol*. 2010;40(10):2942–56. doi:10.1002/eji.201040516

185. **Gomez Perdiguero E, Klapproth K, Schulz C, Busch K, Azzoni E, Crozet L, et al.** Tissue-resident macrophages originate from yolk-sac-derived erythro-myeloid progenitors. *Nature*. 2015;518(7540):547–51. doi:10.1038/nature13989

186. **Hoeffel G, Chen J, Lavin Y, Low D, Almeida FF, See P, et al.** C-Myb+ Erythro-Myeloid Progenitor-Derived Fetal Monocytes Give Rise to Adult Tissue-Resident Macrophages. *Immunity*. 2015;42(4):665–78. doi:10.1016/j.immuni.2015.03.011

187. **Frame JM, McGrath KE, Palis J**. Erythro-myeloid progenitors: "Definitive" hematopoiesis in the conceptus prior to the emergence of hematopoietic stem cells. Vol. 51, Blood Cells, Molecules, and Diseases. 2013. p. 220–5. doi:10.1016/j.bcmd.2013.09.006

188. **Mass E, Ballesteros I, Farlik M, Halbritter F, Günther P, Crozet L, et al.** Specification of tissue-resident macrophages during organogenesis. *Science (80-)*. 2016;353(6304). doi:10.1126/science.aaf4238

189. **Plein A, Fantin A, Denti L, Pollard JW, Ruhrberg C**. Erythro-myeloid progenitors contribute endothelial cells to blood vessels. *Nature*. 2018;562(7726):223–8. doi:10.1038/s41586-018-0552-x

190. **Nally FK, De Santi C, McCoy CE**. Nanomodulation of Macrophages in Multiple Sclerosis. *Cells*. 2019;8(6):543. doi:10.3390/cells8060543

191. **Tran EH, Hoekstra K, van Rooijen N, Dijkstra CD, Owens T**. Immune invasion of the central nervous system parenchyma and experimental allergic encephalomyelitis, but not leukocyte extravasation from blood, are prevented in macrophage-depleted mice. *J Immunol*. 1998;

192. **Brosnan CF, Bornstein MB, Bloom BR**. The effects of macrophage depletion on the clinical and pathologic expression of experimental allergic encephalomyelitis. *J Immunol*. 1981;126(2).

193. **Huitinga I, van Rooijen N, de Groot CJA, Uitdehaag BMJJ, Dijkstra CD, Huitinga BI, et al.** Suppression of experimental allergic encephalomyelitis in lewis rats after elimination of macrophages. *J Exp Med*. 1990;172(4):1025–33. doi:10.1084/jem.172.4.1025

194. **Moreno MA, Burns T, Yao P, Miers L, Pleasure D, Soulika AM**. Therapeutic depletion of monocyte-derived cells protects from long-term axonal loss in experimental autoimmune encephalomyelitis. *J Neuroimmunol*. 2016;290:36–46.

doi:10.1016/j.jneuroim.2015.11.004

195. **Ajami B, Bennett JL, Krieger C, McNagny KM, Rossi FMV V**. Infiltrating monocytes trigger EAE progression, but do not contribute to the resident microglia pool. *Nat Neurosci*. 2011;14(9):1142–50. doi:10.1038/nn.2887

196. **Heppner FL, Greter M, Marino D, Falsig J, Raivich G, Hövelmeyer N, et al.** Experimental autoimmune encephalomyelitis repressed by microglial paralysis. *Nat Med*. 2005;11(2):146–52. doi:10.1038/nm1177

197. **Henderson APD, Barnett MH, Parratt JDE, Prineas JW**. Multiple sclerosis: Distribution of inflammatory cells in newly forming lesions. *Ann Neurol*. 2009;66(6):739–53. doi:10.1002/ana.21800

198. **Brück W, Porada P, Poser S, Rieckmann P, Hanefeld F, Kretzschmarch HA, et al.** Monocyte/macrophage differentiation in early multiple sclerosis lesions. *Ann Neurol*. 1995;38(5):788–96. doi:10.1002/ana.410380514

199. **Hauser SL, Bhan AK, Gilles F, Kemp M, Kerr C, Weiner HL**. Immunohistochemical analysis of the cellular infiltrate in multiple sclerosis lesions. *Ann Neurol*. 1986;19(6):578–87. doi:10.1002/ana.410190610

200. **Bitsch A, Schuchardt J, Bunkowski S, Kuhlmann T, Brück W**. Acute axonal injury in multiple sclerosis: Correlation with demyelination and inflammation. *Brain*. 2002;123(6):1174–83. doi:10.1093/brain/123.6.1174

201. **Izikson L, Klein RS, Charo IF, Weiner HL, Luster AD**. Resistance to experimental autoimmune encephalomyelitis in mice lacking the CC chemokine receptor (CCR)2. *J Exp Med*. 2000;192(7):1075–80. doi:10.1084/jem.192.7.1075

202. **Gaupp S, Pitt D, Kuziel WA, Cannella B, Raine CS**. Experimental autoimmune encephalomyelitis (EAE) in CCR2-/- mice: Susceptibility in multiple strains. *Am J Pathol*. 2003;162(1):139–50. doi:10.1016/S0002-9440(10)63805-9

203. **Huang D, Wang J, Kivisakk P, Rollins BJ, Ransohoff RM**. Absence of monocyte chemoattractant protein 1 in mice leads to decreased local macrophage recruitment and antigen-specific T helper cell type 1 immune response in experimental autoimmune encephalomyelitis. *J Exp Med*. 2001;193(6):713–25. doi:10.1084/jem.193.6.713

204. **Fife BT, Huffnagle GB, Kuziel WA, Karpus WJ**. CC chemokine receptor 2 is critical for induction of experimental autoimmune encephalomyelitis. *J Exp Med*. 2000;192(6):899–905. doi:10.1084/jem.192.6.899

205. **Gordon S, Taylor PR**. Monocyte and macrophage heterogeneity. Vol. 5, Nature Reviews Immunology. 2005. p. 953–64. doi:10.1038/nri1733

206. **King IL, Dickendesher TL, Segal BM**. Circulating Ly-6C + myeloid precursors migrate to the CNS and play a pathogenic role during autoimmune demyelinating disease. *Blood*. 2009;113(14):3190–7. doi:10.1182/blood-2008-07-168575

207. **Ziegler-Heitbrock L, Ancuta P, Crowe S, Dalod M, Grau V, Hart DN, et al.** Nomenclature of monocytes and dendritic cells in blood. Vol. 116, Blood. 2010. doi:10.1182/blood-2010-02-258558

208. **Chuluundorj D, Harding SA, Abernethy D, La Flamme AC**. Expansion and preferential activation of the CD14+ CD16 + monocyte subset during multiple sclerosis. *Immunol Cell*

Biol. 2014;92(6):509–17. doi:10.1038/icb.2014.15

209. **Chuluundorj D, Harding SA, Abernethy D, La Flamme AC**. Glatiramer acetate treatment normalized the monocyte activation profile in MS patients to that of healthy controls. *Immunol Cell Biol*. 2017;95(3):297–305. doi:10.1038/icb.2016.99

210. **Bergh FT, Dayyani F, Ziegler-Heitbrock L**. Impact of type-I-interferon on monocyte subsets and their differentiation to dendritic cells: An in vivo and ex vivo study in multiple sclerosis patients treated with interferon-beta. *J Neuroimmunol*. 2004;146(1–2):176–88. doi:10.1016/j.jneuroim.2003.10.037

211. **Ingersoll MA, Spanbroek R, Lottaz C, Gautier EL, Frankenberger M, Hoffmann R, et al.** Comparison of gene expression profiles between human and mouse monocyte subsets. *Blood*. 2010;115(3). doi:10.1182/blood-2009-07-235028

212. **Van Der Voorn P, Tekstra J, Beelen RHJ, Tensen CP, Van Der Valk P, De Groot CJA**. Expression of MCP-1 by reactive astrocytes in demyelinating multiple sclerosis lesions. *Am J Pathol*. 1999;154(1):45–51. doi:10.1016/S0002-9440(10)65249-2

213. **Prins M, Dutta R, Baselmans B, Brevé JJP, Bol JGJM, Deckard SA, et al.** Discrepancy in CCL2 and CCR2 expression in white versus grey matter hippocampal lesions of Multiple Sclerosis patients. Vol. 2, Acta Neuropathologica Communications. 2014. doi:10.1186/s40478-014-0098-6

214. **McManus C, Berman JW, Brett FM, Staunton H, Farrell M, Brosnan CF**. MCP-1, MCP-2 and MCP-3 expression in multiple sclerosis lesions: An immunohistochemical and in situ hybridization study. *J Neuroimmunol*. 1998;86(1):20–9. doi:10.1016/S0165-5728(98)00002-2

215. **Simpson JE, Newcombe J, Cuzner ML, Woodroofe MN**. Expression of monocyte chemoattractant protein-1 and other β- chemokines by resident glia and inflammatory cells in multiple sclerosis lesions. *J Neuroimmunol*. 1998;84(2):238–49. doi:10.1016/S0165-5728(97)00208-7

216. **Mantovani A, Sica A, Sozzani S, Allavena P, Vecchi A, Locati M**. The chemokine system in diverse forms of macrophage activation and polarization. *Trends Immunol*. 2004;25(12):677–86. doi:10.1016/j.it.2004.09.015

217. **Miron VE, Boyd A, Zhao JW, Yuen TJ, Ruckh JM, Shadrach JL, et al.** M2 microglia and macrophages drive oligodendrocyte differentiation during CNS remyelination. *Nat Neurosci*. 2013;16(9):1211–8. doi:10.1038/nn.3469

218. **Weber MS, Prod'homme T, Youssef S, Dunn SE, Rundle CD, Lee L, et al.** Type II monocytes modulate T cell-mediated central nervous system autoimmune disease. *Nat Med*. 2007;13(8):935–43. doi:10.1038/nm1620

219. **Rapalino O, Lazarov-Spiegler O, Agranov E, Velan GJ, Yoles E, Fraidakis M, et al.** Implantation of stimulated homologous macrophages results in partial recovery of paraplegic rats. *Nat Med*. 1998;4(7):814–21. doi:10.1038/nm0798-814

220. **Rawji KS, Mishra MK, Yong VW**. Regenerative capacity of macrophages for remyelination. Vol. 4, Frontiers in Cell and Developmental Biology. 2016. p. 47. doi:10.3389/fcell.2016.00047

221. **Jiang Z, Jiang JX, Zhang GX**. Macrophages: A double-edged sword in experimental

autoimmune encephalomyelitis. Vol. 160, Immunology Letters. 2014. p. 17. doi:10.1016/j.imlet.2014.03.006

222. **Locatelli G, Theodorou D, Kendirli A, Jordão MJC, Staszewski O, Phulphagar K, et al.** Mononuclear phagocytes locally specify and adapt their phenotype in a multiple sclerosis model. *Nat Neurosci*. 2018;21(9):1196–208. doi:10.1038/s41593-018-0212-3

223. **Girvin AM, Dal Canto MC, Miller SD**. CD40/CD40L interaction is essential for the induction of EAE in the absence of CD28-mediated co-stimulation. *J Autoimmun*. 2002;18(2):83–94. doi:10.1006/jaut.2001.0573

224. **Kigerl KA, Gensel JC, Ankeny DP, Alexander JK, Donnelly DJ, Popovich PG**. Identification of Two Distinct Macrophage Subsets with Divergent Effects Causing either Neurotoxicity or Regeneration in the Injured Mouse Spinal Cord. *J Neurosci*. 2009;29(43):13435–44. doi:10.1523/JNEUROSCI.3257-09.2009

225. **Nikić I, Merkler D, Sorbara C, Brinkoetter M, Kreutzfeldt M, Bareyre FM, et al.** A reversible form of axon damage in experimental autoimmune encephalomyelitis and multiple sclerosis. *Nat Med*. 2011;17(4):495–9. doi:10.1038/nm.2324

226. **Yamasaki R, Lu H, Butovsky O, Ohno N, Rietsch AM, Cialic R, et al.** Differential roles of microglia and monocytes in the inflamed central nervous system. *J Exp Med*. 2014;211(8):1533–49. doi:10.1084/jem.20132477

227. **Hill KE, Zollinger L V., Watt HE, Carlson NG, Rose JW**. Inducible nitric oxide synthase in chronic active multiple sclerosis plaques: Distribution, cellular expression and association with myelin damage. *J Neuroimmunol*. 2004;151(1–2):171–9. doi:10.1016/j.jneuroim.2004.02.005

228. **Kuhlmann T, Lingfeld G, Bitsch A, Schuchardt J, Brück W**. Acute axonal damage in multiple sclerosis is most extensive in early disease stages and decreases over time. *Brain*. 2002;125(10):2202–12. doi:10.1093/brain/awf235

229. **Liu C, Li Y, Yu J, Feng L, Hou S, Liu Y, et al.** Targeting the Shift from M1 to M2 Macrophages in Experimental Autoimmune Encephalomyelitis Mice Treated with Fasudil. *PLoS One*. 2013;8(2):54841. doi:10.1371/journal.pone.0054841

230. **Fiorentino DF, Zlotnik A, Vieira P, Mosmann TR, Howard M, Moore KW, et al.** IL-10 acts on the antigen-presenting cell to inhibit cytokine production by Th1 cells. *J Immunol*. 1991;

231. **Gordon S**. Alternative activation of macrophages. Vol. 3, Nature Reviews Immunology. 2003. p. 23–35. doi:10.1038/nri978

232. **Greenhalgh AD, Passos dos Santos R, Zarruk JG, Salmon CK, Kroner A, David S**. Arginase-1 is expressed exclusively by infiltrating myeloid cells in CNS injury and disease. *Brain Behav Immun*. 2016;56:61–7. doi:10.1016/j.bbi.2016.04.013

233. **Jiang HR, Milovanović M, Allan D, Niedbala W, Besnard AG, Fukada SY, et al.** IL-33 attenuates EAE by suppressing IL-17 and IFN-γ production and inducing alternatively activated macrophages. *Eur J Immunol*. 2012;42(7):1804–14. doi:10.1002/eji.201141947

234. **Tierney JB, Kharkrang M, La Flamme AC**. Type II-activated macrophages suppress the development of experimental autoimmune encephalomyelitis. *Immunol Cell Biol*.

2009;87(3):235–40. doi:10.1038/icb.2008.99

235. **Kotter MR, Zhao C, Van Rooijen N, Franklin RJM**. Macrophage-depletion induced impairment of experimental CNS remyelination is associated with a reduced oligodendrocyte progenitor cell response and altered growth factor expression. *Neurobiol Dis*. 2005;18(1):166–75. doi:10.1016/j.nbd.2004.09.019

236. **Giles DA, Washnock-Schmid JM, Duncker PC, Dahlawi S, Ponath G, Pitt D, et al.** Myeloid cell plasticity in the evolution of central nervous system autoimmunity. *Ann Neurol*. 2018;83(1):131–41. doi:10.1002/ana.25128

237. **Béchade C, Colasse S, Diana MA, Rouault M, Bessis A**. NOS2 expression is restricted to neurons in the healthy brain but is triggered in microglia upon inflammation. *Glia*. 2014;62(6):956–63. doi:10.1002/glia.22652

238. **Mendiola AS, Ryu JK, Bardehle S, Meyer-Franke A, Ang KKH, Wilson C, et al.** Transcriptional profiling and therapeutic targeting of oxidative stress in neuroinflammation. *Nat Immunol*. 2020;21(5):513–24. doi:10.1038/s41590-020-0654-0

239. **Prinz M, Tay TL, Wolf Y, Jung S**. Microglia: Unique and common features with other tissue macrophages. Vol. 128, Acta Neuropathologica. 2014. p. 319–31. doi:10.1007/s00401-014-1267-1

240. **Goldmann T, Prinz M**. Role of microglia in CNS autoimmunity. Vol. 2013, Clinical and Developmental Immunology. 2013. doi:10.1155/2013/208093

241. **Bogie JFJJ, Stinissen P, Hendriks JJAA**. Macrophage subsets and microglia in multiple sclerosis. *Acta Neuropathol*. 2014;128(2):191–213. doi:10.1007/s00401-014-1310-2

242. **Ponomarev ED, Shriver LP, Maresz K, Dittel BN**. Microglial cell activation and proliferation precedes the onset of CNS autoimmunity. *J Neurosci Res*. 2005;81(3):374–89. doi:10.1002/jnr.20488

243. **Bhasin M, Wu M, Tsirka SE**. Modulation of microglial/macrophage activation by macrophage inhibitory factor (TKP) or tuftsin (TKPR) attenuates the disease course of experimental autoimmune encephalomyelitis. *BMC Immunol*. 2007;8. doi:10.1186/1471-2172-8-10

244. **Boven LA, Van Meurs M, Van Zwam M, Wierenga-Wolf A, Hintzen RQ, Boot RG, et al.** Myelin-laden macrophages are anti-inflammatory, consistent with foam cells in multiple sclerosis. *Brain*. 2006;129(2):517–26. doi:10.1093/brain/awh707

245. **Liu Y, Hao W, Letiembre M, Walter S, Kulanga M, Neumann H, et al.** Suppression of microglial inflammatory activity by myelin phagocytosis: Role of p47-PHOX-mediated generation of reactive oxygen species. *J Neurosci*. 2006;26(50):12904–13. doi:10.1523/JNEUROSCI.2531-06.2006

246. **Ransohoff RM**. A polarizing question: Do M1 and M2 microglia exist. Vol. 19, Nature Neuroscience. 2016. p. 987–91. doi:10.1038/nn.4338

247. **Van Hove H, Martens L, Scheyltjens I, De Vlaminck K, Pombo Antunes AR, De Prijck S, et al.** A single-cell atlas of mouse brain macrophages reveals unique transcriptional identities shaped by ontogeny and tissue environment. *Nat Neurosci*. 2019; doi:10.1038/s41593-019-0393-4

248. **Mrdjen D, Pavlovic A, Hartmann FJ, Schreiner B, Utz SG, Leung BP, et al.** High-Dimensional Single-Cell Mapping of Central Nervous System Immune Cells Reveals Distinct Myeloid Subsets in Health, Aging, and Disease. *Immunity*. 2018;48(2):380-395.e6. doi:10.1016/j.immuni.2018.01.011

249. **Tallantyre EC, Bø L, Al-Rawashdeh O, Owens T, Polman CH, Lowe JS, et al.** Clinico-pathological evidence that axonal loss underlies disability in progressive multiple sclerosis. *Mult Scler*. 2010;16(4):406–11. doi:10.1177/1352458510364992

250. **Friese MA, Schattling B, Fugger L**. Mechanisms of neurodegeneration and axonal dysfunction in multiple sclerosis. Vol. 10, Nature Reviews Neurology. 2014. p. 225–38. doi:10.1038/nrneurol.2014.37

251. **Fischer MT, Wimmer I, Höftberger R, Gerlach S, Haider L, Zrzavy T, et al.** Disease-specific molecular events in cortical multiple sclerosis lesions. *Brain*. 2013;136(6):1799–815. doi:10.1093/brain/awt110

252. **Trapp BD, Stys PK**. Virtual hypoxia and chronic necrosis of demyelinated axons in multiple sclerosis. Vol. 8, The Lancet Neurology. 2009. p. 280–91. doi:10.1016/S1474-4422(09)70043-2

253. **Witte ME, Geurts JJG, de Vries HE, van der Valk P, van Horssen J**. Mitochondrial dysfunction: A potential link between neuroinflammation and neurodegeneration? Vol. 10, Mitochondrion. 2010. p. 411–8. doi:10.1016/j.mito.2010.05.014

254. **Mecocci P, MacGarvey U, Kaufman AE, Koontz D, Shoffner JM, Wallace DC, et al.** Oxidative damage to mitochondrial DNA shows marked age-dependent increases in human brain. *Ann Neurol*. 1993;34(4):609–16. doi:10.1002/ana.410340416

255. **Campbell GR, Ziabreva I, Reeve AK, Krishnan KJ, Reynolds R, Howell O, et al.** Mitochondrial DNA deletions and neurodegeneration in multiple sclerosis. *Ann Neurol*. 2011;69(3):481–92. doi:10.1002/ana.22109

256. **Mahad D, Ziabreva I, Lassmann H, Turnbull D**. Mitochondrial defects in acute multiple sclerosis lesions. *Brain*. 2008;131(7):1722–35. doi:10.1093/brain/awn105

257. **Witte ME, Lars B, Rodenburg RJ, Belien JA, Musters R, Hazes T, et al.** Enhanced number and activity of mitochondria in multiple sclerosis lesions. *J Pathol*. 2009;219(2):193–204. doi:10.1002/path.2582

258. **Campbell GR, Ohno N, Turnbull DM, Mahad DJ**. Mitochondrial changes within axons in multiple sclerosis: An update. Vol. 25, Current Opinion in Neurology. 2012. p. 221–30. doi:10.1097/WCO.0b013e3283533a25

259. **de Barcelos IP, Troxell RM, Graves JS**. Mitochondrial dysfunction and multiple sclerosis. *Biology (Basel)*. 2019;8(2). doi:10.3390/biology8020037

260. **Moini H, Packer L, Saris NEL**. Antioxidant and prooxidant activities of α-lipoic acid and dihydrolipoic acid. Vol. 182, Toxicology and Applied Pharmacology. 2002. p. 84–90. doi:10.1006/taap.2002.9437

261. **Klopstock T, Yu-Wai-Man P, Dimitriadis K, Rouleau J, Heck S, Bailie M, et al.** A randomized placebo-controlled trial of idebenone in Leber's hereditary optic neuropathy. *Brain*. 2011;134(9):2677–86. doi:10.1093/brain/awr170

262. **Kosa P, Wu T, Phillips J, Leinonen M, Masvekar R, Komori M, et al.** Idebenone does not

inhibit disability progression in primary progressive MS. *Mult Scler Relat Disord*. 2020;45. doi:10.1016/j.msard.2020.102434

263. **Waslo C, Bourdette D, Gray N, Wright K, Spain R**. Lipoic Acid and Other Antioxidants as Therapies for Multiple Sclerosis. Vol. 21, Current Treatment Options in Neurology. 2019. doi:10.1007/s11940-019-0566-1

264. **Loy BD, Fling BW, Horak FB, Bourdette DN, Spain RI**. Effects of lipoic acid on walking performance, gait, and balance in secondary progressive multiple sclerosis. *Complement Ther Med*. 2018;41:169–74. doi:10.1016/j.ctim.2018.09.006

265. **Spain R, Powers K, Murchison C, Heriza E, Winges K, Yadav V, et al.** Lipoic acid in secondary progressive MS. *Neurol Neuroimmunol NeuroInflammation*. 2017;4(5). doi:10.1212/NXI.0000000000000374

266. **Reese TA, Liang HE, Tager AM, Luster AD, Van Rooijen N, Voehringer D, et al.** Chitin induces accumulation in tissue of innate immune cells associated with allergy. *Nature*. 2007;447(7140):92–6. doi:10.1038/nature05746

267. **Feng G, Mellor RH, Bernstein M, Keller-Peck C, Nguyen QT, Wallace M, et al.** Imaging Neuronal Subsets in Transgenic Mice Expressing Multiple Spectral Variants of GFP. *Neuron*. 2000;28(1):41–51. doi:10.1016/S0896-6273(00)00084-2

268. **Moechars D, Dewachter I, Lorent K, Reversé D, Baekelandt V, Naidu A, et al.** Early phenotypic changes in transgenic mice that overexpress different mutants of amyloid precursor protein in brain. *J Biol Chem*. 1999;274(10):6483–92. doi:10.1074/jbc.274.10.6483

269. **Bayraktar EC, Baudrier L, Özerdem C, Lewis CA, Chan SH, Kunchok T, et al.** MITO-Tag Mice enable rapid isolation and multimodal profiling of mitochondria from specific cell types in vivo. *Proc Natl Acad Sci U S A*. 2019;116(1):303–12. doi:10.1073/pnas.1816656115

270. **Fecher C, Trovò L, Müller SA, Snaidero N, Wettmarshausen J, Heink S, et al.** Cell-type-specific profiling of brain mitochondria reveals functional and molecular diversity. *Nat Neurosci*. 2019;22(10):1731–42. doi:10.1038/s41593-019-0479-z

271. **Tai Y-H**. Mitochondrial pathology in acute and chronic neuroinflammation. 2020.

272. **Adelmann M, Wood J, Benzel I, Fiori P, Lassmann H, Matthieu JM, et al.** The N-terminal domain of the myelin oligodendrocyte glycoprotein (MOG) induces acute demyelinating experimental autoimmune encephalomyelitis in the Lewis rat. *J Neuroimmunol*. 1995;63(1):17–27. doi:10.1016/0165-5728(95)00124-7

273. **R Core Development Team, R Core Team, Team RDC**. R: A Language and Environment for Statistical Computing. Vienna, Austria. 2019.

274. **Van Rossum, Guido and Drake FL, van Rossum G, Drake FL**. Python 3 Reference Manual. Scotts Valley, CA. 2009.

275. **Laemmli UK**. Cleavage of structural proteins during the assembly of the head of bacteriophage T4. *Nature*. 1970;227(5259):680–5. doi:10.1038/227680a0

276. **Abdul-Majid KB, Jirholt J, Stadelmann C, Stefferl A, Kjellén P, Wallström E, et al.** Screening of several H-2 congenic mouse strains identified H-2(q) mice as highly susceptible to MOG-induced EAE with minimal adjuvant requirement. *J Neuroimmunol*.

2000;111(1–2):23–33. doi:10.1016/S0165-5728(00)00360-X

277. **Miller SD, Karpus WJ**. Experimental Autoimmune Encephalomyelitis in the Mouse. In: Current Protocols in Immunology. 2007. p. 181–94. doi:10.1002/0471142735.im1501s77

278. **Martin E, El-Behi M, Fontaine B, Delarasse C**. Analysis of microglia and monocyte-derived macrophages from the central nervous system by flow cytometry. *J Vis Exp*. 2017;2017(124):55781. doi:10.3791/55781

279. **Ramesha S, Rayaprolu S, Rangaraju S**. Flow cytometry approach to characterize phagocytic properties of acutely-isolated adult microglia and brain macrophages in vitro. *J Vis Exp*. 2020;2020(160):1–12. doi:10.3791/61467

280. **Hermiston ML, Xu Z, Weiss A**. CD45: A critical regulator of signaling thresholds in immune cells. Vol. 21, Annual Review of Immunology. 2003. p. 107–37. doi:10.1146/annurev.immunol.21.120601.140946

281. **Solovjov DA, Pluskota E, Plow EF**. Distinct roles for the α and β subunits in the functions of integrin αMβ2. *J Biol Chem*. 2005;280(2):1336–45. doi:10.1074/jbc.M406968200

282. **Christensen JE, Andreasen S, Christensen JP, Thomsen AR**. CD11b expression as a marker to distinguish between recently activated effector CD8+ T cells and memory cells. *Int Immunol*. 2001;13(4):593–600. doi:10.1093/intimm/13.4.593

283. **Dong D, Zheng L, Lin J, Zhang B, Zhu Y, Li N, et al.** Structural basis of assembly of the human T cell receptor–CD3 complex. *Nature*. 2019;573(7775):546–52. doi:10.1038/s41586-019-1537-0

284. **Cascalho M, Wong J, Brown J, Jäck H-M, Steinberg C, Wabl M**. A B220–, CD19– population of B cells in the peripheral blood of quasimonoclonal mice. *Int Immunol*. 2000;12(1):29–35. doi:10.1093/intimm/12.1.29

285. **Isobe M, Huebner K, Maddon PJ, Littman DR, Axel R, Croce CM**. The gene encoding the T-cell surface protein T4 is located on human chromosome 12. *Proc Natl Acad Sci U S A*. 1986;83(12):4399–402. doi:10.1073/pnas.83.12.4399

286. **Kantzer CG, Boutin C, Herzig ID, Wittwer C, Reiß S, Tiveron MC, et al.** Anti-ACSA-2 defines a novel monoclonal antibody for prospective isolation of living neonatal and adult astrocytes. *Glia*. 2017;65(6):990–1004. doi:10.1002/glia.23140

287. **Sommer I, Schachner M**. Monoclonal antibodies (O1 to O4) to oligodendrocyte cell surfaces: An immunocytological study in the central nervous system. *Dev Biol*. 1981;83(2):311–27. doi:10.1016/0012-1606(81)90477-2

288. **Kuhn S, Gritti L, Crooks D, Dombrowski Y**. Oligodendrocytes in Development, Myelin Generation and Beyond. Vol. 8, Cells. 2019. p. 1424. doi:10.3390/cells8111424

289. **Podbielska M, Banik NL, Kurowska E, Hogan EL**. Myelin recovery in multiple sclerosis: The challenge of remyelination. Vol. 3, Brain Sciences. 2013. p. 1282–324. doi:10.3390/brainsci3031282

290. **Nishiyama A, Komitova M, Suzuki R, Zhu X**. Polydendrocytes (NG2 cells): Multifunctional cells with lineage plasticity. *Nat Rev Neurosci*. 2009;10(1):9–22. doi:10.1038/nrn2495

291. **Karayel O, Michaelis AC, Mann M, Schulman BA, Langlois CR**. DIA-based systems biology approach unveils E3 ubiquitin ligase-dependent responses to a metabolic shift. doi:10.1073/pnas.2020197117/-/DCSupplemental

292. **Love MI, Huber W, Anders S**. Moderated estimation of fold change and dispersion for RNA-seq data with DESeq2. *Genome Biol 2014 1512*. 2014;15(12):1–21. doi:10.1186/S13059-014-0550-8

293. **Wang S, Li W, Hu L, Cheng J, Yang H, Liu Y**. NAguideR: Performing and prioritizing missing value imputations for consistent bottom-up proteomic analyses. *Nucleic Acids Res*. 2020;48(14):83. doi:10.1093/nar/gkaa498

294. **Anders S, Huber W**. Differential expression analysis for sequence count data. *Genome Biol 2010 1110*. 2010;11(10):1–12. doi:10.1186/GB-2010-11-10-R106

295. **Lakens D**. Calculating and reporting effect sizes to facilitate cumulative science: A practical primer for t-tests and ANOVAs. *Front Psychol*. 2013; doi:10.3389/fpsyg.2013.00863

296. **Cohen J**. Statistical Power Analysis for the Behavioural Science (2nd Edition). Statistical Power Anaylsis for the Behavioral Sciences. 1988.

297. **Benjamini Y, Hochberg Y**. Controlling the False Discovery Rate: A Practical and Powerful Approach to Multiple Testing. *J R Stat Soc Ser B*. 1995;57(1):289–300.

298. **McInnes L, Healy J, Melville J**. UMAP: Uniform Manifold Approximation and Projection for Dimension Reduction. 2018;

299. **Subramanian A, Tamayo P, Mootha VK, Mukherjee S, Ebert BL, Gillette MA, et al.** Gene set enrichment analysis: A knowledge-based approach for interpreting genome-wide expression profiles. *Proc Natl Acad Sci U S A*. 2005;102(43):15545–50. doi:10.1073/pnas.0506580102

300. **Szklarczyk D, Gable AL, Lyon D, Junge A, Wyder S, Huerta-Cepas J, et al.** STRING v11: Protein-protein association networks with increased coverage, supporting functional discovery in genome-wide experimental datasets. *Nucleic Acids Res*. 2019;47(D1):D607–13. doi:10.1093/nar/gky1131

301. **Chen EY, Tan CM, Kou Y, Duan Q, Wang Z, Meirelles G V., et al.** Enrichr: Interactive and collaborative HTML5 gene list enrichment analysis tool. *BMC Bioinformatics*. 2013;14(1):1–14. doi:10.1186/1471-2105-14-128

302. **Qiao W, Wang W, Laurenti E, Turinsky AL, Wodak SJ, Bader GD, et al.** Intercellular network structure and regulatory motifs in the human hematopoietic system. *Mol Syst Biol*. 2014;10(7):741. doi:10.15252/msb.20145141

303. **Calvo SE, Clauser KR, Mootha VK**. MitoCarta2.0: An updated inventory of mammalian mitochondrial proteins. *Nucleic Acids Res*. 2016;44(D1):D1251–7. doi:10.1093/nar/gkv1003

304. **Kanehisa M, Furumichi M, Sato Y, Ishiguro-Watanabe M, Tanabe M**. KEGG: Integrating viruses and cellular organisms. *Nucleic Acids Res*. 2021;49(D1):D545–51. doi:10.1093/nar/gkaa970

305. **Kanehisa M**. Toward understanding the origin and evolution of cellular organisms. Vol. 28, Protein Science. 2019. p. 1947–51. doi:10.1002/pro.3715

306. **Kanehisa M, Goto S**. KEGG: Kyoto Encyclopedia of Genes and Genomes. Vol. 28, Nucleic Acids Research. 2000. p. 27–30. doi:10.1093/nar/28.1.27

307. **Efremova M, Vento-Tormo M, Teichmann SA, Vento-Tormo R**. CellPhoneDB: inferring cell–cell communication from combined expression of multi-subunit ligand–receptor complexes. *Nat Protoc*. 2020;15(4):1484–506. doi:10.1038/s41596-020-0292-x

308. **Wang J, Wang J, Wang J, Yang B, Weng Q, He Q**. Targeting microglia and macrophages: A potential treatment strategy for multiple sclerosis. *Front Pharmacol*. 2019;10(MAR). doi:10.3389/fphar.2019.00286

309. **Van Wageningen TA, Vlaar E, Kooij G, Jongenelen CAM, Geurts JJG, Van Dam AM**. Regulation of microglial TMEM119 and P2RY12 immunoreactivity in multiple sclerosis white and grey matter lesions is dependent on their inflammatory environment. *Acta Neuropathol Commun*. 2019;7(1). doi:10.1186/s40478-019-0850-z

310. **Cahoy JD, Emery B, Kaushal A, Foo LC, Zamanian JL, Christopherson KS, et al.** A Transcriptome Database for Astrocytes, Neurons, and Oligodendrocytes: A New Resource for Understanding Brain Development and Function. *J Neurosci*. 2008;28(1):264–78. doi:10.1523/JNEUROSCI.4178-07.2008

311. **Hoogendijk AJ, Pourfarzad F, Aarts CEM, Meijer AB**. Dynamic Transcriptome-Proteome Correlation Networks Reveal Human Myeloid Differentiation and Neutrophil-Specific Programming Graphical Abstract Highlights d Dissection of transcriptome-proteome networks underlying neutrophil differentiation d Distinct patterns of RNA-protein kinetics correlate with biological processes d Discordant dynamics allows for functional annotation of granule proteins d Anabolic collapse paradoxically coincides with gain in neutrophil function. 2019; doi:10.1016/j.celrep.2019.10.082

312. **Papayannopoulos V, Zychlinsky A**. NETs: a new strategy for using old weapons. Vol. 30, Trends in Immunology. 2009. p. 513–21. doi:10.1016/j.it.2009.07.011

313. **Schenten V, Plançon S, Jung N, Hann J, Bueb JL, Bréchard S, et al.** Secretion of the phosphorylated form of S100A9 from neutrophils is essential for the proinflammatory functions of extracellular S100A8/A9. *Front Immunol*. 2018;9(MAR):447. doi:10.3389/fimmu.2018.00447

314. **Trinchieri G, Aste-Amezaga M, Ma X, Sartori A**. Molecular Mechanisms of the Induction of IL-12. 2021.

315. **Erdei A, Lukácsi S, Mácsik-Valent B, Nagy-Baló Z, Kurucz I, Bajtay Z**. Non-identical twins: Different faces of CR3 and CR4 in myeloid and lymphoid cells of mice and men. Vol. 85, Seminars in Cell and Developmental Biology. 2019. p. 110–21. doi:10.1016/j.semcdb.2017.11.025

316. **Canton M, Sánchez-Rodríguez R, Spera I, Venegas FC, Favia M, Viola A, et al.** Reactive Oxygen Species in Macrophages: Sources and Targets. *Front Immunol*. 2021;12:4077. doi:10.3389/FIMMU.2021.734229/BIBTEX

317. **Bergaglio T, Luchicchi A, Schenk GJ**. Engine Failure in Axo-Myelinic Signaling: A Potential Key Player in the Pathogenesis of Multiple Sclerosis. *Front Cell Neurosci*. 2021;15:17. doi:10.3389/FNCEL.2021.610295/BIBTEX

318. **Tai Y-H, Engels D, Merkler D, Misgeld T, Kerschensteiner M**. Targeting TCA cycle

dysbalance can amend widespread axonal energy deficits in neuroinflammatory lesions (2022, in preparation).

319. **Mosmann TR, Coffman RL**. Heterogeneity of Cytokine Secretion Patterns and Functions of Helper T Cells. *Adv Immunol*. 1989;46(C):111–47. doi:10.1016/S0065-2776(08)60652-5

320. **Mills CD, Kincaid K, Alt JM, Heilman MJ, Hill AM**. M-1/M-2 Macrophages and the Th1/Th2 Paradigm. *J Immunol*. 2000;164(12):6166–73. doi:10.4049/jimmunol.164.12.6166

321. **O'Garra A, Murphy K**. Role of cytokines in determining T-lymphocyte function. *Curr Opin Immunol*. 1994;6(3):458–66. doi:10.1016/0952-7915(94)90128-7

322. **Munder M, Eichmann K, Morán JM, Centeno F, Soler G, Modolell M**. Th1/Th2-regulated expression of arginase isoforms in murine macrophages and dendritic cells. *J Immunol*. 1999;163(7):3771–7.

323. **Kroncke KD, Fehsel K, Kolb-Bachofen V**. Inducible Nitric Oxide Synthase and Its Product Nitric Oxide, a Small Molecule with Complex Biological Activities. *Biol Chem Hoppe Seyler*. 1995;376(6):327–56. doi:10.1515/BCHM3.1995.376.6.327

324. **Cross AH, Manning PT, Keeling RM, Schmidt RE, Misko TP**. Peroxynitrite formation within the central nervous system in active multiple sclerosis. *J Neuroimmunol*. 1998;88(1–2):45–56. doi:10.1016/S0165-5728(98)00078-2

325. **Brundin L, Morcos E, Olsson T, Wiklund NP, Andersson M**. Increased intrathecal nitric oxide formation in multiple sclerosis; cerebrospinal fluid nitrite as activity marker. *Eur J Neurol*. 1999;6(5):585–90. doi:10.1046/j.1468-1331.1999.650585.x

326. **Svenningsson A, Petersson A-S, Andersen O, Hansson GK**. Nitric oxide metabolites in CSF of patients with MS are related to clinical disease course. *Neurology*. 1999;53(8):1880–1880. doi:10.1212/WNL.53.8.1880

327. **Giovannoni G**. Cerebrospinal fluid and serum nitric oxide metabolites in patients with multiple sclerosis. *Mult Scler J*. 1998;4(1):27–30. doi:10.1177/135245859800400107

328. **Johnson AW, Land JM, Thompson EJ, Bolanos JP, Clark JB, Heales SJ**. Evidence for increased nitric oxide production in multiple sclerosis. *J Neurol Neurosurg Psychiatry*. 1995;58(1):107–107. doi:10.1136/jnnp.58.1.107

329. **Peltola J, Ukkonen M, Moilanen E, Elovaara I**. Increased nitric oxide products in CSF in primary progressive MS may reflect brain atrophy. *Neurology*. 2001;57(5):895–6. doi:10.1212/WNL.57.5.895

330. **Yamashita T, Ando Y, Obayashi K, Uchino M, Ando M**. Changes in nitrite and nitrate (NO2−/NO3−) levels in cerebrospinal fluid of patients with multiple sclerosis. *J Neurol Sci*. 1997;153(1):32–4. doi:10.1016/S0022-510X(97)00183-4

331. **Smith KJ, Lassmann H**. The role of nitric oxide in multiple sclerosis. *Lancet Neurol*. 2002;1(4):232–41. doi:10.1016/S1474-4422(02)00102-3

332. **Smith KJ, Kapoor R, Felts PA**. Demyelination: The Role of Reactive Oxygen and Nitrogen Species. *Brain Pathol*. 2006;9(1):69–92. doi:10.1111/j.1750-3639.1999.tb00212.x

333. **Yang Z, Ming X-F**. Functions of Arginase Isoforms in Macrophage Inflammatory

Responses: Impact on Cardiovascular Diseases and Metabolic Disorders. *Front Immunol*. 2014;5(OCT). doi:10.3389/FIMMU.2014.00533

334. **Funes SC, Rios M, Escobar-Vera J, Kalergis AM**. Implications of macrophage polarization in autoimmunity. *Immunology*. 2018;154(2):186–95. doi:10.1111/IMM.12910

335. **Mishra MK, Wee Yong V**. Myeloid cells-targets of medication in multiple sclerosis. *Nat Rev Neurol*. 2016;12(9):539–51. doi:10.1038/nrneurol.2016.110

336. **Prinz M, Priller J**. The role of peripheral immune cells in the CNS in steady state and disease. Vol. 20, Nature Neuroscience. 2017. doi:10.1038/nn.4475

337. **Goldmann T, Wieghofer P, Müller PF, Wolf Y, Varol D, Yona S, et al.** A new type of microglia gene targeting shows TAK1 to be pivotal in CNS autoimmune inflammation. *Nat Neurosci*. 2013;16(11). doi:10.1038/nn.3531

338. **Vogel DYS, Vereyken EJF, Glim JE, Heijnen PDAM, Moeton M, van der Valk P, et al.** Macrophages in inflammatory multiple sclerosis lesions have an intermediate activation status. *J Neuroinflammation*. 2013;10(1):1. doi:10.1186/1742-2094-10-35

339. **Mikita J, Dubourdieu-Cassagno N, Deloire MS, Vekris A, Biran M, Raffard G, et al.** Altered M1/M2 activation patterns of monocytes in severe relapsing experimental rat model of multiple sclerosis. Amelioration of clinical status by M2 activated monocyte administration. *Mult Scler J*. 2011;17(1):2–15. doi:10.1177/1352458510379243

340. **Weng Q, Wang J, Wang J, Wang J, Sattar F, Zhang Z, et al.** Lenalidomide regulates CNS autoimmunity by promoting M2 macrophages polarization article. *Cell Death Dis*. 2018;9(2). doi:10.1038/s41419-018-0290-x

341. **Butovsky O, Landa G, Kunis G, Ziv Y, Avidan H, Greenberg N, et al.** Induction and blockage of oligodendrogenesis by differently activated microglia in an animal model of multiple sclerosis. *J Clin Invest*. 2006;116(4). doi:10.1172/JCI26836

342. **Cignarella F, Filipello F, Bollman B, Cantoni C, Locca A, Mikesell R, et al.** TREM2 activation on microglia promotes myelin debris clearance and remyelination in a model of multiple sclerosis. *Acta Neuropathol*. 2020;140(4). doi:10.1007/s00401-020-02193-z

343. **Schnoor M, Cullen P, Lorkowski J, Stolle K, Robenek H, Troyer D, et al.** Production of Type VI Collagen by Human Macrophages: A New Dimension in Macrophage Functional Heterogeneity. *J Immunol*. 2008;180(8). doi:10.4049/jimmunol.180.8.5707

344. **Bowery NG, Bettler B, Froestl W, Gallagher JP, Marshall F, Raiteri M, et al.** International Union of Pharmacology. XXXIII. Mammalian γ-aminobutyric acidb receptors: Structure and function. Vol. 54, Pharmacological Reviews. 2002. doi:10.1124/pr.54.2.247

345. **Bhandage AK, Olivera GC, Kanatani S, Thompson E, Loré K, Varas-Godoy M, et al.** A motogenic gabaergic system of mononuclear phagocytes facilitates dissemination of coccidian parasites. *Elife*. 2020;9. doi:10.7554/eLife.60528

346. **Alam S, Laughton DL, Walding A, Wolstenholme AJ**. Human peripheral blood mononuclear cells express GABAA receptor subunits. *Mol Immunol*. 2006;43(9):1432–42. doi:10.1016/J.MOLIMM.2005.07.025

347. **Bhat R, Axtell R, Mitra A, Miranda M, Lock C, Tsien RW, et al.** Inhibitory role for GABA in autoimmune inflammation. *Proc Natl Acad Sci U S A*. 2010;107(6).

doi:10.1073/pnas.0915139107

348. **Januzi L, Poirier JW, Maksoud MJE, Xiang YY, Veldhuizen RAW, Gill SE, et al.** Autocrine GABA signaling distinctively regulates phenotypic activation of mouse pulmonary macrophages. *Cell Immunol*. 2018;332. doi:10.1016/j.cellimm.2018.07.001

349. **Shi X, Wan Y, Wang N, Xiang J, Wang T, Yang X, et al.** Selection of a picomolar antibody that targets CXCR2-mediated neutrophil activation and alleviates EAE symptoms. *Nat Commun 2021 121*. 2021;12(1):1–14. doi:10.1038/s41467-021-22810-z

350. **Peerlings D, Mimpen M, Damoiseaux J**. The IL-2 – IL-2 receptor pathway: Key to understanding multiple sclerosis. *J Transl Autoimmun*. 2021;4:100123. doi:10.1016/J.JTAUTO.2021.100123

351. **Sabelko-Downes KA, Cross AH, Russell JH**. Dual Role for Fas Ligand in the Initiation of and Recovery from Experimental Allergic Encephalomyelitis. *J Exp Med*. 1999;189(8):1195. doi:10.1084/JEM.189.8.1195

352. **Mehta N, Maddineni S, Mathews II, Andres Parra Sperberg R, Huang PS, Cochran JR**. Structure and Functional Binding Epitope of V-domain Ig Suppressor of T Cell Activation. *Cell Rep*. 2019;28(10):2509-2516.e5. doi:10.1016/J.CELREP.2019.07.073

353. **Wang L, Rubinstein R, Lines JL, Wasiuk A, Ahonen C, Guo Y, et al.** VISTA, a novel mouse Ig superfamily ligand that negatively regulates T cell responses. *J Exp Med*. 2011;208(3):577–92. doi:10.1084/JEM.20100619

354. **ElTanbouly MA, Zhao Y, Schaafsma E, Burns CM, Mabaera R, Cheng C, et al.** VISTA: A Target to Manage the Innate Cytokine Storm. *Front Immunol*. 2021;11:3643. doi:10.3389/FIMMU.2020.595950/BIBTEX

355. **Yeboah M, Papagregoriou C, Des CJ, Claude Chan HT, Hu G, McPartlan JS, et al.** LILRB3 (ILT5) is a myeloid cell checkpoint that elicits profound immunomodulation. *JCI Insight*. 2020;5(18). doi:10.1172/JCI.INSIGHT.141593

356. **Yang Y, Ye Y-C, Chen Y, Zhao J-L, Gao C-C, Han H, et al.** Crosstalk between hepatic tumor cells and macrophages via Wnt/β-catenin signaling promotes M2-like macrophage polarization and reinforces tumor malignant behaviors. *Cell Death Dis 2018 98*. 2018;9(8):1–14. doi:10.1038/s41419-018-0818-0

357. **Feng Y, Ren J, Gui Y, Wei W, Shu B, Lu Q, et al.** Wnt/β-Catenin–Promoted Macrophage Alternative Activation Contributes to Kidney Fibrosis. *J Am Soc Nephrol*. 2018;29(1):182–93. doi:10.1681/ASN.2017040391

358. **Vergadi E, Ieronymaki E, Lyroni K, Vaporidi K, Tsatsanis C**. Akt Signaling Pathway in Macrophage Activation and M1/M2 Polarization. *J Immunol*. 2017;198(3):1006–14. doi:10.4049/JIMMUNOL.1601515

359. **Orecchioni M, Ghosheh Y, Pramod AB, Ley K**. Macrophage polarization: Different gene signatures in M1(Lps+) vs. Classically and M2(LPS-) vs. Alternatively activated macrophages. *Front Immunol*. 2019;10(MAY):1084. doi:10.3389/FIMMU.2019.01084/BIBTEX

360. **Han H, Lee S, Lee I**. NGSEA: Network-Based Gene Set Enrichment Analysis for Interpreting Gene Expression Phenotypes with Functional Gene Sets. *Mol Cells*. 2019;42(8):579. doi:10.14348/MOLCELLS.2019.0065

361. **Alexeyenko A, Lee W, Pernemalm M, Guegan J, Dessen P, Lazar V, et al.** Network enrichment analysis: extension of gene-set enrichment analysis to gene networks. *BMC Bioinforma 2012 131*. 2012;13(1):1–11. doi:10.1186/1471-2105-13-226

362. **Ping YQ, Mao C, Xiao P, Zhao RJ, Jiang Y, Yang Z, et al.** Structures of the glucocorticoid-bound adhesion receptor GPR97–Go complex. *Nature*. 2021;589(7843):620–6. doi:10.1038/s41586-020-03083-w

363. **Bai M, Grieshaber-Bouyer R, Wang J, Schmider AB, Wilson ZS, Zeng L, et al.** CD177 modulates human neutrophil migration through activation-mediated integrin and chemoreceptor regulation. *Blood*. 2017;130(19):2092–100. doi:10.1182/blood-2017-03-768507

364. **Hojgaard A, Close R, Dunn DM, Weiss RB, Weis JJ, Weis JH**. Altered localization of CXCL13 expressing cells in mice deficient in Pactolus following an inflammatory stimulus. *Immunology*. 2006;119(2):212–23. doi:10.1111/j.1365-2567.2006.02426.x

365. **Yamamoto S, Higuchi Y, Yoshiyama K, Shimizu E, Kataoka M, Hijiya N, et al.** ADAM family proteins in the immune system. Vol. 20, Immunology Today. 1999. p. 278–84. doi:10.1016/S0167-5699(99)01464-4

366. **Brinkmann V, Reichard U, Goosmann C, Fauler B, Uhlemann Y, Weiss DS, et al.** Neutrophil Extracellular Traps Kill Bacteria. *Science (80-)*. 2004;303(5663):1532–5. doi:10.1126/SCIENCE.1092385

367. **Garcia-Romo GS, Caielli S, Vega B, Connolly J, Allantaz F, Xu Z, et al.** Netting Neutrophils Are Major Inducers of Type I IFN Production in Pediatric Systemic Lupus Erythematosus. *Sci Transl Med*. 2011;3(73):73ra20-73ra20. doi:10.1126/scitranslmed.3001201

368. **Söderberg D, Segelmark M**. Neutrophil Extracellular Traps in ANCA-Associated Vasculitis. *Front Immunol*. 2016;7(JUN). doi:10.3389/fimmu.2016.00256

369. **Doster RS, Rogers LM, Gaddy JA, Aronoff DM**. Macrophage Extracellular Traps: A Scoping Review. Vol. 10, Journal of Innate Immunity. 2018. p. 3–13. doi:10.1159/000480373

370. **Halder LD, Abdelfatah MA, Jo EAH, Jacobsen ID, Westermann M, Beyersdorf N, et al.** Factor H Binds to Extracellular DNA Traps Released from Human Blood Monocytes in Response to Candida albicans. *Front Immunol*. 2016;7(JAN). doi:10.3389/FIMMU.2016.00671

371. **Je S, Quan H, Yoon Y, Na Y, Kim B-J, Seok SH**. Mycobacterium massiliense Induces Macrophage Extracellular Traps with Facilitating Bacterial Growth. *PLoS One*. 2016;11(5):e0155685. doi:10.1371/JOURNAL.PONE.0155685

372. **Wang S, Song R, Wang Z, Jing Z, Wang S, Ma J**. S100A8/A9 in Inflammation. *Front Immunol*. 2018;9(JUN):1298. doi:10.3389/FIMMU.2018.01298

373. **Tydén H, Lood C, Gullstrand B, Jönsen A, Ivars F, Leanderson T, et al.** Pro-inflammatory S100 proteins are associated with glomerulonephritis and anti-dsDNA antibodies in systemic lupus erythematosus. *Lupus*. 2017;26(2):139–49. doi:10.1177/0961203316655208

374. **Kang KY, Woo J-W, Park S-H**. S100A8/A9 as a biomarker for synovial inflammation and

joint damage in patients with rheumatoid arthritis. *Korean J Intern Med*. 2014;29(1):12. doi:10.3904/KJIM.2014.29.1.12

375. **Björk P, Björk A, Vogl T, Stenström M, Liberg D, Olsson A, et al.** Identification of Human S100A9 as a Novel Target for Treatment of Autoimmune Disease via Binding to Quinoline-3-Carboxamides. *PLOS Biol*. 2009;7(4):e1000097. doi:10.1371/JOURNAL.PBIO.1000097

376. **Brunmark C, Runström A, Ohlsson L, Sparre B, Brodin T, Åström M, et al.** The new orally active immunoregulator laquinimod (ABR-215062) effectively inhibits development and relapses of experimental autoimmune encephalomyelitis. *J Neuroimmunol*. 2002;130(1–2):163–72. doi:10.1016/S0165-5728(02)00225-4

377. **Giovannoni G, Knappertz V, Steinerman JR, Tansy AP, Li T, Krieger S, et al.** A randomized, placebo-controlled, phase 2 trial of laquinimod in primary progressive multiple sclerosis. *Neurology*. 2020;95(8):e1027–40. doi:10.1212/WNL.0000000000010284

378. **Polman C, Barkhof F, Sandberg-Wollheim M, Linde A, Nordle O, Nederman T**. Treatment with laquinimod reduces development of active MRI lesions in relapsing MS. *Neurology*. 2005;64(6):987–91. doi:10.1212/01.WNL.0000154520.48391.69

379. **Thöne J, Linker RA**. Laquinimod in the treatment of multiple sclerosis: a review of the data so far. *Drug Des Devel Ther*. 2016;10:1111. doi:10.2147/DDDT.S55308

380. **Wang N, Liang H, Zen K**. Molecular Mechanisms That Influence the Macrophage M1–M2 Polarization Balance. *Front Immunol*. 2014;5(NOV). doi:10.3389/FIMMU.2014.00614

381. **Biswas SK, Mantovani A**. Macrophage plasticity and interaction with lymphocyte subsets: cancer as a paradigm. *Nat Immunol 2010 1110*. 2010;11(10):889–96. doi:10.1038/ni.1937

382. **Ma L, Sun P, Zhang J-C, Zhang Q, Yao S-L**. Proinflammatory effects of S100A8/A9 via TLR4 and RAGE signaling pathways in BV-2 microglial cells. *Int J Mol Med*. 2017;40(1):31. doi:10.3892/IJMM.2017.2987

383. **Ehrchen JM, Sunderkötter C, Foell D, Vogl T, Roth J**. The endogenous Toll-like receptor 4 agonist S100A8/S100A9 (calprotectin) as innate amplifier of infection, autoimmunity, and cancer. *J Leukoc Biol*. 2009;86(3):557–66. doi:10.1189/jlb.1008647

384. **Reynolds JM, Martinez GJ, Chung Y, Dong C**. Toll-like receptor 4 signaling in T cells promotes autoimmune inflammation. *Proc Natl Acad Sci*. 2012;109(32):13064–9. doi:10.1073/PNAS.1120585109

385. **Sauer R-S, Hackel D, Morschel L, Sahlbach H, Wang Y, Mousa SA, et al.** Toll like Receptor (TLR)-4 as a Regulator of Peripheral Endogenous Opioid-Mediated Analgesia in Inflammation. *Mol Pain*. 2014;10(1):1744-8069-10–10. doi:10.1186/1744-8069-10-10

386. **Orr JS, Puglisi MJ, Ellacott KLJ, Lumeng CN, Wasserman DH, Hasty AH**. Toll-like Receptor 4 Deficiency Promotes the Alternative Activation of Adipose Tissue Macrophages. *Diabetes*. 2012;61(11):2718–27. doi:10.2337/db11-1595

387. **Urushima H, Fujimoto M, Mishima T, Ohkawara T, Honda H, Lee H, et al.** Leucine-rich

alpha 2 glycoprotein promotes Th17 differentiation and collagen-induced arthritis in mice through enhancement of TGF-β-Smad2 signaling in naïve helper T cells. *Arthritis Res Ther*. 2017;19(1):137. doi:10.1186/s13075-017-1349-2

388. **Listik E, Horst B, Choi AS, Lee NY, Győrffy B, Mythreye K**. A bioinformatic analysis of the inhibin-betaglycan-endoglin/CD105 network reveals prognostic value in multiple solid tumors. *PLoS One*. 2021;16(4):e0249558. doi:10.1371/JOURNAL.PONE.0249558

389. **Mirshafiey A, Mohsenzadegan M**. TGF-β as a promising option in the treatment of multiple sclerosis. *Neuropharmacology*. 2009;56(6–7):929–36. doi:10.1016/J.NEUROPHARM.2009.02.007

390. **Rathore KI, Berard JL, Redensek A, Chierzi S, Lopez-Vales R, Santos M, et al.** Lipocalin 2 Plays an Immunomodulatory Role and Has Detrimental Effects after Spinal Cord Injury. *J Neurosci*. 2011;31(38):13412–9. doi:10.1523/JNEUROSCI.0116-11.2011

391. **Nam Y, Kim J-H, Seo M, Kim J-H, Jin M, Jeon S, et al.** Lipocalin-2 Protein Deficiency Ameliorates Experimental Autoimmune Encephalomyelitis. *J Biol Chem*. 2014;289(24):16773–89. doi:10.1074/jbc.M113.542282

392. **Mucha M, Skrzypiec AE, Schiavon E, Attwood BK, Kucerova E, Pawlak R**. Lipocalin-2 controls neuronal excitability and anxiety by regulating dendritic spine formation and maturation. *Proc Natl Acad Sci*. 2011;108(45):18436–41. doi:10.1073/pnas.1107936108

393. **Nimer F Al, Elliott C, Bergman J, Khademi M, Dring AM, Aeinehband S, et al.** Lipocalin-2 is increased in progressive multiple sclerosis and inhibits remyelination. *Neurol Neuroimmunol Neuroinflammation*. 2016;3(1):e191. doi:10.1212/NXI.0000000000000191

394. **Ubil E, Caskey L, Holtzhausen A, Hunter D, Story C, Earp HS**. Tumor-secreted Pros1 inhibits macrophage M1 polarization to reduce antitumor immune response. *J Clin Invest*. 2018;128(6):2356–69. doi:10.1172/JCI97354

395. **Trapp BD, Ransohoff R, Rudick R**. Axonal pathology in multiple sclerosis: relationship to neurologic disability. *Curr Opin Neurol*. 1999;12(3):295–302. doi:10.1097/00019052-199906000-00008

396. **Singh S, Dallenga T, Winkler A, Roemer S, Maruschak B, Siebert H, et al.** Relationship of acute axonal damage, Wallerian degeneration, and clinical disability in multiple sclerosis. *J Neuroinflammation*. 2017;14(1):57. doi:10.1186/s12974-017-0831-8

397. **Criste G, Trapp B, Dutta R**. Axonal loss in multiple sclerosis. In: Handbook of clinical neurology. 2014. p. 101–13. doi:10.1016/B978-0-444-52001-2.00005-4

398. **Bjartmar C, Wujek J., Trapp B.** Axonal loss in the pathology of MS: consequences for understanding the progressive phase of the disease. *J Neurol Sci*. 2003;206(2):165–71. doi:10.1016/S0022-510X(02)00069-2

399. **Lassmann H, van Horssen J**. Oxidative stress and its impact on neurons and glia in multiple sclerosis lesions. *Biochim Biophys Acta - Mol Basis Dis*. 2016;1862(3):506–10. doi:10.1016/J.BBADIS.2015.09.018

400. **Dutta R, McDonough J, Yin X, Peterson J, Chang A, Torres T, et al.** Mitochondrial dysfunction as a cause of axonal degeneration in multiple sclerosis patients. *Ann Neurol*.

2006;59(3):478–89. doi:10.1002/ana.20736

401. **Rosenkranz SC, Shaposhnykov AA, Träger S, Engler JB, Witte ME, Roth V, et al.** Enhancing mitochondrial activity in neurons protects against neurodegeneration in a mouse model of multiple sclerosis. *Elife*. 2021;10:1–60. doi:10.7554/ELIFE.61798

402. **Giladi A, Wagner LK, Li H, Dörr D, Medaglia C, Paul F, et al.** Cxcl10+ monocytes define a pathogenic subset in the central nervous system during autoimmune neuroinflammation. *Nat Immunol*. 2020;21(5):525–34. doi:10.1038/s41590-020-0661-1

403. **Jordão MJC, Sankowski R, Brendecke SM, Sagar, Locatelli G, Tai Y, et al.** Single-cell profiling identifies myeloid cell subsets with distinct fates during neuroinflammation. *Science (80-)*. 2019;363(6425):eaat7554. doi:10.1126/science.aat7554

404. **Alvarez-Castelao B, Schanzenbächer CT, Hanus C, Glock C, Dieck S tom, Dörrbaum AR, et al.** Cell-type-specific metabolic labeling of nascent proteomes in vivo. *Nat Biotechnol 2017 3512*. 2017;35(12):1196–201. doi:10.1038/nbt.4016

405. **Mendel I, Yacov N, Salem Y, Propheta-Meiran O, Ishai E, Breitbart E**. Identification of Motile Sperm Domain–Containing Protein 2 as Regulator of Human Monocyte Migration. *J Immunol Author Choice*. 2017;198(5):2125. doi:10.4049/JIMMUNOL.1601662

406. **Yacov N, Kafri P, Salem Y, Propheta-Meiran O, Feldman B, Breitbart E, et al.** MOSPD2 is a therapeutic target for the treatment of CNS inflammation. *Clin Exp Immunol*. 2020;201(2):105–20. doi:10.1111/CEI.13448

Publications

Jafari, M., Schumacher, AM., Snaidero, N., *et al*. Phagocyte-mediated synapse removal in cortical neuroinflammation is promoted by local calcium accumulation. Nat Neurosci 24, 355–367 (2021). https://doi.org/10.1038/s41593-020-00780-7

(contributed to the computational re-analysis of snRNA-seq data from Schirmer *et at.*)

Tai, Y-H., *et al*. Targeting TCA cycle dysbalance can amend widespread axonal energy deficits in neuroinflammatory lesions. In preparation (2022)

(contributed to the computational analysis of the mitochondrial proteome)

Tai Y-H. Mitochondrial pathology in acute and chronic neuroinflammation. Dissertation. 2020.

(contributed to the computational analysis of the mitochondrial proteome)

Acknowledgments

I would like to thank Prof. Dr. Martin Kerschensteiner for the excellent scientific supervision and guidance at the Institute of Clinical Neuroimmunology and for creating an inspiring environment to grow ideas, insights and knowledge. Furthermore, I thank the whole team of the Kerschensteiner and Bareyre lab.

Prof. Dr. Mikael Simons and Prof. Dr. Veit Rothhammer were excellent theses committee members and very supportive during fruitful and helpful discussions about this project. Thank you.

I would like to thank Prof. Dr. Felix Meissner, Dr. Kshiti Meera Phulphagar and Jingyuan Cheng from the Max Planck Institute of Biochemistry for their great contribution and collaboration.

I thank Dr. Yi-Heng Tai for a fruitful internal collaboration on the mitochondria project.

I would like to thank Lea Merkel and Florian Hubl, who significantly contributed to unravel the transcriptomes and further assessed potential hits deriving from this project.

Last but not least, the biggest thanks goes to my mother, my grandparents and Charlotte.

Supplement

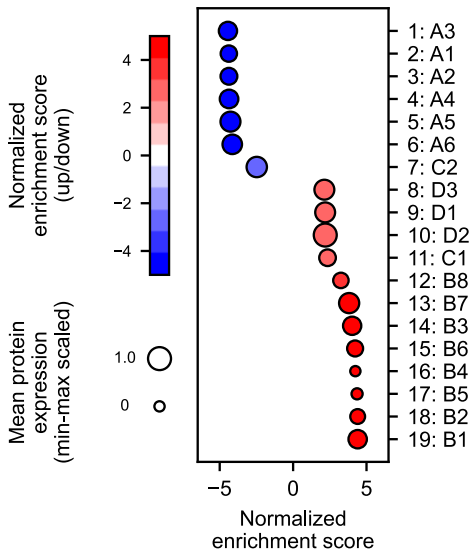

Supplement Figure 1: Graphical output from gene set enrichment analysis from the *NezzworGS* algorithm. Dots represent enriched gene sets. Their normalized enrichment score (NES) is color-coded. The dot size encodes the mean expression of the underlying proteins/genes (in this case drawn from a random distribution).

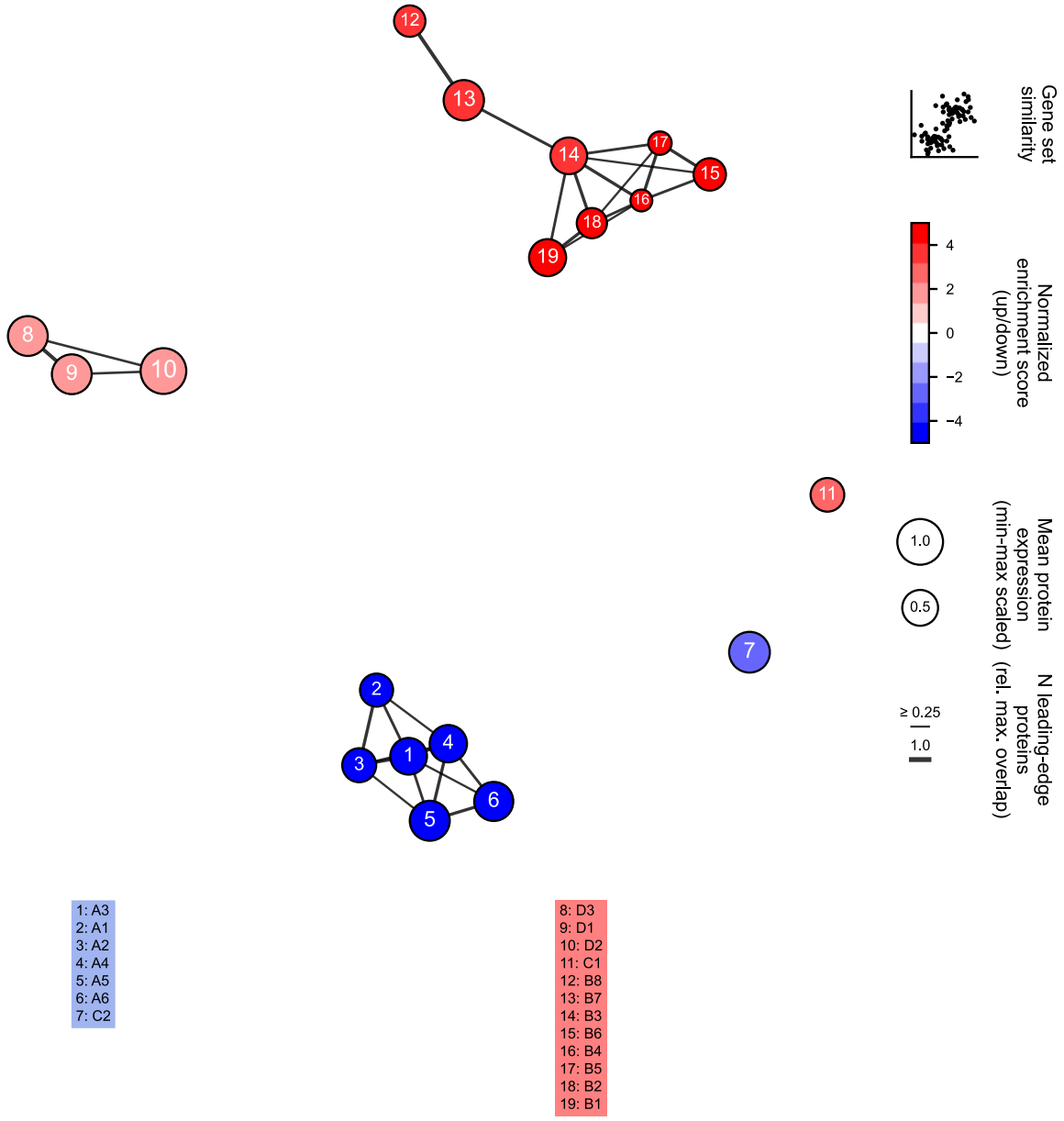

Supplement Figure 2: Graphical output from the network analysis (normalized enrichment scores) of gene sets enriched in the differential expression matrix (*NezzworGS*). Gene sets are displayed as vertices, their normalized enrichment score (NES) is color-coded. The area of each vertex represents the mean expression of the gene sets' underlying proteins/genes. The thickness of edges represents the fraction of leading-edge proteins/genes which two gene sets have in common (the highest fraction of the two gene sets was taken into account). The spatial distribution in the Cartesian space encodes the similarity of two gene sets as defined by the number of genes/proteins they share.

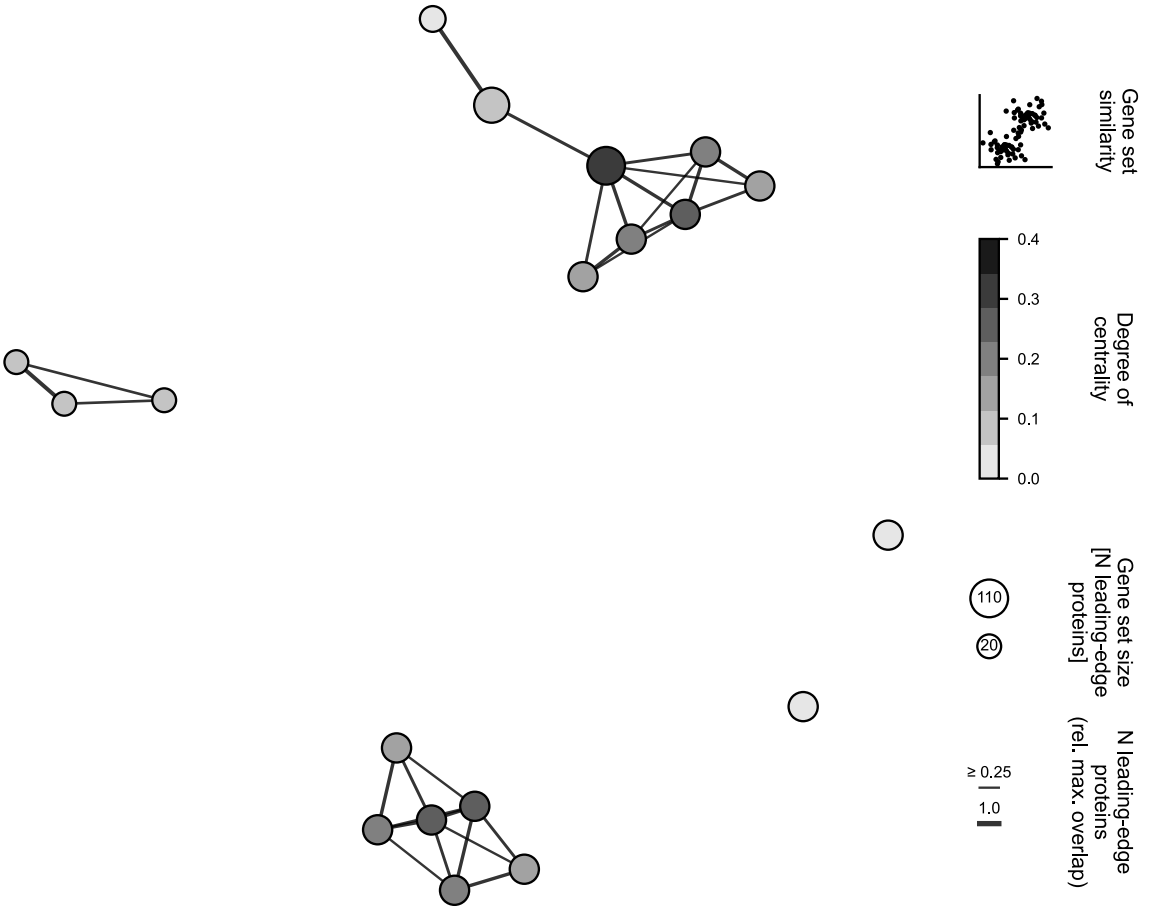

Supplement Figure 3: Graphical output from the network analysis (centrality) of gene sets enriched in the differential expression matrix (*NezzworGS*). Gene sets are displayed as vertices, their degree of centrality is color-coded. The area of each vertex represents the gene set size (number of underlying genes). The thickness of edges represents the fraction of leading-edge proteins/genes which two gene sets have in common (the highest fraction of the two gene sets was taken into account). The spatial distribution in the Cartesian space encodes the similarity of two gene sets as defined by the number of genes/proteins they share.

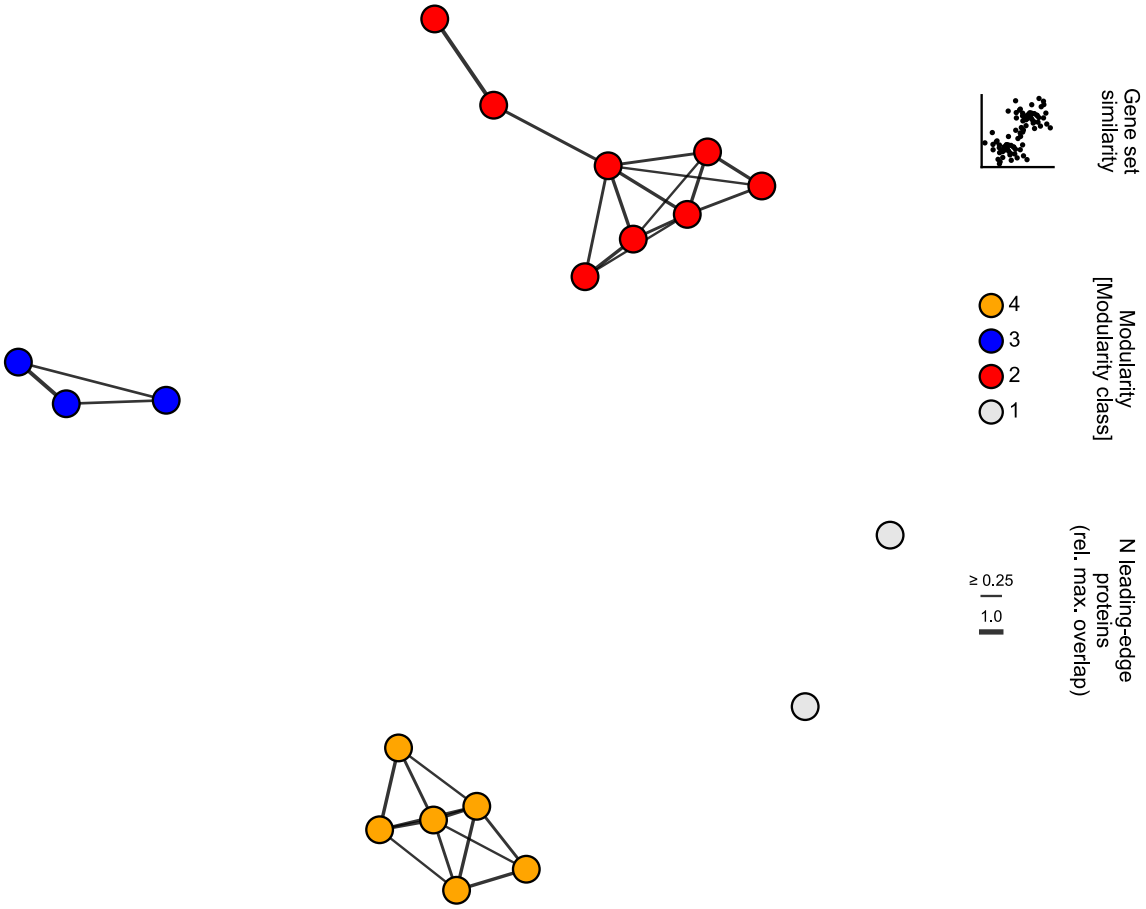

Supplement Figure 4: Graphical output from the network analysis (modularity) of gene sets enriched in the differential expression matrix (*NezzworGS*). Gene sets are displayed as vertices, their modularity class is color-coded. The spatial distribution in the Cartesian space encodes the similarity of two gene sets as defined by the number of genes/proteins they share.

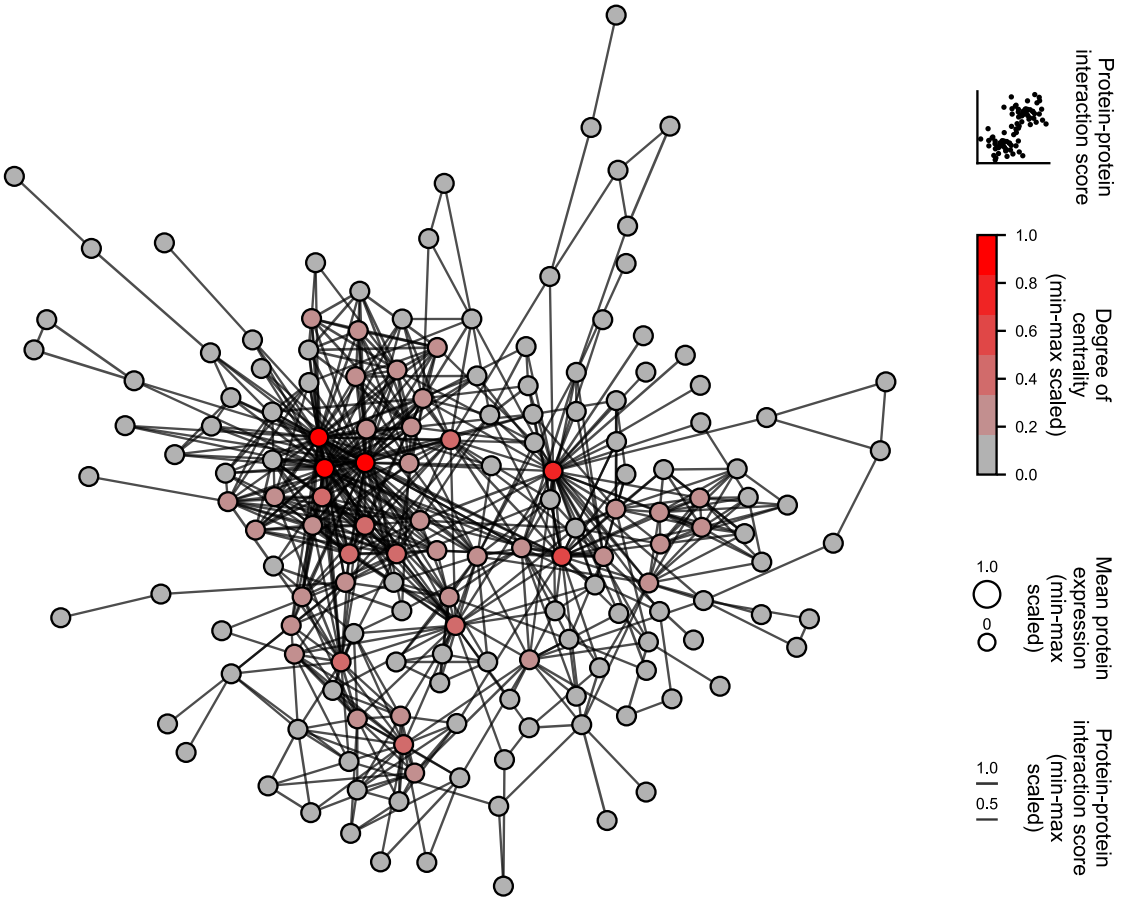

Supplement Figure 5: Functional protein-protein interaction network analysis (*FUPPINA*) of a random list of gene names. Nodes represent proteins/genes, edges display their functional protein-protein interaction according to the STRING database. The degree of centrality of each node was color-coded. The edge thickness as well as the distance between two nodes encode the protein-protein interaction score. Expression values were not taken into account and arbitrarily set to 1.

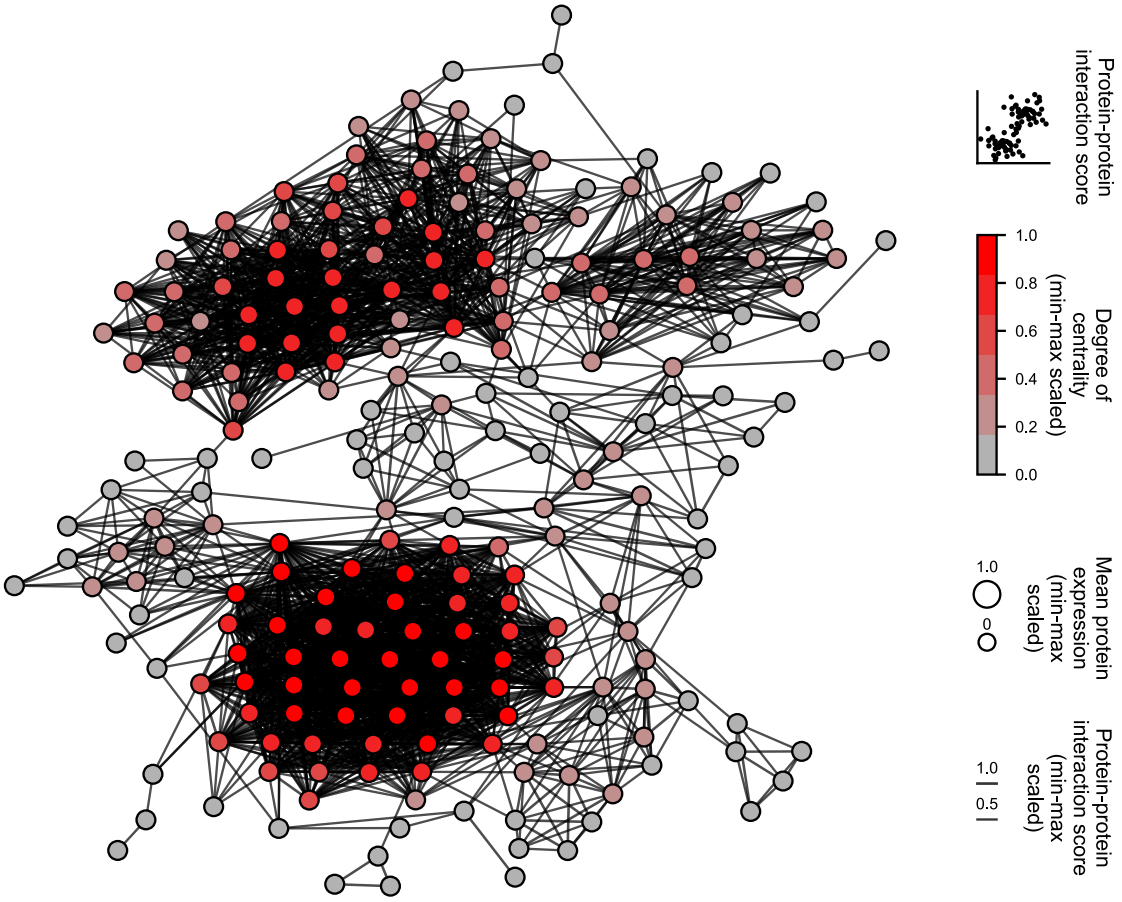

Supplement Figure 6: Functional protein-protein interaction network analysis (FUPPINA) of a list of gene names extracted from 5 randomly selected gene sets from the Reactome gene set library. Nodes represent proteins/genes, edges display their functional protein-protein interaction according to the STRING database. The degree of centrality of each node was color-coded. The edge thickness as well as the distance between two nodes encode the protein-protein interaction score. Expression values were not taken into account and arbitrarily set to 1.

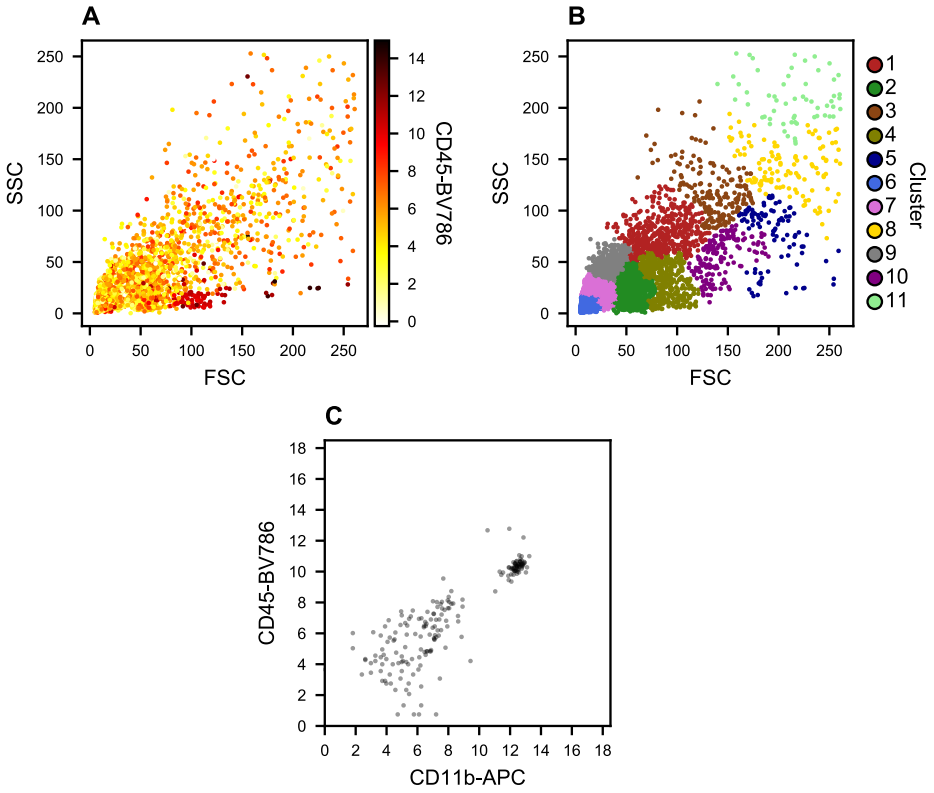

Supplement Figure 7: Flow cytometry analysis of cells isolated from the spinal cord of a healthy mouse. Single cell suspensions from the spinal cord from 1 healthy mouse. **A**: SSC/FSC analysis of all events. Log_2-transformed CD45-BV786 FI is color-coded. **B**: Unsupervised cluster analysis (agglomerative clustering) of events characterized by SSC and FSC. **C**: CD45-BV786 and CD11b-APC FI of $CD45^+$ cluster 4. Compared to EAE mice, there was only 1 $CD45^+CD11b^+$ cluster. SSC and FSC FI were divided by 10^3. All other FI were log_2-transformed. All FI are depicted as area of the signals. Maximum values (oversaturated signals) or minimum values (undersaturated signals) were excluded from the analysis. FI: fluorescence intensity

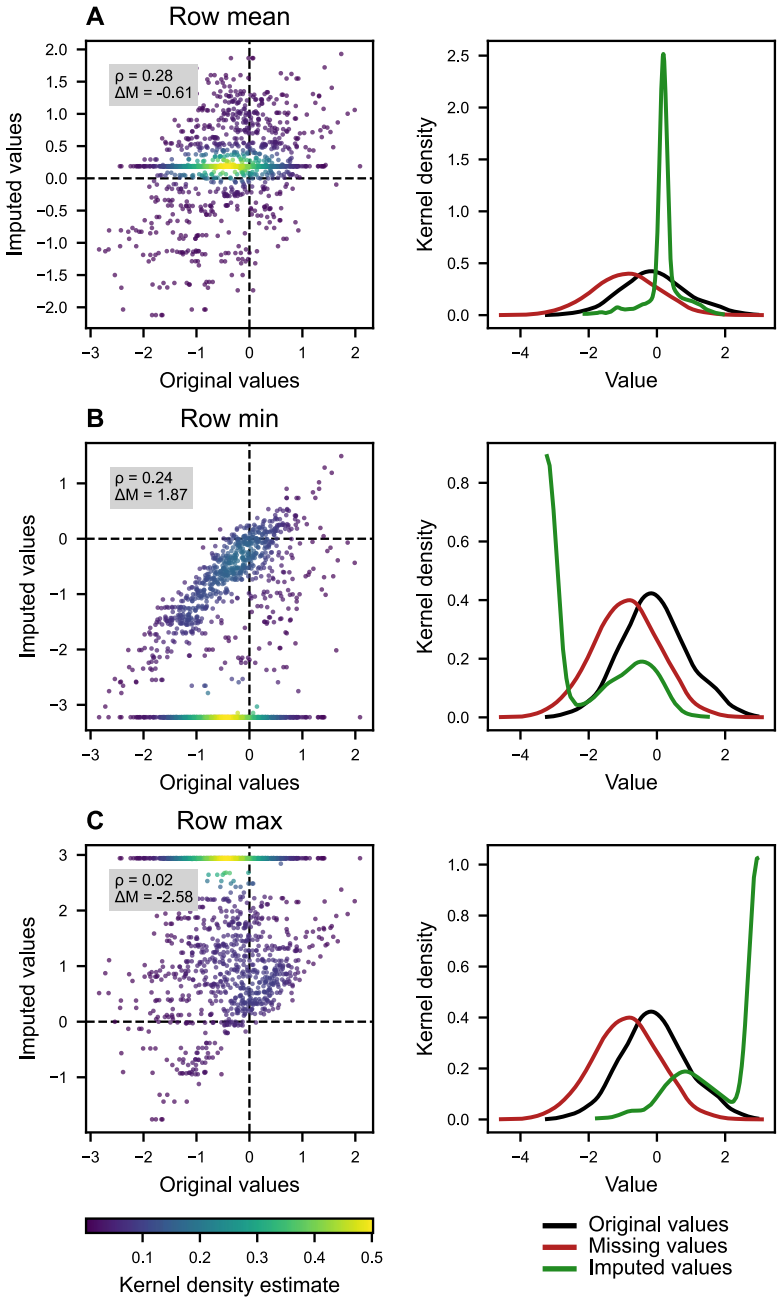

Supplement Figure 8: Single value imputations. Left panels: Correlation between original and imputed values of a test matrix. The probability density function was estimated using Gaussian kernels. Right panels: Distribution of the original, missing and imputed values. **A** – **C**: Different imputation algorithms applied to a test matrix with missing values mimicking the original dataset. The mean values of each protein in the test matrix were drawn from a standard normal distribution with the mean standard deviation of the protein expression values of the original dataset. Missing values were substituted by the row mean (**A**), row minimal (min, **B**) or row maximal (max, **C**) value, where each row represents one protein (r: Pearson's correlation coefficient, DM: difference in mean between original and imputed values).

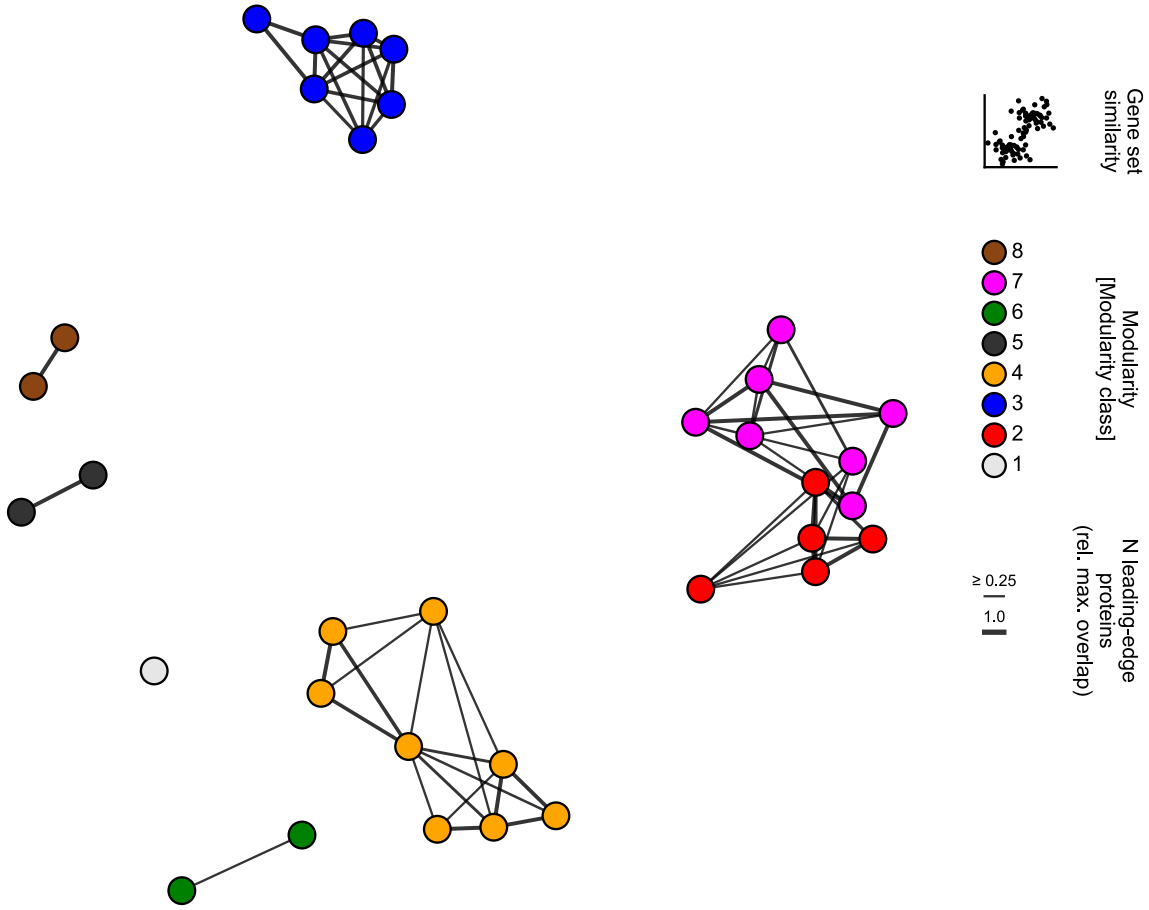

Supplement Figure 9: Gene set enrichment network analysis (Reactome) of M1 and M2 proteomes (modularity analysis). Proteins which were significantly differently expressed in M1 versus M2 macrophages ($|FC| > 1.5$ and $q \leq 0.05$) were subjected to gene set enrichment analysis (GSEA, Reactome). Gene sets are displayed as nodes. The color indicates to which module a node belongs. The thickness of edges represents the fraction of leading-edge proteins two gene sets have in common (the highest fraction of the two gene sets was taken into account). The spatial distribution in the Cartesian space encodes the similarity of two gene sets as defined by the number of genes/proteins they share.

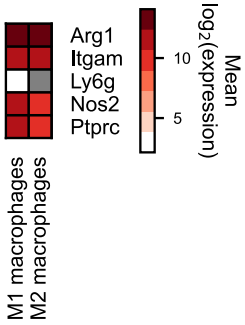

Supplement Figure 10: Gene expression of M1 and M2 signature genes. Mean logarithmic normalized expression of genes whose proteins were used to identify M1 and M2 macrophages for cell sorting (M1: $CD45^{+}CD11b^{+}Ly6G^{-}iNOS^{+}$ and M2: $CD45^{+}CD11b^{+}Ly6G^{-}Arginase\text{-}1^{+}$, *n* = 3 per group, from EAE onset, grey: not detected).

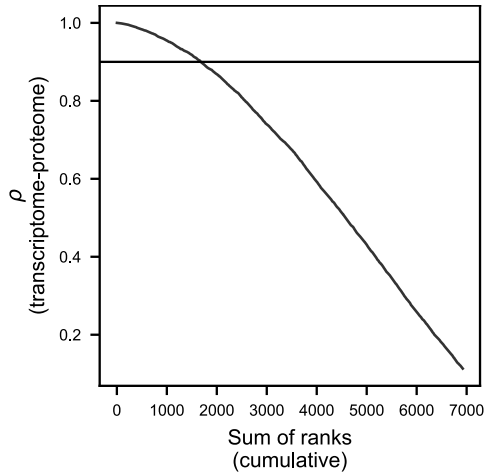

Supplement Figure 11: Correlation coefficients for the correlation between the transcriptome and proteome differential expression in M1 and M2 macrophages. The correlation coefficient was calculated for different numbers of proteins/transcripts from a sorted expression matrix (by the sum of ranks). The number of proteins/transcripts *n* reflects the proteins/transcripts with the *n*/2 uppermost and *n*/2 lowermost sum of ranks. The horizontal line indicates *r* = 0.9 with 838 uppermost and lowermost proteins/transcripts regarding their sum of ranks.

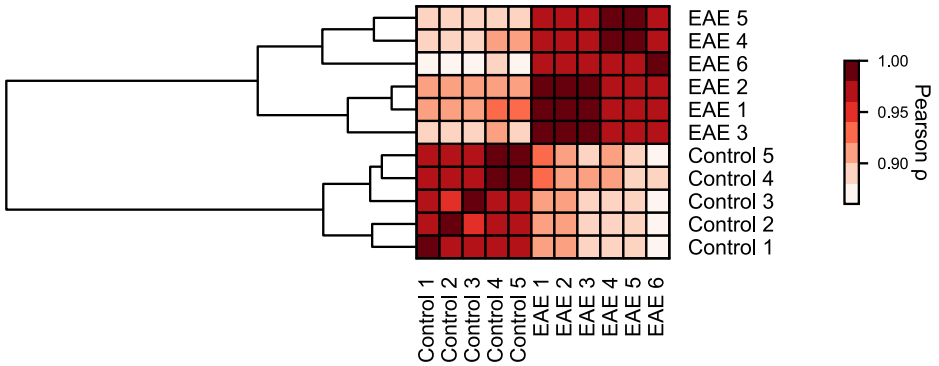

Supplement Figure 12: Correlation analysis of the neuronal mitochondrial proteomes from EAE and healthy controls. Color-coded correlation coefficients (Pearson) for the correlation between each sample acquired in this study. The dendrogram is based on the Euclidean distance between the correlation vectors and indicates the sample similarity.

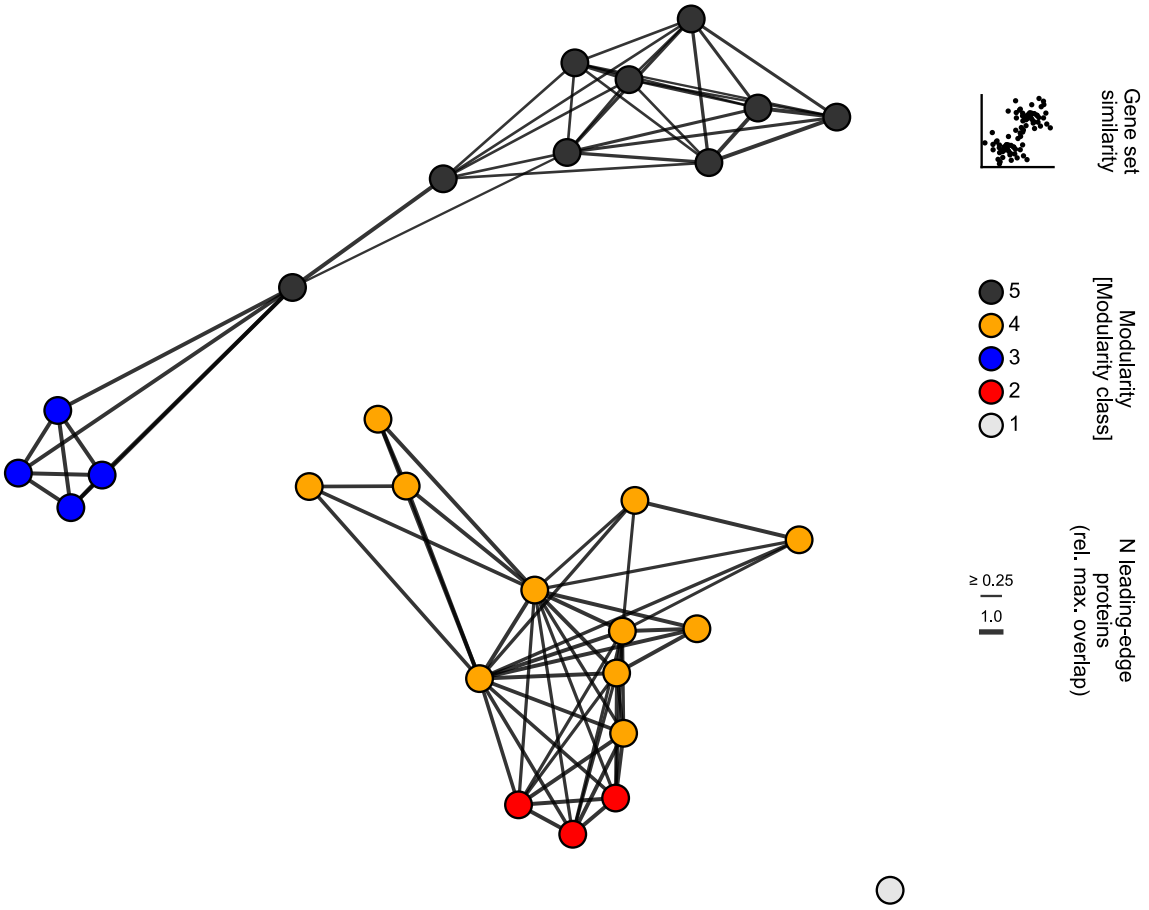

Supplement Figure 13: Gene set enrichment analysis (Reactome) of the neuronal mitochondria proteome in EAE and healthy control (modularity analysis). Nodes display gene sets, edges represent the relative maximal overlap of leading-edge proteins between two gene sets. The spatial distribution of nodes represents the similarity of two neighboring gene sets (as defined as the number of genes they have in common). Modularity classes are color-coded.

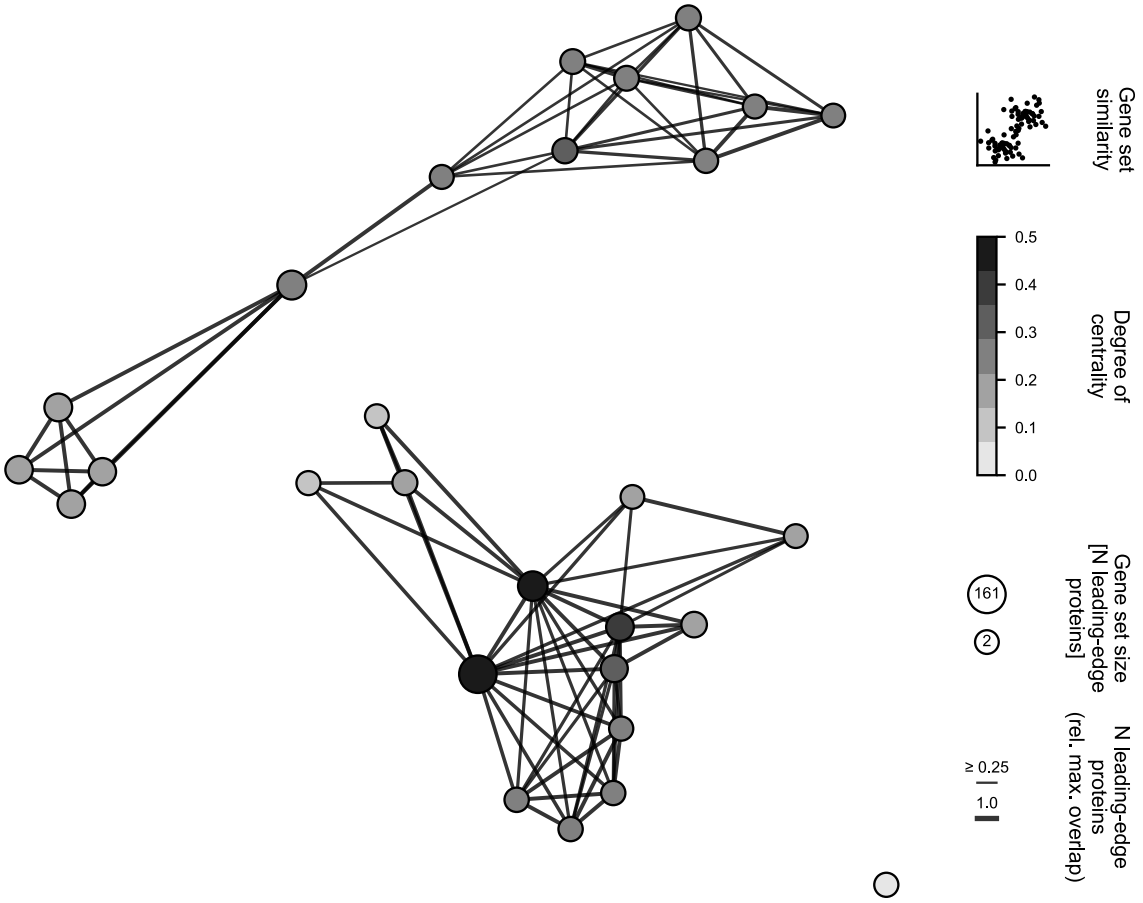

Supplement Figure 14: Gene set enrichment analysis (Reactome) of the neuronal mitochondria proteome in EAE and healthy control (degree of centrality). Nodes display gene sets and edges indicate the number of leading-edge proteins which two gene sets have in common. The area of the node encodes the number of leading-edge proteins in the respective gene set as a measure of the size of the gene set. The color of the node displays the degree of centrality. The spatial distribution of the nodes encodes the similarity of gene sets.

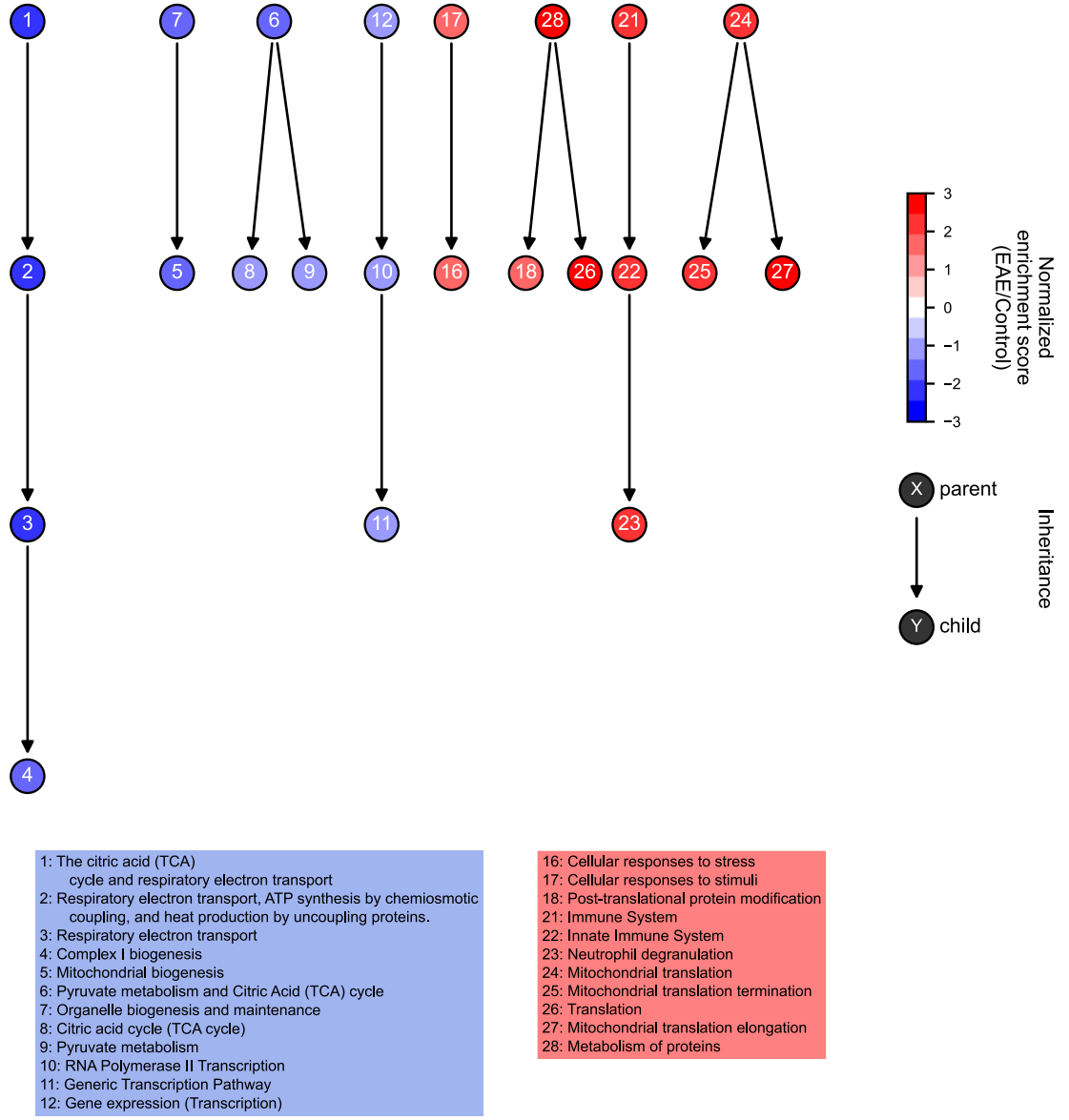

Supplement Figure 15: Gene set hierarchy analysis of gene sets enriched in the EAE and healthy control neuronal mitochondria proteome. Directed network analysis with vertices representing gene sets enriched in the EAE (normalized enrichment score > 0, red) or healthy control (normalized enrichment score > 0, blue) neuronal mitochondria proteome. Edges indicate the direction of inheritance.

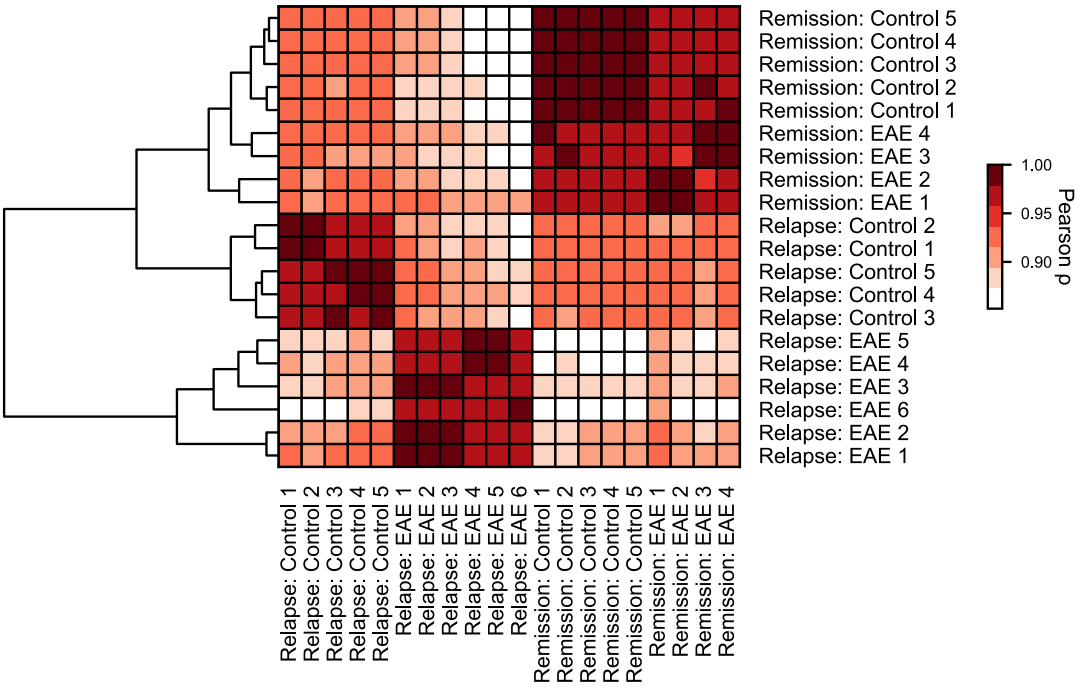

Supplement Figure 16: Correlation analysis of the neuronal mitochondrial proteomes from EAE and healthy controls at different time points of the disease course. Color-coded correlation coefficients (Pearson) for the correlation between each sample acquired in this study. The dendrogram is based on the Euclidean distance between the correlation vectors and indicates the sample similarity.

Finis operis